



Comprehensive approach of post-plasma catalytic process for trichloroethylene abatement in air on Cerium doped Birnessite-like MnO₂ through the study of O₃ and HCHO catalytic elimination

Grâce Abdallah

► To cite this version:

Grâce Abdallah. Comprehensive approach of post-plasma catalytic process for trichloroethylene abatement in air on Cerium doped Birnessite-like MnO₂ through the study of O₃ and HCHO catalytic elimination. Catalysis. Université de Lille; Universiteit Gent, 2021. English. NNT : 2021LILUR051 . tel-03917133

HAL Id: tel-03917133

<https://theses.hal.science/tel-03917133>

Submitted on 1 Jan 2023

HAL is a multi-disciplinary open access archive for the deposit and dissemination of scientific research documents, whether they are published or not. The documents may come from teaching and research institutions in France or abroad, or from public or private research centers.

L'archive ouverte pluridisciplinaire **HAL**, est destinée au dépôt et à la diffusion de documents scientifiques de niveau recherche, publiés ou non, émanant des établissements d'enseignement et de recherche français ou étrangers, des laboratoires publics ou privés.

Joint Doctoral Ph.D.

For the obtention of the degrees of

Doctor of Engineering delivered by
Ghent University, Doctoral school of (Bioscience) Engineering

AND

Doctor of "Molécules et Matière Condensée" delivered by
**Lille University, Doctoral school of Sciences of matter, radiation and environment,
Faculty of Sciences and Technologies**

Presented by
ABDALLAH Grêce

Defended on 17 December 2021

***Comprehensive Approach of Post-Plasma Catalytic Process for
Trichloroethylene Abatement in Air on Cerium Doped Birnessite-Like MnO₂
through the Study of O₃ and HCHO Catalytic Elimination***

Thesis supervision:

Rino MORENT, Professor, Ghent University

Co-director

Jean-François LAMONIER, Professor, Lille University

Co-director

Jean-Marc GIRAUDON, Associate Professor, Lille University

*Advisor for Lille
University*

Jury members:

Filip DE TURCK, Professor, Ghent University

*Co-Chair
Chair*

Patrick DA COSTA, Professor, Sorbonne University

Examiner

Anton NIKIFOROV, Doctor, Ghent University

Reviewer

Jean-Marc CLACENS, Director of research CNRS, Poitiers University

Reviewer

Cyril THOMAS, Research associate CNRS, Sorbonne University

Examiner

Jean-Marc GIRAUDON, Associate Professor, Lille University

THESE EN COTUTELLE

Pour obtenir le grade de

Docteur en «Ingénierie» délivré par
Université de Gand, Ecole Doctorale d'Ingénierie (Biosciences)

ET

Docteur en « Molécules et Matière Condensée » délivré par
**Université Lille, Ecole Doctorale Sciences de la Matière, du Rayonnement et de
l'environnement, Faculté des Sciences et Technologies**

Présentée par
ABDALLAH Grêce

Soutenue le 17 Décembre 2021

***Approche Intégrée du Processus Post-Plasma Catalyse pour l'Abattement du
Trichloréthylène dans l'Air en Présence de MnO_2 de Type Birnessite Dopé au Cérium,
par l'Etude de l'Elimination Catalytique de O_3 et de $HCHO$***

Encadrement de la thèse:

***Rino MORENT, Professeur, Université de Gand
Jean-François LAMONIER, Professeur, Université de Lille
Jean- Marc GIRAUDON, Maître de Conférences, Université de Lille***

***Co-directeur
Co-directeur
Co-encadrant
pour Université
de lille***

Membres du jury:

***Filip DE TURCK, Professeur, Université de Gand
Patrick DA COSTA, Professeur, Université de Sorbonne
Anton NIKIFOROV, Docteur, Université de Gand
Jean-Marc CLACENS, Directeur de recherche CNRS, Université de Poitiers
Cyril THOMAS, Chargé de recherche CNRS, Université de Sorbonne
Jean-Marc GIRAUDON, Maître de Conférences, Université de Lille***

***Co-Président
Président
Examineur
Rapporteur
Rapporteur
Examineur***



This research was supported by a grant from “INTERREG V France-Wallonie-Flanders (FEDER) (DepollutAir)”, “GoToS3” and “Union Européenne Europese Unie”.

Summary

The world health organization (WHO) estimates the number of deaths due to pollution to be around 9 million per year, which corresponds to 20% of deaths in the worldwide. In Europe 800000 deaths per year are due to air pollution. Poor air quality also greatly increases the death rate from Covid-19.

Among air pollutants, Volatile Organic Compounds (VOCs) are considered as major contributors for air pollution. Indeed, they propagate in the air causing dangerous impact on human health as well as on the environment. Their transformation in the atmosphere result in the formation of tropospheric ozone and photochemical smog. On the other hand, they enhance the greenhouse effect and the destruction of the stratospheric ozone. In addition, VOCs have been proven to be toxic and/or carcinogenic for human health. European legislation has imposed stricter objectives to reduce VOC emissions. The current policy consists in priority to limit the use these compounds, but if it is not possible for technical reasons, it is required to find adequate techniques for radical reduction of VOC emissions. Conventional VOCs removal techniques, such as thermal oxidation, adsorption, condensation, biological oxidation and catalytic oxidation are linked with high energy cost especially when the concentration of VOCs is low.

As a cost and energy efficient alternative, the use of non-thermal plasma (NTP) offers interesting prospects for the removal of a low concentration of pollutants from the air at high flow rates. NTP is quite different from thermal plasma generated by plasma torches and arc discharges. The main advantage of NTP is that the energy delivered to the plasma source is almost entirely consumed to accelerate electrons while the background gas remains near room temperature, so preventing feed gas heating. Another important feature is related to the operation at atmospheric pressure which excludes the use of expensive vacuum equipment. In addition, NTP is characterized by its quick start-up and compact size. Electron impacts cause dissociation, ionization of the background gas and radical production which leads to the decomposition of the targeted VOCs.

Although NTP has been proposed in literature as a possible technology for air cleaning, the formation of undesired gaseous by-products (ozone, NO_x, aerosols and other VOCs) which increase the overall toxicity of the treated gas stream, remains serious roadblocks towards industrial applications. To overcome these technological issues, the combination of NTP and heterogeneous catalysis in a technique called plasma-catalysis has become a hot research topic over the last two decades. In a plasma-catalysis system there are two ways to introduce the

catalyst into the plasma: In Plasma Catalysis (IPC) the catalyst is located in the plasma discharge and in Post Plasma Catalysis (PPC) the catalyst is located downstream of the plasma discharge. As well, the choice of a suitable catalyst will help to optimize the selectivity into environmentally more friendly end products.

The treatment of air pollution by a hybrid system 'NTP and heterogeneous catalysis' requires the development of more accurate experimental conditions and new catalytic systems always more efficient to reduce the energy cost. This doctoral thesis is focused on the use PPC for the abatement of trichloroethylene (TCE), a typical chlorinated volatile organic compound used mainly in industries as a degreaser, diluted in dry/humid air.

In this context, different issues have been established during this thesis work in order to optimize the PPC process. One of the key issues has been to take maximum advantage of NTP generated ozone as a potential source of active oxygen species for the complete oxidation of the NTP generated partially oxidized gaseous compounds at low temperature (100 °C). In that way, the $[O_3]/[TCE]_0$ molar ratio has been adapted to 4, in accordance with the formal reaction of TCE oxidation by O_3 : $C_2Cl_3H + 4O_3 \rightarrow 2CO_2 + HCl + Cl_2 + 4O_2$ by playing on different important parameters such as air flow rate, humidity as well as specific energy input.

The choice of the appropriate catalyst has been made considering some basic requirements such as its ozone decomposition capability, oxygen mobility, high CO_2 selectivity in VOC total oxidation catalysis coupled with chlorine and water tolerance. Birnessite (δ - MnO_2) doped or not with Ce, Ce_xMn ($x = 0.01, 0.1, 0.2$ and 0.5) were prepared from a simple, fast and inexpensive redox reaction performed at 25°C involving potassium permanganate with or without cerium nitrate and sodium lactate. Particular attention has been paid to the activation mode of the catalyst through calcination or acid treatment. These materials have been characterized by a wide variety of physico-chemical analysis techniques and tested for NTP generated ozone decomposition or formaldehyde catalytic oxidation. Afterwards, the best catalysts in each reaction have been used for TCE abatement in dry/humid air in PPC configuration.

The manuscript is divided into 7 chapters. The first chapter outlines an overview of the literature on air pollution (sources, effects on human health as well as on environment, cleaning technologies). Then, the main features of using MnO_x as a catalyst allowing better performances in the reactions expected to occur in the abatement of trichloroethylene in PPC configuration have been reviewed. After that, the use of plasma as an ozoner, including the effect of different factors on ozone production are summarized and as a second step the main features of using

manganese dioxides, in particular birnessite based catalyst for ozone decomposition doped or not with transition metals (Ce) and treated or not with acid, are detailed. In this respect, the structures and physico-chemical characteristics of birnessite are reviewed. Finally, in a last part, the current state of the use of birnessite as a catalyst for the oxidation of formaldehyde (HCHO) in order to give us more information related to the catalytic performances and catalyst structure is discussed. The objective, strategy and methodology of this work are given in **chapter 2**. The details of the experimental conditions used for the characterizations and synthesis of the different materials as well as the experimental conditions followed for the different catalytic tests are presented in **chapter 3**. The **fourth** chapter is devoted to formaldehyde catalytic oxidation in order to highlight a correlation between oxygen mobility and catalytic activity. The effects of Ce content, temperature of calcination and relative humidity on the catalytic properties have been particularly discussed. It has been shown that the MnO₂ catalysts modified by low amount of Ce ($x = 0.01$ and 0.1) calcined at 400 °C showed the best catalytic properties towards HCHO total oxidation and good stability in humid air. Numerous Ce-O-Mn interactions as well as high Mn³⁺/Mn⁴⁺ and low Ce³⁺/Ce⁴⁺ ratios have been believed to enhance oxygen mobility at low temperature which may explain the better efficiency of these catalysts.

The **fifth** chapter investigates ozone and nitrogen oxide formations in dry/moist air using a negative DC (Direct Current) corona discharge at atmospheric pressure in a 10-pin-to-plate reactor. The effect of flow rate (Q), Energy density (ED) and relative humidity (RH) are discussed. It has been shown that ozone production increases as a function of ED and Q while it decreases as a function of RH. **Chapter 6** presents the results of NTP generated ozone decomposition at low temperature (20 - 40 °C) in dry/moist air over the Ce doped birnessites (Ce/Mn = 0, 0.01, 0.1, 0.2 and 0.5) treated with nitric acid (0.2M HNO₃, at 50°C for 6 hours) to be compared to the fresh ones. It has been shown that the acid-treated Ce_{0.01}MnO_x catalysts is the most efficient towards O₃ decomposition. The beneficial effect of acid treatment has been ascribed to high density of active sites in line with high density of oxygen vacancies and active sites.

Finally, in the last chapter TCE abatement in PPC configuration has been investigated over the two best catalysts in terms of formaldehyde oxidation and ozone decomposition. Plasma assisted acid-treated Ce_{0.01}MnO_x catalyst shows the best CO₂ yield with a minimization of gaseous chlorinated by-products as compared to Ce_{0.01}MnO_x calcined at 400°C. Such results

can be linked concomitantly to the introduction of acid sites allowing a better activation of TCE and to an increase of active sites in accordance with enhanced specific surface areas.

Samenvatting

De Wereldgezondheidsorganisatie (WHO) schat het aantal sterfgevallen als gevolg van luchtverontreiniging op ongeveer 9 miljoen per jaar, wat overeenkomt met 20% van het totaal aantal sterfgevallen wereldwijd. In Europa zijn 800000 sterfgevallen per jaar te wijten aan luchtverontreiniging. Een slechte luchtkwaliteit verhoogt ook het sterftecijfer door covid-19 aanzienlijk.

Onder de luchtverontreinigende stoffen worden vluchtige organische stoffen (VOS) beschouwd als de belangrijkste veroorzakers van luchtverontreiniging. Ze verspreiden zich in de lucht en hebben een negatief effect op de menselijke gezondheid en het milieu. Hun omzetting in de atmosfeer leidt tot de vorming van troposferisch ozon en fotochemische smog. Anderzijds versterken zij het broeikasgaseffect en zijn ze verantwoordelijk voor de vernietiging van de stratosferisch ozon. Bovendien is bewezen dat VOS toxisch en/of carcinogeen zijn voor de menselijke gezondheid. De Europese wetgeving heeft daarom strengere doelstellingen opgelegd om de VOS-emissies te verminderen. Het huidige beleid bestaat erin prioriteit te geven aan het niet gebruiken van VOS, maar indien dit om technische redenen niet mogelijk is, is het nodig om adequate technieken te vinden voor een radicale vermindering van de VOS-emissies. De conventionele VOS-verwijderingstechnieken, zoals thermische oxidatie, adsorptie, condensatie, biologische oxidatie en katalytische oxidatie, gaan gepaard met hoge energiekosten, vooral wanneer de VOS concentratie te laag is.

Als kost- en energie-efficiënt alternatief biedt het gebruik van niet-thermisch plasma (NTP) interessante vooruitzichten voor de verwijdering van lage concentraties verontreinigende stoffen uit de lucht bij hoge debieten. Niet-thermisch plasma verschilt sterk van thermisch plasma dat door plasmatoortsen en boogontladingen wordt gegenereerd. NTP's, zogenaamde koude plasma's, blijken efficiënter te zijn dan de conventionele technieken. Het belangrijkste voordeel van NTP is dat de aan de plasmabron geleverde energie bijna volledig wordt verbruikt om elektronen te versnellen, terwijl het achtergrondgas dicht bij kamertemperatuur blijft, zodat verhitting van het voedingsgas voorkomen wordt. Een ander belangrijk voordeel is de werking ervan bij atmosferische druk, waardoor het gebruik van een uitgebreide vacuüminstallatie vermeden wordt. Bovendien wordt NTP gekenmerkt door zijn snelle opstart en compacte afmetingen. Ook kunnen gemengde afvalstromen worden behandeld met niet-thermisch plasma. De elektronen impact dissociatie en ionisatie van het achtergrondgas veroorzaken radicaalproductie die leidt tot de afbraak van de beoogde VOS.

Hoewel NTP voor luchtreiniging vaak in de literatuur is voorgesteld, blijft de vorming van ongewenste nevenproducten (ozon, NO_x, aerosols, fosgeen en andere VOS), die de algemene toxiciteit van de behandelde gasstroom verhogen, een ernstige hinderpaal voor industriële toepassingen. Om deze problemen op te lossen, is de combinatie van NTP en heterogene katalyse een techniek die plasmakatalyse wordt genoemd, de laatste twee decennia een populair onderzoeksthema geworden. In een plasmakatalyse-systeem zijn er twee manieren om de katalysator in het plasma te brengen: In Plasma katalyse (IPC) waarbij de katalysator zich in de plasmaontlading bevindt en Post Plasma katalyse (PPC) waarbij de katalysator zich stroomafwaarts van de plasmaontladingen bevindt. Ook zal de keuze van een geschikte katalysator helpen om de selectiviteit naar milieuvriendelijke eindproducten te optimaliseren.

De behandeling van luchtvervuiling door een hybride systeem 'Niet-Thermisch Plasma (NTP) en heterogene katalyse' vereist de optimalisatie van de experimentele condities en de ontwikkeling van nieuwe katalytische systemen die steeds efficiënter zijn om de energiekost te reduceren. Dit proefschrift richt zich in het bijzonder op de koppeling van plasmakatalysetechnologieën, voor de reductie van trichloorethyleen (TCE), een gechloreerde vluchtige organische verbinding die voornamelijk in de industrie als ontvetter wordt gebruikt.

In het kader van de vermindering van trichloorethyleen door Post-Plasma Katalyse werden tijdens dit thesiswerk verschillende parameters onderzocht om het PPC-proces te optimaliseren. Een van de belangrijkste parameters was het benutten van de door de NTP uitgestoten ozon als een potentiële bron van actieve zuurstofsoorten voor de verdere oxidatie bij zeer lage temperatuur (100 °C) van onbehandeld trichloorethyleen en van de potentiële gasvormige gevaarlijke bijproducten van de NTP. Aldus werd de molaire verhouding [O₃] / [TCE]₀ aangepast tot 4, in overeenstemming met de formele reactie van TCE-oxidatie door O₃: $\text{C}_2\text{Cl}_3\text{H} + 4\text{O}_3 \rightarrow 2\text{CO}_2 + \text{HCl} + \text{Cl}_2$ door het variëren van de verschillende sleutelparameters zoals energiedichtheid, debiet en vochtigheid van de NTP.

Bij de keuze van de katalysator werd rekening gehouden met een aantal basisvereisten zoals ozonafbraakvermogen, zuurstofmobiliteit, en hoge CO₂-selectiviteit gekoppeld aan chloor- en watertolerantie. Birnessiet (δ-MnO₂) al dan niet gedoteerd met Ce, Ce_xMn (x= 0.01, 0.1, 0.2 en 0.5) werd gesynthetiseerd via een eenvoudige, snelle en goedkope redoxreactie van kaliumpermanganaat en natriumlactaat bij omgevingstemperatuur met toevoeging van ceriumnitraat. Deze reacties werden uitgevoerd in een overmaat KMnO₄ (69 %). Bijzondere aandacht werd besteed aan de activeringsmodus van de katalysator door de invloed van de calcinatietemperatuur na te gaan. De katalysator werd gecalcineerd bij 200, 300 en 400°C. Ook

werd een zuurbehandeling uitgevoerd om de tolerantie voor chloor en water te verhogen. Deze verschillende materialen werden gekarakteriseerd door middel van diverse analysetechnieken en getest als katalysator voor de TCE-reductie in een PPC-configuratie, voor ozonafbraak gebruikmakende van plasma als ozonisator en ook voor de formaldehyde katalytische oxidatie.

Het proefschrift is onderverdeeld in 7 hoofdstukken. In het eerste hoofdstuk wordt een overzicht gegeven van de literatuur omtrent luchtverontreiniging (bronnen, effect op de menselijke gezondheid en op het milieu, zuiveringstechnologieën). Vervolgens worden de belangrijkste kenmerken van het gebruik van MnO_x als katalysator bij de bestrijding van trichloorethyleen in een PPC-configuratie besproken. Daarna wordt een overzicht gegeven van het gebruik van plasma als ozonisator, inclusief het effect van verschillende factoren op de ozonproductie. In een tweede stap worden de belangrijkste kenmerken van het gebruik van mangaandioxide, met name katalysatoren op basis van birnessiet voor de ontleding van ozon, al dan niet gedoteerd met overgangsmetalen (Ce) en al dan niet behandeld met zuur, in detail besproken. In dit verband worden de structuren en kenmerken van birnessiet onder de loep genomen. Tenslotte wordt in een laatste deel de huidige stand van zaken van het gebruik van birnessiet als katalysator voor de oxidatie van formaldehyde (HCHO) besproken om ons meer informatie te verschaffen met betrekking tot de katalytische prestaties en de katalysatorstructuur. De doelstrategie en methodologie van dit werk worden besproken in hoofdstuk 2. De technieken die werden gebruikt voor de karakterisering en de synthese van de verschillende materialen, evenals de experimentele katalytische condities, worden gepresenteerd in hoofdstuk 3. Het vierde hoofdstuk is gewijd aan het bespreken van de resultaten rond de formaldehyde katalytische oxidatie, om een correlatie tussen de hoeveelheid zuurstof *vacancies* en de katalytische activiteit te benadrukken. Verschillende parameters worden besproken, zoals het effect van het Ce-gehalte, de calcinatietemperatuur en de relatieve vochtigheid. Er werd aangetoond dat katalysatoren met een laag Ce-gehalte ($x = 0,01$ en $0,1$), gecalcineerd bij $400\text{ }^\circ\text{C}$, het meest efficiënt zijn door een verbeterde lokale omgeving van de actieve sites, gekoppeld aan talrijke Ce-O-Mn interacties, een hoge $\text{Mn}^{3+}/\text{Mn}^{4+}$ atoomverhouding, een lagere $\text{Ce}^{3+}/\text{Ce}^{4+}$ ratio, en een hoge mobiliteit van zuurstof bij lage temperatuur. Het vijfde hoofdstuk presenteert de vorming van ozon en gelijktijdige stikstofoxiden door negatieve DC (gelijkstroom) corona-ontlading bij atmosferische druk met behulp van een 10-pins-to-plate reactor. Het effect van het debiet (Q), de energiedichtheid (ED) en de relatieve vochtigheid worden besproken. Er werd aangetoond dat de ozonproductie toeneemt in functie van de energiedichtheid en het debiet, terwijl deze afneemt in functie van

de relatieve vochtigheid. In hoofdstuk 6 wordt de afbraak van ozon door Ce-gedoteerd birnessiet, al dan niet behandeld met salpeterzuur, onderzocht bij lage temperatuur (20 - 40 °C). Het effect van het Ce-gehalte ($\text{Ce/Mn} = 0, 0.01, 0.1, 0.2$ en 0.5), de behandeling met salpeterzuur (0.2M HNO_3 , bij 50 °C gedurende 6 uur), en de stikstofhoudende co-polluenten en water worden besproken. Hieruit bleek dat de met zuur behandelde lage Ce-katalysatoren het meest efficiënt zijn door de aanwezigheid van een grote hoeveelheid zuurstof *vacancies* in lijn met de aanwezigheid van een grote hoeveelheid zuur sites. Tenslotte wordt in het laatste hoofdstuk de TCE reductie in het PPC proces besproken. De twee beste katalysatoren voor formaldehyde-oxidatie en ozonafbraak werden gekozen. De plasma-geassisteerde $\text{Ce}_{0.01}\text{Mn}$ katalysator behandeld met zuur geeft de beste CO_2 opbrengst met een minimale vorming van gasvormige gechloreerde bijproducten in vergelijking met $\text{Ce}_{0.01}\text{Mn}$ gecalcineerd bij 400 °C . Beide katalysatoren vertonen een goede stabiliteit ten opzichte van chloor en water in functie van de tijd. Deze resultaten worden toegeschreven aan een hoog gehalte aan zuurstof vacancies met een hoger gehalte aan Mn^{3+} , aan een verbeterd specifiek oppervlak en aan een sterke zuurtegraad van het oppervlak.

Résumé

L'optimisation du traitement d'oxydation de COVs par un système hybride PPC (Post-Plasma Catalyse) nécessite de travailler dans des conditions expérimentales appropriées en utilisant des systèmes catalytiques toujours plus efficaces pour optimiser les rendements en CO_2 et réduire les coûts énergétiques. Pour ce faire, on a étudié l'oxydation catalytique du trichloroéthylène (TCE), un composé organique chloré volatil, par PPC en s'attachant à bénéficier au mieux des effets bénéfiques de l'ozone généré par le plasma en sortie de réacteur pour le décomposer en oxygènes actifs devant permettre une meilleure minéralisation du COV chloré.

L'un des points clés était de bénéficier de l'ozone émis par le NTP comme source potentielle d'espèces réactives de l'oxygène pour une oxydation à très basse température (100°C) du trichloréthylène non traité par le plasma et des sous-produits gazeux potentiellement dangereux du NTP. Ainsi, le rapport molaire $[\text{O}_3]/[\text{TCE}]_0$ a été adapté à 4, conformément à la réaction d'oxydation du TCE par O_3 , en jouant sur différents paramètres clés tels que la densité énergétique, le débit et l'humidité du NTP. De plus, le choix du catalyseur a été fait en tenant compte de sa capacité à décomposer l'ozone, sa mobilité de l'oxygène et sa sélectivité élevée en CO_2 en oxydation complète de COVs couplée à une bonne tolérance au chlore et à l'eau. Dans ce travail, des birnessites ($\delta\text{-MnO}_2$) dopées ou non avec le Ce, Ce_xMn ($x = 0.01, 0.1, 0.2$ et 0.5) ont été préparées à partir d'une réaction redox simple, rapide et peu coûteuse, utilisant du permanganate de potassium et du lactate de sodium à température ambiante avec ajout de nitrate de cérium. Une attention particulière a été portée sur le mode d'activation du catalyseur par modulation de la température de calcination. Un traitement acide a été également effectué pour améliorer la tolérance à l'eau et au chlore. En termes d'activité catalytique, trois approches ont été adoptées. Dans une première partie, ces catalyseurs ont été testés pour l'oxydation catalytique du formaldéhyde afin de mettre en évidence une corrélation entre l'activité catalytique et la mobilité d'oxygène. Il a été montré que les catalyseurs à faible teneur en Ce ($x = 0,01$ et $0,1$) calcinés à 400°C sont les plus efficaces en raison d'un meilleur environnement local des sites actifs lié à de nombreuses interactions Ce-O-Mn, d'un rapport atomique élevé $\text{Mn}^{3+}/\text{Mn}^{4+}$, d'un rapport $\text{Ce}^{3+}/\text{Ce}^{4+}$ plus faible et d'une forte mobilité de l'oxygène à basse température. Dans une deuxième partie, il a été montré l'efficacité des catalyseurs à faible teneur en Ce traités à l'acide en termes de décomposition de l'ozone en présence de co-polluants azotés produits par le PNT en utilisant l'air comme flux gazeux. L'efficacité de ces catalyseurs

a été expliquée par la présence concomitante d'une grande quantité de lacunes d'oxygène en interaction avec des sites acides générés par le traitement acide. Enfin, les deux meilleurs catalyseurs en termes d'oxydation du formaldéhyde et de la décomposition de l'ozone générée par PNT ont été choisis pour l'oxydation complète du TCE sous air en configuration PPC à 100°C. Le catalyseur $\text{Ce}_{0.01}\text{Mn}$ traité à l'acide présente un meilleur rendement en CO_2 avec une minimisation de la formation de sous-produits organiques chlorés gazeux par comparaison avec le catalyseur $\text{Ce}_{0.01}\text{Mn}$ calciné à 400°C. Ces deux catalyseurs présentent néanmoins une stabilité relative vis-à-vis du chlore et de l'eau en fonction du temps. Une surface spécifique plus importante, une forte densité de lacunes d'oxygène et de sites acide, une valeur élevée du rapport $\text{Mn}^{3+}/\text{Mn}^{4+}$ permettent de rendre compte du meilleur comportement du catalyseur $\text{Ce}_{0.01}\text{Mn}$ traité à l'acide Pour l'oxydation du TCE en configuration PPC.

Acknowledgements

As Helen Keller once said “Alone we can do so little. Together we can do so much”. This doctoral dissertation is the result of the collective effort of various researchers, scientists, mentors and a team of wonderful people. I would like to take this opportunity to sincerely thank everyone who has helped and supported me over the past four years to make my dream a reality.

First of all, I would like to express my sincere gratitude towards, Prof. Dr. Rino Morent, Prof. Dr. Jean-François Lamonier and Assistant Professor Dr. Jean Marc Giraudon for offering me the opportunity to carry out this doctoral dissertation in Ghent and Lille Universities.

I would like to express my appreciation to Assistant Professor Dr. Jean Marc Giraudon, with whom I had the opportunity to benefit from his experience. Your enthusiasm and willingness in helping me plan my experiments and those stimulating discussions really inspired me to give my best. Without your enormous expertise I would never be able to succeed to grasp the complexity of the plasma-catalytic processes. I also want to say thank you to Prof. Dr. Jean-François Lamonier for all the effort you put in my work, for teaching me, for trusting me and encouraging me, for being patient and listening me, for transmitting me your knowledge. In addition, you two have helped me through some difficult times in my life. A few sentences are obviously not enough to describe what you have done for me in the past few years.

I would like to thank Prof. Rino Morent for the fruitful collaborations, all the scientific discussions, technical inputs, insights and also, for the guidance during my research stay in RUPT, UGhent. Also, I would like to express my gratitude to Prof. Nathalie De Geyter for all her help and support during my PhD.

I would like to thank the members of the examination committee for taking interest in my work and providing the valuable suggestions to improve this thesis. Thanks to Prof. Dr. Filip DE TURCK, Prof. Dr. Patrick DA COSTA, Dr. Anton NIKIFOROV, Dr. Jean-Marc CLACENS and Dr. Cyril THOMAS.

Hoping not to omit anyone, my thanks also go to the whole team of the UCCS ULILLE, in particular to Olivier GARDOLL, Martine TRENTESAUX, Joëlle THURIOT-ROUKOS, Laurence BURYLO, Christine LANCELOT, Nora DJELAL, Pardis SIMONE, Jean-Charles MORIN, Nicolas NUNS, for their help, their explanations and their enthusiasm concerning the various physico-chemical characterizations and also I would like to thank the secretariat of the UCCS for their help in the administrative papers, in particular Sandrine BERTON and Barbara

DECLERCK-BOULANGER. I would also like to thank the whole team of RUPT UGent, in particular Tim POELMAN and Joris PEELMAN who were always ready to help with the design and modification of the reactors and the troubleshooting of technical problems with the plasma equipment.

I warmly thank all my colleagues at UCCS and RUPT for creating the best possible working environment. These last years were not only about doing a PhD, but also about making real friends with whom I shared the ups and downs, the laughs and the tears, not to mention the coffee breaks. In particular Guillaume, Carmen, Bertrand, Herman, Maya, Zhiping, Victor, Yuanshuang, Shuo, Tanushree, Helori, Parnian, Dayan, Nicolas, Ibrahim, Bertha, Mhammad, Balsam, Bakytzhan, Wafa, Noura, Xiu, Paola, Julien, Shreya, Nassim in France and Savita, Sharmin, Rim, Rouba, Elise, Parisa, Moazameh, Tim in Belgium. A special thank you to Shilpa, my colleague in France and Belgium, "the chance made us colleagues but the fun and laughter made us friends".

My thanks would not be complete without expressing my deep gratitude and appreciation to all my friends in Lebanon and in France, for all the support and pleasure they have brought to my life. Thanks to Joumana, Dayan, Jenny, Carla, Gaëlle, Tonine, Marie Therese, Sahar, Eliane, Sara, Bachar, Yara, Charbel, Joy, Ralph, Emile Khawla, Adelina, Rachad, and Rita. A special thanks to Mirna for always being there for me in moments of sadness as well as in moments of joy, "because of you I laugh a little more, I cry a little less and I smile a lot more".

I also thank my family without whom this work would never have been executed, especially my parents Abdallah and Ghada, my brothers Georges and Elie and my sisters Faten, Leila and Denise who, in all circumstances, have always been able to offer me their support, their understanding, their encouragement, their patience and their affection throughout my studies. I also warmly thank my second mother, my aunt Rosette. I also thank my cousins Joseph and Jennifer "Born as cousins, because parents couldn't handle us as brothers and sisters".

Finally, I would like to thank Jesus-Christ, my savior, without whom nothing would be.

So thank you to all these people, for this very enriching adventure on a professional and personal level.

List of Publications

A.1 International journal publications

1. **Grâce Abdallah**, Rim Bitar, Savita Kaliya Perumal Veerapandian, Jean-Marc Giraudon, Nathalie De Geyter, Rino Morent, Jean-François Lamonier

Acid treated Ce modified birnessite-type MnO₂ for ozone decomposition at low temperature: effect of nitrogen containing co-pollutants and water

Applied Surface Science, **2022**, 571, 151240

IF 2021: 6.707. Ranking it 1 out of 21 in Materials Science

2. **Grâce Abdallah**, Jean-Marc Giraudon, Rim Bitar, Nathalie De Geyter, Rino Morent, Jean-François Lamonier

Post Plasma Catalysis for Trichloroethylene Abatement with Ce-Doped Birnessite Downstream DC Corona Discharge Reactor

Catalysts, **2021**, 11, 946

IF 2021: 4.146

3. Zhiping.Ye, Jean-Marc Giraudon, Nicolas Nuns, **Grâce Abdallah**, Ahmed. Addad, Rino Morent, Nathalie De Geyter, Jean-François Lamonier

Preferential dissolution of copper from Cu-Mn oxides in strong acid medium: effect of the starting binary oxide to get new efficient copper doped MnO₂ catalysts in toluene oxidation

Applied Surface Science, **2021**, 537, 147993

IF 2021: 6.707. Ranking it 1 out of 21 in Materials Science

C.4 Active international conference participations

1. **Grâce Abdallah**, Jean-Marc Giraudon, Nathalie De Geyter, Rino Morent, Jean-François Lamonier

Catalytic performances of Ce_{0.01}Mn in Post-Plasma Catalysis for dilute Trichloroethylene abatement

Plasma Processing and Technology, International conference (PlasmaTech), Paris, France, **2021**, 'Poster presentation'

2. **Grâce Abdallah**, Savita Kaliya Perumal Veerapandian, Jean-Marc Giraudon, Nathalie De Geyter, Rino Morent, Jean-François Lamonier

Investigation of O₃ formation using negative direct current corona discharge for dichloromethane abatement

Fourth International conference on advanced Complex Inorganic Nanomaterials (ACIN), Namur, Belgium, **2018**, 'Oral presentation'

3. **Grâce Abdallah**, Savita Kaliya Perumal Veerapandian, Jean-Marc Giraudon, Nathalie De Geyter, Rino Morent, Jean-François Lamonier

Ozone and nitrogen oxide formation through 10 pins to plate negative DC corona discharge in air

First international conference on Cold Plasma Sources and Applications (COPSA), Ypres, Belgium, **2018**, 'Poster presentation'

Table of contents

Summary	1
Samenvatting	5
Résumé	9
Acknowledgements	12
List of Publications	15
Table of contents.....	17
List of figures	17
List of tables	21
Chapter 1:	25
LITERATURE OVERVIEW	25
1-1- Air pollution	26
1-2- Volatile organic compounds (VOC)	26
1-2-1- Definition	26
1-2-2- Sources	26
1-2-3- Effect on human health and environment.....	27
1-3- Conventional VOC abatement technologies	28
1-3-1- Thermal oxidation	28
1-3-2- Catalytic oxidation	28
1-3-3- Non-thermal plasma (NTP).....	29
1-3-4- Plasma-Catalysis	30
1-4- Trichloroethylene (TCE).....	31
1-4-1- Physico-chemical properties, Production and Use of TCE.....	31
1-4-2- Health effect and legislation	33
1-4-3- TCE abatement	34
1-5- Plasma as ozoner and ozone decomposition	39
1-5-1- NTP and ozone generation	39
1-5-2- Ozone catalytic decomposition	41
1-5-3- Mechanisms for ozone decomposition in dry and humid air	43
1-5-4- Deactivation mechanism	44
1-5-5- Acid treatment to increase MnO ₂ hydrophobicity	45
1-5-6- Mechanism for ozone decomposition over birnessite treated with nitric acid	45
1-6- Birnessite	46
1-6-1- Birnessite crystalline structure	46

1-6-2- Birnessite synthesis methods	50
1-6-3- Variability in the composition of sheet and interfoliare	51
1-6-4- Birnessite properties (amount of alkaline metals) and capacity of ion exchange	53
1-7- Formaldehyde	54
1-7-1- Formaldehyde catalytic decomposition	55
1-7-2- Mechanism for HCHO oxidation	57
References	58
Chapter 2:	67
STRATEGIC METHODOLOGY	67
Chapter 3:	71
MATERIAL AND METHODS	71
3-1- Catalyst preparation	72
3-1-1- Synthesis of birnessite and cerium doped birnessite through a redox precipitation method	72
3-1-2- Calcination procedure	74
3-1-3- Acid treatment	74
3-2- Catalyst characterizations	75
3-2-1- Thermal Gravimetric Analysis (TGA) and Differential Thermal Analysis (DTA)	75
3-2-2- X-Ray Diffraction (XRD)	75
3-2-3- Transmission Electron Microscopy (TEM)	76
3-2-4- Inductively coupled plasma-optical emission spectrometry (ICP-OES)	77
3-2-5- Textural properties analysis via Brunauer-Emmett-Teller (BET) and Barret-Joyner-Halenda (BJH)	77
3-2-6- Hydrogen-Temperature Programmed Reduction (H ₂ -TPR)	78
3-2-7- Temperature programed desorption (O ₂ -TPD)	79
3-2-8- X-ray photoelectron spectroscopy (XPS)	80
3-2-9- Infrared spectroscopy (IR)	82
3-2-10- Pyridine adsorption followed by infrared spectroscopy (IR pyridine)	82
3-2-11- Raman spectroscopy	83
3-2-12- Time of Flight Secondary ion Mass spectrometry (ToF-SIMS)	84
3-3- Determination of catalytic properties of materials for the total oxidation of formaldehyde	85
3-3-1- Description of the set-up	85
3-3-2- HCHO and CO ₂ calibration	88
3-3-3- Experimental procedure of HCHO oxidation	88
3-4- Determination off catalytic properties of materials for ozone decomposition	90
3-4-1- Description of the plasma Set-up for Ozone generation and TCE abatement	90

3-4-2- <i>Experimental procedure for using plasma as ozoner:</i>	97
3-4-3- <i>Experimental procedure for catalytic ozone decomposition</i>	98
3-5- Determination of catalytic properties of materials for TCE abatement	100
3-5-1- <i>Calibration FTIR</i>	100
3-5-2- <i>Experimental procedure for trichloroethylene in PPC process</i>	100
References	102
Chapter 4:	103
CERIUM DOPED (K, Na) - BIRNESSITE LIKE MnO₂ FOR LOW TEMPERATURE OXIDATION OF FORMALDEHYDE: EFFECT OF CALCINATION TEMPERATURE	103
4-1- Introduction	104
4-2- Experimental conditions	105
4-3- Results and discussion	105
4-3-1- <i>Characterizations of the fresh samples</i>	105
4-3-2- <i>Characterization of the calcined samples</i>	115
4-3-3- <i>Catalytic activity</i>	127
4-4- Conclusion	136
4-5- References	138
Chapter 5:	142
OZONE AND NITROGEN OXIDE FORMATION THROUGH 10 PIN-TO-PLATE NEGATIVE DC CORONA DISCHARGE	142
5-1- Introduction	143
5-2- Experimental conditions	143
5-3- Experimental results	144
5-3-1- <i>Effect of energy density (ED)</i>	145
5-3-2- <i>Influence of Flow rate (Q)</i>	147
5-3-3- <i>Influence of Relative Humidity (RH):</i>	150
5-4- Conclusion	152
References	153
Chapter 6:	155
ACID TREATED Ce MODIFIED BIRNESSITE-TYPE MnO₂ FOR OZONE DECOMPOSITION AT LOW TEMPERATURE: EFFECT OF NITROGEN CONTAINING CO-POLLUTANTS AND WATER	155
6-1- Introduction	156
6-2- Experimental conditions	157
6-3- Results and discussion	157
6-3-1- <i>Characterization studies of the acid-treated catalysts</i>	157
6-3-2- <i>Catalytic tests for ozone decomposition</i>	166

6-3-3- Gas phase characterization by FTIR	169
6-3-4- Characterizations studies after O ₃ testing	171
6-3-5- Effect of nitrogen containing co-pollutants for gaseous ozone decomposition	177
6-4- Conclusion	179
6-5- References	180
Chapter 7:	183
POST PLASMA CATALYSIS FOR TRICHLOROETHYLENE ABATEMENT WITH Ce DOPED BIRNESSITE DOWNSTREAM DC CORONA DISCHARGE REACTOR.....	183
7-1- Introduction.....	184
7-2- Experimental conditions.....	185
7-3- Results and discussion	185
7-3-1- Main physicochemical characterizations of the fresh materials	185
7-3-2- O ₃ decomposition over Ce _{0.01} Mn-400 and Ce _{0.01} Mn-AT samples using non-thermal plasma (NTP) as ozoner	189
7-3-3- TCE abatement by non-thermal plasma (NTP).....	190
7-3-4-TCE abatement by Post plasma catalysis (PPC)	192
7-3-5- TCE abatement in post plasma catalysis (PPC) configuration RH = 15%	194
7-4- XPS characteriations of the used catalysts after PPC process.....	196
7-5- Conclusion	198
7-6- References.....	199
General conclusion and outlook.....	202
Conclusion	202
Outlook.....	205
Appendix A	207

List of figures

Figure 1 - 1: Use of TCE ‘INERIS, Institut national de l’environnement industriel et des risques, Trichloréthylène, 2003’	33
Figure 1 - 2: Reaction scheme for TCE abatement in PPC	37
Figure 1 - 4: Different discharge regimes of a negative DC excited glow discharge: (a) corona regime; (b) glow regime; (c) spark regime	41
Figure 1 - 3: Current voltage characteristic of a negative DC geometry	41
Figure 1 - 5: Mechanism of ozone decomposition on α -MnO ₂ in a) dry air b) humid air.....	43
Figure 1 - 6 : Mechanism for gaseous ozone decomposition over acid treated birnessite	46
Figure 1 - 7: Scheme of the crystal structure of a triclinic birnessite : alternation of a chain of Mn(III)O ₆ and two chains of Mn(IV)O ₆ [114]	477
Figure 1 - 8: Crystalline structure of hexagonal birnessite: a predominantly Mn(IV) chain sheet with gaps, interlayer cations are H ⁺ and Mn ²⁺ /Mn ³⁺ which are positioned below and above the deficiencies [115]	48
Figure 1 - 9: XRD pattern for a) birnessite b) vernadite	50
Figure 1 - 10: Inner sphere complexes crystallographic position: Me represents metal; ^E Me represents edge sharing.....	52
Figure 1 - 11: Relation between the concentration of oxygen vacancies and the total oxidation of HCHO	577
 Figure 2 - 1: Concept of post plasma catalysis.....	68
Figure 2 - 2: Schematic of the operation of the plasma as an ozoner.....	69
Figure 2 - 3: Schematic presentation of HCHO oxidation	70
Figure 2 - 4: Schematic presentation of O ₃ decomposition	70
Figure 2 - 5: Schematic presentation of TCE abatement in PPC process.....	70
 Figure 3 - 1: Scheme of the calcination conditions	74
Figure 3 - 2: Pyridine bond on the surface	83
Figure 3 - 3: Scheme of the set-up of formaldehyde catalytic oxidation	85
Figure 3 - 4: Dynacal permeation tubes	86
Figure 3 - 5: Experimental Set-Up	90
Figure 3 - 6: (a) MFC, (b) Testo 445 climate measurement device with temperature/humidity probe, (c) Pressure indicator	91
Figure 3 - 7: Photo of the plasma reactor with 10 electrodes pins	92
Figure 3 - 8: Photo of DC power source	92
Figure 3 - 9: Electrical scheme of the 10 pin to plate.....	933
Figure 3 - 10: Overview of the catalytic reactor component with (a) oven, (b) temperature controller and	944
Figure 3 - 11: (a) Bruker Vertex 70 FT-IR spectrometer, (b) Gas cell.....	955

Figure 3 - 12: Teledyne ozone monitor Model 465M.....	96
Figure 3 - 13: Selected FT-IR band for ozone calibration.....	977
Figure 4 - 1: XRD patterns of the as-synthesized samples.....	106
Figure 4 - 2: FTIR-ATR spectra of the as-synthesized samples	10707
Figure 4 - 3: (a) N ₂ isotherms and (b) PDS of the as-synthesized samples	108
Figure 4 - 4: TEM of the fresh (a)- (b) Ce _{0.01} Mn and (c)-(d) Ce _{0.1} Mn catalysts.....	109
Figure 4 - 5: XPS (a) Ce 4d, (b) Mn 3s core levels (c) O1s and (d) Mn 2p _{3/2} for the as-synthesized samples. ...	111
Figure 4 - 6: H ₂ -TPR traces of the as-synthesized samples.....	1122
Figure 4 - 7: (a) TGA b) DTA and (c) DSC profiles for the as-synthesized samples	1144
Figure 4 - 8: XRD patterns of the samples after TG analysis.....	1144
Figure 4 - 9: Temporal evolution during TGA under helium (a) of the signal m/z =17, 18, 28 and 44 and (b) of the signal m/z =32 for Ce _{0.1} Mn.	1155
Figure 4 - 10: (a) XRD patterns for the calcined samples and (b) XRD zoom for first peak in the following analysis conditions: 10-20°, step size: 0.2°, step time: 5s.....	116
Figure 4 - 11: FTIR-ATR spectra of the calcined samples	11717
Figure 4 - 12: (a) TGA, (b) DTA and (c) DSC profiles for the calcined Ce _{0.01} Mn and Ce _{0.1} Mn (d) dehydroxylation and O release for Ce _{0.01} Mn and Ce _{0.1} Mn	11818
Figure 4 - 13: (a) N ₂ isotherms and (b) PDS of the calcined samples	1200
Figure 4 - 14: H ₂ -TPR traces of the calcined samples	1211
Figure 4 - 15: Raman spectra of Ce _{0.1} Mn (a) ex situ as-synthesized and calcined at 200, 300 and 400 °C and (b) in-situ calcined at 400°C for 1h and for 3h	1222
Figure 4 - 16: O ₂ -TPD traces of the calcined samples at 400 °C	1233
Figure 4 - 17: XPS (a) O1s and (b) Mn 2p _{3/2} core levels of the calcined samples.....	124
Figure 4 - 18: ToF-SIMS positive ion spectra (a) and (b) in the 200-220 m/z range and (c) and (d) n the range 135-160 m/z of Ce _{0.01} Mn-400 and Ce _{0.1} Mn-400.	1266
Figure 4 - 19: Light-off curves over (a) Mn-B-400, CexMn-400 and Hop-300; (b) Ce _{0.01} Mn-X00 and (c) Ce _{0.1} Mn-X00 catalysts. HCHO = 100 ppm, O ₂ = 20%, N ₂ balance, GHSV = 60 L/(gcat.h); (d) Arrhenius plot of the tested samples.....	128
Figure 4 - 20: Effect of RH on HCHO elimination and HCHO conversion over (a) Ce _{0.01} Mn-400 and (b) Ce _{0.1} Mn -400. T = 50 °C, HCHO = 100 ppm, O ₂ = 20%, N ₂ balance, GHSV = 60 L/(gcat.h).....	131
Figure 4 - 21: Effect of RH on HCHO elimination and HCHO conversion over Hopcalite. T = 75 °C, HCHO = 100 ppm, O ₂ = 20%, N ₂ balance, GHSV = 60 L/(gcat.h).	131
Figure 4 - 22: HCHO-TPD (a) HCHO adsorption as a function of time, (b) evolution of gaseous species (HCHO and CO ₂) and (c) evolution of the atomic ratio O/ (Mn+Ce) as a function of temperature in HCHO oxidation under helium of Ce _{0.1} Mn-400, Ce _{0.01} Mn-400 and Ce _{0.01} Mn-300.....	133
Figure 4 - 23: FTIR-ATR spectra of the fresh and used catalysts after stability tests.....	135
Figure 4 - 24: Scheme of the possible reaction pathway of HCHO oxidation over Ce doped birnessite	136
Figure 5 - 1: FT-IR spectrum of the plasma generated gaseous species. Dry air; F = 1L/min; ED = 150J/L	144

Figure 5 - 2: Scheme of N_2O_5 and HNO_3 production via NO_x oxidation by O_3	145
Figure 5 - 3: Ozone concentration as a function of ED. Dry air; $Q = 1$ L/min.....	146
Figure 5 - 4: I_x/I_{250} as a function of ED; Dry air; $Q = 1$ L/min.....	147
Figure 5 - 5: Evolution of $[O_3]$ as a function of ED. Dry air; $Q = 0.5, 1$ and 1.5 L/min	148
Figure 5 - 6: Effect of Q on $[O_3]$ and r_{O_3}	149
Figure 5 - 7: Evolution of the integrated area as a function of Q . Dry air; ED = 150 J/L	149
Figure 5 - 8: Evolution of $[O_3]$ as a function of ED in dry air and humid air; $Q = 0.5$ L/min.....	150
Figure 5 - 9: FT-IR for the plasma generated gaseous species in dry air and in 15 % as relative humidity. $Q = 0.5$ L/min; ED = 250 J/L	151
Figure 6 - 1: XRD patterns of the fresh acid- treated samples	158
Figure 6 - 2: TEM images of $Ce_{0.1}Mn$ -AT	159
Figure 6 - 3: (a) N_2 adsorption-desorption isotherms and (b) pore size distribution of the fresh acid-treated samples	160
Figure 6 - 4: H_2 -TPR traces of the fresh acid-treated samples	161
Figure 6 - 5: Pyridine-FTIR spectra before and after acid treatment for (a) $Ce_{0.01}Mn$ and (b) $Ce_{0.2}Mn$	162
Figure 6 - 6: Amount of adsorbed water normalized to the specific surface area.....	163
Figure 6 - 7: XPS spectra of the fresh acid treated samples	165
Figure 6 - 8: O_3 conversion (O_3 inlet concentration: 300 ppm) vs time in nearly dry air, 20 °C (a) on the pristine catalysts, GHSV = 600 L/(g h); (b) on the acid-treated catalysts, GHSV = 1200 L/(g h).....	167
Figure 6 - 9: O_3 conversion (O_3 inlet concentration: 300 ppm) vs time over $Ce_{0.01}Mn$ in O_2/Ar and air, GHSV = 600 L/(g h)	167
Figure 6 - 10: O_3 conversion vs time on the acid treated catalysts (O_3 inlet concentration: 300 ppm, GHSV = 1200 L/(g h)) (a) in moist air RH = 30 %; 40 °C; (b) in moist air RH = 30 %; 30 °C.	168
Figure 6 - 11: Temporal evolution of the gas phase species for O_3 decomposition in air (RH~0.7 %) over (a) $Ce_{0.01}Mn$, (b) $Ce_{0.01}Mn$ -AT	170
Figure 6 - 12: Temporal evolution of the gas phase species for O_3 decomposition in moist air (RH~30 %) over $Ce_{0.01}Mn$ -AT	171
Figure 6 - 13: X-ray photoelectron spectra of the N 1s core level of the tested catalysts (a) untreated; (b-c) acid treated.....	172
Figure 6 - 14: Correlation between O_3 conversion and poisoning of active sites by N adspecies for the catalysts treated with acid	173
Figure 6 - 15: FTIR-ATR spectra of the tested catalysts (a): at RH = 0.7 % ; (b) at RH = 30 % and (c) reference FTIR-ATR spectra of metal alkali nitrates ; (d) FTIR-ATR spectra of $Ce_{0.01}Mn$ -AT-03-H30 and after heating at 200 °C for 4 h.....	174
Figure 6 - 16: Temporal evolution during TPD (a) of the signal $m/z = 30$ and (b) of the signal $m/z = 32$ for Mn -B-AT- O_3 , $Ce_{0.01}Mn$ -AT- O_3 and $Ce_{0.1}Mn$ -AT- O_3	177
Figure 6 - 17: Correlation between O_3 conversion and T_{onset} for the acid treated catalysts	178
Figure 7 - 1: XRD patterns of $Ce_{0.01}Mn$ -400 and $Ce_{0.01}Mn$ -AT samples	186

Figure 7 - 2: (a) N ₂ adsorption desorption (b) pore size distribution of Ce _{0.01} Mn-400 and Ce _{0.01} Mn-AT samples.....	187
Figure 7 - 3: FTIR spectra of the Py region obtained after Py adsorption at 105°C for dried Ce _{0.01} Mn and Ce _{0.01} Mn-AT samples.....	188
Figure 7 - 4: XPS Mn2p _{3/2} core level decomposition for Ce _{0.01} Mn-400 and Ce _{0.01} Mn-AT samples	189
Figure 7 - 5: Ozone conversion over Ce _{0.01} Mn-400 and Ce _{0.01} Mn-AT ([O ₃] = 300 ppmv, GHSV = 1200 L/(g _{cata} h); RH = 0.7 %).....	1900
Figure 7 - 6: CO _x , CO and CO ₂ yields obtained in NTP TCE abatement with RH of 0.7 % and 15 % (ED = 150 J/L; Q= 1 L/min; [TCE] ₀ = 150 ppmv)	1911
Figure 7 - 7: FT-IR spectra in the range 2500-1700cm ⁻¹ and 1110-700cm ⁻¹ of outlet stream after NTP in 0.7 % and 15 % as relative humidity (ED = 150 J/L, Q= 1 L/min) (PG : phosgene; DCAC : dichloroacetylchloride and TCAD : trichloroacetaldehyde).....	1922
Figure 7 - 8: CO _x and CO ₂ yields obtained for TCE abatement (RH = 0.7%) in PPC configuration with Ce _{0.01} Mn-400 and Ce _{0.01} Mn-AT as catalysts	1933
Figure 7 - 9: FT-IR spectra of the inlet TCE and outlet gaseous stream after PPC process (RH = 0.7 %) as a function of time with Ce _{0.01} Mn-400 as catalyst (PG : phosgene; DCAC : dichloroacetylchloride ;TCAD : trichloroacetaldehyde).....	1944
Figure 7 - 10: FT-IR spectra of the inlet TCE and outlet gaseous stream after PPC process (RH = 0.7 %) as a function of time with Ce _{0.01} Mn-AT as catalyst (PG: phosgene; DCAC: dichloroacetylchloride; TCAD: trichloroacetaldehyde).....	1944
Figure 7 - 11: CO _x and CO ₂ yields obtained for TCE abatement (RH = 15%) in PPC configuration with Ce _{0.01} Mn-AT as catalyst.....	195
Figure 7 - 12: FT-IR spectra of the inlet TCE and outlet gaseous stream after PPC process (RH = 15 %) as a function of time with Ce _{0.01} Mn-AT as catalyst (PG: phosgene; DCAC: dichloroacetylchloride; TCAD: trichloroacetaldehyde).....	196
Figure 7 - 13: XPS (a) Mn2p _{3/2} and (b) Cl2p core levels decomposition after PPC process.....	197
Figure A - 1: Survey XPS spectra of Mn-B	20707

List of tables

Table 1 - 1: Physical and Chemical properties of TCE	33
Table 1 - 2: Summarizing table of the different catalysts used in PPC for TCE abatement with the different plasma conditions.....	38
Table 1 - 3: Summary table of the different synthesis procedure of birnessite, K/Mn and Na/Mn ratios reported in literature	54
Table 3 - 1: The required amount of chemicals for the synthesis of Mn-B	73
Table 3 - 2: Weight of potassium permanganate and cerium nitrate required for each Ce/Mn ratio.	74
Table 3 - 3: Analytical conditions in gas chromatography analysis	88
Table 3 - 4: Specifications of the Ozone monitor.....	96
Table 4 - 1: Experimental conditions	105
Table 4 - 2: Textural properties of the as-synthesized samples.....	107
Table 4 - 3: ICP analysis of the as-synthesized samples	109
Table 4 - 4: Quantified results by obtained XPS analysis	111
Table 4 - 5: Binding energy (eV) determined by XPS analysis	111
Table 4 - 6 : H ₂ -TPR of the as-synthesized samples.....	112
Table 4 - 7: Weight loss as a function of temperature for the as-synthesized samples	114
Table 4 - 8: Weight loss as a function of temperature for the calcined samples.....	119
Table 4 - 9: Textural properties of the calcined samples.....	119
Table 4 - 10: ICP analysis of the calcined samples	120
Table 4 - 11: H ₂ -TPR of the calcined samples	121
Table 4 - 12: O ₂ -TPD quantitative analysis of the calcined samples at 400°C.....	124
Table 4 - 13: Quantified results by XPS analysis for the calcined samples	125
Table 4 - 14: Binding energy (eV) determined by XPS analysis for the calcined samples	125
Table 4 - 15: ToF-SIMS results.....	126
Table 4 - 16: Secondary ions of the positive and negative ToF-SIMS of Ce _{0.1} Mn-400	127
Table 4 - 17: Catalytic results	128
Table 4 - 18: Overview study for HCHO catalytic oxidation	128
Table 4 - 19: Adsorption and thermo-desorption of formaldehyde results.....	13434
Table 6 - 1: Experimental conditions	15757
Table 6 - 2: Chemical composition, textural and redox roperties of the fresh acid-treated samples	15959
Table 6 - 3: Water loss between 25 °C and 100 °C determined from TGA measurements expressed in mg/gcat.....	16363
Table 6 - 4: XPS rezults of the fresh acid-treated samples	16565
Table 6 - 5: ToF-SIMS results of the Fresh acid-treated samples	16666

Table 6 - 6: N1s componenets and N/Mn XPS ratios for the treated catalysts.....	17373
Table 6 - 7: Nitrogen containing secondary ions from ToF-SIMS spectra in polarity (-) of the tested catalysts.....	17676
Table 6 - 8: ToF-SIMS data in positive polarity for Ce _{0.1} Mn before and after ozone decomposition	17676
Table 7 - 1: Experimental conditions	18585
Table 7 - 2: Weight composition and atomic ratio for Ce _{0.01} Mn-400 and Ce _{0.01} Mn-AT samples	18686
Table 7 - 3: Textural properties of the Ce _{0.01} Mn-400 and Ce _{0.01} Mn-AT samples.....	18787
Table 7 - 4: Semi quantitative XPS analysis for used (PPC) catalysts	197
Conclusion Table 1: Summary of the important results obtained in this work.....	204

Chapter 1:
LITERATURE OVERVIEW

1-1- Air pollution

Air pollution is a major problem that has been recognized a 100 years ago. We hear about the various forms of pollution and read about it through the mass media. Air pollution is one such form that refers to the contamination of the air, irrespective of indoor or outdoor. A physical, biological or chemical alteration of the air in the atmosphere can be termed as pollution. It occurs when any harmful gases, dust, smoke enter into the atmosphere and makes it difficult for plants, animals and humans to survive as the air becomes dirty. Air pollution has become one of the main environmental health risks in the world. According to the world health organization (WHO) report, 7 million people die prematurely from pollution worldwide (2012), including 3.3 million due to indoor air pollution and 2.6 million due to outdoor air pollution, equivalent to one death every 2.7 seconds [1,2]. Air pollutants could be discharged to the atmosphere through natural sources such as plants and volcanic eruptions or by several human activities. But the greatest contributions to air pollution today are those resulting of human impact. These are largely the result of human reliance on fossil fuels and heavy industry but can also be due to the accumulation of waste, modern agriculture, and other man-made processes. The main primary pollutants monitored in air are: Carbon monoxide (CO), nitrogen oxides (NO_x), sulfur oxides (SO_x), particulate matter (PM), volatile organic compounds (VOCs)...

1-2- Volatile organic compounds (VOC)

1-2-1- Definition

A volatile organic compound is defined as an organic substance which, excluding methane, is composed of carbon and hydrogen in the gaseous state under normal pressure and temperature conditions. The molecule may also contain other heteroatoms such as halogens, sulfur, oxygen, phosphorus, with the exception of carbon oxides and carbonates [3]. Although, there is no general quantitative definition of what VOCs are, a more restrictive definition of VOCs has been given in Article 2 of the European Directive 1999/13 / EC (VOC): "A volatile organic compound is defined as any compound having a vapor pressure of more than 10.3 Pa at normal pressure and temperature". Their high volatility causes them to rapidly evaporate and enter the earth's atmosphere [4-6].

1-2-2- Sources

Emission sources of VOC can be divided into biogenic or anthropogenic depending on whether they are released to the environment by biological life or humans respectively [7,8].

➤ Natural sources: Globally, VOC emissions are mainly of natural origin and account for nearly 90% of total emissions. There is no real solution to prevent this kind of emission, it has significant effect on the chemical composition and physical characteristics of the atmosphere. The natural sources that emit NMVOCs (methane excepted) are the Plants that emit a very wide variety of VOCs and Geological areas that contain coal or natural gas. However, natural sources that are sources of methane which is the major biogenic VOCs are swamps and animals. Therefore, biogenic sources become less important in the industrialized regions where anthropogenic sources produce large amount of VOCs.

➤ Anthropogenic sources: Are divided into two categories. On one hand, indoor pollution that comes mainly from household products such as insulation materials, solvents, cleaning products, insecticides, aerosols, printers, restaurants and domestic kitchens, paints and varnishes. On the other hand, external pollution that comes from transportation and industrial processes such as chemical plants, electronic components factories, pharmaceutical, refineries, car manufacturers, food manufacturers, textile manufacturers.

1-2-3- Effect on human health and environment

VOCs have long-term adverse effects on human health and the environment. Therefore, their incorporation, most often by inhalation, sometimes by digestion or skin penetration, can be at the origin of a multitude of pathologies of unequal gravities. The penetration of VOCs in the body is likely to produce, by reaction with proteins or nucleic acids, various toxic metabolites that spread in the organs. On the other hand, it is established that VOCs harm health indirectly, by favoring complex chemical reactions taking place in the atmosphere (photo-oxidation). Air pollution emitted by biogenic or anthropogenic sources is released to the troposphere. The tropospheric chemistry is essential for their chemical transformation such as emission, transport, exchange, distribution and deposition.

Moreover, from one VOC to another, the danger varies according to the molecule concerned and its concentration. Some are carcinogenic, others can cause respiratory diseases. The danger is further amplified by the “cocktail effect” resulting from the uncontrolled combination of these molecules with each other. Besides, the age at which a person is exposed to these substances also plays a role. In addition, after chemical reactions, chlorinated volatile organic compounds (CVOCs) cause a number of indirect pollution problems such as ozone and smog formation in the troposphere, and depletion of the ozone layer in the stratosphere.

1-3-Conventional VOC abatement technologies

To limit the release of VOCs, it is necessary in the first step to try to minimize their emissions by replacing them with other substances by using less harmful VOCs. If no preventive solution is technically or economically feasible, it remains to treat the effluents loaded with VOCs. There are different methods, but each one has its limitations depending on the compound and its concentration, the source of the emission, the possibility or not to valorize the recovered products. These methods are divided into two categories well separated [9-11,12].

- Recovery methods: condensation, adsorption, absorption and membrane technique.
- Methods of destruction: thermal oxidation, biological oxidation and catalytic oxidation

1-3-1- Thermal oxidation

Thermal oxidation is the oldest method and is still the most widely used due to its simplicity of installation. VOCs are oxidized to CO_2 and H_2O at very high temperatures (700-1000°C). The major disadvantages of this technique are that it requires high operating costs and can generate harmful by-products such as dioxins and nitrogen oxides (NO_x) [12].

1-3-2- Catalytic oxidation

Catalytic oxidation is one of the most effective and currently developed solutions for VOC abatement. Indeed, unlike thermal oxidation, catalytic oxidation operates at lower temperatures which offers considerable savings in costs thus leading to lower energy consumption. The catalytic oxidation causes a decrease in the production of harmful by-products. The addition of a catalyst accelerates the rate of VOC oxidation into CO_2 and H_2O when considering a $\text{C}_x\text{H}_y\text{O}_z$ organic VOC. Investigations on adsorption and desorption of gas molecules at a catalytically active surface, and interaction of these molecules with each other on this surface, as well as with the surface itself might lead to various reaction mechanisms such as Langmuir-Hinshelwood, Eley -Rideal or Mars Van Krevelen. It has to be mentioned that the operating temperature range differs from the nature of the VOCS and is of 200-350°C, 370-540°C and 200-500°C for heavy, light and halogenated VOCs, respectively. Generally, the catalysts for VOC abatement can be ranked into 2 categories: those relative to noble metal based catalysts which are generally known as being the more efficient for VOC abatement. However, their high cost and limited availability have led researchers to try to replace them with transition metal oxides (TMO) which are cheaper and more abundant. Copper, cobalt and manganese oxides are the most commonly TMO studied in total oxidation reactions of VOCs. Moreover, one major drawback of this method is that it becomes cost inefficient (high energy

consumption) when low VOC concentrations need to be treated (< 1000 ppmv). The design of a catalytic oxidation system should be carefully considered, as its sensitivity to VOC inlet stream, flow conditions and catalyst deactivation, limits its applicability for many industrial processes [13–17].

1-3-3- Non-thermal plasma (NTP)

Among the different methods for the abatement of dilute VOCs from waste gas streams and indoor air, Non-Thermal Plasma (NTP) has attracted attention about 30 years ago. NTP was previously used for the removal of NO_x and SO_x from flue gas [18–20]. Plasma is normally referred to the fourth state of matter, due to its distinctive physical and chemical properties. The term plasma was first introduced by Langmuir in 1928. Langmuir wrote: “Except near the electrodes, where there are sheets containing very few electrons, the ionized gas contains ions and electrons in about equal numbers so that the resultant space charge is very small. We shall use the plasma to describe this region containing balanced charges of ions and electrons”. There are two sources to produce plasma. Natural source such as solar corona, solar wind lightening and Aurora Borealis, or artificial through the injection of a sufficient amount of energy to cause gas excitation. The energy is in different form: by heating, photoionization, exposing neutral gas to beam of charged ions or electrons or by electrical discharge. Non-Thermal Plasma can be classified from several standpoints. One of these standpoints deals with an equilibrium between the temperature of ions and electrons. When the temperature ($\approx 10,000$ K) of ions and electrons are the same we speak about Thermal Plasma (TP). High power density e.g. from 100 W cm^{-3} to 10 kW cm^{-3} is required to obtain TP. On the other hand, when the temperature of electrons (i.e. $10,000 \text{ K}$ to $20,000 \text{ K}$) is much higher than the temperature of ions which remain at ambient temperature we speak about Non-Thermal Plasma (NTP). The NTP energy electron is between 1 and 20 eV , the collision between this electrons and neutral gas produce excited gas molecules (N_2^* , O_2^*) which lose their excess energy by emitting photons or heat. Next to excitation, other reactions like ionization, dissociation and electron attachment occur in the discharge zone. Unstable reactive species like ions and free radicals are formed through these channels of reactions. In NTP, ionizations and chemical reactions are directly determined by the electron temperature and are not so sensitive to thermal process and the gas temperature. Many elementary processes lead to NTP generation which can be divided into primary and secondary processes. The primary processes include charge transfer, ionization, excitation and dissociation reactions with typical timescales between 10^{-15} and 10^{-8} seconds. The secondary processes are relative to the subsequent chemical reactions between the

products of primary processes (electrons, radicals, ions and excited molecules). Additional radicals and reactive molecules (O_3 , HO_2 and H_2O_2) are also formed by radical and recombination reactions. The timescale of the secondary processes is around 10^{-3} seconds. The generation of NTP at atmospheric pressure and room temperature have been the subject of many research papers in the last two decades. This type of plasma has found wide applications in the industrial, environmental and medical fields. The first environmental application of NTP is the generation of ozone for water treatment and it is still one of the most important applications [21]. Some of the NTP applications are: polymer processing, the hydrogenation of CO_2 , the sterilization and disinfection of contaminated surfaces including living tissues, the removal of air contaminants such as SO_2 , NO_x , VOC and ozone generation [15,22–28]. The use of NTP for air pollution control has several advantageous features resulting from its operating conditions such as: quick start-up, rapid response to changes in the composition of the waste gas and operation at ambient conditions which excludes the use of expensive vacuum systems [29–32]. However, the key advantage of NTP is the directed energy consumption. NTPs are attractive in such a way that almost no energy is dissipated in heating up the entire gas flow. On the other hand, the energy delivered to the system is efficiently used to create an intense electric field in which electrons are selectively accelerated, hence, multiple chemical processes such as excitation, ionization and dissociation are initiated by collisions between background molecules (N_2 , O_2 , H_2O) and these highly energetic electrons. This leads to the formation of active, unstable species (radicals, ions, photons) which are responsible for the decomposition of VOCs. Due to the previously enounced advantages NTP has been used for the removal of VOCs from dilute atmospheric pressure gas streams. But one major drawback of the NTP removal technique for VOC removal abatement in polluted air is the possible formation of undesired by-products such as O_3 , NO_x , aerosols, plasma generated VOCs even more toxic than the VOC to be treated. Since 2000, the combination of NTP with other techniques has been an active area of research for better VOC abatement efficiency.

1-3-4- Plasma-Catalysis

In these last decades, the combination of NTP with heterogeneous catalysis referred to as plasma-catalysis, has gained increased interest. The integration of a catalyst in the process may accelerate the chemical reactions by providing alternative reaction pathways with a lower energy barrier to get the most environmental friendly final products such as CO_2 and H_2O . Plasma-catalysis *a priori* is able to enhance the performance of NTP alone in VOC abatement through the concomitant improvement of the three main weaknesses of NTP [33,34]:

Incomplete oxidation with emission of harmful compounds, poor energy efficiency and low mineralization degree (non-selective process). Depending on the location of the catalyst with respect to the NTP, plasma-catalysis can be divided into two categories: In-Plasma Catalysis (IPC) and Post Plasma Catalysis (PPC).

In-Plasma Catalysis

The configuration where the catalyst is integrated in the NTP reactor refers to In-plasma catalysis. In that case all the highly reactive plasma generated species can play a role at the surface of the catalyst [35]. Furthermore, the possibility to get adsorbed species on the catalyst surface leads to an increase of the retention time promoting the interactions between the short lived oxygen based entities with the adsorbed VOC and adsorbed related degradation intermediates enabling a more complete oxidation in line with the textural properties of the support. Additionally, it has been shown that the presence of the catalyst in the discharge zone can also affect the plasma discharge type resulting in an enhanced production of reactive species through an increase of the oxidizing power of the plasma discharge. Besides, the NTP can also have beneficial effects on the catalyst properties [19].

Post-Plasma Catalysis

Post-plasma catalysis is a two stage arrangement with two reactors in series: A NTP reactor and a catalytic reactor where the catalyst is located downstream of the NTP reactor. This configuration precludes direct interaction of the NTP with the catalyst surface and it is found that only O₃ and nitrogen oxides as reactive oxygen species which can reach the catalytic surface [35]. The concept of PPC is to take advantage of the catalytic ozone dissociation to produce very active oxygen species promoting the oxidation of the plasma generated by-products and of the remaining initial VOC. PPC has a simpler configuration compared to IPC, which facilitates the replacements of the used catalyst in practical applications.

1-4- Trichloroethylene (TCE)

The aim of this work is to remove TCE with the lowest possible energy cost in line with a good selectivity towards CO₂, HCl and H₂O using a post plasma catalysis process.

1-4-1- Physico-chemical properties, Production and Use of TCE

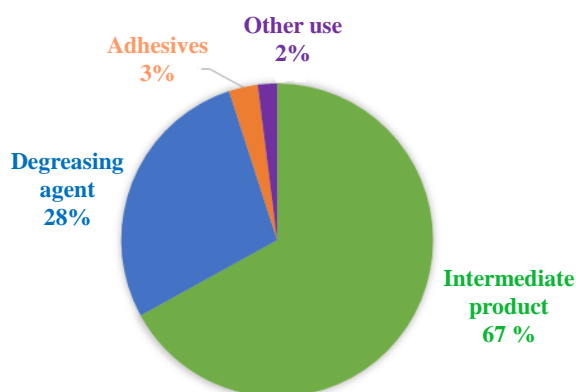
Trichloroethylene is a partially chlorinated C₂-Hydrocarbon with the formula C₂HCl₃. It is classified as chlorinated volatile organic compound (ClVOC). TCE is a colorless liquid, with a sweet smell reminiscent of chloroform and detectable from 50 to 100 ppm of substance in the air (with risk of rapid olfactory fatigue). It is practically insoluble in water (0.1 g/100 mL

of water at 20°C) but miscible with most organic solvents (acetone, ethanol, diethyl ether, chloroform, carbon disulphide...); it is completely miscible with glacial acetic acid. Further chemical and physical properties are listed in **Table 1-1** [36,37].

TCE was first prepared in 1864 by Emil Fisher in experiments on the reduction of hexachloroethane with hydrogen. In 1920 commercial production of TCE began in Germany and in 1925 in USA [37]. It is an excellent solvent for a wide range of applications due to favorable properties such as high solvency, low flammability, non-corrosiveness, high stability, low specific heat, low boiling point, low heat of vaporization and low production cost. Therefore, it is widely used as an industrial solvent to clean and degrease metal and semiconductor parts. TCE has however numerous other uses including heat transfer medium, extraction agent for greases, oils and fats, chemical intermediate in the production of chlorofluorocarbons and other organic chemicals and as an ingredient in many products for industrial and consumer use (**Figure 1-1**). It is for example used in dyes, printing inks, paint removers, adhesives, type writer correction fluids as well as spot removers [37–39]. **Figure 1-1** present the % of TCE used in the different processes. However, according to Registration, Evaluation, Authorization and restriction of Chemical substances (REACH) registration information which is available on European Chemical Agency's (ECHA'), TCE is manufactured and/or imported in the European Economic area in 10,000 to 100,000 tonnes/year [40].

Table 1 - 1: Physical and Chemical properties of TCE

PROPERTY	VALUE
Chemical formula	C ₂ HCl ₃
CAS number	79-01-6
Molecular weight	131.39 g mol ⁻¹
Density	1.46 g cm ⁻³ (20°C)
Boiling point	87.2°C
Melting point	-73.0°C
Vapor exposure	7.6 kPa (20°C)
Auto ignition point	410 °C
Solubility in water	1.28 gL ⁻¹
Conversion factor	1 ppm = 5.37 mg.m ⁻³ (25C°)
Upper explosive limit in air	41 vol, %
Lower explosive limit in air	11 vol, %

**Figure 1 - 1:** Use of TCE 'INERIS, Institut national de l'environnement industriel et des risques, Trichloréthylène, 2003'

1-4-2- Health effect and legislation

TCE is detected in all media but mostly in air due to its volatility. Release of TCE at ambient to outdoor and indoor air can occur during degreasing operations and consumption of related products [38]. Contamination of groundwater and water supplies is possible during production and disposal processes, and through leaching from landfills or underground storage tanks due to its moderate solubility in water, widespread use and persistency in the environment. Human exposure to TCE may therefore occur through inhalation, ingestion and dermal contact. Inhalation can affect the central nervous system and is known to cause acute symptoms including sleepiness, fatigue, dizziness, headache, confusion, facial numbness and feelings of euphoria [38]. Toxicologic studies have also reported human health impacts such as speech and

hearing impairments, disturbed vision, liver problems, skin rashes, kidney diseases, urinary tract, cardiac arrhythmias and blood disorders [41,42]. Furthermore, TCE has been extensively studied for its potential carcinogenicity.

The Scientific Committee of Occupational Exposure Limits (SCOEL) reports TCE being well absorbed *via* all major routes of exposure in humans, with quantitative data available showing an uptake between 28 and 80% by inhalation, with absolute uptake increasing with increasing physical exercise. Although the International Agency for Research on Cancer (IARC) listed TCE as potentially carcinogenic (Group 2A), recent evaluation based on new data has however proven that there is sufficient evidence to conclude that TCE is carcinogenic to humans (Group 1) [43]. It causes cancer of the kidney, liver, cervix and lymphatic system. The French National Institute for Industrial Environment and Risks (INERIS), reports that the Occupational Exposure Limit (OEL) for 8 hours is 75 ppmv and the Short-Term Exposure Limit (STEL) for 15 min is 200 ppmv. The predicted number of cancer deaths in the European Union (EU) in 2010 attributed to TCE exposure were 34, 13 and 12 deaths for cancer of liver, kidney and non-Hodgkin lymphoma (NHL), respectively. The Institute of Occupational Medicine (IOM) reported estimations on the numbers of deaths and health costs between 2010 and 2069 in case no action is taken regarding carcinogen pollutants. Among them, exposure to TCE which potentially concerns 74,076 workers in Europe is expected to cause 4,800 cases of cancers and 3,300 deaths in 2069, with estimated health costs between € 1,582m-5,657m.

1-4-3- TCE abatement

Development and optimization of different processes for TCE treatment are crucial issues for the improvement of air quality.

Thermal oxidation

The first method used is the thermal oxidation. It has been proved to successfully decompose TCE but it has major drawbacks. First, temperature must be superior to 1000 °C for the complete pollutant destruction making it an uneconomical process. In addition, the high temperature reached in this process generates a higher quantity of NO_x and chlorinated by-products and finally, this technique is not very effective with low pollutant concentrations streams [44].

Catalytic oxidation

The catalytic oxidation of TCE represents an interesting alternative that permits to operate at lower temperature (250 -550 °C) with a drastic reduction of energetic costs compared

with the thermal process and can be efficiently operated in dilute pollutants that cannot be thermally combusted without additional fuel [45]. Furthermore, a specific catalyst design can favor the reaction selectivity in the direction of desired products (CO_2 , H_2O and HCl), limiting the by-product formation of NO_x . In addition, the desired objective for the catalytic oxidation is to achieve complete conversion of TCE [46]. Noble metal based catalysts show a high activity for TCE abatement but due to high and fluctuating cost and scarcity, their application is restricted. Solid acid catalysts such as zeolites and alumina based materials have also been proposed to catalyze the decomposition of TCE, because Brönsted acidity is believed to play a key role in activities [44]. Modified zeolites by other metals (Fe_xO_y , Cr_2O_3 , CeO_2) show an improvement in catalytic activity due to interaction between zeolite and metal. Additionally, zeolite modified by MnO_x has been reported as a good catalyst for CIVOC abatement such as dichloromethane and trichloroethylene [47]. Also bulk TMOs have been used for TCE oxidation such as CeO_2 , Mn doped CeO_2 microspheres. CeO_2 has been reported as an efficient oxidation catalyst because CeO_2 has unique redox property and high oxygen storage capacity [48,49]. Li *et al.* [45] demonstrated that Mn doped CeO_2 has better activity compared with pure ceria, as its specific surface area increases, the amount of oxygen vacancies as well as the mobility of oxygen increase, which are responsible for the high catalytic performance. The major drawback for the catalytic oxidation is the catalyst deactivation caused by the strong adsorption of chlorine species produced from TCE decomposition leading to the blockage of the active sites and the decrease of the surface active oxygen [44,45].

Non thermal plasma

The destruction of TCE with NTP takes place through many possible pathways [18,50]. Electron attachment of TCE leading to the formation of C_2HCl_2 and a chlorine anion is one of the possible initial step for TCE decomposition. Metastable nitrogen molecules are also considered as dominant dissociation species occurring in a NTP destruction process of VOC polluted air streams [18]. Overall, the initial steps of TCE decomposition may occur from electron impact dissociative attachment or reactions with metastable molecules (N_2^* , O_2^*). Vandenbroucke *et al.* [51] investigate the decomposition of TCE using 5 pins to plate NTP reactor using a DC negative corona discharge and identified along with CO and CO_2 the formation of polychlorinated gaseous by-products by combining the qualitative data from mass spectrometry and Fourier-transform infrared spectroscopy. Phosgene (PG), dichloroacetylchloride (DCAC) and trichloroacetaldehyde (TCAD) are identified as incomplete oxidation products. According to Vandenbroucke *et al.* [51], the ClO^* radical oxidizes TCE

leading to the formation of significant amount of DCAC by the following reaction: $C_2HCl_3 + ClO^{\bullet} \rightarrow CHCl_2COCl + Cl^{\bullet}$ [9,18,19]. Hydrogen chloride, chlorine and ozone are also detected in the outlet stream. Overall the high reactivity towards TCE removal is tempered by a low selectivity into $CO_2/H_2O/HCl$ due to the production of toxic by-products such as PG, DCAD, TCAD and O_3 .

Post-Plasma catalysis

Since these two last decades NTP technology has partly regained interest through the combination with heterogeneous catalysis. Vandenbroucke *et al.* have reviewed the efficiency of different plasma catalytic processes for TCE abatement in air [52]. Although several studies have however shown enhanced performance of different catalysts in PPC rather than IPC [53]. However, in IPC, both catalyst and plasma simultaneously affect each other, resulting in a complex interaction. In a two stage process such as PPC the operating parameters can be separately optimized enhancing the feasibility of adopting this two-stage configuration in commercialized processes. In PPC the TCE contaminated gas stream to be treated passes first through the plasma reactor and then through the catalytic reactor. After NTP treatment the nature of the gaseous effluent changes in line with the high reactivity of the plasma towards TCE and its poor CO_2 and HCl selectivity. A typical reactional scheme for TCE abatement in PPC configuration shown in **Figure 1-2** has been reported by Vandenbroucke *et al.* [51] using a 5 pins to plate NTP reactor configuration working with a DC negative corona discharge and MnO_2 as catalysts positioned downstream of the NTP reactor.

As stated previously the main issues to address is the total oxidation of the NTP generated gaseous polychlorinated by-products such as DCAC, TCAD and $COCl_2$ along with the elimination of O_3 . In PPC configuration the NTP generated O_3 is decomposed on the catalyst surface producing active oxygen species enabling further oxidation at low temperatures of the NTP non processed parent VOC and NTP gaseous hazardous by-products owing to path 1. But on the other hand, the detection of polychlorinated C1 species such as CCl_4 and HCl_3 at the exit of the catalytic reactor can result from the C-C bond breaking of the in C_2 polychlorinated compounds allowing the formation of CCl_3 and $HCCl_2$ species able to react with adsorbed chlorine (path 2). Overall, this resulting hybrid technology can overpass NTP and total oxidation catalysis in terms of TCE removal efficiency and energy cost at low temperature [35].

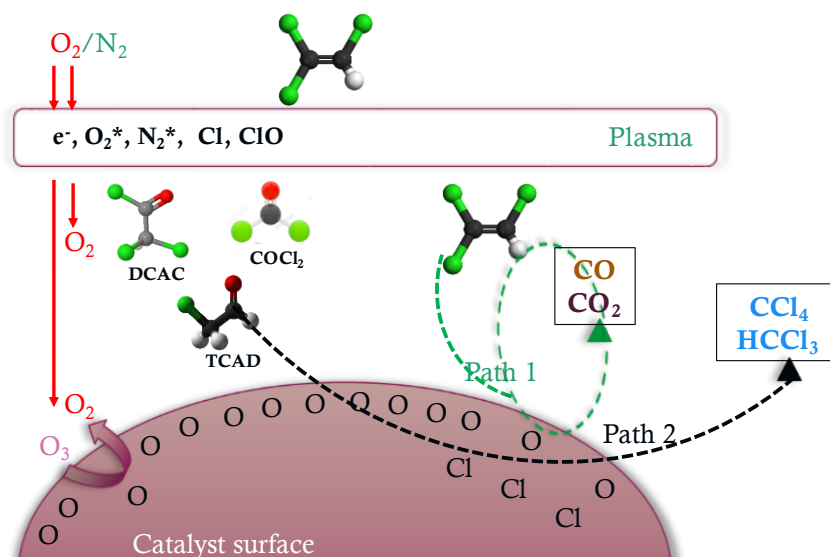


Figure 1 - 2: Reaction scheme for TCE abatement in PPC

Based on this previous scheme of TCE degradation which is complex, it turns out that the catalyst has to be very active for NTP generated ozone degradation allowing to get a relevant production of active oxygen species to oxidize the polychlorinated C2 by-products into CO_2 . Additionally, the effect of the presence of oxygenated nitrogen species (not mention in the scheme) as well as water leaving the NTP reactor has to be taken into account as these species can compete for the active sites of O_3 decomposition. The stability of the catalyst has also to be taken into account as a possible partial chlorination of the catalyst in the course of the reaction may induce catalytic chlorination reactions in line with the detection of CCl_4 and $HCCl_3$ at the exit of the catalytic reactor (Path 2 in **Figure 1 - 1**). Hence the catalyst must be also resistant to mineral chlorine (Cl_2 , HCl) and to chlorinated organic species which can poison the catalyst as well.

Taking into account the activity for O_3 decomposition as the main criteria for the catalyst design, MnO_x based catalysts have been chosen to be tested for TCE oxidation in PPC configuration based on previous work of T. Oyama *et al.* [80] which showed MnO_2 as the most promising catalyst for O_3 decomposition among different TMOs. With that respect, the performances of various Mn based oxides have been studied by our team in PPC configuration for TCE abatement in dry and/or moist air using a multi-pin-to-plate NTP reactor working in a DC negative corona discharge. The obtained results are summed up in **Table 1-2**. Regarding the different catalysts, we have a commercial MnO_2 [9], a perovskite, $LaMnO_3$ synthesized by the citrate method [54] and modified manganese oxides with (i) Ce (a poorly crystallized Ce- (MnO_x) synthesized by a redox-precipitation route) [55], with (ii) Fe (a cryptomelane (Fe-K-

OMS-2) synthesized by a co-precipitation method) [56] and with Cu (a crystallized Cu:Mn oxide, namely CuMn_2O_4 synthesized by co-precipitation) [57].

Unfortunately, a direct comparison between the different PPC processes in terms of CO_x ($x = 1$ and 2; Y_{CO_x}) and CO_2 (Y_{CO_2}) yields is not possible due to different experimental conditions. In that way it must be stated that the NTP reactor configuration has been optimized in the last set of experiments in doubling the number of pins to increase the residence time in the reactor. Additionally, the initial concentration of TCE, the weight of catalyst as well as the temperature of catalytic bed have been decreased over time to reduce the costs of the process. Irrespective of the catalyst formulation, high TCE removal efficiency (up to 97%) can be reached in line with the high reactivity of NTP. Additionally, a decrease of the initial TCE concentration accompanied with a decrease of the supply air flow rate (higher catalyst contact time) allows to improve CO_2 yield (up to 62% but for just short periods (~ 15 min) with NTP assisted Fe-K-OMS2). Nonetheless, the production of CO is always important highlighting the fact that the oxidation of CO into CO_2 has to be promoted. On purpose, the beneficial role of Cu in CuMn_2O_4 has been highlighted as it is for this catalyst that the $Y_{\text{CO}_x}/Y_{\text{CO}_2}$ value of 1.34 is the lowest with the highest Y_{CO_2} of 50% after 5h of treatment. In any case, O_3 is not detected at the exit of the catalytic reactor which shows that the catalysts are highly efficient for O_3 decomposition. However, the formation of C1 chlorinated compounds shows that the partial chlorination of the catalyst surface whatever the catalyst under concern as evidenced by the presence of a Cl $2p_{3/2}$ component at a BE of 198.5 ± 0.5 eV which plays an important role in the selectivity of the process despite the addition of water in the gas feed to be treated which can help for the removal of chlorinated organic ad-species. The production of NTP generated by-products, namely PG, DCAC and TCAD, is strongly decreased after passing through the NTP assisted catalyst owing: $\text{LaMnO}_3 > \text{Ce}-(\text{MnO}_x) > \text{CuMn}_2\text{O}_4 - \text{P4} \gg \text{Fe-K-OMS-2}$. However, the concomitant production of chlorinated C1 products, namely CCl_4 and CHCl_3 , and the presence of chlorinated ad-species which strongly interact with the active sites precludes to get higher CO_2 yields.

Table 1 - 2: Summarizing table of the different catalysts used in PPC for TCE abatement with the different plasma conditions

Catalyst	NTP (pin-to-plate)*	m cata /g	[TCE] / $\mu\text{mol}/\text{min}$ (ppm)	Q /L/h	T /°C	RH /%	ED /J/L	GHSV /L/g.h	Time/ min	RE /%	Y CO_x / %	Y CO_2 / %	ref
MnO_2	5	1	10 (600)	30	300	0	240	30	30	90	54	22	[9]
LaMnO_3	5	1	41(600)	120	150	18	460	120	30	93	75	29	[54]
CeMnO_4	5	1	30 (400)	120	150	18	240	120	30	97	57	30	[55]
Fe-K-OMS	10	0.5	6 (300)	30	150	15	120	60	15	83	83	62	[56]
CuMn_2O_4 -P4	10	0.5	6 (300)	30	150	15	120	60	60	65	65	50	[57]

*: Number of pins
RE: Removal efficiency

1-5- Plasma as ozoner and ozone decomposition

1-5-1- NTP and ozone generation

Usually, ozone is generated by ultraviolet rays (UV lamp) or by Non-thermal plasma (NTP). UV ozone generator is a simple construction, with low cost, low nitric oxide production and is not affected by the presence of humidity in air. The main disadvantage is that it does not produce high concentrations of ozone (2 mg/h) and as a result air needs to be exposed to the UV lamps for a longer time.—By comparison, NTP technology is able to produce high concentrations of ozone from air instantaneously accompanied with the formation of nitrogen oxides. The production of ozone is a function of different factors such as discharge type, discharge polarity and plasma reactor configuration.

The main types of electrical discharges to produce ozone by NTP at atmospheric pressure are dielectric barrier discharge and corona discharge. Comparing these two electrical discharges, corona discharge is an easy method for generate NTP with high flow rates. The main disadvantage is the active volume of the ionization region which is very much smaller than the total discharge volume confined between the two electrodes at atmospheric pressure [9,27,58–60]. The corona discharge is initiated by acceleration of free electrons and subsequent electron collision processes. A series of gas-phase reactions controlled by the energetic electrons created in the corona discharge leads to ozone production. The initial step in O₃ formation results from electron impact dissociations of molecular O₂ and N₂ according to the following equations [9,61–65].



The oxygen atom can further react with O₂ and a third collision partner (O₂, N₂) to produce O₃ as:



The NTP discharges are subdivided by the type of the power supply such as DC, AC or pulsed depending on the temporal behavior of the sustaining electric field. Taking into consideration cost-performance, DC corona discharge is superior to the other discharges [66]. Furthermore, DC corona processing efficiency for ozone generation is different when using different discharge polarities. A positive DC corona discharge is formed when the electrode with the strongest curvature is connected to the positive output of the power supply. On the other hand, when the sharp electrode is connected to the negative output a negative DC corona discharge is

generated. In the negative corona plasma, the total number of electrons is more than 50 times that produced in the positive corona as observed by Zhang *et al.* [66]. This can be explained by the fact that the plasma size of the plasma region (where electron-impact reactions are significant) is greater in a negative discharge. In fact, the plasma region in positive corona discharge coincides with the active ionization region but in the negative corona, the plasma region extends beyond the ionization region. Due to the significant difference in the number of electrons in positive and negative coronas, it's reasonable to assume the production of ozone to be far greater in the negative corona than in the positive corona. In contrast, the mechanism for ozone production is independent in the discharge polarity [60,62,67–69]. However, NTP in DC discharge are created in closed discharge vessels using interior electrodes. Depending on the current and discharge voltage, different type of discharge can be obtained. The formula between the discharge current and the inter electrode voltage is: $I = CV(V - V_0)$, where C is a constant depending on the geometry [70]. According to this formula, three regimes of DC discharge are observed as shown in **Figure 1-3, 1-4**. At a voltage V_0 , the corona discharge is initiated, and the corona regime increases linearly with increasing the voltage. In the glow discharge, intermediate regime, the relationship is exponential and nonlinear. The third regime is when the corona transfers to spark regime [9,27,59]. The transition to glow discharge, is marked by a decrease in the voltage and increase in the current and also the active volume of the ionization region is the bigger one compared with the other regimes leading to more ozone production. To maintain this NTP regime of “glow discharge”, a multi-pin-to-plate reactor is used, with a specific geometry of electrodes. This type of reactor was first proposed by Akishev *et al.* [71,72]. The electrodes consist of crenellated pins (cathode) which allow the discharge to ignite at different points contributing to a better diffusion of the current. The anode is a plate containing hemi-spherical surfaces facing the pins. This type of reactor is used in our work with 10 pin-to-plates.

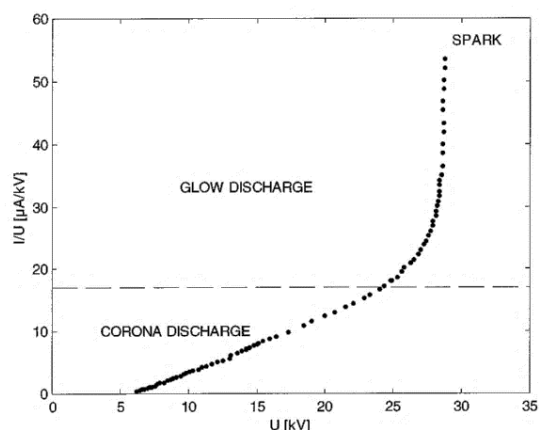


Figure 1 - 4: Current voltage characteristic of a negative DC geometry

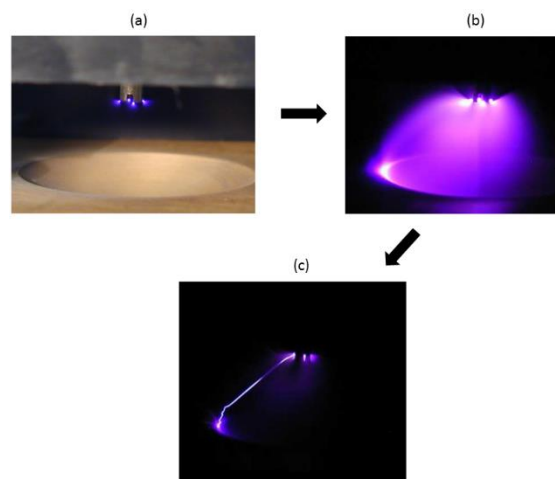


Figure 1 - 3: Different discharge regimes of a negative DC excited glow discharge: (a) corona regime; (b) glow regime; (c) spark regime

1-5-2- Ozone catalytic decomposition

Various techniques such as thermal decomposition [73], photocatalytic decomposition [74], adsorption [75] and catalytic decomposition were investigated and used for ozone decomposition. Among them, catalytic decomposition was the most effective method for gaseous ozone decomposition because it was a safe, economical and efficient method. Noble metal catalysts (such as Ag [76], Au [77], Pd [78]) showed excellent activity for ozone decomposition but their price limit their practical application. In that way, various transition metal based catalysts were investigated as noble metal-free substitutes for ozone decomposition (Ni, Co, Ce, Cu and Mn [79]) and it was found that p-type semi-conductors were the most active catalysts for ozone decomposition [80,81]. Dhandapani and Oyama [82] reported previously that among the different TMOs, MnO_2 exhibited the best activity for ozone decomposition. The high ozone decomposition of manganese oxides was attributed to its multiple and changeable Mn valence and oxygen vacancies. However, MnO_2 showed several different crystalline structures such as α , γ , β , λ and δ - MnO_2 , where the MnO_6 octahedral were linked in different ways which could result in different catalytic properties. With that respect, Jia *et al.* investigated the ozone decomposition over three different tunnel structures of MnO_2 (α , β and γ - MnO_2) and reported that α - MnO_2 , a manganese oxide with a one-dimensional tunnel structure with inside dimensions of $0.46 \times 0.46 \text{ nm}^2$ that is composed of MnO_6 octahedra sharing common edges (2×2) and common vertices, possessed the highest activity, which was ascribed to its highest content of oxygen vacancies and largest specific surface area [83]. Catalytic decomposition of

gaseous ozone (O_3) over todorokite with enlarged tunnel dimensions and the effects of cerium modification was investigated by Y. Liu *et al.* [84]. Catalytic activity and stability were greatly improved over Ce-modified MnO_2 (Ce- MnO_2), which increased with the increase of Ce/Mn atomic ratios from 0.06 to 0.28. Larger surface area and enhancement in the crystal boundaries between MnO_2 and CeO_2 resulted in the formation of more oxygen vacancies, which act as the active sites for O_3 decomposition. In another study [85] α - MnO_2 nanofiber with high concentration of surface oxygen vacancy was obtained via a vacuum deoxidation method. The activity of α - MnO_2 strongly depends on the concentration and extent of oxygen vacancy, which can be adjusted by tuning the temperature and duration of vacuum deoxidation. As a consequence, the oxygen vacancy formation enhanced the ratio of Mn^{3+}/Mn^{4+} , which changed the charge distribution on the α - MnO_2 nanofiber, resulting in a significant improvement of the adsorption of ozone on the surface of the catalyst

Compared with pure manganese oxide, the beneficial effects of introducing another TMO to get a TM modified manganese-metal oxides were often highlighted. MnO_x doped with different TM such as Ce, Co, Fe, W and V exhibited better performances towards O_3 decomposition due to an enhancement of the specific area and an increase in the content of oxygen vacancies [84,86–89]. In particular as exposed before, Ce doped todorokite type- MnO_2 with Ce/Mn atomic ratio of 0.28 exhibited the best activity and stability for O_3 decomposition due to largest surface areas inducing the concomitant increase of amount of oxygen vacancies and of crystal boundaries between MnO_2 and CeO_2 [84]. Ma *et al.* [86] studied the effect of TM (such as Ce, Co and Fe) in TM doped α - MnO_2 and found that Ce doped α - MnO_2 exhibited the best activity for ozone decomposition. The speciation of Ce, as Ce^{4+} , which partially replaced K^+ in the tunnels and Mn^{4+} in the MnO_2 framework might explain such beneficial effect. Similarly, Liu *et al.* [90] highlighted the formation of an efficient mixed oxide for O_3 decomposition after doping γ - MnO_2 with Ce resulting from an increase of the surface area and of surface defects in ozone decomposition. In another recent study, Ma *et al.* [89] investigated the synthesis of Ce doped Mn_aO_x by a precipitation method instead of hydrothermal method (which is a common method used for the synthesis of Ce doped MnO_x for ozone decomposition). They found that Ce doped Mn_aO_x with $a = 10$ (which represents the molar ratio of Mn over Ce) was highly efficient for ozone decomposition under high GHSV (840 L/(g_{cata}.h) and 40 ppm of initial ozone concentration. The addition of Ce in MnO_x contributed to a significant improvement of the catalytic performance in O_3 decomposition reaction owing to (i) an increase in surface area, (ii) a decrease in crystallinity, and (iii) a larger amount of surface

oxygen vacancies [88]. It was believed that the oxygen transfer between Ce^{4+} and Ce^{3+} species on the catalyst surface allowed abundant oxygen species storage and leads to superior redox properties compared to those obtained with simple manganese oxides [91,92]. Overall, these results indicated that Ce was an excellent additive for MnO_2 to improve O_3 decomposition performances.

1-5-3- Mechanisms for ozone decomposition in dry and humid air

The mechanism and the kinetics of the elementary reactions involved in the ozone decomposition were investigated in numerous studies on transition metal oxide (TMO) [81,82,87,90]. In general, the mechanism for ozone decomposition followed four steps which were illustrated in **Figure 1-5-a** which gave the mechanism for ozone decomposition on $\alpha\text{-MnO}_2$ [85]. After the surface oxygen vacancy formed, the oxygen coordination number around Manganese site reduced from six to five, where the mononuclear five-oxygen coordinated Manganese site was regarded as the active center of ozone decomposition. Firstly, an ozone molecule was adsorbed on an oxygen vacancy (state 2) to form a dioxygen molecule and an oxygen species (O_2^- , state 3) by electron transfer. Then, the active oxygen species O_2^- could react with another ozone molecule to form a peroxide species (O_2^{2-} , state 5). Finally, the peroxide species (O_2^{2-}) transformed into O_2 and the oxygen vacancy was restored.

Hence, oxygen vacancy was beneficial for ozone adsorption and decomposition on the catalyst surface.

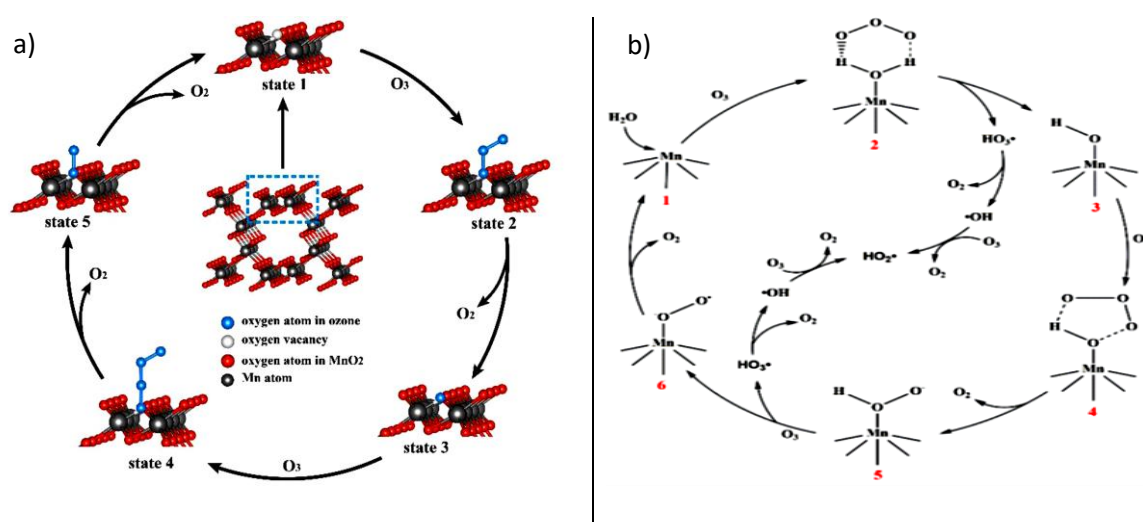


Figure 1 - 5: Mechanism of ozone decomposition on $\alpha\text{-MnO}_2$ in a) dry air b) humid air

Furthermore, in the presence of humidity another pathway (**Figure 1-5 b**) for ozone decomposition was proposed in which water adsorbed on oxygen vacancy to produce surface- OH_2^+ . Under the influence of electrostatic forces and hydrogen bonding, a six-membered ring was formed with the O_3 molecule [85]. This ring was unstable and transformed into a surface hydroxyl group with the release of HO_3^* . At the same time, the ozone molecule reacted with the surface hydroxyl group and formed a five-membered ring (state 4). Then the five-membered ring transformed into a surface hydroperoxyl anion (HO_2^-) with the release of O_2 . Then O_2^- was formed by reaction between the surfaces HO_2^- with O_3 . Finally, O_2^- was released as an oxygen molecule from the surface to regenerate the oxygen vacancy on the surface. If RH was too high, water adsorption increased and blocked the surface active sites.

1-5-4- Deactivation mechanism

Although MnO_x catalysts were widely studied due to their excellent properties, they were prone to deactivation under both wet and dry atmospheres. After reacting with ozone, manganese oxides adsorbed oxygen species leading concomitantly to a higher Mn valence state and a decrease of oxygen vacancies which were the main causes for catalyst deactivation in dry and in humid air. However, under humid atmosphere, in addition to the deactivation due to the accumulation of oxygen intermediates, the causes of deactivation were more complex and varied due to the presence of water molecules. The deactivation of MnO_x under humid atmosphere was mainly caused by competitive adsorption of water molecules and O_3 molecules. The adsorbed H_2O molecule was difficult to desorb from the surface oxygen vacancy, resulting in a rapid decrease in the ozone removal rate.

These two deactivation mechanisms did not take into account the deactivation due to related nitrogen oxides species. Indeed, once ozone was generated using air as a carrier gas, it was accompanied by NO_x , especially when the plasma was the source of ozone. Additionally the amount of nitrogen oxides generated by the plasma was higher compared to UV lamp. Mehandjevi *et al.* [93] showed that the main reason of $\alpha\text{-FeO}_2$ deactivation for O_3 decomposition by producing ozone through an ozone generator in dry air was due to the adsorption of some nitrogen oxides species transforming to nitrate ions on the catalyst surface. To support this result, Touati *et al.* [94] reported recently on the deactivation for ozone decomposition of $\text{Pd/Al}_2\text{O}_3$ catalyst due to NO_x poisoning.

1-5-5- Acid treatment to increase MnO_2 hydrophobicity

Additionally, the hydrophobicity of MnO_2 was investigated in order to increase the catalytic performance for ozone decomposition. The addition of noble metals such as Ag [95] was one method to enhance the hydrophobicity. However, ammonium or acid treatments were the most encountered routes. T. Gopi *et al.* investigated for the first time the ozone decomposition over a layered structure of MnO_2 (birnessite), a nanostructured $\text{K-}\delta\text{-MnO}_2$ (synthesized by hydrothermal method) and $\text{H-}\delta\text{-MnO}_2$. They found that the exchange of K^+ by H^+ when using a HNO_3 (1M at 70°C for 6 hours) treatment, led to higher surface area, lower Mn average oxidation state (AOS) and increase in the surface oxygen vacancies. These modifications result in a better activity and stability towards ozone decomposition in dry and humid air [96]. Y. Liu *et al.* [97], reported that a birnessite synthesized by a redox method using KMnO_4 and CH_3OH and subsequently treated with HNO_3 (0.2M at 50°C for 6 hours) possessed high activity for ozone decomposition due to the fact that after acid treatment the surface area of the catalyst increases together with the formation of a large amount of acid sites and oxygen vacancies. Furthermore, ozone molecules reacted as Lewis bases on Lewis sites [80,97,98]. Acid-treated [97] or ammonium-treated [99] birnessite investigated as two approaches to increase the water-resistant property in other term to increase the material hydrophobicity.

1-5-6- Mechanism for ozone decomposition over birnessite treated with nitric acid

After acid treatment, Liu *et al.* [97] showed by DFT calculation that the formation energy for oxygen vacancy was two times lower as compared with the as-synthesized birnessite, which indicated that oxygen vacancies could be formed much more easily over the acid treated birnessite. Additionally, a high amount of acid sites were formed on the catalyst surface. Based on these results, Liu *et al.* [97] proposed a reaction mechanism for gaseous ozone decomposition which was given in **Figure 1-6**. The catalyst surface was composed of adjacent oxygen vacancy and acid site.

O_3 molecule was firstly adsorbed on a surface acid site *via* one terminal oxygen atom through hydrogen bond. Secondly, the other terminal oxygen atom of the O_3 molecule inserted into an oxygen vacancy site, leading to the formation of an O^{2-} species which was released as an oxygen molecule into the gas phase resulting in the regeneration of the acid site. Third, another O_3 molecule formed hydrogen bond with surface acid site and its free terminal oxygen atom interacted with the formerly formed O^{2-} species to produce a peroxide (O_2^{2-}) with release of an oxygen molecule. Finally, the O_2^{2-} decomposed was transformed into oxygen molecule which was released in the gas phase allowing the regeneration of the oxygen vacancy.

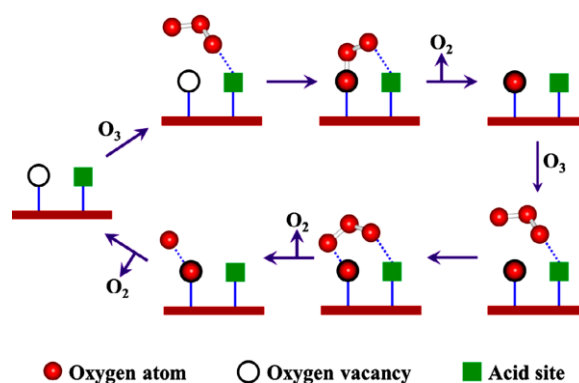


Figure 1 - 6 : Mechanism for gaseous ozone decomposition over acid treated birnessite

In order to meet most of the criteria discussed above, a higher amount of oxygen vacancy, resistance to water and chlorine undoped or Ce-doped birnessite materials, treated or not with nitric acid, were chosen as defective structures for ozone decomposition and TCE oxidation enabling to work at low temperatures.

1-6- Birnessite

The birnessite is chosen as a powerful catalyst which has been recognized to decompose different VOCs at low temperature mainly due to its redox properties as explained in more detail in the following section. Birnessite is a manganese dioxide known as δ - MnO_2 . It has been first discovered by Jones and Milne (1956) in the Birness region of Scotland, who gave it the formula $\text{Na}_{0.7}\text{Ca}_{0.3}\text{Mn}_7\text{O}_{14} \cdot 2.8\text{H}_2\text{O}$. This mineral is omnipresent in soils and sediments and is one of the most common Mn oxides [100–102]. In the natural environment, birnessite is characterized by low crystallinity [102–104]. It is a mixed valence manganese oxide $\text{Mn}^{3+}/\text{Mn}^{4+}$. Birnessite is a 2D layered manganese oxide material with edge shared MnO_6 octahedra forming the layer with an interlayer separation of about 0.7 nm. It has a significant amount of water and stabilizing cations such as Na^+ and K^+ between the sheets. This mineral, whose sheets are negatively charged (~ 0.2 - 0.35 charge per Mn) has a high capacity for adsorption and ion exchange. In addition, the presence of heterovalent cations in the layers (Mn^{2+} , Mn^{3+} , Mn^{4+}) confers redox properties [105] which are involved in the adsorption mechanisms of certain cations: As, Cr, Co for example [104,106].

1-6-1- Birnessite crystalline structure

Birnessite is defined according to two criteria: its layers are rich in manganese and the interfoliar distance is close to 7\AA . This very succinct definition does not account for very large structural variations existing among the different varieties of birnessite known to date. The first structural studies carried out on natural birnessite collected in marine or terrestrial sediments

have identified a hexagonal or pseudo-hexagonal structure [102,107]. Another study conducted by Tan *et al.* (2010) [108] states the existence of triclinic symmetry in addition to hexagonal.

The structural study of synthetic birnessite by X-ray diffraction and Rietveld refinement was performed for the first time by Post and Veblen, (1990) [109] studying the structure of a birnessite synthesized by oxidation of Mn (II) in basic medium [55,84,86,110–112]. The structure obtained was described as monoclinic. Studies by Drits *et al.* (1997) [103] and Silvester *et al.* (1997) [104] extended the structural analysis and confirmed the monoclinic symmetry of birnessite synthesized under basic conditions and described a hexagonal structure for that synthesized by the reduction of Mn (VII) in an acidic medium according to the McKenzie protocol (1971)[113]. The monoclinic structure of birnessite synthesized in a basic medium has nonetheless been questioned by Post *et al.* (2002) [114] who demonstrated that it was more of a triclinic symmetry.

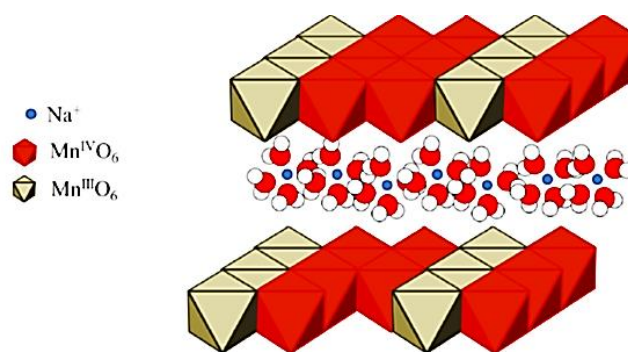


Figure 1 - 7: Scheme of the crystal structure of a triclinic birnessite : alternation of a chain of Mn(III)O₆ and two chains of Mn(IV)O₆ [114]

The triclinic birnessite studied by Post and Veblen (1990) [109] has sodium cations in the interlayer space, its chemical formula has been described as $\text{Na}_{0.58} (\text{Mn}^{4+}_{1.42} \text{Mn}^{3+}_{0.58}) \text{O}_4 \cdot 1.5\text{H}_2\text{O}$. The structure of this type of Birnessite is shown in **Figure 1-7**. It is formed of non-lacunar layers of thickness 2 Å with an equidistance of 7 Å. The layers consist of MnO₆-sharing octahedra containing Mn³⁺ / Mn⁴⁺ mixed valence cations [109,114]. The layers have been described as being an alternation of an octahedral chain of Mn (III) O₆ and two octahedral Mn (IV) O₆ chains distributed along the b axis [103,104,115]. In the layers of birnessite, manganese is in octahedral symmetry. The electronic configuration of Mn (III) being [Ar] 3d⁴, it suffers by Jahn-Teller effect, a distortion of its symmetry (non-regular octahedron). This is not the case of Mn (IV) of electronic configuration [Ar] 3d³. Therefore, a layer formed only by Mn (IV) O₆ octahedra would have hexagonal symmetry, but the presence of Mn (III) O₆ decreases symmetry due to the Jahn-Teller effect [121] The substitution of the Mn (IV) cations by Mn (III) creates a negative charge of the sheets which is compensated by the presence of hydrated

interlayer cations (eg, $\text{Na} + (\text{H}_2\text{O})_n$) which occupy the space between the sheets [114]. Interlayer sodium can be exchanged by a variety of cations: Li^+ , K^+ , Cs^+ , Be^{2+} , Sr^{2+} , Ba^{2+} without affecting the structure of birnessite [116–118]. The exchange by Ca^{2+} , Mg^{2+} or Ni^{2+} causes hydration of birnessite and its conversion to buserite [116]. The hydration energy of the intercalated cation, related to its size and its charge, controls the binding force between the latter and the water. Hydration degree varies with the type of interfoliar cation [119].

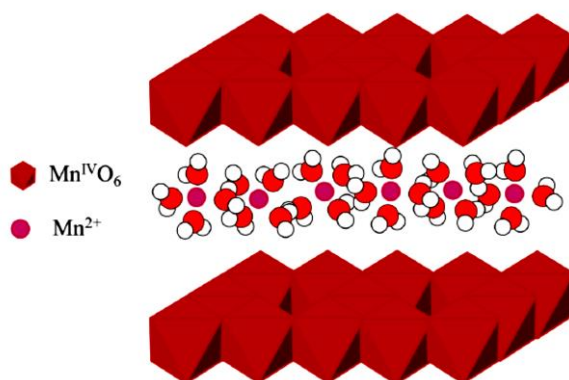


Figure 1 - 8: Crystalline structure of hexagonal birnessite: a predominantly Mn(IV) chain sheet with gaps, interlayer cations are H^+ and $\text{Mn}^{2+}/\text{Mn}^{3+}$ which are positioned below and above the deficiencies [115]

In the birnessite of hexagonal symmetry, manganese is mainly in its oxidation state (IV). The presence of octahedral deficiencies is the major cause of layer slip deficiency [115] (**Figure 1-8**). This deficit is offset by the presence of protons and interlayer Mn (II) / Mn (III) that lie below and above the deficiencies [104]. The interlayer distance is 7 Å. The formula proposed by Lanson and al. (2000) for the birnessite hexagonal is $\text{H}^+_{0.33}\text{Mn}^{3+}_{0.111}\text{Mn}^{2+}_{0.055}(\text{Mn}^{4+}_{0.722}\text{Mn}^{3+}_{0.111}\square_{0.167})\text{O}_2$ where \square represents the gaps in the layers. The sheets have about 72% Mn (IV), 11% Mn (III) and 17% deficiencies [121].

Birnessite symmetry transformation from one type to another is possible. This can be the result of a change in the pH of the reaction medium [103] or the presence of a cation that causes redox reactions with the manganese contained in the birnessite [104,120]. Lanson *et al.* [121] reported the transformation of triclinic Na-Birnessite into H-Birnessite in acidic medium (pH 2-5). They found that hexagonal phase is only possible at $\text{pH} \leq 3$. This study shows that, when a triclinic Na birnessite is placed in acidic medium, a Na^+/H^+ exchanges takes place in the interfoliar space and a dismutation reaction of Mn (III) into Mn (IV) which remains in the layer, and into Mn (II) which migrates into the interfolaire distance takes place. The dismutation reaction reduces the amount of Mn (III) and leads to the formation of gaps. However, hexagonal

birnessite maintained in alkaline solution NaOH can transform into Na triclinic birnessite as reported by Zhao *et al.* [120].

Vernadite: Another variety of birnessite is the vernadite structure. Vernadite has been first described by McMurdie (1948) [122] who assumes the material to be a poorly crystallized variety of cryptomelane, while other studies conducted at the same time concluded that this synthetic compound had a structure similar to pyrochroite [123]. More recently, using synchrotron techniques (XANES), Manceau *et al.* (1992) hypothesized that vernadite had a tunnel-like structure composed of chains of varying sizes and lengths [121]. In fact, a number of studies have studied the behavior of vernadite under the assumption that they have been dealing with a hydrous manganese oxide. Vernadite is also commonly referred to as "hydrous manganese oxides - H.M.O", a denomination that assumes that the oxide is, again, amorphous [124]. However, the true nature of vernadite, and its relationship to birnessite were discovered by R. Giovanoli in the 1970s. He was the first to describe vernadite as a turbostratic form (without three-dimensional order, which is to say with translations and/or random rotations between two successive sheets) of birnessite. This discovery engaged then strong discussions with a Russian team led by F.V. Chukhrov [107]. This team thought that birnessite and vernadite were two independent minerals. Their hypothesis was based in particular on the fact that the visible basal reflections on diffractograms of birnessite at 7.2Å (001) and 3.6Å (002) were totally absent in the diffractograms of the vernadite. Whereas, when Jones and Milne (1956) first described birnessite, they noted only a series of four diffraction peaks corresponding to basal distances of 7.27 Å, 3.60 Å, 2.44 Å and 1.412 Å, which could indicate a low crystallinity level. However, this lack of basal reflections is explained by the nanometric nature of the vernadite. Villalobos [114] showed that vernadite is nanometric in size in all three dimensions of space, and that the number of stacked sheets along the c^* axis is on average about 2-3. In fact, basal reflections are extremely attenuated, and it is possible that they have been completely masked if the diffractometers used by the F.V. Chukhrov team were less efficient than at present, and/or if the particles studied were even smaller in size. It is now accepted that vernadite are turbostratic birnessite, but the structural characterization of these minerals remains difficult, and the word "vernadite" ultimately refers only to a turbostratic and nano particulate variation of a non-stoichiometric Mn^{IV} oxide. Due to its low crystallinity and turbostratic character, vernadite has a diffractogram in which the first two Bragg rays of birnessite are almost absent (not well defined and broad) (**Figure 1-9**), and has only two diffraction bands in the angular region 30 -80° 2 Θ CuK α classically used in mineralogical studies.

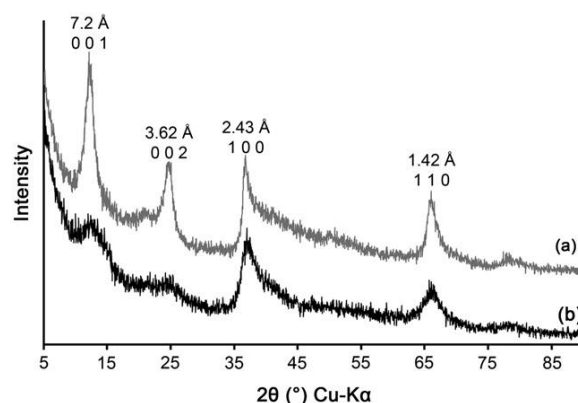


Figure 1 - 9

Figure 1 - 9: XRD pattern for a) birnessite b) vernadite

1-6-2- Birnessite synthesis methods

There are several chemical routes to obtain birnessite. The symmetry as well as the chemical composition of birnessite depends on the synthesis methods. A synthesis carried out in an acidic medium results in a hexagonal symmetry, whereas a synthesis carried out in a basic medium results in a triclinic symmetry. It is possible to classify the synthesis methods in four groups according to the reaction conditions.

I- Oxidation of Mn (II) by oxygen in an alkaline solution: This is the oldest method, based

on the oxidation of pyrochroïte $\text{Mn}(\text{OH})_2$ by oxygen in the presence of alkaline solution. The birnessite obtained has a triclinic symmetry with K^+ or Na^+ as interlayer cations, depending on the alkaline solution used KOH or NaOH [125,126].

II- Reduction of Mn (VII) in acidic medium. The oldest process in the Mckenzie procedure

[113], where the reduction of KMnO_4 is carried out using a concentrated acid HCl, which makes this method restrictive. It remains quite reactive because it allows to obtain hexagonal symmetry. Different other reducing agents have been used such as alcohols[127], ethylene glycol [128], sugars [164] and more **recently lactate** [130].

III- Transformation of another manganese oxide: this method is not often used. Cornell and

Giovanali [101] investigated successively the direct conversion of hausmannite to birnessite in a highly alkaline environment.

IV- Synthesis using the couple $\text{MnO}_4^-/\text{Mn}^{2+}$. This synthesis is based on a redox reaction

between MnO_4^- and Mn^{2+} in alkaline medium. It generally involves the use of three reagents: A salt of Mn (II) (MnCl_2 , MnSO_4 or $\text{Mn}(\text{NO}_3)_2$), a permanganate solution (KMnO_4 or NaMnO_4) and a base (KOH or NaOH). This method is intensively studied because of its ease of use and contributes to the formation of triclinic birnessite [131–133].

1-6-3- Variability in the composition of sheet and interfoliare

The layers of birnessite are mainly composed of Mn (IV). The leaflet may also contain a number of octahedral sites whose manganese is vacant, so we shall speak of gaps. In parallel with the presence of gaps, the leaflet may include a number of Mn IV substitutions by Mn III. In the case where the amounts of Mn III in the layer are small, and / or the Mn III is not organized in rows, the symmetry of the layers is hexagonal. In the case where the Mn III is sufficiently abundant and organized, the layer loses its hexagonal symmetry and becomes triclinic. It should be noted that the replacement of manganese by other cations, of size close to Mn III, IV, in the birnessite layer has already been observed, as for example nickel or cobalt [106]. The modeling of the structure of the layer is a fundamental parameter for understanding the reactivity of the birnessite. Indeed, if the stoichiometric structure of the layer of a phyllomanganate such as birnessite is theoretically MnO_2 , the various studies made on this mineral and its synthetic analogues have shown that, practically, the chemical composition was of the form:



In this formula, the species in brackets make up the layers and the species to the left of the brackets are in the interlayer distance. Inter represents any interstitial cation, H_2O water molecules related to these cations and free water. Me represent any cation presents in the leaflet, other than manganese, and finally \square represents the gaps in the leaflet.

The charge deficit of the layers can thus be induced either by the presence of vacant sites or by the substitution of a Mn^{4+} of the layers, by Mn^{3+} more often. Depending on the origin of the charge deficit, the reactivity will be strongly different. Indeed, a site vacancy will create a locally high load deficit (4 charges), while substituting a Mn^{4+} for a Mn^{3+} will only create a single charge. According to the different studies conducted on the birnessite, a charge deficit created by the substitution of Mn^{4+} by Mn^{3+} will be compensated by cations situated relatively far from the layers, most commonly in the middle of the interlayer distance, according to a mode called adsorption in outer sphere complex, a vacant site will most often lead to the adsorption of cations just above or below these vacancies; we shall then speak of an internal sphere complex. However, the inner-sphere complexes can be located at different

crystallographic positions such as triple corner sharing (TC), triple edge sharing (TE) and double corner sharing (DC) **Figure 1-10**.

- Triple corner sharing: the cation is located at the bottom of a gap, and is coordinated to three oxygens of the sheet. The cation is also coordinated to water molecules in the interlayer, but this number is variable. For example, zinc (Zn) can be in octahedral coordination (coordinated to three water molecules), but when adsorbed on a birnessite with low coverage, it coordinates tetrahedrally (coordinate to only one water molecule in the interlayer) with the coordination sphere forming a pyramid with a triangular base formed by three sheet oxygen atoms [115,134,135]
- Triple edge sharing (TE): The cation shares three edges with the sheet above which it is adsorbed overhanging a tridentate cavity. This position is much less frequent than the TC position. This crystallographic position, a priori less stable than the TC position, can however be explained by a cation bound to two un-saturated oxygen of an octahedral gap. Or in the case where the sheet contains for example Mn^{3+} , the third oxygen to which the cation is bound is also un-saturated. This position could be favored when a cation is absorbed on the other side of the vacant octahedral site. The number of water molecules coordinating the cation in the interfoliar distance is not fixed and is dependent on the cation as with TCS [115,134,135] .
- Double corner sharing (DC): The cation, located at the edge of the sheet, is coordinated to two oxygens of the sheet and the rest of coordination ensured by water molecules, one of which is located in the plane of the sheet oxygen atoms [115,134,135].

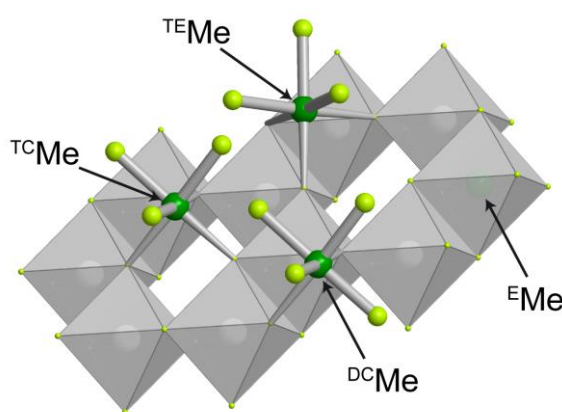


Figure 1 - 10: Inner sphere complexes crystallographic position: Me represents metal; ^EMe represents edge sharing

1-6-4- Birnessite properties (amount of alkaline metals) and capacity of ion exchange

The various synthesis procedures, precursors and reaction conditions, including reagent concentration, aging time and reaction temperature, constitute the main difficulty in determining a correct chemical formula for birnessite summarized in **Table 1-3**. The negative charge of the birnessite layers is compensated by alkali metals and / or protons from the reaction medium. These cations can be adsorbed on the surface or intercalated in the interlayer surface. However, layer cation vacancies are associated with interlayer cations. On other way, the vacancy problem is related to the problem of the valence of Mn cations. Under ideal conditions, the amount of alkali metals should be equal to the amount of Mn^{3+} in the layers, the latter is estimated to be 1/3 [103,136]. The best known are birnessite Na and K, the following section will focus on the amount of Na and K observed in the literature as interlayer cations in birnessite.

The K/Mn ratio varies between 0.06 and 0.32 [103,125,137–143], while the Na/Mn ratio varies between 0.09 and 0.58 [137,138,140,141]. Prieto *et al.* [144] has studied the variation of alkali/Mn ratio, and they found that variation in the experimental molar ratio influences the amount of K and Na measured in the interlayer distance, but for K the amount is limited to 0.31 which means that the maximum of K^+ that can be in the interlayer distance is 0.31. Varying the two ratios influences the average manganese oxidation state (AOS); increasing or decreasing the alkali metal/Mn ratio results in a decrease in the AOS of Mn [136]. However, the typical value for birnessite AOS is between 3.6 - 3.8 [137]. Kulish *et al.* [138] have synthesized Na-Birnessite with Na/Mn = 0.22 and K-Birnessite with K/Mn = 0.6 as the result Mn AOS is 3.78 and 3.37 respectively, a higher alkali cation content in the interlayer space leads to a larger proportion of Mn^{3+} . Moreover, Zhu *et al.* [91], have been found a collapse of the birnessite structure with a K/Mn = 0.06 into an amorphous manganese structure. For Na-birnessite the amount of Na should be between 0.17-0.33, which corresponds well to the Mn AOS (3.6-3.8) [103,115,125,137–140,145]. Birkner *et al.* [141], has synthesized sodium birnessite by keeping the amount Na/Mn 0.09 as a result they obtained Mn AOS = 3.56. Zhang *et al.* [145], have reported Na-birnessite with a high amount (Na/Mn = 0.58) of Na in the interlayer distance resulting on a Mn AOS = 3.42. However, washing can affect the amount of the alkali metals. It has been reported that birnessite is washed by different solvents such as water alcohol and acetone. Feng *et al.* [146] has found that washing with alcohol or acetone resulted in a finer powder as compared to washing with water. The washing is needful as reported by Prieto *et al.* [144] to remove the excess of alkali metal. Moreover, Kulish *et al.*

[138] has done the washing with water, intensively more for Na-birnessite (20 times) over K-Birnessite (3 times) (the volume of water is not given, typically they may be the same amount of water for each washing) due to its less hygroscopic nature.

Table 1 - 3: Summary table of the different synthesis procedure of birnessite, K/Mn and Na/Mn ratios reported in literature

Oxydant/reductant (molar ratio)	Medium	Washing	aging	K/Mn	Na/Mn	Ref
KMnO ₄ / HCl (1/2)	Acid	water	10 min	0.20		[147]
KMnO ₄ / HCl (0.2/0.36)	Acid	water	12h	0.17		[148]
KMnO ₄ / NH ₂ OH.HCl (0.02/0.006)	Acid	water		0.14		[149]
KMnO ₄ / HCl (0.20/0.27)	Acid	water	overnight	0.15		[150]
KMnO ₄ / HCl (0.20/0.27)	Acid	water	overnight	0.20		[151]
KMnO ₄ / HCl (0.20/0.27)	Acid	water	overnight	0.22		[152]
KMnO ₄ / C ₂ H ₂ O ₄ (0.001/0.0015)	Acid	Water	30 min	0.14		[153]
KMnO ₄ / C ₂ H ₂ O ₄ (2/3)	Acid		30 min	0.39		[154]
NaMnO ₄ / HNO ₃ (100/1)	Acid		4 days /170°C		0.69	[155]
NaMnO ₄ / Ethanol (excess of NaMnO ₄)	NaOH		40 days		0.33	[140]
NaMnO ₄ / Ethanol (excess of ethanol)	NaOH		40 days		0.33	[140]
KMnO ₄ / Ethanol (excess of NaMnO ₄)	KOH		40 days	0.30		[140]
KMnO ₄ / Ethanol (excess of ethanol)	KOH		40 days	0.32		[140]

Capacity of ions exchange: On this part we will focus on Na-Birnessite because it is more studied in the literature. The interlayer cations of hexagonal and triclinic birnessite are exchangeable with a wide variety of metal or organic cations. Na birnessite has a cation exchange capacity of about 240 meq/100g [130]. Studies on the substitution of sodium interfoliar with monovalent cations: K⁺, Li⁺, Cs⁺ and divalent cations: Ca²⁺, Ba²⁺, Be²⁺ and Sr²⁺ have been performed [103,116,118,119]. In the studies carried out at pH 4 on Na⁺/M²⁺ exchange (M²⁺ = Pb²⁺, Cd²⁺ and Zn²⁺), [103,106,115] showed the formation of vacancies in the layers after reaction with H⁺ and the adsorption of divalent cations onto these vacancies. Similarly, a more recent study established the selectivity of hexagonal birnessite towards divalent metals and the following classification was obtained: Pb²⁺>Cu²⁺>Zn²⁺>Co²⁺>Cd²⁺ [178]. Another study was interested on the selectivity of Na birnessite with respect to monovalent cations by analyzing sodium released in solution. The selectivity thus deduced decreases in the following orders: Cs⁺ >K⁺ ≥ NH₄⁺ >Na⁺ >Li⁺. This selectivity depends on the ionic radius of the intercalated species and its degree of hydration [156].

1-7- Formaldehyde

Formaldehyde or methanal or formal aldehyde is an organic compound of the aldehyde family, with the chemical formula HCHO (or H₂CO). It's a colorless gas under normal conditions of temperature and pressure with a strong, pungent, suffocating and highly irritating odor. HCHO is a highly reactive product that can both polymerize or form explosive mixtures

in air [157]. Furthermore, formaldehyde is very toxic and dangerous for human health. Formaldehyde is a toxic and dangerous volatile organic compounds, it has been classified in 2015 as a group 1 (definite human carcinogen) carcinogen by the International Agency for Research on Cancer (IARC). However, the Scientific Committee on occupational exposure limits (SCOEL) recommends 0.2 ppm (0.25 mg m^{-3}) as a limit exposure value for 8 hours and 0.4 ppm (0.5 mg m^{-3}) as limit exposure value for short term (15 min) [158]. Formaldehyde, is widely used material and present in industry, it should also be considered as a pollutant in indoor air. It's established that HCHO is one of the most major pollutants in indoor air and there are several sources of HCHO emission in our indoor air such as plywood coatings, wallpaper, paint is considered HCHO emitting material. Indeed, many other indoor products are likely to emit HCHO in indoor air such as, cigarettes, wood, oils, plastics and some household and cosmetics products [159]. However, the catalytic oxidation of this molecule is chosen in our work as an approach to validate the density of oxygen vacancies on our material which will be discussed in details in the following part.

1-7-1- Formaldehyde catalytic decomposition

Several transition metal mainly in oxide form have been used for HCHO oxidation. However, Sekine *et al.* [160], in 2001, study the catalytic decomposition of HCHO over different metal oxides such as: Ag_2O , PdO , CuO , CoO , ZnO , Fe_2O_3 , TiO_2 , La_2O_3 , WO_3 , CeO_2 , V_2O_5 and MnO_2 . Manganese dioxide was found to be the most active catalyst among aforementioned series. Furthermore, MnO_2 has advantages to be cost-effective, environmentally friendly and easy to get. In terms of MnO_2 crystal structure, birnessite type MnO_2 was recognized to be the most active catalyst in HCHO oxidation [161]. Birnessite type MnO_2 is a two-dimensional layered structure, composed of alternating stacked Mn–O layers (edge-shared MnO_6 octahedra) and hydrated alkali cations (Na^+ , K^+ , etc.) restricted in the interlayer region [24-27]. Wang *et al.* [163] reported on the beneficial role of interspacing water to promote the formaldehyde decomposition [163]. Wang *et al.* [164] investigated the nature of the intercalated ion and found that K-birnessite achieved the best CO_2 yield at ambient. K^+ was believed to enhance the surface oxygen activity facilitating the regeneration of surface hydroxyls by activating H_2O . In order to promote the catalytic performances of such materials significant experimental researches were recently focused on defective birnessite materials with proper surface electronic properties [29-31]. Wang *et al.* [168] reported on the introduction of manganese vacancies (V_{Mn}) in K-birnessite obtained from a redox-precipitation route whose relative content was tuned by affecting the oxidant/reductant atomic ratio. The MnO_2 with

higher content of V_{Mn} showed a better performance for formaldehyde decomposition. The promotion effect of K^+ in HCHO oxidation was herein supposed to be accomplished through activation of surface oxygen species. In addition, Rong *et al.* [169] reported about the existence of an optimal K^+ content to promote the activity in Mn vacancy-rich birnessite-type. A too high K^+ content increased the amount and strength of surface basic sites making the CO_2 desorption more difficult and in that way partially inhibited the catalyst. Taking into account these considerations, Li *et al.* [170] reported on K-birnessite with poor crystallinity with a medium K^+ concentration for obtaining a highly active birnessite in HCHO oxidation.

Element incorporation was also another followed strategy to obtain a more active catalyst. In that way, incorporation of suitable transition metals (TM) or lanthanide cations (Ln cations) was investigated to promote activity by seeking to decrease energy formation of oxygen vacancy [171]. On purpose, Tang *et al.* [172] investigated MnO_x - CeO_2 oxide catalysts for complete oxidation of formaldehyde through the effect of preparation method and calcination temperature taking advantage of the redox properties of nano sized CeO_2 for oxygen storage and release. A catalyst ($Ce / Ce+Mn=0.5$) prepared by a modified co-precipitation method and calcined at 500 °C exhibited much higher catalytic activity toward complete oxidation of formaldehyde where CeO_2 and α - MnO_2 phases segregated. A high oxidation state of Mn^{4+} and huge amount of surface lattice oxygen was claimed to play a role in the reaction. On contrary, a synergistic effect on the catalytic activity for 20 ppm HCHO oxidation performed at high space velocity was ascribed to high Mn^{3+}/Mn^{4+} and O_{ads}/O_{latt} surface atomic ratios on a $MnO_2(x)$ - CeO_2 ($x = Ce/Mn = 0.66$) catalyst [173]. Liu *et al.* [174] investigated the performances of MnO_x - CeO_2 catalysts with different Mn/Ce ratios in HCHO oxidation. The enhancement of reactivity in HCHO oxidation was ascribed to the activation of lattice oxygen species in MnO_x due to CeO_2 addition. Recently, following a strategy of rational design of defects to enhance catalytic activity, Zhu *et al.* [91] reported on the performances for HCHO oxidation of Ce modified-type MnO_2 with different Ce / Mn ratios obtained from a redox-precipitation method followed by a drying step at 105 °C for 12 h. Ce- MnO_2 (1:10) was shown to be the most performant catalyst. Higher content of oxygen vacancies resulting from a close contact between CeO_2 and MnO_2 nanoparticles was postulated to be responsible for its high activity in HCHO oxidation.

Since then, different investigations were carried out in HCHO oxidation over MnO_2 [175–179]. The activity of manganese oxide involves oxygen activation and oxygen transfer through redox cycle between manganese species (Mn^{4+}/Mn^{3+}). The surface structure of the catalyst, crystallinity, valence state of manganese, morphology and the surface defects all may

have effect on the catalytic activity. Thus, it is supposed that, surface modification to form unsaturated sites could be greatly improved the catalytic performance of manganese oxides [175,177,180].

1-7-2- Mechanism for HCHO oxidation

Selvakumar *et al.* [178] propose a mechanism for the catalytic oxidation of HCHO by birnessite based on ToF-SIMS and XPS. First, HCHO adsorbs on the surface of manganese. Partial oxidation of adsorbed HCHO by reduction of manganese allows the formation of several reaction intermediates: formates (mono- or dentate or bridged), dioxymethylene, methoxy or carbonates. The oxidation of these reaction intermediates to CO₂ and H₂O is considered the limiting step in the oxidation reaction of HCHO. The oxidation is carried out by the active oxygen species from the manganese oxides. Furthermore the activity of surface oxygen species is directly related to the amount of oxygen vacancies. However, Rochard *et al.* [181], have been investigated that the oxygen vacancies played a double role in enhancing the HCHO catalytic activity as shown in **Figure 1-11** over Au/Co-promoted CeO₂ catalysts.

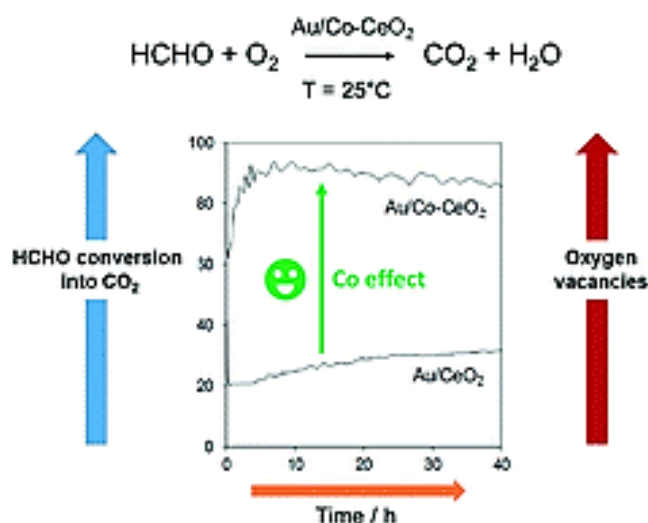


Figure 1 - 11: Relation between the concentration of oxygen vacancies and the total oxidation of HCHO

References

- [1] V. Vijayan, H. Paramesh, S. Salvi, A.K. Dalal, *Lung India* 32 (2015) 473.
- [2] J. Lelieveld, J.S. Evans, M. Fnais, D. Giannadaki, A. Pozzer, *Nature* 525 (2015) 367–371.
- [3] N. Soltys, *Procédés des traitements des COV ou composés organique volatile Doc.J3928*, 13.
- [4] J. Peng, S. Wang, *Applied Catalysis B: Environmental* 73 (2007) 282–291.
- [5] E. Hertog, *MonTI Monografias de traduccion e interpretation* 7 (2015) 73–100.
- [6] A. Guides, R. Aide, D. Ied, S. Texte, 2017 (2017).
- [7] R. Beauchet, PhD Université de Poitiers (2008) 173.
- [8] L.F. Liotta, *Applied Catalysis B: Environmental* 100 (2010) 403–412.
- [9] A. Vandenbroucke, PhD Ghent University (2015) 371.
- [10] M.V. Twigg, *Johnson Matthey Technology Review* 62 (2018) 81–85.
- [11] Z. Shareefdeen, A. Singh, eds., *Biotechnology for Odor and Air Pollution Control*, Springer-Verlag, Berlin, 2005.
- [12] H.S. Kim, T.W. Kim, H.L. Koh, S.H. Lee, B.R. Min, *Applied Catalysis A: General* 280 (2005) 125–131.
- [13] T.T. Zhang, J.D. Song, J.X. Chen, A.P. Jia, M.F. Luo, J.Q. Lu, *Applied Surface Science* 425 (2017) 1074–1081.
- [14] Z. El Assal, S. Ojala, S. Pitkääaho, L. Pirault-Roy, B. Darif, J.D. Comparot, M. Bensitel, R.L. Keiski, R. Brahmi, *Chemical Engineering Journal* 313 (2017) 1010–1022.
- [15] Z. Abd Allah, J.C. Whitehead, P. Martin, *Environmental Science & Technology* 48 (2014) 558–565.
- [16] Z. Ye, PhD Ghent and Lille Universities (2018) 230.
- [17] K. Everaert, *Journal of Hazardous Materials* 109 (2004) 113–139.
- [18] A.M. Vandenbroucke, R. Aerts, W. Van Gaens, N. De Geyter, C. Leys, R. Morent, A. Bogaerts, *Plasma Chemistry and Plasma Processing* 35 (2015) 217–230.
- [19] A.M. Vandenbroucke, R. Morent, N. De Geyter, C. Leys, *Journal of Advanced Oxidation Technologies* (2011).
- [20] Z. Ye, S.K.P. Veerapandian, I. Onyshchenko, A. Nikiforov, N. De Geyter, J.M. Giraudon, J.F. Lamonier, R. Morent, *Industrial and Engineering Chemistry Research* 56 (2017) 10215–10226.
- [21] H.-H. Kim, *Plasma Processes and Polymers* 1 (2004) 91–110.
- [22] H.L. Chen, H.M. Lee, S.H. Chen, M.B. Chang, *Industrial & Engineering Chemistry Research* 47 (2008) 2122–2130.
- [23] B. Eliasson, U. Kogelschatz, *IEEE Transactions on Plasma Science* 19 (1991) 1063–1077.
- [24] M.J. Pavlovich, Z. Chen, Y. Sakiyama, D.S. Clark, D.B. Graves, *Plasma Processes and Polymers* 10 (2013) 69–76.
- [25] C. Tendero, C. Tixier, P. Tristant, J. Desmaison, P. Leprince, *Spectrochimica Acta Part B*:

Atomic Spectroscopy 61 (2006) 2–30.

- [26] H.S. Uhm, Y.C. Hong, D.H. Shin, Plasma Sources Science and Technology 15 (2006) S26–S34.
- [27] H. Conrads, M. Schmidt, Plasma Sources Sci. Technol. 9 (2000) 441.
- [28] A.J. Al-abduly, PhD Newscatle University (2015) 224.
- [29] a M. Vandenbroucke, M. Mora, N.D. Geyter, C. Leys, (2013) 4–7.
- [30] S. Müller, R.-J. Zahn, Contributions to Plasma Physics 47 (2007) 520–529.
- [31] B.R. Raju, E.L. Reddy, J. Karuppiah, P.M.K. Reddy, C. Subrahmanyam, Journal of Chemical Sciences 125 (2013) 673–678.
- [32] T. Zhu, Chemistry Emission Control, Radioactive pollution and Indoor air quality, Chapter 4: Removal of VOCs using Nonthermal plasma technology, 53.
- [33] X. Tang, F. Feng, L. Ye, X. Zhang, Y. Huang, Z. Liu, K. Yan, Catalysis Today 211 (2013) 39–43.
- [34] H.H. Kim, Y. Teramoto, N. Negishi, A. Ogata, Catalysis Today 256 (2015) 13–22.
- [35] J.C.Whitehead, Journal of Physics D: Applied Physics 49 (2106) 243001.
- [36] IARC Working Group on the Evaluation of Carcinogenic Risks to Humans, International Agency for Research on Cancer, World Health Organization, eds., Household Use of Solid Fuels and High-Temperature Frying, International Agency for Research on Cancer ; Distributed by WHO Press, Lyon, France : Geneva, 2010.
- [37] B. Huang, C. Lei, C. Wei, G. Zeng, Environment International 71 (2014) 118–138.
- [38] C. Wu, J. Schaum, Environmental Health Perspectives 108 (2000) 359–363.
- [39] R.E. Doherty, Environmental Forensics 1 (2000) 69–81.
- [40] L. Vogel, Social policy in the European Union: State of play (2108) 18.
- [41] C.S. Scott, V.J. Coglian, Environmental Health Perspectives 108 (2000) 159–160.
- [42] W.A. Chiu, J. Jinot, C.S. Scott, S.L. Makris, G.S. Cooper, R.C. Dzubow, A.S. Bale, M.V. Evans, K.Z. Guyton, N. Keshava, J.C. Lipscomb, S. Barone, J.F. Fox, M.R. Gwinn, J. Schaum, J.C. Caldwell, Environmental Health Perspectives 121 (2013) 303–311.
- [43] I. Rusyn, W.A. Chiu, L.H. Lash, H. Kromhout, J. Hansen, K.Z. Guyton, Pharmacology & Therapeutics 141 (2014) 55–68.
- [44] N. Blanch-Raga, A.E. Palomares, J. Martínez-Triguero, S. Valencia, Applied Catalysis B: Environmental 187 (2016) 90–97.
- [45] H. Li, G. Lu, Q. Dai, Y. Wang, Y. Guo, Y. Guo, Applied Catalysis B: Environmental 102 (2011) 475–483.
- [46] R. Cucciniello, A. Intiso, S. Castiglione, A. Genga, A. Proto, F. Rossi, Applied Catalysis B: Environmental 204 (2017) 167–172.
- [47] J. Gutierrezortiz, Journal of Catalysis 218 (2003) 148–154.
- [48] H. Li, G. Lu, Q. Dai, Y. Wang, Y. Guo, Y. Guo, ACS Appl. Mater. Interfaces 2 (2010) 838–846.
- [49] Q. Dai, X. Wang, G. Lu, Catalysis Communications 8 (2007) 1645–1649.

- [50] S. Sultana, A. Vandenbroucke, C. Leys, N. De Geyter, R. Morent, *Catalysts* 5 (2015) 718–746.
- [51] A.M. Vandenbroucke, M.T.N. Dinh, J.M. Giraudon, R. Morent, N. De Geyter, J.F. Lamonier, C. Leys, *Plasma Chemistry and Plasma Processing* (2011).
- [52] D. Ye, D. Gao, G. Yu, X. Shen, F. Gu, *Journal of Hazardous Materials* 127 (2005) 149–155.
- [53] M. Laroussi, *Plasma Process. Polym.* 2 (2005) 391–400.
- [54] M.T.N. Dinh, J.M. Giraudon, J.F. Lamonier, A. Vandenbroucke, N. De Geyter, C. Leys, R. Morent, *Applied Catalysis B: Environmental* (2014).
- [55] M.T.N. Dinh, J.M. Giraudon, A.M. Vandenbroucke, R. Morent, N. De Geyter, J.F. Lamonier, *Applied Catalysis B: Environmental* 172–173 (2015) 65–72.
- [56] S. Sultana, Z. Ye, S.K.P. Veerapandian, A. Löfberg, N. De Geyter, R. Morent, J.M. Giraudon, J.F. Lamonier, *Catalysis Today* (2016) 0–1.
- [57] S.K.P. Veerapandian, Z. Ye, J.-M. Giraudon, N. De Geyter, R. Morent, J.-F. Lamonier, *Journal of Hazardous Materials* 379 (2019) 120781.
- [58] E. Marotta, A. Callea, X. Ren, M. Rea, C. Paradisi, *Plasma Processes and Polymers* 5 (2008) 146–154.
- [59] J.S. Chang, P.A. Lawless, T. Yamamoto, *IEEE Transactions on Plasma Science* 19 (1991) 1152–1166.
- [60] J. Chen, J.H. Davidson, *Plasma Chemistry and Plasma Processing* 23 (2003) 83–102.
- [61] R. Morent, C. Leys, *Ozone: Science & Engineering* 27 (2005) 239–245.
- [62] J. Chen, J.H. Davidson, *Plasma Chemistry and Plasma Processing* 23 (2003) 501–518.
- [63] X. Zhang, B.J. Lee, H.G. Im, M.S. Cha, *IEEE transactions on plasma science* 44 (2016) 2288–2296.
- [64] R. Peyrous, *Ozone: Science & Engineering* 12 (1990) 41–64.
- [65] L. Sivachandiran, A. Khacef, *RSC Adv.* 6 (2016) 29983–29995.
- [66] X. Zhang, W. Feng, Z. Yu, S. Li, J. Zhu, K. Yan, *International Journal of Environmental Science and Technology* 10 (2013) 1377–1382.
- [67] A. Yehia, A. Mizuno, *International Journal of Plasma Environmental Science and Technology* 2 (2008) 44–49.
- [68] J. Chen, J.H. Davidson, *Plasma Chemistry and Plasma Processing* 22 (2002) 495–522.
- [69] A. Yehia, M. Abdel-Salam, A. Mizuno, *Journal of Physics D: Applied Physics* 33 (2000) 831–835.
- [70] Y.S. Akishev, M.E. Grushin, V.B. Karal, N.I. Trushkin, 27 (2001) 563–572.
- [71] Y. Akishev, O. Goossens, T. Callebaut, C. Leys, A. Napartovich, N. Trushkin, *Journal of Physics D: Applied Physics* 34 (2001) 2875–2882.
- [72] T. Callebaut, I. Kochetov, Y. Akishev, A. Napartovich, C. Leys, *Plasma Sources Science and Technology* 13 (2004) 245–250.
- [73] S.W. Benson, A.E. Axworthy, *The Journal of Chemical Physics* 26 (1957) 1718–1726.

- [74] Q. Yu, M. Zhao, Z. Liu, X. Zhang, L. Zheng, Y. Chen, M. Gong, *Chinese Journal of Catalysis* 30 (2009) 1–3.
- [75] S. Yang, Z. Zhu, F. Wei, X. Yang, *Building and Environment* 125 (2017) 60–66.
- [76] S. Imamura, M. Ikebata, T. Ito, T. Ogita, *Ind. Eng. Chem. Res.* 30 (1991) 217–221.
- [77] P. Zhang, B. Zhang, R. Shi, *Front. Environ. Sci. Eng. China* 3 (2009) 281–288.
- [78] Q. Yu, H. Pan, M. Zhao, Z. Liu, J. Wang, Y. Chen, M. Gong, *Journal of Hazardous Materials* 172 (2009) 631–634.
- [79] Y. Liu, P. Zhang, *The Journal of Physical Chemistry C* 121 (2017) 23488–23497.
- [80] S.T. Oyama, *Catalysis Reviews* 42 (2000) 279–322.
- [81] W. Li, G.V. Gibbs, S.T. Oyama, R.V. April, *J. Am. Chem. Soc.* 120 (1998) 9041–9046.
- [82] B. Dhandapani, S.T. Oyama, *Applied Catalysis B: Environmental* 11 (1997) 129–166.
- [83] J. Jia, P. Zhang, L. Chen, *Applied Catalysis B: Environmental* 189 (2016) 210–218.
- [84] Y. Liu, P. Zhang, *Applied Catalysis A: General* 530 (2017) 102–110.
- [85] G. Zhu, J. Zhu, W. Jiang, Z. Zhang, J. Wang, Y. Zhu, Q. Zhang, *Applied Catalysis B: Environmental* 209 (2017) 729–737.
- [86] J. Ma, C. Wang, H. He, *Applied Catalysis B: Environmental* 201 (2017) 503–510.
- [87] X. Li, J. Ma, H. He, *Journal of Environmental Sciences* 94 (2020) 14–31.
- [88] Z. Lian, J. Ma, H. He, *Catalysis Communications* 59 (2015) 156–160.
- [89] J. Ma, X. Li, C. Zhang, Q. Ma, H. He, *Applied Catalysis B: Environmental* 264 (2020) 118498.
- [90] X. Li, J. Ma, L. Yang, G. He, C. Zhang, R. Zhang, H. He, *Environ. Sci. Technol.* 52 (2018) 12685–12696.
- [91] L. Zhu, J. Wang, S. Rong, H. Wang, P. Zhang, *Applied Catalysis B: Environmental* 211 (2017) 212–221.
- [92] Y. Liu, P. Zhang, *Applied Catalysis A: General* 530 (2017) 102–110.
- [93] D. Mehandjiev, A. Naidenov, *Ozone: Science & Engineering* 14 (1992) 277–282.
- [94] H. Touati, A. Guerin, Y. Swesi, C.B. Dupeyrat, R. Philippe, V. Meille, J.-M. Clacens, *Catalysis Communications* 148 (2021) 106163.
- [95] X. Li, J. Ma, C. Zhang, R. Zhang, H. He, *Journal of Environmental Sciences* 80 (2019) 159–168.
- [96] T. Gopi, G. Swetha, S. Chandra Shekar, C. Ramakrishna, B. Saini, R. Krishna, P.V.L. Rao, *Catalysis Communications* 92 (2017) 51–55.
- [97] Y. Liu, W. Yang, P. Zhang, J. Zhang, *Applied Surface Science* 442 (2018) 640–649.
- [98] K.M. Bulanin, J.C. Lavalley, A.A. Tsyganenko, *Colloids and Surfaces A: Physicochemical and Engineering Aspects* 101 (1995) 153–158.
- [99] R. Cao, P. Zhang, Y. Liu, X. Zheng, *Applied Surface Science* 495 (2019) 143607.
- [100] R.M. Taylor, *Journal of Soil Science* 19 (1968) 77–80.
- [101] R.M. Cornell, *Clays and Clay Minerals* 36 (1988) 249–257.

- [102] J.R. Bargar, C.C. Fuller, M.A. Marcus, A.J. Brearley, M. Perez De la Rosa, S.M. Webb, W.A. Caldwell, *Geochimica et Cosmochimica Acta* 73 (2009) 889–910.
- [103] V.A. Drits, E. Silvester, A.I. Gorshkov, A. Manceau, *American Mineralogist* 82 (1997) 946–961.
- [104] E. Silvester, A. Manceau, V.A. Drits, *American Mineralogist* 82 (1997) 962–978.
- [105] A.T. Stone, J.J. Morgan, *Environmental Science & Technology* 18 (1984) 617–624.
- [106] A. Manceau, V.A. Drits, E. Silvester, (n.d.) 26.
- [107] F.V. Chukhrov, B.A. Sakharov, A.I. Gorshkov, V.A. Drits, Yu.P. Dikov, *International Geology Review* 27 (1985) 1082–1088.
- [108] W. Zhao, Q.Q. Wang, F. Liu, G.H. Qiu, W.F. Tan, X.H. Feng, *Journal of Soils and Sediments* 10 (2010) 870–878.
- [109] J.E. Post, D.R. Vebelen, *American Mineralogist* 75 (1990) 13.
- [110] Y. Liu, H. Zhou, R. Cao, T. Sun, W. Zong, J. Zhan, L. Liu, *Materials Chemistry and Physics* 221 (2019) 457–466.
- [111] B. Wang, C. Chi, M. Xu, C. Wang, D. Meng, *Chemical Engineering Journal* 322 (2017) 679–692.
- [112] G. Wang, Z. Ma, G. Zhang, C. Li, G. Shao, *Electrochimica Acta* 182 (2015) 1070–1077.
- [113] R.M. McKenzie, *Mineralogical Magazine* 38 (1971) 493–502.
- [114] J.E. Post, P.J. Heaney, J. Hanson, *Powder Diffraction* 17 (2002) 218.
- [115] B. Lanson, V.A. Drits, Q. Feng, A. Manceau, *American Mineralogist* 87 (2002) 1662–1671.
- [116] D.C. Golden, *Clays and Clay Minerals* 34 (1986) 511–520.
- [117] C.L. Lopano, P.J. Heaney, J.E. Post, J. Hanson, S. Komarneni, *American Mineralogist* 92 (2007) 380–387.
- [118] K. Kuma, A. Usui, W. Paplawsky, B. Gedulin, G. Arrhenius, *Mineralogical Magazine* 58 (1994) 425–447.
- [119] E.A. Johnson, J.E. Post, *American Mineralogist* 91 (2006) 609–618.
- [120] H. Zhao, M. Zhu, W. Li, E.J. Elzinga, M. Villalobos, F. Liu, J. Zhang, X. Feng, D.L. Sparks, *Environ. Sci. Technol.* 50 (2016) 1750–1758.
- [121] B. Lanson, V.A. Drits, E. Silvester, A. Manceau, *American Mineralogist* 85 (2000) 826–838.
- [122] H.F. McMurdie, E. Golovato, *Journal of Research of the National Bureau of Standards* 41 (1948) 589.
- [123] W. Feitknecht, W. Marti, *Helvetica Chimica Acta* 28 (1945) 129–148.
- [124] T. Boonfueng, L. Axe, Y. Xu, T.A. Tyson, *Journal of Colloid and Interface Science* 303 (2006) 87–98.
- [125] R. Giovanoli, E. Stähli, W. Feitknecht, *Helvetica Chimica Acta* 53 (1970) 209–220.
- [126] P. Strobel, J. Durr, M.-H. Tuilier, J.-C. Charenton, *J. Mater. Chem.* 3 (1993) 453.
- [127] Y. Ma, J. Luo, S.L. Suib, *Chemistry of Materials* 11 (1999) 1972–1979.

- [128] L.-X. Yang, Y.-J. Zhu, G.-F. Cheng, *Materials Research Bulletin* 42 (2007) 159–164.
- [129] S. Ching, M.L. Jorgensen, N. Duan, S.L. Suib, C.-L. O’Young, *Inorganic chemistry* 36 (1997) 883–890.
- [130] M. Händel, T. Rennert, K.U. Totsche, *Geoderma* 193–194 (2013) 117–121.
- [131] J. Luo, Q. Zhang, S.L. Suib, *Inorganic Chemistry* 39 (2000) 741–747.
- [132] J. Luo, S.L. Suib, *J. Phys. Chem. B* 101 (1997) 10403–10413.
- [133] M. Villalobos, B. Toner, J. Bargar, G. Sposito, *Geochimica et Cosmochimica Acta* 67 (2003) 2649–2662.
- [134] S. Grangeon, PhD Université de Grenoble (2009) 225.
- [135] A. Manceau, S.N. Steinmann, *ACS Earth Space Chem.* 5 (2021) 66–76.
- [136] S. Grangeon, B. Lanson, M. Lanson, *Acta Crystallogr B Struct Sci Cryst Eng Mater* 70 (2014) 828–838.
- [137] S. Ching, D.J. Petrovay, M.L. Jorgensen, S.L. Suib, *Inorg. Chem.* 36 (1997) 883–890.
- [138] L.D. Kulish, R. Scholtens, G.R. Blake, *Phys. Rev. B* 100 (2019) 214435.
- [139] P. Le Goff, N. Baffier, S. Bach, J.P. Pereira-Ramos, *Materials Research Bulletin* 31 (1996) 63–75.
- [140] Y. Ma, J. Luo, S.L. Suib, *Chemistry of Materials* 11 (1999) 1972–1979.
- [141] N. Birkner, A. Navrotsky, *Proc Natl Acad Sci USA* 114 (2017) E1046–E1053.
- [142] M.A. Cheney, P.K. Bhowmik, S. Qian, S.W. Joo, W. Hou, J.M. Okoh, *Journal of Nanomaterials* 2008 (2008) 1–8.
- [143] B. Lanson, V.A. Drits, Q. Feng, A. Manceau, *American Mineralogist* 87 (2002) 1662–1671.
- [144] O. Prieto, M. Darco, V. Rives, *Journal of Materials and Sciences* 38 (2003) 2815–2824.
- [145] X. Zhang, Z. Hou, X. Li, J. Liang, Y. Zhu, Y. Qian, *J. Mater. Chem. A* 4 (2016) 856–860.
- [146] Q. Feng, L. Liu, K. Yanagisawa, (n.d.) 4.
- [147] M. Villalobos, B. Toner, J. Bargar, G. Sposito, *Geochimica et Cosmochimica Acta* 67 (2003) 2649–2662.
- [148] L. Liu, M. Min, F. Liu, H. Yin, Y. Zhang, G. Qiu, *Journal of Power Sources* 277 (2015) 26–35.
- [149] L. Liu, Y. Luo, W. Tan, Y. Zhang, F. Liu, G. Qiu, *Journal of Colloid and Interface Science* 482 (2016) 183–192.
- [150] Z. Qin, Q. Xiang, F. Liu, J. Xiong, L.K. Koopal, L. Zheng, M. Ginder-Vogel, M. Wang, X. Feng, W. Tan, H. Yin, *Chemical Geology* 466 (2017) 512–523.
- [151] H. Yin, X. Feng, G. Qiu, W. Tan, F. Liu, *Journal of Hazardous Materials* 188 (2011) 341–349.
- [152] H. Yin, H. Li, Y. Wang, M. Ginder-Vogel, G. Qiu, X. Feng, L. Zheng, F. Liu, *Chemical Geology* 381 (2014) 10–20.
- [153] N. Subramanian, B. Viswanathan, T.K. Varadarajan, *RSC Adv.* 4 (2014) 33911–33922.
- [154] S. Absus, R. Zulfa, A. Awaluddin, S. Anita, S.S. Siregar, Prasetya, in: *Surabaya, Indonesia*, (2018). 020009.

- [155] R. Chen, T. Chirayil, P. Zavalij, M.S. Whittingham, *Solid State Ionics* 86–88 (1996) 1–7.
- [156] L. Al-Attar, A. Dyer, *Land Contamination & Reclamation* 15 (2007) 427–436.
- [157] X. Tang, Y. Bai, A. Duong, M.T. Smith, L. Li, L. Zhang, *Environment International* 35 (2009) 1210–1224.
- [158] M. Lippmann, G.D. Leikauf, eds., *Environmental Toxicants: Human Exposures and Their Health Effects*, Fourth edition, Wiley, Hoboken, NJ, 2020.
- [159] T. Salthammer, S. Mentese, R. Marutzky, *Chem. Rev.* 110 (2010) 2536–2572.
- [160] Y. Sekine, *Atmospheric Environment* 36 (2002) 5543–5547.
- [161] B. Bai, Q. Qiao, J. Li, J. Hao, *Chinese Journal of Catalysis* 37 (2016) 102–122.
- [162] A.-C. Gaillot, *Docteur de l'Université Joseph Fourier – Grenoble I* (2002) 1–392.
- [163] J. Wang, P. Zhang, J. Li, C. Jiang, R. Yunus, J. Kim, *Environmental Science & Technology* 49 (2015) 12372–12379.
- [164] J. Wang, D. Li, P. Li, P. Zhang, Q. Xu, J. Yu, *RSC Advances* 5 (2015) 100434–100442.
- [165] W. Yang, Y. Zhu, F. You, L. Yan, Y. Ma, C. Lu, P. Gao, Q. Hao, W. Li, *Applied Catalysis B: Environmental* 233 (2018) 184–193.
- [166] Q. Wang, P. Yang, M. Zhu, *Geochimica et Cosmochimica Acta* 250 (2019) 292–310.
- [167] N. Ma, S. Kosasang, P. Chomkhuntod, S. Duangdangchote, N. Phattharasupakun, W. Klysubun, M. Sawangphruk, *Journal of Power Sources* 455 (2020) 227969.
- [168] J. Wang, J. Li, C. Jiang, P. Zhou, P. Zhang, J. Yu, *Applied Catalysis B: Environmental* 204 (2017) 147–155.
- [169] S. Rong, K. Li, P. Zhang, F. Liu, J. Zhang, *Catal. Sci. Technol.* 8 (2018) 1799–1812.
- [170] J. Ji, X. Lu, C. Chen, M. He, H. Huang, *Applied Catalysis B: Environmental* 260 (2020) 118210.
- [171] Y. Lou, X.-M. Cao, J. Lan, L. Wang, Q. Dai, Y. Guo, J. Ma, Z. Zhao, Y. Guo, P. Hu, G. Lu, *Chem. Commun.* 50 (2014) 6835–6838.
- [172] X. Tang, Y. Li, X. Huang, Y. Xu, H. Zhu, J. Wang, W. Shen, *Applied Catalysis B: Environmental* 62 (2006) 265–273.
- [173] S. Guan, Q. Huang, J. Ma, W. Li, A.T. Ogunbiyi, Z. Zhou, K. Chen, Q. Zhang, *Ind. Eng. Chem. Res.* 59 (2020) 596–608.
- [174] X. Liu, J. Lu, K. Qian, W. Huang, M. Luo, *Journal of Rare Earths* 27 (2009) 418–424.
- [175] R. Averlant, S. Royer, J.-M. Giraudon, J.-P. Bellat, I. Bezverkhyy, G. Weber, J.-F. Lamonier, *ChemCatChem* 6 (2014) 152–161.
- [176] J. Zhang, Y. Li, L. Wang, C. Zhang, H. He, *Catalysis Science & Technology* 5 (2015) 2305–2313.
- [177] J. Wang, G. Zhang, P. Zhang, *J. Mater. Chem. A* 5 (2017) 5719–5725.
- [178] S. Selvakumar, N. Nuns, M. Trentesaux, V.S. Batra, J.-M. Giraudon, J.-F. Lamonier, *Applied Catalysis B: Environmental* 223 (2018) 192–200.

- [179] Y. Xu, J. Dhainaut, G. Rochard, J.-P. Dacquin, A.-S. Mamede, J.-M. Giraudon, J.-F. Lamonier, H. Zhang, S. Royer, *Chemical Engineering Journal* 388 (2020) 124146.
- [180] J. Wang, D. Li, P. Li, P. Zhang, Q. Xu, J. Yu, *RSC Advances* 5 (2015) 100434–100442.
- [181] G. Rochard, J.-M. Giraudon, L.F. Liotta, V. La Parola, J.-F. Lamonier, *Catal. Sci. Technol.* 9 (2019) 3203–3213.

Chapter 2:
STRATEGIC METHODOLOGY

The aim of this chapter is to provide the readers with a clear overview of the strategic methodology that was applied during the course of this PhD. The objective of the thesis is to optimize the Post-Plasma-Catalysis (PPC) process for the abatement of trichloroethylene. That means, a low energy consumption and high selectivity and good tolerance of the catalyst towards Cl and H₂O near ambient. The concept of the PPC process is illustrated in **Figure 2-1**.

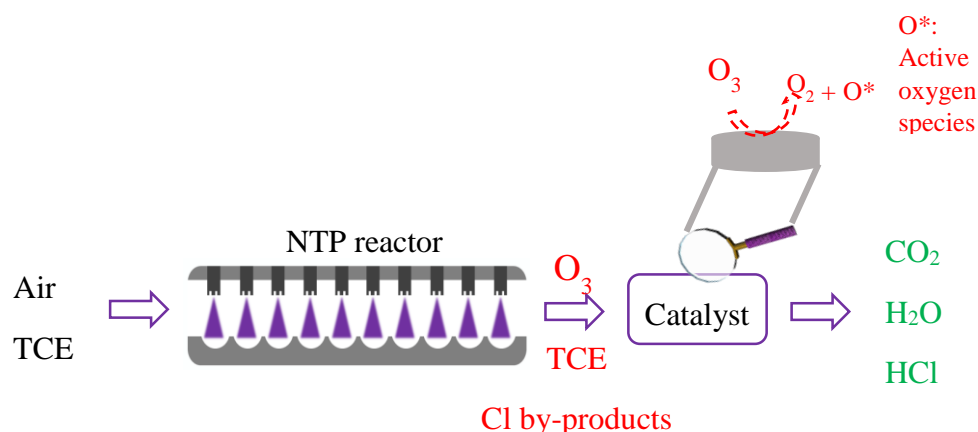


Figure 2 - 1: Concept of post plasma catalysis

The use of catalytic ozone decomposition is a crucial step in this type of procedure. Bulk and supported manganese-based catalysts recognized as the most efficient catalysts for O₃ degradation in active oxygen species have been previously used.

Until now, as we have seen above (chapter 1), different manganese-based catalysts have been used using NTP. However, a direct comparison of the plasma assisted catalytic performances is difficult due to changes in the initial TCE concentration and changes of flow rates. Additionally, the number of modules of the NTP reactor has increased, going from 5 pins to 10 pins.

Further improvement in terms of the energy efficiency as keeping the process to be highly selective into CO₂ could be realized by improving the operating parameters of the process enabling the catalyst to work at a temperature close to 25 °C which would exclude further catalyst heating.

One important point is to be able to properly adapt the molar ratio of produced O₃ to the initial concentration of TCE, namely $[O_3]/[TCE]_0$ to supply enough reactive oxygen species to quantitatively oxidize TCE into CO₂ in dry air. The target $[O_3]/[TCE]_0$ ratio is expected to be 4 according to the following accepted formal reaction:



These considerations hold if the catalytic formulation is adapted to quantitatively degrade O_3 in the course of the experiment. This also implies the catalyst to be stable with time, in other terms to be water tolerant and resistant to chlorine with time.

To address these issues, the adopted strategy and related methodology are the following:

- 1- $[\text{O}_3]/[\text{TCE}]_0$ optimization: Study the performances of the NTP as an ozoner (**Figure 2-2**) to be able to tune the O_3 production as a function of the different key processing parameters. On purpose the effect of air flow rate (Q), specific energy density (SED) and humidity (RH) will be carried out. The obtained results are discussed in [chapter 5](#).

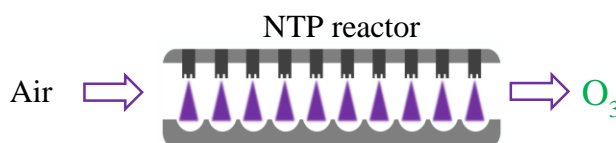


Figure 2 - 2: Schematic of the operation of the plasma as an ozoner

- 2- Improved catalytic formulations: The catalytic formulations are based on MnO_2 type materials (birnessite - δ - MnO_2) doped or not with Ce known as highly efficient for O_3 decomposition. In order to optimize the catalyst design special attention is paid to the activation mode of the catalyst through the influence of the temperature of calcination. A HNO_3 treatment is also performed to enhance the water tolerance and ozonation performances because it's well-known that acid treatment increase the number of active sites.
- 3- Validation approaches:
 - First the catalytic performances are tested towards formaldehyde oxidation (**Figure 2-3**) as this reaction is well known to correlate with the density of oxygen vacancies in the material. The effect of Ce doped birnessite, the calcination temperature as well as the effect of relative humidity on the catalytic performance are investigated. This part is explained in details in [chapter 4](#).

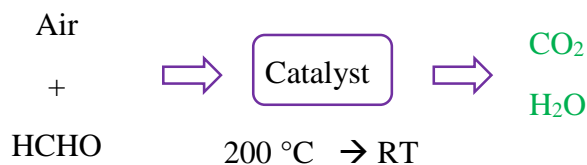


Figure 2 - 3: Schematic presentation of HCHO oxidation

- The efficiency of the catalysts is investigated also in terms of ozone degradation ability in the presence of others pollutants such as nitrogen oxide species in dry and humid air using the NTP as an ozoner (**Figure 2-4**). The experimental conditions are chosen in order to discriminate efficiently the catalysts in terms of catalytic performances. The effect of Ce content as well as the effect of acid treatment are investigated. The obtained results are presented in **chapter 6**.

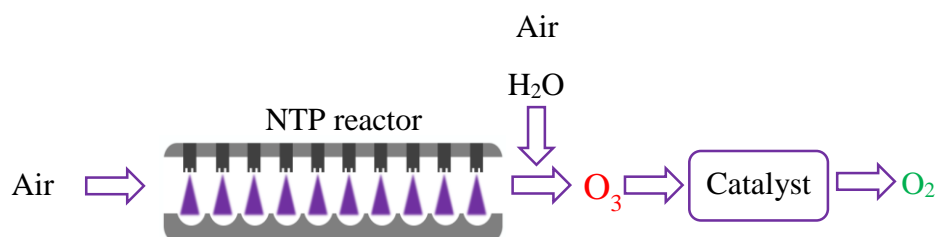


Figure 2 - 4: Schematic presentation of O₃ decomposition

- The catalysts are then tested in the total oxidation of TCE in dry and humid air in PPC configuration (**Figure 2-5**). Based on that, the performances of the processes are discussed in terms of TCE removal efficiency, CO_x yields, and carbon-balance and in terms of cost energy saving. These results are discussed in terms of the physico-chemical characterization of the catalysts which are presented in **chapter 7**.

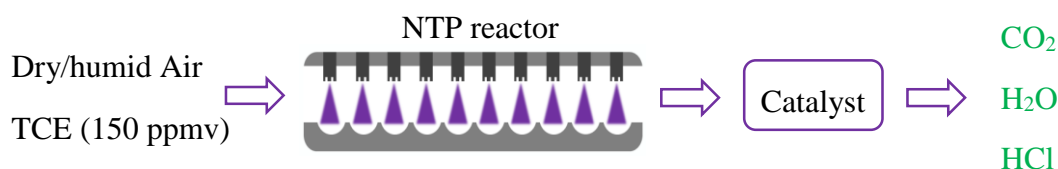


Figure 2 - 5: Schematic presentation of TCE abatement in PPC process

Chapter 3:
MATERIAL AND METHODS

Throughout this chapter, the experimental part concerning the abatement of trichloroethylene (TCE) in Post plasma catalysis process is presented in details. However, the use of non-thermal plasma as ozoner in combination with catalyst to decompose ozone in order to improve the VOCs decomposition in the hybrid system plasma catalysis is also described. The way in which the experiments of formaldehyde (HCHO) catalytic oxidation will be conducted is also explained in this chapter. Thus this chapter is devised into **5 parts**.

The **first** part consists to the description of the preparation of the catalysts and the **second** part to the presentation of the different techniques used for the characterization of the materials. Synthesis and characterization were conducted at Lille University.

The **third** part is dedicated to the catalytic oxidation of formaldehyde. All experiments described in this section were conducted at Lille University.

The **fourth** part, concerns the use of plasma as ozoner, and the catalytic decomposition of ozone. All experiments described in this section were conducted at Ghent University.

The **fifth** part consists to use the Post-Plasma-Catalysis process for the abatement of trichloroethylene. All the experiments described in this section were conducted at Ghent University.

3-1- Catalyst preparation

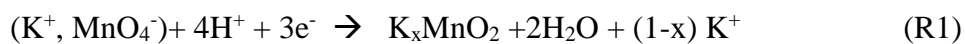
3-1-1- Synthesis of birnessite and cerium doped birnessite through a redox precipitation method.

Birnessite was prepared following a redox method inspired from that of Händel *et al.*[1]. Typically, 4.0 g (25.3 mmol) of KMnO_4 (Fluka, $\geq 99\%$) was dissolved into 400 mL of distilled water under stirring (350 rpm). 4 mL (22.54 mmol) of $\text{NaC}_3\text{H}_5\text{O}_3$ (50 % w/w) (Fisher Chemical, solution 60% w/w) was added dropwise to the aqueous KMnO_4 solution. Thus the synthesis was performed with a ratio $\text{KMnO}_4 / \text{NaC}_3\text{H}_5\text{O}_3 = 1.2$. The resulting brown suspension was stirred for 2 h. After centrifugation (4000 rpm for 20 min) the collected brown precipitate was washed 2 times (25 mL of distilled water each time) and finally dried in an oven at 40 °C for 48 h to give a black powder Mn-B.

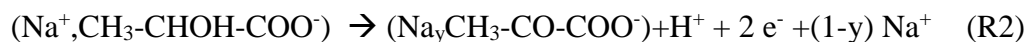
The Ce-doped MnO₂ (x: Ce/Mn atomic ratio of 0.01, 0.1, 0.2 and 0.5) were prepared based on the same procedure except that Ce (NO₃)₃.6H₂O (Alfa Aesar; ≥ 99.5 %) was dissolved concomitantly with KMnO₄. The as-prepared samples were labelled Ce_xMn.

The main reactions occurring during the synthesis of birnessite were the following:

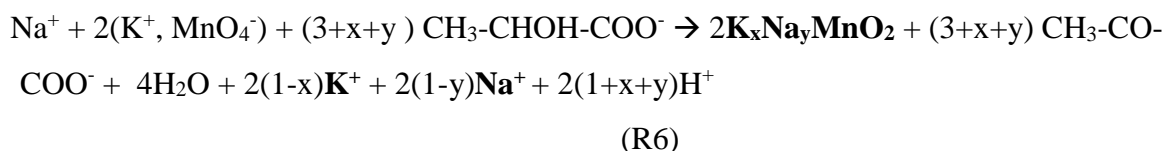
Reduction reaction:



Oxidation reactions:



According to equation 1 and 2, the balance sheet equation is:



Where, x and y are the amounts of Na and K that are intercalated in the lamellar structure

Table 3-1, presents the required amount for the synthesis of Mn-B in excess of potassium permanganate conditions.

Table 3 - 1: The required amount of chemicals for the synthesis of Mn-B

	KMnO ₄	NaC ₃ H ₅ O ₃
n (mol)	2.53 x 10 ⁻²	2.254 x 10 ⁻²
M (g/mol)	158.03	112.06
ρ (Kg/L)		1.33 x 10 ³
C (mol/L)	0.0633	5.635
m req (g)	4	
Vreq (mL)		4±0.01

m req: Required weight
Vreq: Required volume

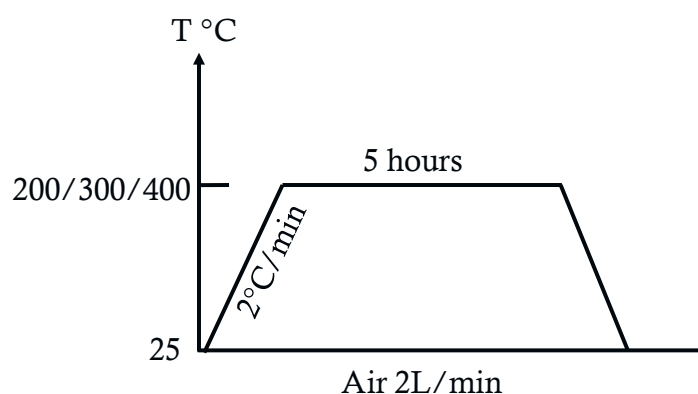
For the preparation of Ce doped MnO₂ the amount of sodium lactate remains the same regardless of x (Ce/Mn) value, because only the Ce/Mn ratio change and the other experimental conditions are the same. However, **Table 3-2**, presents the amount of potassium permanganate and cerium nitrate used for the preparation of Ce_xMn samples.

Table 3 - 2: Quantity of potassium permanganate and cerium nitrate required for each Ce_xMn preparation.

Name	n (Ce/Mn)	n (Mn) (mol)	n (Ce) (mol)	m (KMnO_4) (g)	m ($\text{Ce}(\text{NO}_3)_3 \cdot 6\text{H}_2\text{O}$) (g)
$\text{Ce}_{0.01}\text{Mn}$	0.01	0.0247	$3 \cdot 10^{-4}$	3.9033	0.1074
$\text{Ce}_{0.1}\text{Mn}$	0.1	0.0227	$2.27 \cdot 10^{-3}$	3.5872	0.9868
$\text{Ce}_{0.2}\text{Mn}$	0.2	0.0208	$4.2 \cdot 10^{-3}$	3.2922	1.8237
$\text{Ce}_{0.5}\text{Mn}$	0.5	0.0167	$8.3 \cdot 10^{-3}$	2.6338	3.6041

3-1-2- Calcination procedure

The dried samples were calcined at $T_c = 400^\circ\text{C}$ for 5 h in flowing dry air (1.0 g; 2 L/h; $2^\circ\text{C}/\text{min}$) (**Figure 3-1**). $\text{Ce}_{0.1}\text{Mn}$ was calcined also at 200°C and 300°C and $\text{Ce}_{0.01}\text{Mn}$ at 300°C in similar conditions to those at 400°C . The suffix X00 was added to the labeling of the samples.

**Figure 3 - 1:** Scheme of the calcination conditions

3-1-3- Acid treatment

The dried samples were also treated with 0.2 M HNO_3 solution (VWR 68%), with a ratio $m_{\text{catalyst}} (\text{g}) / V_{\text{HNO}_3} (\text{mL}) = 1/20$, for 6 hours at 50°C under a vigorous stirring (500 rpm). Then, the black suspension was filtered and washed continuously with distilled water until the pH of the eluate reached ~ 7 . After washing, the resulting black solid was dried at 105°C for 18 h. The suffix AT was added to the labelling of the acid treated samples.

3-2- Catalyst characterizations

3-2-1- *Thermal Gravimetric Analysis (TGA) and Differential Thermal Analysis (DTA)*

Gravimetric and differential thermal analyzes are two techniques that measure the variation of the mass of a sample as a function of temperature and the exchange of heat between the sample and the medium as a function of temperature simultaneously. The choice of gas sent to the sample is very important because it determines the type of reaction that can occur: oxidation, reduction, adsorption, desorption etc. ... The experiment can be performed under air or inert atmosphere.

In the laboratory, a thermal analysis apparatus is used which simultaneously performs thermogravimetric and differential thermal analysis experiments. The instrument consists of a waterproof enclosure that controls the atmosphere of the sample, a microbalance, an oven to manage the temperature, a thermocouple to measure the temperature and a computer to control the instrument and record the data. At the end of the experiment, the ATG and ATD curves are obtained on the same thermogramme.

TGA analyses were performed on sample weight of about 10 mg (5 mg for the acid treated samples) in air flow (100 mL/min) with a heating rate of 10°C/min up to 800°C using a TA instruments TGA-SDT 2960.

3-2-2- *X-Ray Diffraction (XRD)*

X-ray diffraction is a physico-chemical, non-destructive technique. It is the most widespread in the field of solid-state chemistry since it is particularly suitable for the characterization of crystalline materials. The determination of the crystallographic composition of the analyzed sample provides access to physical information about the crystals, including their size and orientation.

Its principle is based on the interaction of X-rays with the electrons of the atoms in the sample. In our case, we use the powder method. This method consists of bombarding the sample with a monochromatic and parallel X-ray beam and collecting the angles of diffraction which it emits. The sample is spread in powder form on a glass slide that rotates uniformly about an axis in its plane, thus increasing the number of possible orientations of the reticular planes and avoiding preferential orientations.

The Bragg's law governing diffraction is as follows: $2d(hkl)\sin\theta(hkl) = n\lambda$; with n the order of diffraction (is an integer) and $d(hkl)$ the distance between the reticular planes, where the hkl indices indicate the direction considered in the crystal. For a certain $d(hkl)$ value, and monochromatic incident X-ray radiation, diffracted intensities can only be observed from well-defined $2\theta(hkl)$ angles. The crystalline phases obtained were identified by comparison with the reference diffractograms obtained in the PDF database obtained by the International Center for Diffraction Data (ICDD), which provides access to Joint Committee of Powder Diffraction Standards (JCPDS) sheets. The disadvantage of this technique is that it does not make it possible to demonstrate the phases present in small quantities in the sample. Its sensitivity is about 1% by mass and varies according to the elements contained in the sample to be analyzed.

The diffractometer used is Bruker AXS D8 Advance type equipped with a $\text{CuK}\alpha$ source, a Lynxeye type linear fast detector and a copper anticathode, in θ / θ geometry. The recordings were made with a measurement step of 0.02° in a 2θ domain, ranging from 5 to 80° with an integration time of 1 s.

3-2-3- Transmission Electron Microscopy (TEM)

Transmission microscopy is a particularly important instrument that allows to highlight the micromorphology of the studied solids and the possible presence of crystalline defects, amorphous phase deformations, etc...

The microscope consists of three main components: an electron-optical column, a vacuum system and the electronic elements necessary for its operation (lenses, etc.). The column comprises a succession of electromagnetic lenses which influence the trajectory of the electrons. Two categories of images are formed in TEM: The high-resolution image that results from the interference of the different beams coming from the object and the conventional image which is obtained after the selection of a single beam. The first image allows the observation of the sample at very high magnification, which gives us access to the measurement of the size of the particles, the visualization of the grain boundaries, the atomic planes and columns of the crystallized phases, etc...

Transmission electron microscopy (TEM) characterization was performed using a TECNAI TEM operated at 200 kV. The prepared powders were deposited onto a carbon-coated copper grid for TEM observation

3-2-4- Inductively coupled plasma-optical emission spectrometry (ICP-OES)

The elementary analyses allow to determine the quantity of each species present in the solid. The results are expressed in mass percentage. The elemental analysis was performed by inductively coupled plasma-optic emission spectroscopy 720-ES ICP-OES (Agilent) with axially viewing and simultaneous CCD detection. ICP-OES operates using argon plasma into which an atomized liquid sample is injected. Inductive plasma can be generated by directing the energy from a high frequency generator to a suitable gas, usually argon, the sample is ionized in the plasma and the ions emit light at different characteristic wavelengths which are then measured. The quantitative determination of metal content in the catalysts was made based on the analysis of certificated standard solution. The ICP ExpertTM software (version 2.0.4) provides the concentration of metal in sample allowing estimating the weight percentage of Ce, Cu, K, Na, Mn. The operating parameters of the instrument were continuously monitored to ensure the maximum performance and reliability of the ICP-OES results. All the analyses were performed 40 min after the spectrometer was turned on to achieve a stable plasma as well as constant and reproducible sample introduction.

The sample preparation was made by dissolving 10 mg of dried and ground samples catalyst in concentrated aqua regia solution (HNO₃:HCl) (1:3, v:v). The obtained solution was heated up to 110°C in the Vulcan autodigester for 2 h. Then, the solution was diluted up to 20 ml by ultrapure water before being analyzed by ICP-OES.

3-2-5- Textural properties analysis via Brunauer-Emett-Teller (BET) and Barret-Joyner-Halenda (BJH)

The textural properties of the samples, were studied *via* N₂ adsorption desorption measurements at liquid nitrogen temperature using Tristar II 3020 from micrometrics. BET theory aims to explain the physical adsorption of gas molecules on a solid surface and serves as the basis for the measurement of specific surface areas. BJH analysis is a pore size distribution determination method, which is typically applied to nitrogen desorption data measured on sample at 77K.

The mass used in our study is in the order of 500 mg. A degassing process is carried out in advance to eliminate any impurities that may alter the experiment. For this purpose, the sample is heated at 100 °C under vacuum for four hours. The tube is weighed again to determine the exact sample mass. The adsorption process occurs when the tube is immersed in a Dewar filled with liquid nitrogen. Desorption occurs when the sample is returned to room temperature.

These processes are monitored by a catharometric detector (C T D) to measure the variation in the thermal conductivity of gas streams, resulting from changes in adsorbate concentration. The area of the peaks obtained is proportional to the amount of nitrogen retained at the surface and then desorbed when the sample temperature rises. Knowing that in the case of nitrogen physisorption at the temperature of liquid nitrogen (-196 °C), the surface occupied by a nitrogen molecule is equal to $16.2 \cdot 10^{-20} \text{ m}^2$, the number of adsorbed molecules can be evaluated to determine the total specific area..

3-2-6- Hydrogen-Temperature Programmed Reduction (H₂-TPR)

Temperature programmed reduction is a technique that makes it possible to monitor the behavior of a solid sample under a reducing atmosphere. This technique is often used in the field of heterogeneous catalysis; it consists in heating the oxide material under a flow of reducing mixture.

The monitoring of the quantity of hydrogen consumed as a function of temperature makes it possible to draw a TPR profile and the evolution of reducibility (the quantity of reducible species present in the material and the temperature at which the reduction phenomena take place) of the sample analysis. The quantification of hydrogen consumption also provides access to information such as the average oxidation degree of the active phase.

The TPR analyses were performed on a Micrometrics Autochem II device (2920). The device consists of a thermal conductivity detector TCD (which detects and quantifies the amount of hydrogen), a gas injection system consisting of mass flow meters and several three-way and six-way valves (to accurately control the flow and circulation of the gas stream), a furnace equipped with a thermocouple (to regulate the temperature rise of the sample), a saturator equipped with a heating jacket, a water trap made of a mixture of liquid isopropanol and liquid nitrogen (to protect the detector from the water formed during reduction) and a station.

The sample mass is the function of the quantity of reducible species present in the solid. In order to obtain results with better resolution, two parameters of sensitivity: shape K and resolution P have to be calculated as follows:

$$K = \frac{S_0}{V \cdot C_0} \quad (\text{Eq.1})$$

$$P = K \cdot D \quad (\text{Eq.2})$$

With S_0 : initial quantity of species reducible to mol, V : molar flow of active gas in mol/s and D : rate of temperature rises in $^{\circ}\text{C/s}$.

For convincing results, it is recommended that K and P have values such as $55 < K < 150$ and $20 < P < 50$ [2, 3]. These values are respected in all our measurements.

In our study, 50 mg mass of sample is placed in a U-shaped quartz tube. The analysis begins with degassing with argon for 1 hour at 150°C followed by cooling down to room temperature. Then the temperature was allowed to increase from 25°C to 800°C with a heating rate of 10°C/min under reducing gas which is a mixture of 5 vol.% H_2/Ar at a total flow rate of 50 mL/min.

The surface calibration of the peaks obtained by the TCD is carried out as follows: 5 pulses of 5% H_2/Ar (50 mL/min) without passing through the solid studied, were performed and their average surface is calculated. The volume of the injection loop of the device being 0.4 mL, the amount of hydrogen responsible for the average of the peak areas of the 5 pulses will be evolved and then the amount of hydrogen consumed during our experiments is determined.

3-2-7- Temperature programmed desorption (O_2 -TPD)

Similar to H_2 -TPR, thermo-desorption of oxygen provides valuable information on the RedOx properties of a metal oxide material. The key principle is to heat the material in an inert atmosphere and record spectrum of exhaling gases (O_2 , CO_2 , CO , H_2O) desorbed by mass spectrometer. It is thus possible to quantify and characterize the different types of oxygen from the material as a function of temperature.

Temperature-programmed Desorption of O_2 (O_2 -TPD) tests were carried out with 0.05g of catalyst under 50 mL/min of helium using Micrometrics AutoChem 2920 and the signal for O_2 , CO_2 and H_2O were detected using mass spectrometer. After pretreated at 105°C for 0.5 h in 50 mL/min of helium, the catalyst was exposed to 50 mL/min of 5 vol % O_2/He for 0.5 h at room temperature, then purging with 50 mL/min of helium for 0.5 h to remove the physisorbed O_2 . Then the sample temperature was increased from room temperature to 1000°C with a heating rate of 5°C/min . The flow is analyzed at the output of the assembly *via* a CTD detector and a mass spectrometer Pfeiffer Vacuum, Omsistar, Quadripole ($m/z = 32$, O_2 ; $m/z = 18$, H_2O ; $m/z = 44$, CO_2 , $m/z = 28$, CO).

3-2-8- X-ray photoelectron spectroscopy (XPS)

X-ray photoelectron spectroscopy (XPS) is a surface analysis technique with an analysis depth of 10 nm. It provides qualitative information about the elemental composition, the chemical environment of the elements and their oxidation state within the sample under study and semi-quantitative by determining the relative proportions of the elements constituting the surface of the materials.

XPS spectra are obtained by irradiating a material with X-ray beam and simultaneously measuring the kinetic energy of the electrons and their number emitted from the surface layer of the analyzed material. XPS is a technique based on the photoelectric effect, as enunciated by Einstein in 1905, which consists of bombarding with electromagnetic radiation of $h\nu$ energy in the X-ray range. The surface atoms of this sample are then ionized and core electrons are emitted by photoemission with a Kinetic energy E_k . The kinetic energy of the ejected electrons is characteristic of the element, the energy level from which is derived and the chemical environment of the atom. The use of photons whose wavelength is in the X-ray range (between 10^{-11} and 10^{-8} m) gives rise to x-ray induced photoelectron spectroscopy, which makes it possible to reach the core and valence levels of the elements under consideration.

The energy balance of the photoemission of an electron is written as follows:

$$h\nu = E_b + E_k + \phi \quad (\text{Eq.3})$$

Where $h\nu$ is the energy of the incident photons, E_b is the binding energy of the ejected electron which is the mandatory energy to bring the electron from its initial state to vacuum level, E_k is the kinetic energy of the electron ejected and ϕ is the extraction potential required for the electrons to be ejected in vacuum. During the analysis of weak or non-conductive samples, the ejection of photoelectrons induces a positive charge on the sample surface which decreases the apparent kinetic energy of the photoelectrons. This results in a shift of the peaks towards higher binding energies. The low mean free path of photoelectrons in solids in the kinetic energy range from 300 eV to 1400 eV makes XPS a surface analysis technique.

The XPS analyses were performed on a DLD Kratos Axis Ultra instrument equipped with a monochromatic Al charge neutralization source $K\alpha$ ($h\nu = 1486.6$ eV) under ultra-high vacuum conditions (10^{-9} mbar). The instrument is calibrated to the Au $4f_{7/2}$ level of metallic gold with a binding energy of 83.96 eV. The high-resolution spectra of the different regions are collected using a bandwidth of 20 eV. The spectra are then processed using CasaXPS software.

The atomic concentrations are calculated from the intensity of the phototopics using the different sensitivity factors provided by the software. The effect of static charge is evaluated using the electron coming from the C-(C, H) component of C 1s at 284.8 eV as a reference.

Associated calculation

➤ Calculation of atomic concentration

The stoichiometry of the sample surface can be estimated from the area ratio of XPS peaks. The general formula for the XPS peak area is:

$$I = n F \lambda \sigma T \sin \Theta \quad (\text{Eq.4})$$

Where I is the intensity of XPS peak, n is the atomic concentration of the elements, F is the X-ray flux, σ is the photo electronic cross section for the atomic orbital of interest, Θ is the angular efficiency factor for the instrumental arrangement, λ is the mean free path of the photoelectrons in the samples, T is the detection efficiency for electrons emitted from the sample.

The atomic composition, n_A/n_B between A and B atoms is the following:

$$\frac{I_A}{I_B} = \frac{n_A F \lambda_A \sigma_A T_A \sin \Theta}{n_B F \lambda_B \sigma_B T_B \sin \Theta} \quad (\text{Eq.5})$$

$$\frac{I_A}{I_B} = \frac{n_A \lambda_A \sigma_A T_A}{n_B \lambda_B \sigma_B T_B} \quad (\text{Eq.6})$$

$$\frac{n_A}{n_B} = \frac{I_A \lambda_B \sigma_B T_B}{I_B \lambda_A \sigma_A T_A} \quad (\text{Eq.7})$$

➤ Calculation of average oxidation state

The binding energies of the electrons of the different elements have been calculated. In the specific case of the analysis of manganese, the 3s level of Mn was more particularly studied. Indeed, this photopic has two components which can be explained by the coupling of the un-ionized 3s electron with the 3d electrons of the valence band. The energy gap between these two peaks gives information on the average oxidation state of Mn. The energy gap (ΔE) and the AOS of Mn can be related as follows:

$$\text{AOS} = 8.956 - 1.126 * \Delta E \text{ [4-6]} \quad (\text{Eq.8})$$

Mn AOS was also calculated by decomposition of Mn2p core level. The most intense Mn2p_{3/2} signal was considered for decomposition. Mn2p_{3/2} has been decomposed considering a mixture of Mn (III) and Mn (IV) which can be simulated by a mixture of MnO₂ and Mn₂O₃ in accordance with the fit of M. Biesinger [7]. For MnO₂ a set of multiplet peaks (6 peaks) have been used, with a fixed relative intensity, the full width at half maximum (FWHM) is fixed at the same value for the 6 peaks of each sample which is adapted for the passing energy used herein, and differing in BE each other by a fixed difference. The only parameter left to modify is the position in BE (± 0.2 eV) of the peak located at the lowest BE. For Mn₂O₃ instead of the multiplet an envelope Mn₂O₃ (Mn (III)) was used. The BE of Mn (III) was set at 1 eV of difference with the peak of Mn (IV) located at the lowest BE.

3-2-9- Infrared spectroscopy (IR)

This technique makes it possible to study the details of the molecular structure of the sample. An infrared spectrum is obtained by passing an infrared beam through IR-active samples and measuring the fraction of this incident radiation absorbed by the solid.

For a molecule to have infrared absorption bands, it must have a permanent dipole moment that interacts with the oscillating electric field of the incident infrared radiation. Thus, for a molecule to be active in IR, there must be a change in its dipole moment during the period of vibration.

The term Fourier Transform (FT) refers to a mathematical development in which data is collected and converted from an interference model to an infrared absorption spectrum that is like a molecular "fingerprint".

The various infrared spectra were obtained using a Thermo scientific iS50 total reflection attenuation infrared spectrometer (IR-ATR). The spectra are recorded using a pyroelectric triglycine sulphate detector (DTGS). Samples are pressed directly between the detector window and a diamond tip. For each spectrum, 256 scans are recorded in the range 4000 to 200 cm⁻¹ with a resolution of 2 cm⁻¹.

3-2-10- Pyridine adsorption followed by infrared spectroscopy (IR pyridine)

Pyridine is considered as basic molecule (pK_a = 5.2), because it process as lone pair of electrons at the nitrogen available for donation to other species during bonding, and because it can accept a proton from other species. It has been used to probe for the presence and the nature of surface acid sites. It can bond to the surface in three different mode: First modes involves transfer of proton from surface hydroxyl group to the adsorbate (Pyridinium) and occurs with

the surface acting as Brönsted sites (PyH^+). Second mode involves coordination of the adsorbate through the electron lone pair to the metal of the oxide and take place with the solid acting as Lewis acid sites (PyL) and the third mode is hydrogen bonding (PyH) as shown in **Figure 3-2**. The discrimination of the different adsorption modes can be carried out by an analysis of the vibration modes of the pyridine cycle (ν_{8a} , ν_{8b} , ν_{19a} , ν_{19b}), the position of the bands varying according to the adsorption mode. The strength of the acidic sites can be estimated by the evolution of the quantity of PyL or PyH^+ sites as the spectra recording temperature increases. The stronger the acidic sites, the higher the pyridine desorption temperature will be.

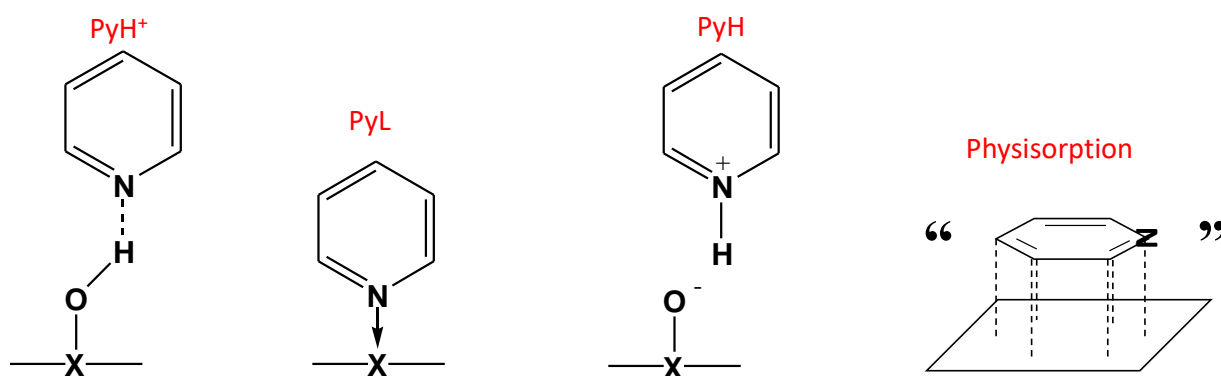


Figure 3 - 2: Pyridine bond on the surface

Pyridine adsorption followed by Fourier Transform Infrared spectroscopy (FTIR-pyridine) were recorded on a Thermo Nicolet 460 protégé instrument equipped with a CSi beam splitter and a MCT detector with a 2 cm^{-1} resolution. 256 scans were collected over the spectral range extending from 4000 to 400 cm^{-1} . The cell was connected to a vacuum line for different treatments. All samples were ground in an agate mortar and were pressed into the form of a self-supporting wafers (1 tonne/cm^2 , $2,01\text{ cm}^2$) then placed in a quartz sample holder and after in a quartz cell equipped with KBr windows. Samples were activated under high vacuum ($P < 10^{-7}\text{ mbar}$) at the temperature of 105°C . Pyridine was adsorbed at the equilibrium (1.2 mbar at 105°C). After that samples were evacuated at 105°C under high vacuum ($P < 10^{-7}\text{ mbar}$) for 30 min and then the spectra acquisition was performed. All recorded spectra were recalculated to a normalized wafer of 10 mg.

3-2-11- Raman spectroscopy

Raman spectroscopy is used in the laboratory for structure analysis and chemical identification of molecules; it provides a wealth of information on molecular and crystalline

structures, the nature of chemical bonds and intermolecular interactions. It is a scattering spectroscopy, as it consists in sending a monochromatic light on the sample, through a laser, and analyzing the scattered light. Like infrared spectroscopy, it is a technique allowing the observation of the vibrational states of the analyzed compound. Raman spectroscopy also allows the observation of rotational states. During a Raman spectroscopy study, it is important that the compound does not give rise to fluorescence since the spectral background becomes too high.

The Laser Raman spectra of Mn based catalysts were performed on a Xplora (Horiba) spectrometer with red laser (785 nm) with 1 % laser intensity and acquisition time of 1h. The laser power on the sample is controlled *via* a software-controlled density filter wheel. A resolution of about 4 cm^{-1} . A $\times 50$ objective was used for the selection of the particles to be analyzed and the recording of the spectra. LabSpec6 software allows data acquisition and processing.

3-2-12- Time of Flight Secondary ion Mass spectrometry (ToF-SIMS)

Time of Flight Secondary Ion Mass Spectrometry (TOF SIMS) is a technique for analyzing the extreme surface (about 1mm) with very high sensitivity. This technique consists in bombarding the sample surface (<4 monolayers) by a pulsed source of primary ions such as Bi_3^+ , Cs^+ , Ga^+ , Au^+ , etc. Once extracted from the surface, these are then accelerated by an electric field to the time-of-flight analyzer and their masses are determined by measuring their time of flight to reach the detector. These ions have the same kinetic energy.

This method of analysis makes it possible to obtain a very good resolution in mass (>10000), a study of the unlimited mass range and a 'parallel' detection of all the secondary ions emitted. The mass spectra obtained are described for secondary ions as a function of the m/z ratio and the isotope fragments can be detected.

In our work ToF-SIMS data were acquired using ToF-SIMS5 spectrometer (ION-TOF GmbH Germany) equipped with bismuth liquid metal ion gun 5LIMG. The powders were crushed using an agate mortar and pestle and the standard tablets were prepared using a press machine. The samples were bombarded with a pulsed Bi^{3+} primary ion beam (25 keV, 0.25 pA) rastered over $100\text{ }\mu\text{m} \times 100\text{ }\mu\text{m}$ surface area (128×128 pixels and 100 scans). The Total fluence did not amount up to 10^{12} ions/cm^2 ensuring static conditions. Charge effects were compensated by means of a 20 eV pulsed electron gun. With a cycle time of 200 μs , data were collected over a mass range $m/z = 0\text{-}3500$ for both positive and negative secondary ions. The

fragments were identified by their exact mass, coupled with the appropriate intensities for the expected isotope pattern. The mass resolution $m/\Delta m$ at $m/z = 55$ for Mn^+ was 2500.

3-3- Determination of catalytic properties of materials for the total oxidation of formaldehyde

3-3-1- Description of the set-up

A schematic representation of the set-up is given in **Figure 3-3**. The complete set up consists of four main parts: a) - formaldehyde generation system, b) - vapor phase water generation system, c) - catalytic reactor, d) - analytical system. The set-up was constructed using Swagelok 1/8-inch diameter stainless steel tubing (except for the catalytic reactor). The carrier gas used for catalytic test is synthetic air consisting of 20% oxygen by volume and 80% nitrogen by volume. The carrier gas used for HCHO termodesorption is He. The total gas flow rate in the catalytic test was set to 100 mL/min using a Bronkhorst mass flow meter.

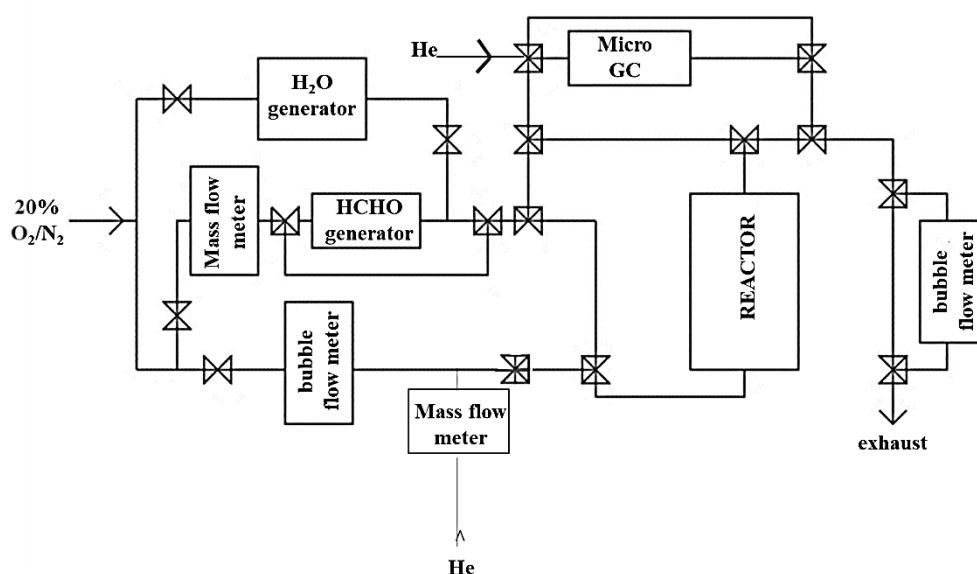


Figure 3 - 3: Scheme of the set-up of formaldehyde catalytic oxidation

a) Gaseous phase formaldehyde generation

The gaseous formaldehyde was generated using a gas generator of the brand VICI Metronics Dynacalibrator Model 150. This device consists of a permeation chamber through which the carrier gas can pass. The temperature of the chamber can be controlled from 5 °C to 110 °C (± 0.01 °C). The total flow rate of gas passing through the permeation chamber is 100 mL/min.

Two permeation tubes (Metronics Dynacal) containing paraformaldehyde (white formaldehyde polymer) are inserted into the permeation chamber. Dynacal permeation devices are small, inert capsules containing a pure chemical compound as shown in **Figure 3-4**. An equilibrium between the solid phase or liquid phase and the gas phase (formaldehyde gas) is established in these inert tubes. The permeation rate of the tube at the chamber temperature is the parameter determining the amount of formaldehyde gas emitted into the permeation chamber through the polytetrafluoroethylene (PTFE) membrane. This parameter, which depends on the length of the tube and its thickness, is given by the producer at the time of purchase. The permeation rate of the tubes that have been used is in the range of ~10100 ng/min at 100°C.

In order to achieve the desired concentration of HCHO (100 ppmv), the temperature of the permeation chamber must be 105 °C. The calculations performed to correlate the concentration and temperature of the permeation chamber are as follows:

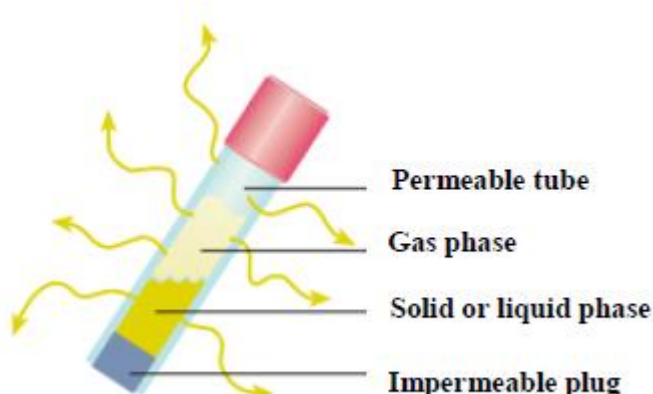


Figure 3 - 4: Dynacal permeation tubes

The concentration of HCHO in the carrier gas leaving the permeation chamber can be calculated

using the following formula: $[HCHO] = \frac{K \times P}{F}$ (Eq.9)

- $K = 24.45 / \text{MM (HCHO)} = 24.45 / 30.03 = 0.814$
- $P = \text{The permeation rate (ng/min)}$
- $F = \text{The flow rate (mL/min)}$

Then the permeation rate at the chamber temperature, can be calculated according to the following equation: $\log (P) = \log P_0 + 0.034 (T-T_0)$

- P: The permeation rate at the temperature of the permeation chamber
- P_0 : The permeation rate at the reference temperature (100 °C)
- T: The temperature of the permeation chamber
- T_0 : The reference temperature

b) Vapor phase water generation system

Humidity is generated by a bronkhorst's CEM (controlled evaporation and mixing) system. This system consists of dispersing a very fine water droplet in an air stream. The CEM is composed from two mass flow controllers, one controlling the air and the second controlling the water flow, and a CEM mixer dispersing the fine water droplets into the air flow. The entire system is thermostatically controlled at 42°C.

c) Catalytic reactor

The catalytic test reactor used is made of pyrex, with a fixed bed reactor and 10 mm as diameter. A 100 mg of catalyst is introduced into it. Then, the reactor is introduced into a tubular furnace equipped with a temperature control thermocouple and a reading thermocouple.

d) Analytical system

Total oxidation of formaldehyde produces carbon dioxide CO_2 and water H_2O . With incomplete oxidation, products such as carbon monoxide CO , formic acid HCOOH and methanol CH_3OH may be formed. To detect and quantify all these products online, a Varian gas chromatography system (model CP4900) equipped with two analysis modules was used. Each module is equipped with an injector, a column and a TCD type detector. The carrier gas used for both modules is helium. Module 1 is equipped with a column of type CO_x (1m) column for the analysis of formaldehyde and carbon dioxide while module 2 is equipped with a CP-Sil 5CB (8m) type column for the analysis of incomplete oxidation products of formaldehyde. The micro gas chromatograph is equipped with a Genie Filter membrane connected in series just before the injection pump to avoid the introduction of liquid or solid particles into the system. A gas micro chromatography analysis is carried out under the conditions reported in **Table 3-3**.

Table 3 – 3: Analytical conditions in gas chromatography analysis

	Module 1	Module 2
Sampling time	30 s	30 s
Analysis time	10 min	10 min
Inlet bottom gas pressure	5.5 bars	5.5 bars
Column pressure	140 kPa	200 kPa
Column temperature	30°C	80°C

3-3-2- HCHO and CO₂ calibration

To calibrate HCHO, the temperature of the permeation chamber is set to a desired value and injections (6 injections) are made with micro chromatography (by pass). Then the specific air of the HCHO peak is integrated. The selected temperatures are 85, 90, 95, 100, 103 and 105°C. Then the calibration curve is drawn: formaldehyde concentration versus specific air and the equation of the linear regression is $y = 0.4213 x$ (x specific air of the HCHO peak, and y is the HCHO concentration) with $R^2 = 0.9943$.

In order to quantify the CO₂ concentration, a gas flow containing different concentrations of HCHO (depending on the temperature of the permeation chamber) is sent over a (manganese and/or platinum) catalyst heated to 300°C, (for each concentration, 6 chromatograms are recorded). HCHO is thus completely converted into CO₂ and H₂O. So according to the HCHO response factor obtained previously, we can calculate the CO₂ concentration, by plotting the calibration curve: HCHO concentration versus CO₂ specific air peak considering that the carbon balance is 100%. The equation of the linear regression obtained is $y = 0.4488 x$ (x specific air of CO₂ peak, and y is the CO₂ concentration with $R^2 = 0.9796$).

3-3-3- Experimental procedure of HCHO oxidation

Light off curves

Oxidation of formaldehyde was carried out in a fixed bed reactor loaded with 100 mg of catalyst. Catalyst activation was carried out over the calcined Ce_xMn pretreated *in situ* at 200 °C for 1 h in 20 vol% O₂/N₂ (100 mL/min). Afterwards, the stabilized reactive flow consisting of 100 ppmv of HCHO mixed with 20 vol% O₂/N₂ was sent towards the fixed bed reactor for 1 h. At that time the temperature was allowed to decrease from 200 °C to 25 °C at a rate of 0.2 °C/min. The total flow rate of 100 mL/h allowed to get a gas hourly space velocity (GHSV) of 60 L/(g_{cat}.h). For commercial Hopcalite (acting as reference from Purelyst MD-101 with a

mixture of Cu oxides and Mn oxides with a surface area of 225 m²/g) the sample was pretreated at 300 °C in similar conditions as above.

The HCHO elimination corresponding to the HCHO removal efficiency from the gas phase was expressed by the HCHO conversion (eq.10) while the HCHO oxidation in CO₂ was expressed from the CO₂ yield (eq.11) as follows:

$$\text{HCHO elimination (\%)} = \frac{[\text{HCHO}]_{\text{in}} - [\text{HCHO}]_{\text{out}}}{[\text{HCHO}]_{\text{in}}} \times 100 \quad (\text{Eq.10})$$

$$\text{HCHO conversion into CO}_2 \text{ (\%)} = \frac{[\text{CO}_2]_{\text{out}}}{[\text{HCHO}]_{\text{in}}} \times 100 \quad (\text{Eq.11})$$

Where [HCHO]_{out} and [CO₂]_{out} were the outlet HCHO and CO₂ concentrations and [HCHO]_{in} the initial HCHO concentration (100 ppmv).

Effect of moisture

Catalyst activation was carried out over the calcined Ce_xMn-400 adopting a similar procedure as given above. The reactor was then cooled down to 50 °C in flowing dry air. Afterwards, the stabilized reactive flow (100 ppmv of HCHO diluted in 20 vol% O₂/N₂) was sent towards the fixed bed reactor and RH was allowed to increase with time. The duration and RH% of the successive steps were specified in the appropriate figures in the text. At the end of the test the reactor was cooled down in static air. In the case of commercial Hopcalite, the stability test was performed after performing the light-off curve. The temperature was allowed to increase up to 75 °C (2 °C/min). At the end of the test the reactor was cooled down in static air. The suffix SF (stability formaldehyde oxidation test) was added for the labelling of the used catalysts.

Adsorption and thermo-desorption of formaldehyde

In order to assess the possible participation of catalyst oxygen in HCHO oxidation, experiments were performed in oxygen free atmosphere. Before each test, catalysts were pretreated for 2h at the temperature of calcination in air flow of 100 mL/min (2°C/min). After cooling down to 25 °C, the catalyst was submitted to gaseous formaldehyde (100 ppmv) / air mixture (100 mL/min) until a steady state was achieved. At that stage catalyst performances were evaluated from 25°C to 480°C with heating rate of 1°C/min under helium at a GHSV of 60 L/(g_{cat}.h).

3-4- Determination off catalytic properties of materials for ozone decomposition

For ozone decomposition, a 10 pin-to-plate negative corona-glow non-thermal plasma (NTP) discharge reactor was used as ozone generator. For TCE abatement discussed in the next the same plasma discharge and reactor are used coupled with catalyst downstream of the plasma reactor is used

3-4-1- Description of the plasma Set-up for Ozone generation and TCE abatement

A schematic representation of the experimental set-up is given in **Figure 3-5**. It consists of three main parts: The gas supply system, the reactor system and the gas analysis system. In the following sections, each of these parts will be presented in more detail.

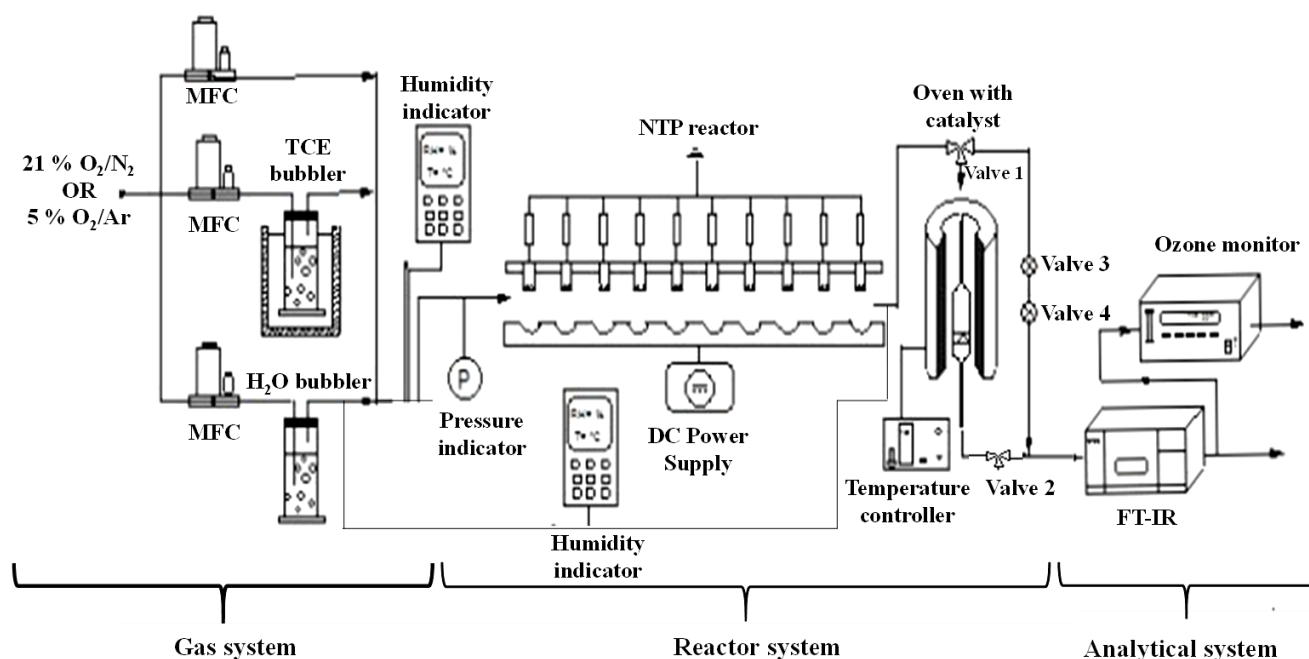


Figure 3 - 5: Experimental Set-Up

a) Gas supply system

Dry air (alphagaz 1, mole percentages: $O_2 = 21\%$ and $N_2 = 79\%$, 200 bar) was acquired from Air liquide. Distilled water was used to adjust the humidity in the NTP reactor (or after the DC reactor), was stored in a gas bubbler, and the bubbler bottle was located in a thermostatic water bath. The flows of air and water were adjusted and maintained by 2 separate mass flow controllers MFC Bronkhorst, (Figure 3.6) the upper MFC (0-10 L/min) was used to adjust the total flow rate of the inlet and the inferior MFC (0-0.5 L/min) was used to regulate the humidity. TCE vapor was generated and its concentration was controlled by varying the flow of dry air

through a bubbling bottle containing liquid TCE (99.99% purity, Acros) by using the middle MFC (0-0.2 L/min). The relative humidity is controlled using the lower MFC (0-0.2 L/min).

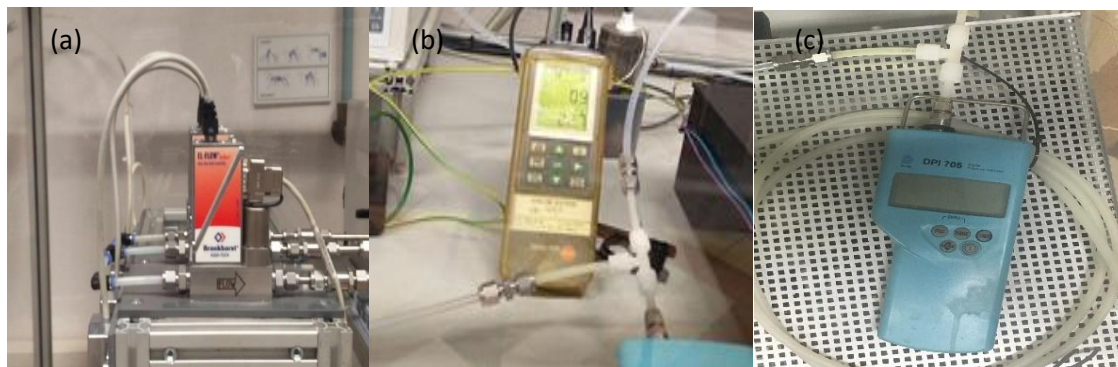


Figure 3 - 6: (a) MFC, (b) Testo 445 climate measurement device with temperature/humidity probe, (c) Pressure indicator

The air humidity and temperature were measured with a testo 445 device. The temperature/humidity probe was therefore located in a closed vessel in which the feed gas circulated. The vessel was placed between the gas supply system and the reactor inlet. The Gas pressure of the air flowing through the set-up was measured by means of a digital pressure Indicator 705 and is controlled by the valves 3 and 4. In order to stabilize the feed gas mixture, the plasma reactor was turned off.

b) Reactor system

➤ Plasma reactor

Figure 3-7, shows the plasma reactor. The cylindrical reactor was made by polytetrafluoroethylene (PTFE), and inserted in a quartz tube which was closed by airtight fittings in order to prevent any leakages. However, the cathodes pins were made by stainless steel and the anodes plates by aluminum. The feed gas also flowed through a rectangular duct with a cross section of 4 cm x 0.9 cm and a length of 25.1 cm, so the volume of the reactor is $V = 4 \times 0.9 \times 25.1 = 90.36 \text{ cm}^3$. The plasma reactor consists of 10 aligned, crenellated cathode pins which were positioned 28 mm from each other. The distance between the cathode pin and anode plate is 10 mm. A DC power supply (Technix, SR40-R-1200) provided the discharge power (**Figure 3-9**). The NTP was generated at atmospheric pressure and room temperature.

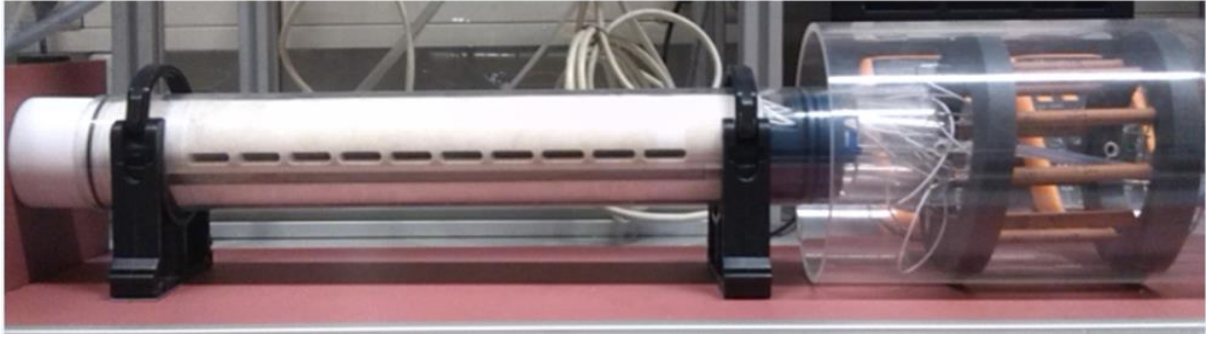


Figure 3 - 7: Photo of the plasma reactor with 10 electrodes pins



Figure 3 - 8: Photo of DC power source

- Measurement of discharge current and voltage.

Figure 3-9, shows the electrical scheme of the discharge. The applied power in the reactor was measured *via* determination of the plasma voltage (U_{pl}) and the discharge current. To determine U_{pl} , a high voltage probe (Fluka 80 K-40, division ratio 1/1000) was used to measure the total voltage U_{tot} , and the discharge current I was determined by recording the voltage signal U_m across a 100Ω resistor R_m placed in series between the counter electrode and ground.

As can be seen from **Figure 3-9**, the plasma voltage was calculated as follows:

$$U_{pl} = U_{tot} - U_b - U_m \quad (\text{Eq.12})$$

$$U_{pl} = U_{tot} - \frac{R_b I}{N} - RI \quad (\text{Eq.13})$$

The radius and depth of coverture for the spherical surface segment was 17, 5 mm and 5 mm respectively. Stable and uniform glow discharge operation was ensured and the gas flow ballasting each cathode pin with a $1.5 \text{ M}\Omega$ resistor R_b . The fraction of the total electrical power that was dissipated in these resistors amounted to 10 % at most.

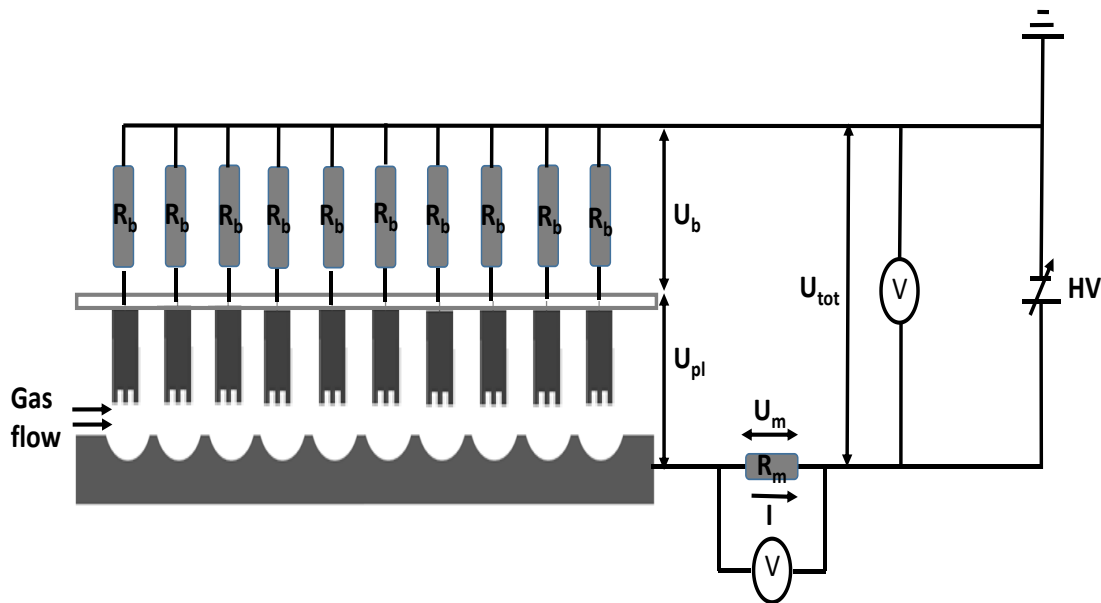


Figure 3 - 9: Electrical scheme of the 10 pin to plate

❖ Measurement of energy.

The energy of the total discharge, also referred to specific input energy (ED), can be calculated according to the following equation:

$$ED(J/L) = \frac{U_{pl} \cdot I}{flow\ rate} \quad (Eq.14)$$

➤ Catalytic reactor

Figure 3-10, show the catalytic reactor system composed of a glass tube, oven and a temperature controller. The tube was made in Pyrex glass and had 20 mm as inner diameter and 100 mm as effective length. Inside the tube, a sintered and porous plate was used to hold the catalyst powder in place. The oven was a homemade model delivered by UCCS from Lille University.

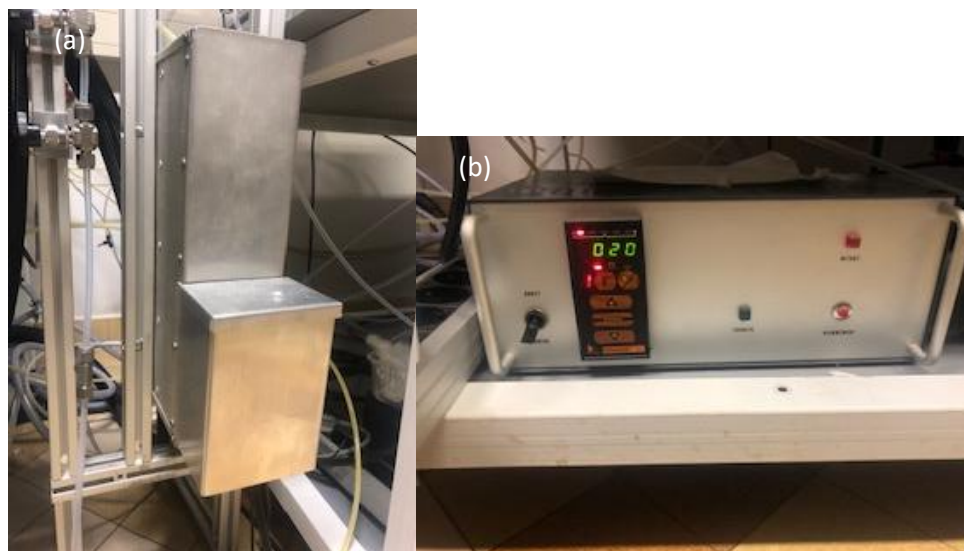


Figure 3 - 10: Overview of the catalytic reactor component with (a) oven, (b) temperature controller and
c) Gas analysis system

➤ FT-IR spectrometer

Infra-red spectroscopy is based on molecules vibration resonance. The absorption of specific wavelength of IR radiation cause a change in the molecules dipoles moments. When absorption occurs, the molecules acquires is clearly defined amount of energy ($E=h\nu$) from the radiation and moves up from a ground state to an excited state.

The frequency at which the molecule will absorb the radiation is determined by the vibrational energy gap. The number of possible absorption peaks is directly related to the number of vibrational freedoms of the molecule. The intensity of absorption peaks is related to the extent of the change in dipole moment and the possibility of the transition of energy levels. Therefore, by analyzing the infrared spectrum, one can readily obtain abundant structural information of a molecule.



Figure 3 - 11: (a) Bruker Vertex 70 FT-IR spectrometer, (b) Gas cell

Figure 3-11 (a), shows the Bruker Vertex 70 FT-IR spectrometer used. The following experimental conditions were used to measure both the background and sample spectrum. The latter measurements were recorded after steady-state condition was reached.

- Resolution: 4 cm^{-1}
- Number of scans: 10
- Scan velocity: 20 KHz
- Aperture: 1.5 mm

The optical bench of the FT-IR was purged with air delivered from a CO_2 -dryer while the sample compartment was purged with dry synthetic air in order to avoid any interference of these compounds. The mercury-cadmium-telluride (MCT) detector was cooled with nitrogen and OPUS (Bruker) software was used to collect and analyze the obtained spectra. The windows of the gas cell used is made by zinc selenium with a 20 cm optical path length and windows diameter of 45mm (**Figure. 3-11-b**).

➤ Ozone monitor

The ozone measurement was carried out with a Teledyne API's model 465M (**Figure 3-12**) and the specific characteristics are summarized in **table 3-4**. The detection of ozone molecules is based on absorption of 254 nm UV light due to an internal electronic resonance of the O_3 molecule. The monitor uses a mercury lamp constructed so that a large majority of the light emitted is at the 254nm wavelength. Light from the lamp shines through an absorption cell through which the sample gas is passed. The ratio of the intensity of light passing through the absorption cell and the intensity of light measured by a reference detector forms a ratio I/I_0 .

This ratio forms the basis for the calculation of the ozone concentration. Ozone monitor is used only to calculate the ozone calibration factor described below.

The Beer-Lambert equation, shown below, calculates the concentration of ozone from the ratio of light intensities.

$$c_{O_3} = -\frac{10^6}{\alpha \cdot L} \cdot \frac{T}{273K} \cdot \frac{14.695}{P} \cdot \ln \frac{I}{I_0} \quad (\text{Eq.15})$$

Where:

I = Intensity of light passed through the sample

I₀ = Intensity of light through sample free of ozone

α = Absorption coefficient

L = Path length

c_{O₃} = Concentration of ozone in parts per million

T = Sample temperature in Kelvin

P = Pressure in pounds per square inch (absolute)



Figure 3 - 12: Teledyne ozone monitor Model 465M

Table 3 - 4: Specifications of the Ozone monitor

Measurement range	0-1000 ppm to 0-10000 ppm
Sample flow rate	0.8 L/min
Resolution	1 ppm
Accuracy	1% of full scale

➤ Ozone calibration.

Ozone was generated by the plasma discharge. The characteristics peaks of ozone can be identified in the range of 1050 to 1000 cm⁻¹, which was the area selected for integration as shown in **figure 3-13**.

Furthermore, the ozone-enriched gas was passed through the FT-IR spectrometer and the measurements were conducted for each voltage 10 times. The effluent gas was passed through the ozone monitor continuously, thus measuring the ozone concentration *in situ*. Based on the measurements at different discharge voltages, the ozone concentration is obtained *via* linear regression applied to the average integration area as a function of monitor ozone concentration and the slope K was used to calculate ozone concentration.

$$k = \frac{C_{\text{ozone}}}{S_{\text{ozone}}} = 1208.06$$

(Eq.16)

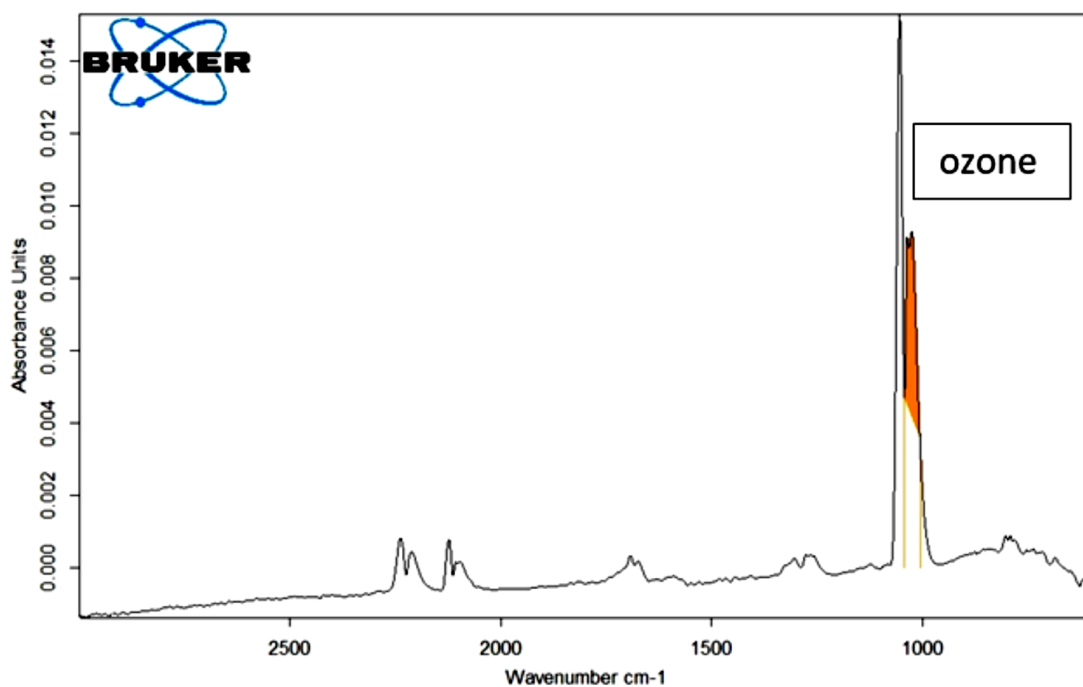


Figure 3 - 13: Selected FT-IR band for ozone calibration

3-4-2- Experimental procedure for using plasma as ozoner:

The 10-pin-to-plate reactor was connected to both the high voltage DC power supply and the gas flow system. Dry or humid air (RH = 15%) was flushed to the NTP reactor at a fixed flow rate (0.5; 1.0; 1.5 L/min) until the RH reach the desired value. In the case of dry air, the RH is equivalent to 0.6-0.7%, which cannot be lower and corresponds to the residual water present in the gas stream. Afterward, the DC power supply was turned on. The nature of the NTP processed gaseous species effluent gases were investigated using FT-IR spectroscopy. The effluent gas was sampled 10 times at intervals of 30s. The ED was allowed to increase between 50 and 250 J/L.

3-4-3- Experimental procedure for catalytic ozone decomposition

In dry air

0.1 g of the as-synthesized samples mixed with 1g of SiC (EMB 45053 Prolabo, 0.150 mm) was activated under air flow (flow rate = 200 mL/min) at 150 °C (heating rate = 1 °C/min) for 8 hours. However, for acid treated samples, 0.05 g catalyst was mixed with 1g of SiC, and the catalyst activity tests were carried out without any activation.

The catalytic activity test was carried out at atmospheric pressure and room temperature (20°C).

1- First a background was taken.

2- Then ozone was generated by flowing 1L/min of dry air (RH = 0.6 / 0.7%) through NTP reactor, by adjusting the applied voltage in order to obtain a certain energy density and thus the desired initial concentration of ozone.

3- In order to estimate the initial ozone concentration, the reactive flow was initially pass through by-pass of the catalyst reactor (close valves 1 and 2). This reactive gas was samples 10 times at intervals of 30 s, where the number of scans for each spectra is 10, using FTIR spectrometer and these FTIR are labeled as plasma alone in **chapter 6**.

4-Then, the reactive flow was diverted through the catalyst reactor (open valves 1 and 2), and the effluent gas was sampled 60 times at intervals of 30 s, and then 135 times at intervals of 120 s, where the number of scans for each spectra is 10. During the test, the catalyst was maintained at room temperature (20°C). At the end of the experiment, the ozone concentration is again measured in order to control the initial concentration of ozone during the experiment by passing the effluent gas through by-pass of the catalyst reactor.

Effect of humidity

0.05 g catalyst was mixed with 1g of SiC, and the catalyst activity tests were carried out without any activation and the catalytic activity test was performed at atmospheric pressure and 30°C. After the same three first steps given previously in dry air were followed.

4- Then plasma was turned off and the water is introduced after the plasma reactor

5- A background in presence of water has been taken

6- The reactive humid flow was pass through by-pass of the catalyst reactor (close valves 1 and 2). This reactive gas was sampled 10 times at intervals of 30s, where the number of scans for each spectra is 10, using FTIR spectrometer and these FTIR are labeled as Inlet CR in **chapter 6**.

7- Then, the reactive humid flow was diverted through the catalyst reactor (open valves 1 and 2), and the effluent gas was sampled 60 times at intervals of 30s, and then 135 times at intervals of 120s, where the number of scans for each spectra is 10. During the test, the catalyst was maintained at room temperature (20°C). At the end of the experiment, the ozone concentration is again measured in order to control the initial concentration of ozone during the experiment by passing the effluent gas through by-pass of the catalyst reactor.

Experiment under 5% O₂/Ar

In order to study the effect of nitrogen oxides generated by NTP on the catalyst activity, experiment has been performed using 0.05 mg of Ce_{0.01}Mn at atmospheric pressure and 20 °C under 1L/min of 5% O₂/Ar as carrier gas. The catalytic activity test procedure is the same as given before using dry air.

Evaluation of the ozone removal efficiency:

The _{ozone} conversion efficiency was calculated using the following equation.

$$\text{O}_3 \text{ conversion} = \frac{[\text{O}_3]_{in} - [\text{O}_3]_{out}}{[\text{O}_3]_{in}} \times 100 \quad (\text{Eq.17})$$

Where, [O₃]_{in} and [O₃]_{out} were the concentration introduced in the reactor and that measured at the exit of the catalytic reactor, respectively. When ozone is decomposed no ozone characteristic band is observed by the FTIR.

In order to know if the ozone concentration is stable at a fix flow rate and energy density, we study the ozone generation with flow rate 1L/min and energy density 150J/L for 5 hours. We found that the ozone generation is stable as a function of time and according to this experiment we calculate the error by calculating the variance and then the standard deviation. The variance is calculated according to the following formula: $S^2 = \frac{\sum(x - \bar{x})^2}{n}$ and the standard deviation is the square root of the variance. The standard deviation is about 3%

3-5- Determination of catalytic properties of materials for TCE abatement

3-5-1- Calibration FTIR

As discussed before the Set-up description is the same. Only a new calibration for CO, CO₂ and TCE has been performed. Therefore the FT-IR spectrometer was calibrated with calibration mixtures delivered by Air liquid. The mixture was flushed through the gas cell, with a flow rate 1L/min (identical to the flow rate applied during the experiment) until a steady state was reached. After 2 spectra were recorded each minute to obtain the required surface area of the adsorption peaks under consideration. The peak areas between 916 -966 cm⁻¹ (TCE), 2388 – 2287 cm⁻¹ (CO₂) and 2140 - 2071 cm⁻¹ (CO) were integrated. Linear regression was applied to the integration area values and the slopes K1, K2 and K3 were used to calculate the concentration of TCE, CO₂ and CO respectively. It should note that by using plasma alone the CO amount is qualitative not quantitative due to the fact that CO band overlaps with ozone and with N₂O band K1, K2 and K3 were defined as following:

$$K1 = \frac{C_{TCE}}{S_{TCE}} = 334.82 \quad (\text{Eq.18})$$

$$K2 = \frac{C_{CO2}}{S_{CO2}} = 54.44 \quad (\text{Eq.19})$$

$$K3 = \frac{C_{CO}}{S_{CO}} = 1251.56 \quad (\text{Eq.20})$$

3-5-2- Experimental procedure for trichloroethylene in PPC process

Trichloroethylene (TCE, 99.99% purity, ACROS) was evaporated by bubbling dry or moist air (RH = 15%) into a saturator and introduced into the plasma reactor after diluting with air. The total flow rate and TCE concentration were maintained at 1 L/min and 150 ppmv respectively, using mass flow controllers (MFC, El-Flow, Bronkhorst). A 10-pin-to-plate plasma reactor configuration was used working in a negative DC corona discharge. 0.1g of catalyst diluted in 1g of SiC (EMB 45053 Prolabo, 0.150 mm) placed in a quartz reactor was activated for 1h in dry air (0.2 L/min) at 100°C.

Evaluation of the TCE removal efficiency and CO_x (x = 1; 2)

The TCE abatement (conversion) efficiency was calculated from:

$$\text{TCE conversion} = \frac{[TCE]_{in} - [TCE]_{out}}{[TCE]_{in}} \times 100 \quad (\text{Eq.21})$$

Where $[TCE]_{in}$ and $[TCE]_{out}$ were the inlet and outlet concentrations, respectively.

The CO_2 , CO and CO_x yields were calculated as follows:

$$YCO_2 (\%) = \frac{[CO_2]_{out}}{2x[TCE]_{in}} \times 100 \quad (Eq.22)$$

$$YCO (\%) = \frac{[CO]_{out}}{2x[TCE]_{in}} \times 100 \quad (Eq.23)$$

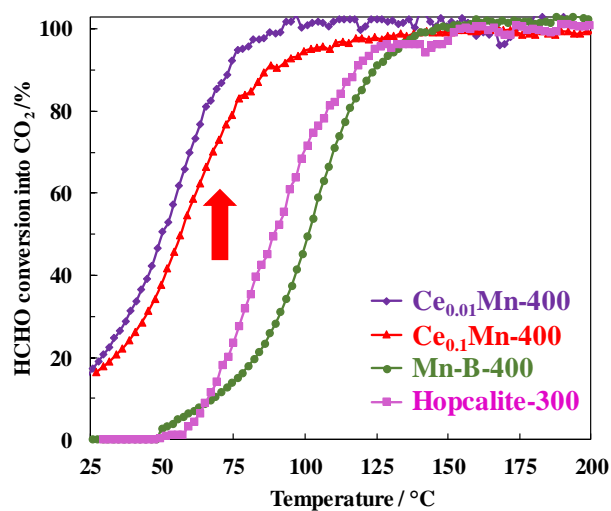
$$YCO_x (\%) = YCO_2 (\%) + YCO (\%) \quad (Eq.24)$$

References

- [1] M. Händel, T. Rennert, K.U. Totsche, *Geoderma* 193–194 (2013) 117–121.
- [2] S.W. Weller, *Chemical Engineering Communications* 13 (1981) 193–194.
- [3] A.B. Monti A.M.Daniele, *Journal of catalysis* 83 (1983) 321–325.
- [4] L. Zhang, J. Tu, L. Lyu, C. Hu, *Applied Catalysis B: Environmental* 181 (2016) 561–569.
- [5] V.R. Galakhov, M. Demeter, S. Bartkowski, M. Neumann, N.A. Ovechkina, E.Z. Kurmaev, N.I. Lobachevskaya, Ya.M. Mukovskii, J. Mitchell, D.L. Ederer, *Phys. Rev. B* 65 (2002) 113102.
- [6] V.P. Santos, M.F.R. Pereira, J.J.M. Órfão, J.L. Figueiredo, *Applied Catalysis B: Environmental* 88 (2009) 550–556.
- [7] M.C. Biesinger, B.P. Payne, A.P. Grosvenor, L.W.M. Lau, A.R. Gerson, R.St.C. Smart, *Applied Surface Science* 257 (2011) 2717–2730.

Chapter 4:

CERIUM DOPED (K, Na) - BIRNESSITE LIKE MnO_2 FOR LOW TEMPERATURE OXIDATION OF FORMALDEHYDE: EFFECT OF CALCINATION TEMPERATURE



$\text{HCHO} = 100 \text{ ppm}$, $\text{O}_2 = 20\%$, N_2 balance, $\text{GHSV} = 60 \text{ L}/(\text{g}_{\text{cat}}\cdot\text{h})$

4-1- Introduction

In order to address our issues, the first validation approach was to study the catalytic oxidation of formaldehyde (HCHO) since this reaction is well known to be correlated with the density of oxygen vacancies in the materials[1–3].

HCHO classified as a volatile organic compounds, is considered as one of the most hazardous pollutants especially in an indoor environment. It is mainly emitted from construction and decoration materials and can cause serious illnesses to human health and is also very toxic to the environment. Among the different approaches proposed for HCHO removal, heterogeneous catalytic oxidation has been recognized to be the most efficient technology.

Noble metal based catalysts exhibit high activity allowing total HCHO oxidation into CO_2 and H_2O at room temperature [4,5]. Rochard *et al.* [6], have been investigated that the oxygen vacancies played a key role in enhancing the HCHO catalytic activity over Au/Co-promoted CeO_2 catalysts. However, their high costs and lack of resources impede their practical applications [7–9]. In 2002, Sekine *et al.* [10], found MnO_2 as the most active noble-metal-free catalyst in HCHO oxidation among various commercial transition metal oxides (TMO). Among the different MnO_2 crystal structure, birnessite type MnO_2 was recognized to be the most active catalyst in HCHO oxidation [8]. In order to promote the catalytic performances of such materials significant experimental researches were recently focused on defective birnessite materials (oxygen and manganese vacancies [11]) with proper surface electronic properties [29–31]. Element incorporation was also another followed strategy to obtain a more active catalyst. In that way, incorporation of suitable transition metals (TM) or alkali cations was investigated to promote activity by seeking to decrease energy formation of oxygen vacancy [15]. In particular, Ce doping in the birnessite structure, among the other different transition metals, was shown to be the most performant catalyst. Higher content of oxygen vacancies resulting from a close contact between CeO_2 and MnO_2 nanoparticles was postulated to be responsible for its high activity in HCHO oxidation.

In this chapter, formaldehyde oxidation over Ce-doped (K, Na) birnessites has been investigated. Particular emphasis was placed herein on the effect of calcination temperature over the as-synthesized catalysts to be discussed with the catalytic performances in HCHO oxidation in dry and moist air.

4-2- Experimental conditions

Table 4-1, summarizes the basic experimental conditions used in this chapter. The detailed experimental conditions can be seen in [chapter 3](#).

Table 4 - 1: Experimental conditions

Gas source	Air liquid, or Helium, Alphagaz 1
Flow rate	0.1 L/min
Relative humidity (RH)	0 % / 50 %/ 75 %
Initial HCHO concentration	100 ppmv
	Produced from para-HCHO tube incorporated in a permeation chamber
Catalyst	Ce _x Mn-T
	0.1 g of catalyst
Activation conditions	100 mL/min, 200 °C for 1 hour
Catalyst temperature	Decreases from 200 °C to RT

4-3- Results and discussion

4-3-1- Characterizations of the fresh samples

The X-ray diffraction pattern of Mn-B exhibits four broad diffraction peaks centered at 12.2 °, 24.5 °, 37.0 °, and 66.2 °, which are the main peaks of birnessite structure (**Figure 4-1**). Their positions and intensities closely resemble those reported by Drits *et al.* [16], for turbostratic stacking of the birnessite with the alternation of one-layer hexagonal (JCPDS No. 04-017-0609) and one-layer monoclinic (JCPDS No. 43-1456). The two peaks in the basal reflections at 12.3 ° and 24.5 ° are common for both symmetries and arises respectively from 001 and 002 reflections. The two peaks observed at higher angles (37.0 °, and 66.2 °) correspond to the two dimensional diffraction peaks having (100) and (110) indices, respectively [16]. The interlayer spacing of 7.2 Å, calculated from the diffraction peak located at 12.2 °, is similar to the one obtained with Händel *et al.* [17]. The poorly resolved (001) and (002) lattice diffraction peaks can be explained by a decrease of the crystallite size or/and to randomly stacked layers along the c axis composed of edge-sharing MnO₆ octahedra [46-47]. However, the d spacing ratio for the peaks at high angles is approximately 1.71, close to 3^{1/2} characteristic for hexagonal symmetry which implies that the monoclinic symmetry doesn't have a strong distortion for the hexagonal symmetry [16].

With low Ce doping (Ce_{0.01}Mn), the XRD pattern reduces to three diffraction peaks at 24.5 °, 37 ° and 66.2 ° (**Figure 4-1**). As the Ce content increased, (Ce_{0.1}Mn) the XRD pattern reduces to two weak diffraction peaks at 37.0 ° and 66.2 ° indicating a poorly crystallized nano-

mineral (**Figure 4-1**). The d-spacing ratio of the two peaks remains close to $3^{1/2}$, suggesting pseudo-hexagonal symmetry in the manganese octahedral layer [48-49].

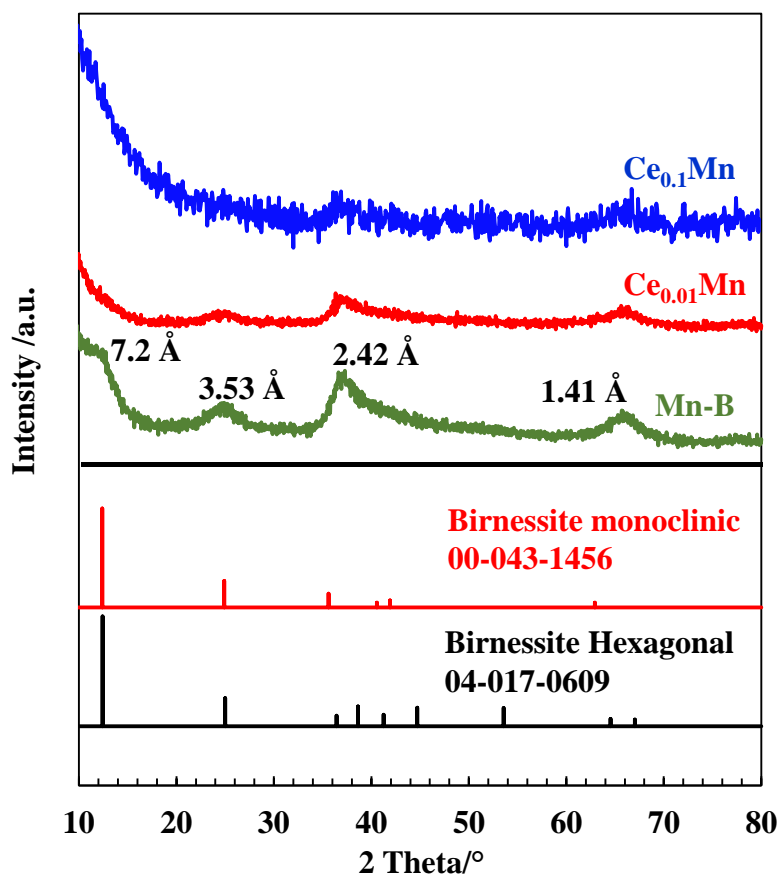


Figure 4 - 1: XRD patterns of the as-synthesized samples

FTIR-ATR spectra of the as-synthesized derived birnessites (**Figure 4-2**) are almost identical. The absorption bands at $3200\text{--}3300\text{ cm}^{-1}$ (H-O-H stretching mode) and 1620 cm^{-1} (H-O-H bending mode) were linked to adsorbed water and water in the interlayer spacing of the birnessite [17]. The lowest bands at 400 cm^{-1} and 480 cm^{-1} relate to vibrational modes of MnO_6 octahedra [21]. The broadening of these structural modes may be related to grain size and local differences in bonding environments [22]. Moreover, some additional bands located around $1500\text{--}1510\text{ cm}^{-1}$, $1405\text{--}1417\text{ cm}^{-1}$, $1313\text{--}1303\text{ cm}^{-1}$ and $1060\text{--}1050\text{ cm}^{-1}$ have been associated to residual CO_3^{2-} and HCO_3^{2-} species.

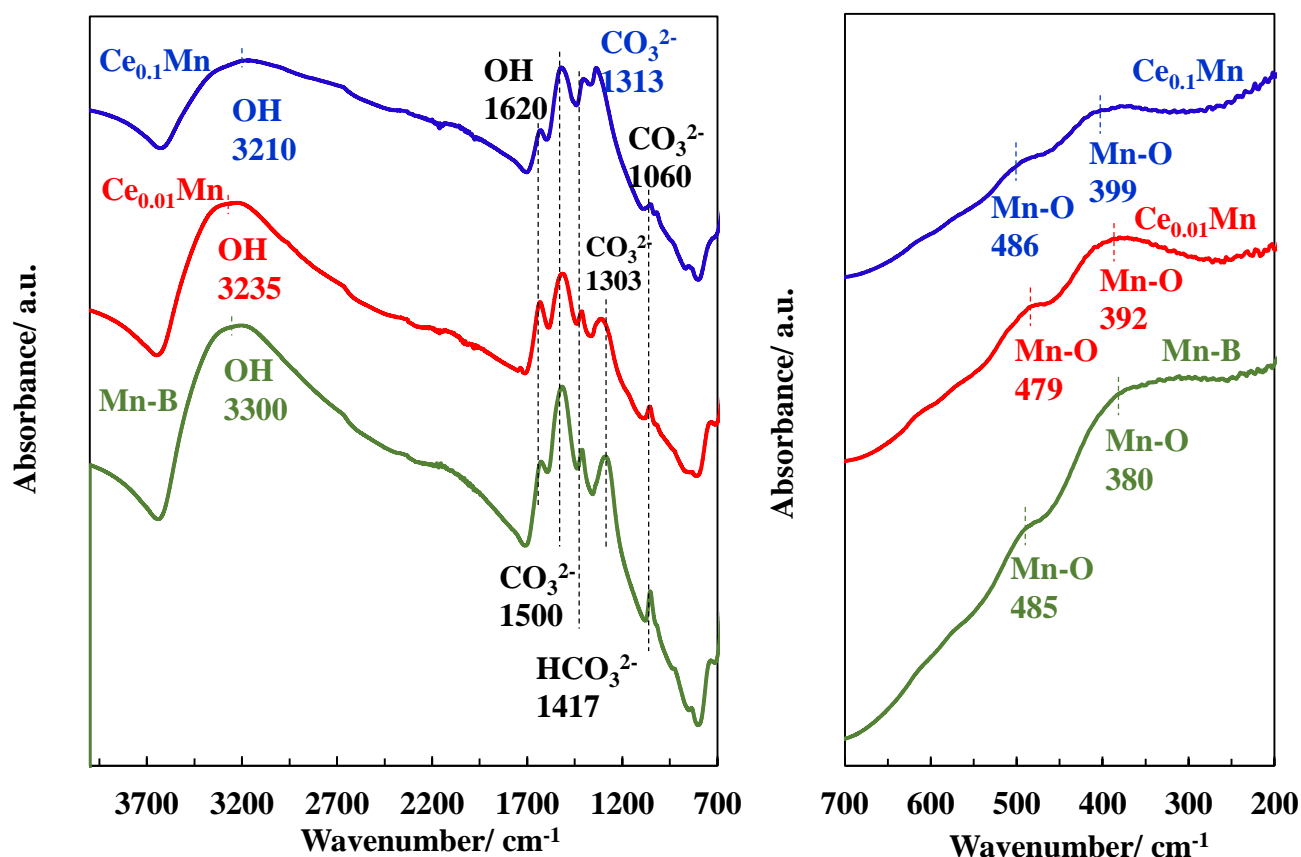


Figure 4 - 2: FTIR-ATR spectra of the as-synthesized samples

N_2 adsorption/desorption isotherms and PSD of the as-synthesized solids are given in **Figure 4-3** and textural properties are listed in **Table 4-2**. The N_2 -sorption isotherms of the as-synthesized samples belong to a type IV isotherm with a H3 (Mn-B, $\text{Ce}_{0.1}\text{Mn}$) and H2 hysteresis ($\text{Ce}_{0.01}\text{Mn}$) loop. V_p increases and D_p decreases after doping with Ce. The BET surface area of the parent birnessite of $44 \text{ m}^2/\text{g}$ increased markedly to $127 \text{ m}^2/\text{g}$ and to $243 \text{ m}^2/\text{g}$ with increasing Ce content. Taking into account a similar evolution, replacement of manganese ions by cerium ions in the lattice has been previously postulated [3].

Table 4 - 2: Textural properties of the as-synthesized samples

Catalyst	S_{BET} (m^2/g)	D_p^{max} (nm)	V_p^{tot} (cm^3/g)
Mn-B	44	4; 22	0.12
$\text{Ce}_{0.01}\text{Mn}$	127	4.3; 6.6; 37	0.32
$\text{Ce}_{0.1}\text{Mn}$	243	3; 4	0.23

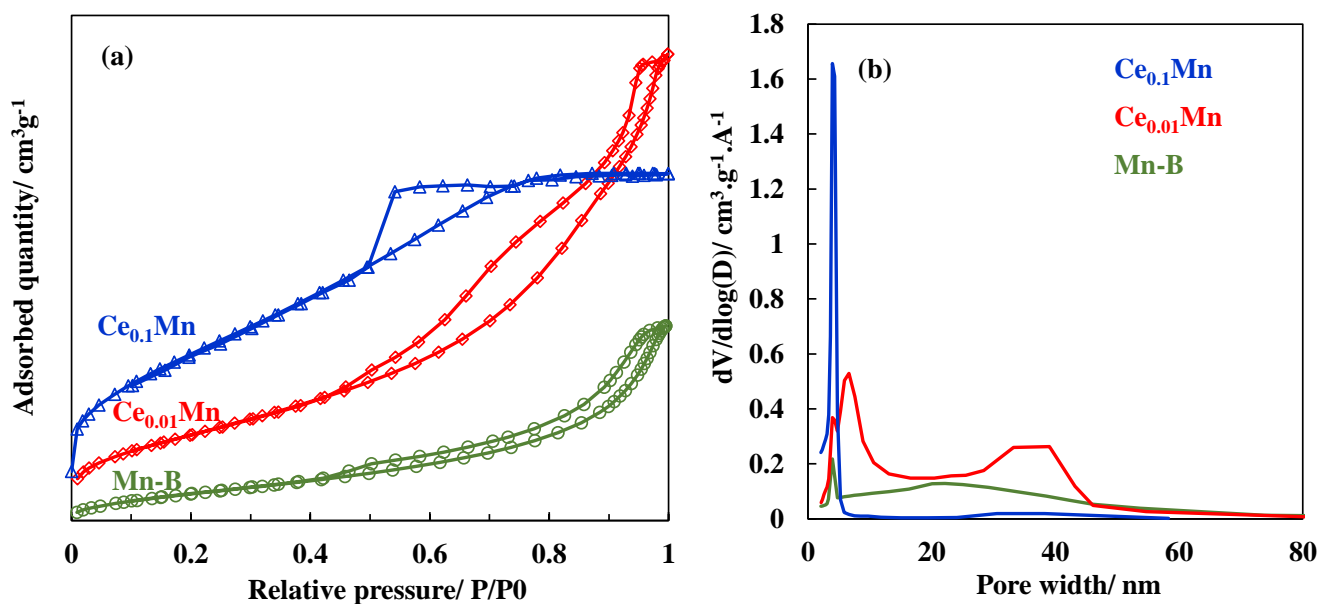
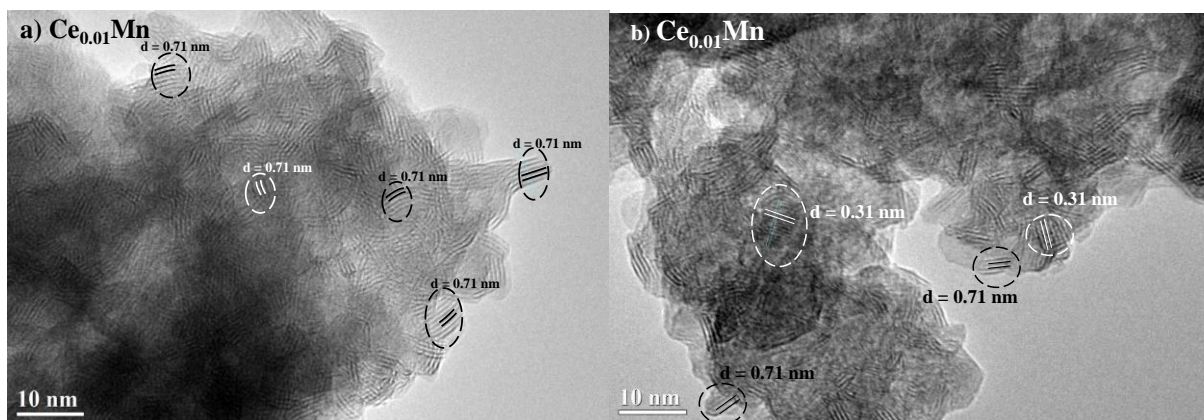


Figure 4 - 3: (a) N_2 isotherms and (b) PDS of the as-synthesized samples

The morphology and structure of the as-prepared Ce_xMn have been investigated by TEM (Figure 4 - 4). The birnessites appear as aggregates of nanosized 2D crystals. The lattice fringes of layers are mostly curved and curled. The curling aspect is indicative of a structure with high-density defects [20] ascribed to the presence of vacancies, of Mn^{x+} substitutions by Ce^{x+} and of the presence of different intercalated cations. High-resolution TEM images show lattice fringes of 0.71 nm spacing assigned to the (100) planes of the birnessite. A lattice spacing of 0.31 nm has also been observed on both Ce-doped samples even at low doping ratio (001). This spacing arises from the (111) lattice planes of CeO_2 . As a consequence, detection of CeO_2 nanocrystals even at low doping ratio, allows a close contact between CeO_2 and MnO_2 nanocrystals. Such grain boundaries have been invoked to play a role in oxygen mobility and activation of oxygen [54-59].



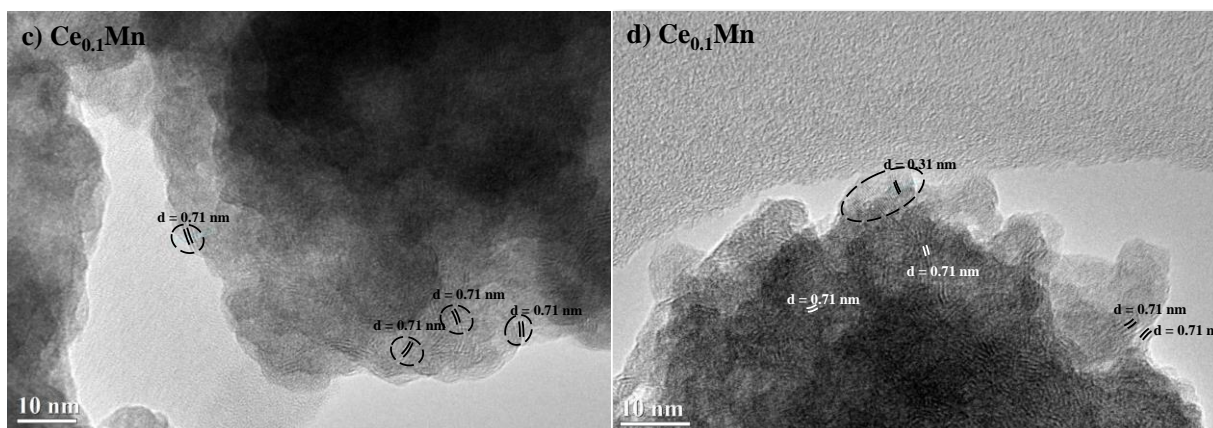


Figure 4 - 4: TEM of the fresh (a)- (b) $\text{Ce}_{0.01}\text{Mn}$ and (c)-(d) $\text{Ce}_{0.1}\text{Mn}$ catalysts.

ICP-OES results show that the doping Ce/Mn ratios are consistent with the nominal ones (**Table 4-3**). For the as-synthesized samples, the K/Mn and Na/Mn ratios of 0.35 ± 0.01 and 0.06 ± 0.01 respectively, compared to the ratio obtained by Händel *et al.* [17] 0.13 and 0.04, K/Mn is substantially higher. Different initial reactant ratios and washing procedures account for such discrepancies. These results thus leave open the possibility of mixed (Na, K)-birnessites and thermodynamic studies support this possibility [29]. Additionally, intercalated cation exchange in birnessite monitored by real-time XRD analysis has been shown to involve continuous shifts in atomic positions rather than the co-existence of end-member configurations [30] which is in contrast to the results of Putnis *et al.* [31] who postulate that exchange processes occur through dissolution of one phase and precipitation of another.

Table 4 - 3: ICP analysis of the as-synthesized samples

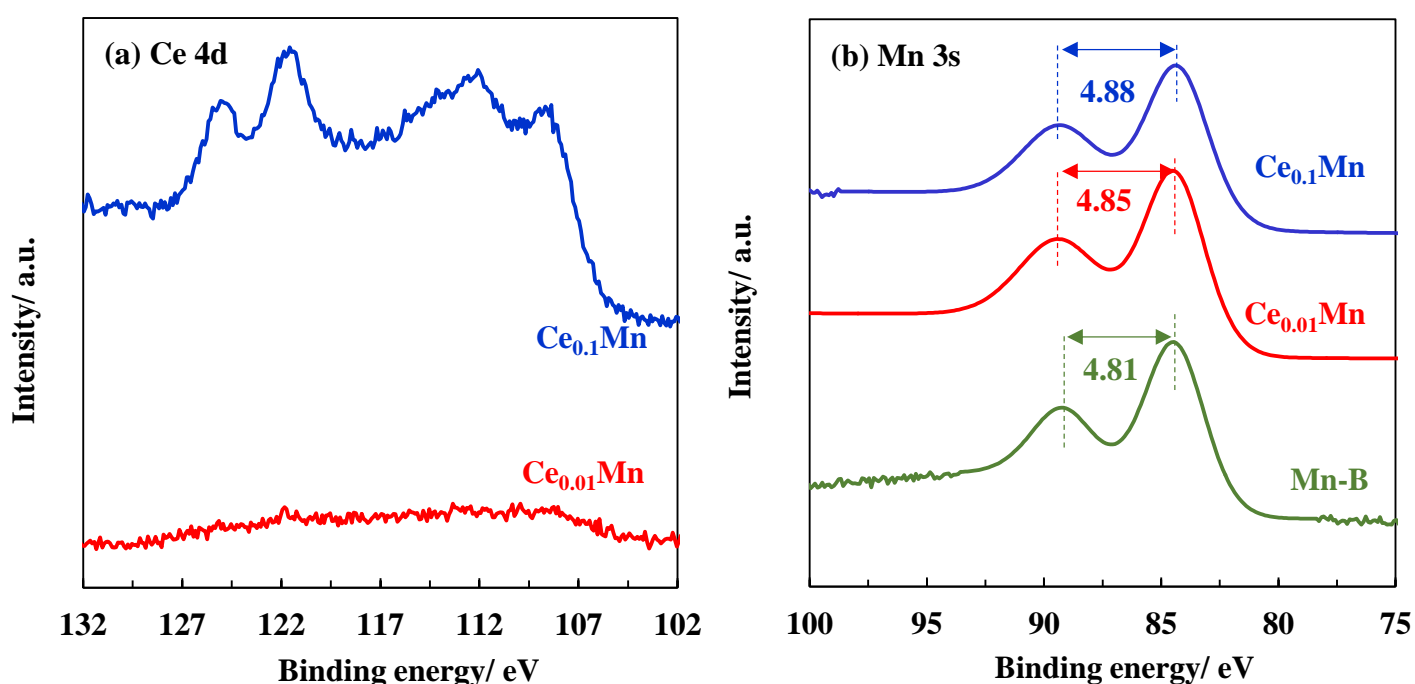
Catalyst	Weight %				Atomic %		
	K	Na	Ce	Mn	K/Mn	Na/Mn	Ce/Mn
Mn-B	7.12	1.87	-	44.1	0.39	0.059	-
$\text{Ce}_{0.01}\text{Mn}$	6.64	2.08	1.11	46.4	0.34	0.063	0.0094
$\text{Ce}_{0.1}\text{Mn}$	6.27	1.90	9.47	38.3	0.39	0.069	0.097

XPS

spectra of

the as-synthesized samples are given in **Figure 4-5**. The quantitative and qualitative results are shown in **Tables 4-4** and **4-5**, respectively. From the survey XPS spectra (**Appendix A**), Na^+ and K^+ are always detected in line with the adopted experimental redox procedure and their position are listed in **Table 4-5**. A slight enrichment of Ce is observed at the surface of the Ce-doped samples and based on the shape of the Ce 4d XPS (**Figure 4-5 a**) envelope it is qualitatively observed to be a slight $\text{Ce}^{3+}/\text{Ce}^{4+}$ decrease with increasing Ce content [32]. As explained in the experimental section Mn 2p_{3/2} has been decomposed as shown in **Fig.4-5 d**, the ratio $\text{Mn}^{3+}/\text{Mn}^{4+}$ was calculated by their peak areas and the results are shown in **Table 4-4**. The ratio $\text{Mn}^{3+}/\text{Mn}^{4+}$ decreases after doping with cerium from 0.24 to 0.17. This result is

consistent with Mn AOS calculated from the Mn3s splitting which decreases from 3.52 to 3.46 after Ce doping (**Table 4-5**). The O 1s core level of the as-synthesized samples shown in **Figure 4-5 c**, can be decomposed in three contributions at positions $P_1 = 529.7\text{-}529.4$ eV, $P_2 = 530.9\text{-}531.4$ eV and $P_3 = 533.4\text{-}533.6$ eV. O_I , O_{II} and O_{III} have been assigned to surface lattice oxygen, surface adsorbed oxygen species (such as O_2^- , O_2^{2-} , O^- , $\text{OH}^-/\text{CO}_3^{2-}$ groups) and adsorbed H_2O on the surface, respectively [33]. The O_{II}/O_I of 0.32 for Mn-B increasing to 0.59 (Ce_xMn) means much more adsorbed oxygen species and especially OH^- when Ce is added (**Table 4-4**). This high level of relative $\text{O}_{\text{adsorbed}}$ species is important as it has been generally recognized to play a key role in HCHO oxidation [4,34–37]



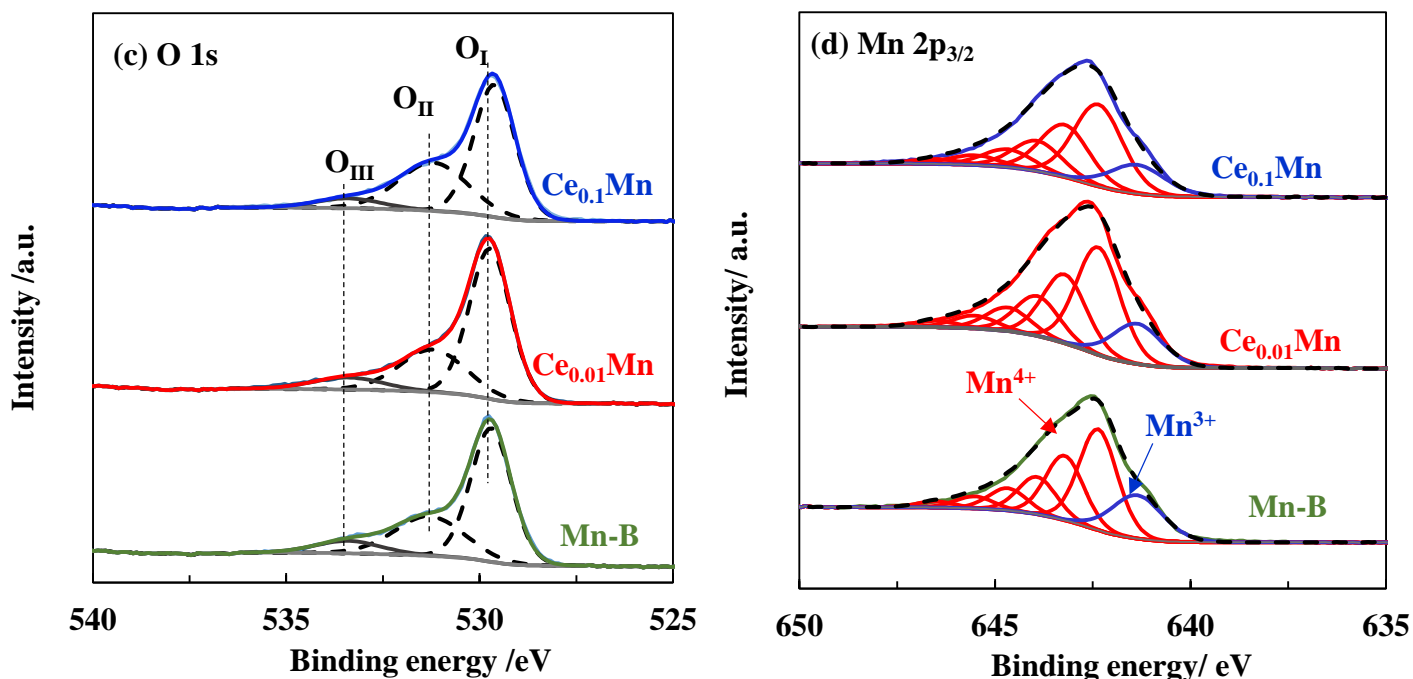


Figure 4 - 5: XPS (a) Ce 4d, (b) Mn 3s core levels (c) O1s and (d) Mn $2p_{3/2}$ for the as-synthesized samples.

Table 4 - 4: Quantified results observed by XPS analysis

Catalyst	O/Mn	K/Mn	Na/Mn	Ce/Mn	$\text{Mn}^{3+}/\text{Mn}^{4+}$	$\text{O}_{\text{II}}/\text{O}_{\text{I}}$
Mn-B	2.24	0.28	0.13	-	0.24	0.32
$\text{Ce}_{0.01}\text{Mn}$	2.13	0.24	0.12	0.016	0.18	0.48
$\text{Ce}_{0.1}\text{Mn}$	2.49	0.21	0.12	0.13	0.17	0.59

Table 4 - 5: Binding energy (eV) determined by XPS analysis

Catalyst	O_{I}	O_{II}	O_{III}	K $2p_{3/2}$ (FWHM)	K $2p_{1/2}$ (FWHM)	Na 1s	ΔE Mn3s (AOS)
Mn-B	529.7	531.4	533.4	292.5 (1.35)	295.4 (1.39)	1070.7	4.81 (3.52)
$\text{Ce}_{0.01}\text{Mn}$	529.7	531.1	533.4	292.5 (1.43)	295.3 (1.62)	1070.8	4.85 (3.49)
$\text{Ce}_{0.1}\text{Mn}$	529.6	531.2	533.4	292.6 (1.46)	295.4 (1.52)	1070.9	4.88 (3.46)

The reducibility of the as-synthesized samples has been investigated by H_2 -TPR to differentiate the activity of surface oxygen. As shown in **Figure 4-6**, the H_2 -TPR curves could be fitted into four principal peaks. The α peak at the lowest temperature represents the consumption of surface adsorbed oxygen species while, β , γ , and δ peaks correspond to the successive reductions : $\text{Na}_x\text{K}_y\text{MnO}_2 \rightarrow \text{Mn}_2\text{O}_3$ (Mn_3O_4) \rightarrow MnO [38–40]. The maximum temperature of the four peaks for the as synthesized samples are present in **Table 4-6**. For Ce_xMn , the four reduction peaks shift to lower temperature as comparing with Mn-B. However, with increasing the Ce content, α remain shifting to low temperature (LT), but γ , and δ shift to higher temperature. By cerium doping the reduction onset temperature decreases significantly.

This indicates that cerium improves the reducibility of the material leading to higher mobility of oxygen [41,42].

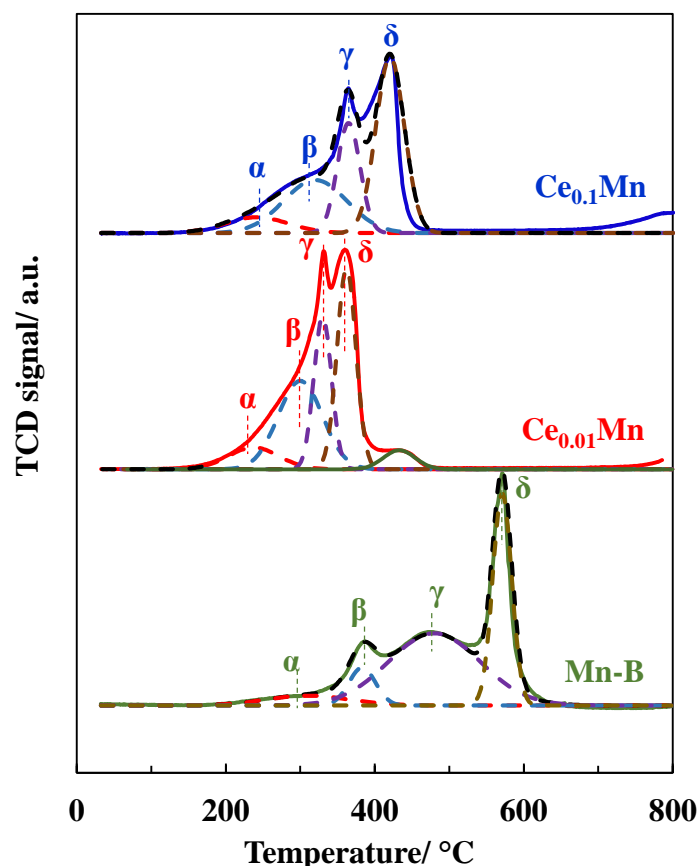


Figure 4 - 6: H_2 -TPR traces of the as-synthesized samples

Table 4 - 6 : H_2 -TPR of the as-synthesized samples

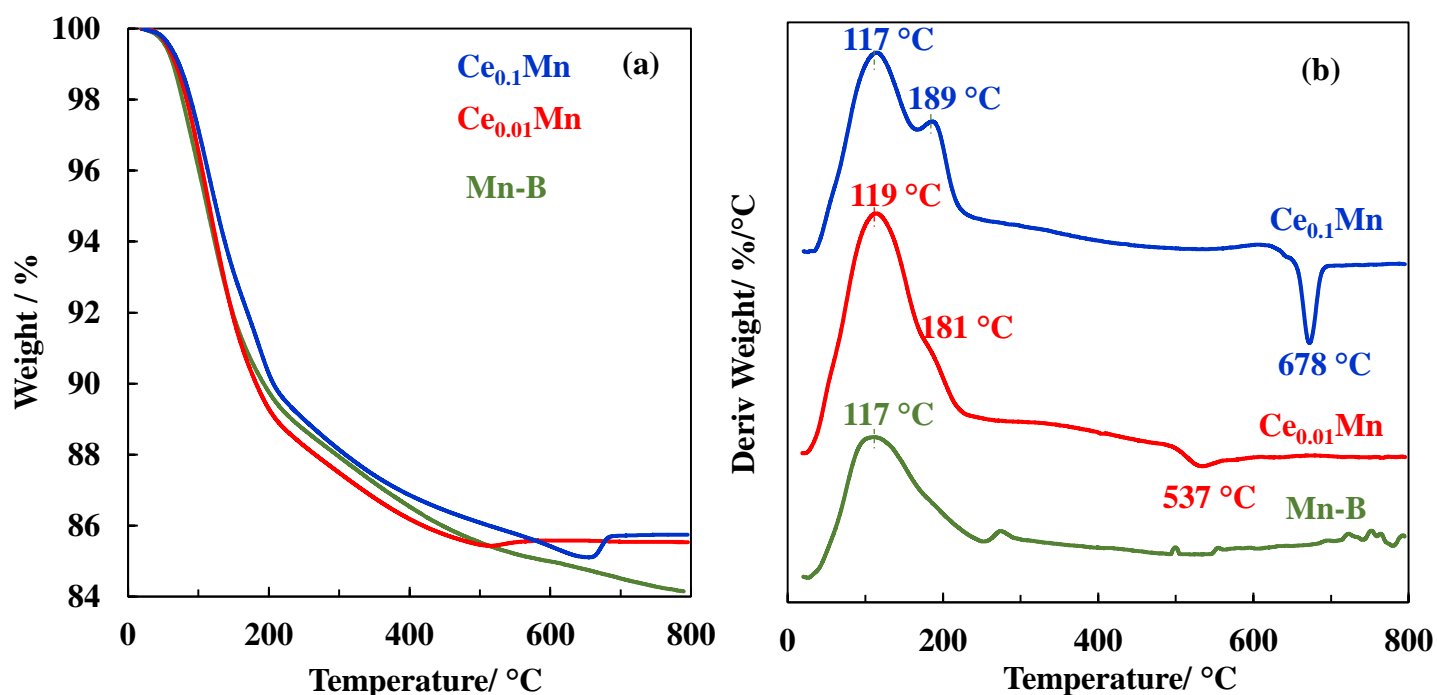
Catalyst	T_{onset}^* (°C)	Temperature peak (°C)					n (H_2) (mmol/g _{cat})
		α peak	β peak	γ peak	δ peak	λ peak	
Mn-B	250	299	388	477	516		7.55
$\text{Ce}_{0.01}\text{Mn}$	150	237	300	330	362	433	7.03
$\text{Ce}_{0.1}\text{Mn}$	170	241	320	364	420		4.93

*: onset temperature of reduction

TG/DTG/DSC analyses have been performed on the undoped and Ce-doped samples (**Figure 4-7 and Table 4-7**) in order to study their thermal stability in dry air. The TG curve (Figure 4-7-a) of Mn-B shows globally two weight losses. The first weight loss below 220°C of 10.7 wt% has been ascribed to the successive release of adsorbed and interlayer water [43] while the second one of 5.1 wt% corresponds to dehydroxylation [29] followed by oxygen release [43,44] of the MnO_6 layers in relation to the partial reduction of Mn^{4+} into Mn^{3+} up to the transformation of the birnessite into cryptomelane. The Ce-doped birnessites follow globally a similar multi-step weight loss except that a small weight gain due to O_2 uptake is

seen as usually observed for birnessite-cryptomelane transformation in air [45,46]. Interestingly, this transformation is delayed from 136 °C when increasing the Ce amount. This clearly shows that Ce doping promotes the thermal stability of the birnessite like material. Ce is either incorporated in the layer structure or it will be present on particles edges, as a consequence it can be assumed that Ce substitution of Mn reduces the content of Mn^{3+} in Ce containing layered precursors and slow triggering the transformation into tunnel structure. In contrast when the Ce content is high it can be supposed that Ce will be present on particles edges rather than incorporated into the structure and that the hydrolysis and polymerization of Ce (hydr)oxide fragments in birnessite interlayers is favored over the migration of Mn^{3+} from the layer into the interlayer leading to birnessite transformation into cryptomelane [47,48].

However, the exothermic peak around 200 °C for the as-synthesized samples could be ascribed to the release of residual organic compound (detected also by FTIR-ATR discussed above) and the additional DSC peak observed at 686 °C for $\text{Ce}_{0.01}\text{Mn}$ can be ascribed to the appearance of a cristallized K-rich birnessite as evidenced by XRD (see below). The XRD patterns recorded after TG (**Figure 4-8**) show the presence of a cryptomelane-type structure for all samples. However, for $\text{Ce}_{0.01}\text{Mn}$, the relative high intensity of the peak at approximately 12.5 ° and the emergence of an additional peak at 25.3 ° indicate the formation of a supplementary K-rich birnessite (hexagonal unit cell, space group = $\text{P6}_3/\text{mmc}$, $a = 2.84 \text{ \AA}$, and $c = 14.16 \text{ \AA}$) [49,50] previously observed through the thermal decomposition of KMnO_4 . This new phase is not observed in the XRD pattern of $\text{Ce}_{0.1}\text{Mn}$ after TG which reveals however new peaks at 33.1 °, 47.5 ° and 56.3 ° assigned to the cubic CeO_2 phase.



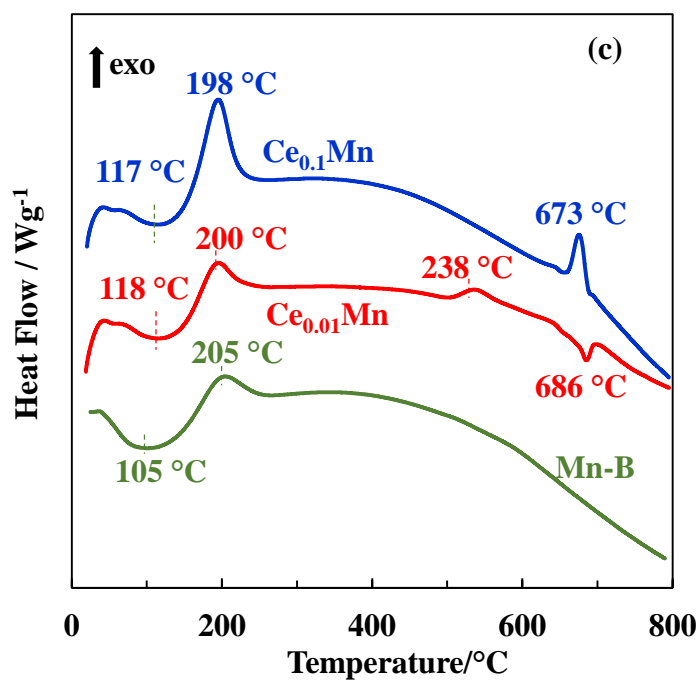


Figure 4 - 7: (a) TGA b) DTA and (c) DSC profiles for the as-synthesized samples

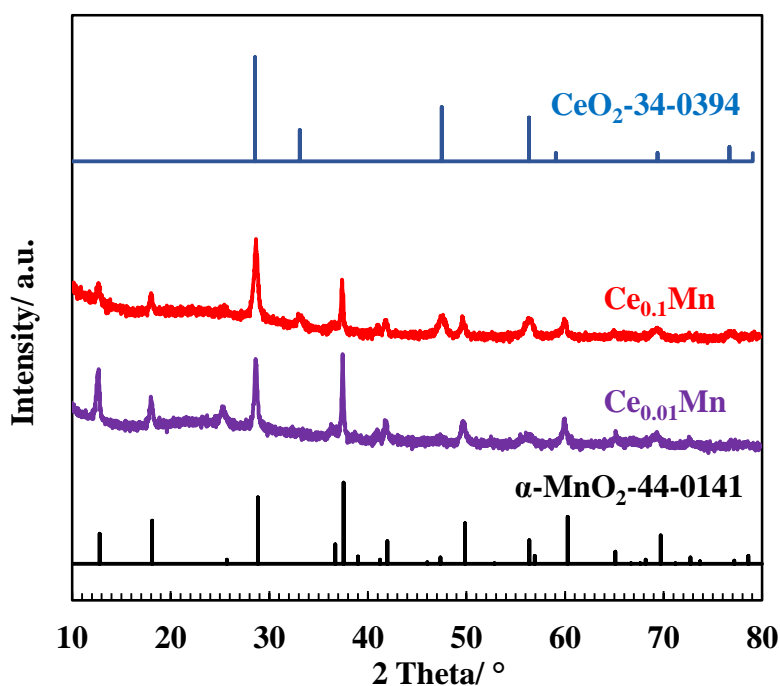


Figure 4 - 8: XRD patterns of the samples after TG analysis

Table 4 - 7: Weight loss as a function of temperature for the as-synthesized samples

Catalyst	Total loss (%)	25-220°C (100-220°C) (%)	220°C-T _t * (%)	Weight gain (%)
Mn-B	15.8	10.7 (6.8)	5.1 (-)	-
Ce _{0.01} Mn	14.4	11.1 (7.6)	3.4 (520)	0.14
Ce _{0.1} Mn	14.3	10.5 (7.3)	4.4 (680)	0.60

*: T_t: temperature of phase transformation

In order to obtain more information on the species released as a function of temperature and on the thermal behavior of birnessite, a TGA analysis under helium followed by MS was performed on $\text{Ce}_{0.1}\text{Mn}$. The signal $m/z = 44$ characterized for CO_2 shows a peak at 200 °C which can be correlated with the exothermic DSC peak indicating the release of residual organic compound which is not the case for the signal $m/z = 28$ (also characteristic for CO_2) indicating that this release of CO_2 is not very important (**Figure 4-9a**). The $m/z = 17$ and 18 signals characteristics for water confirm that the weight loss observed up to 220°C corresponds to adsorbed and interlayer water. Furthermore, as shown in **Figure 4- 9a** this water release is continuous up to 400°C which is also the case for the signal $m/z = 32$ (**Figure 4-9b**) corresponding to the release of O_2 , this indicates that it can be more correlated to the hydroxylation process. Moreover, the peak at 644°C observed with the O_2 signal is correlated to the phase transformation.

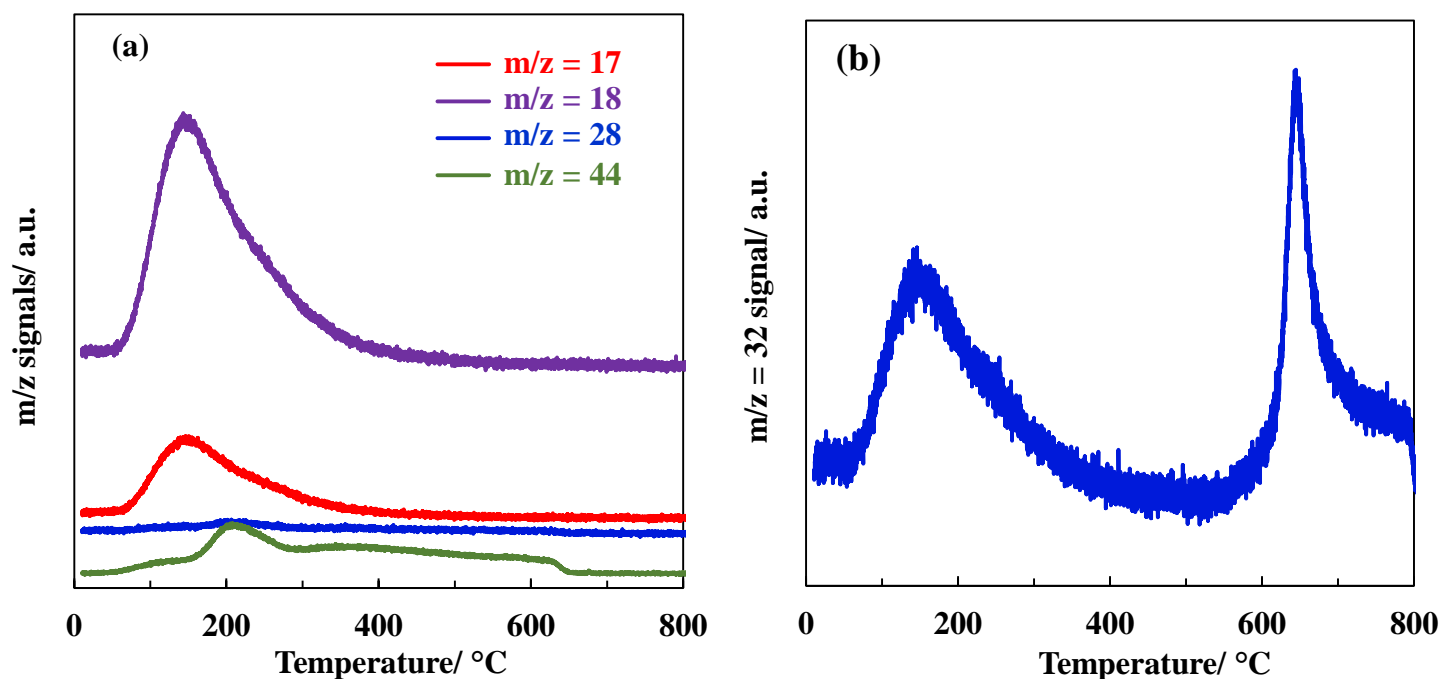


Figure 4 - 9: Temporal evolution during TGA under helium (a) of the signal $m/z = 17, 18, 28$ and 44 and (b) of the signal $m/z = 32$ for $\text{Ce}_{0.1}\text{Mn}$.

4-3-2- Characterization of the calcined samples

XRD patterns of all calcined samples (**Figure 4-10-a**) have overall similar features than those of the as-synthesized samples except $\text{Ce}_{0.01}\text{Mn}$, after calcination at 300 and 400°C, the first peak around 12° appears again. These results suggest that the birnessite structure is stable as a function of temperature. However, it is observed that the interlayer spacing decreases from

0.72 nm to 0.67 nm when calcining Mn-B and $\text{Ce}_{0.01}\text{Mn}$ at 400 °C (**Figure 4-10-b**) in accordance with the interlayer water removal.

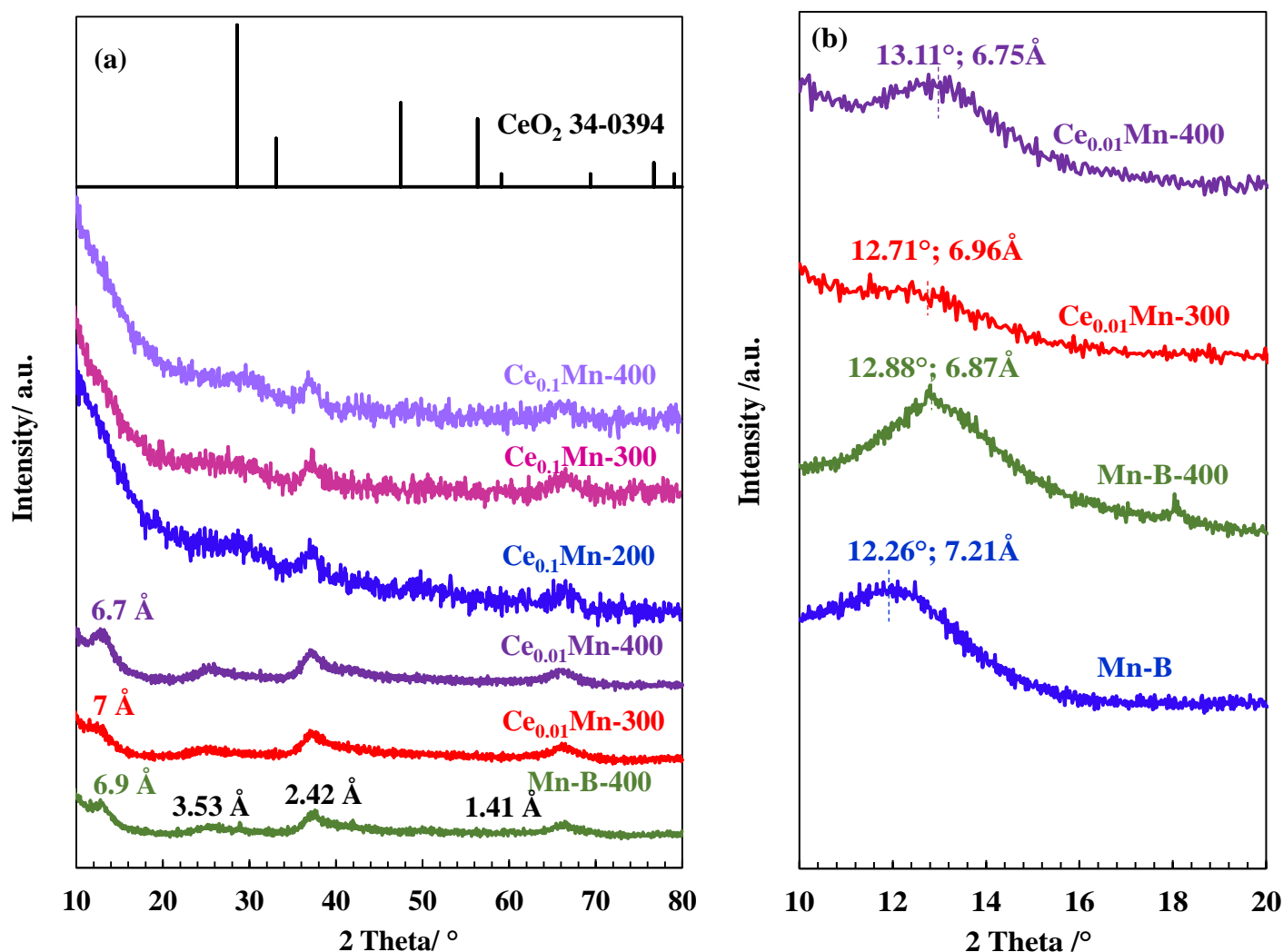


Figure 4 - 10: (a) XRD patterns for the calcined samples and (b) XRD zoom for first peak in the following analysis conditions: 10-20°, step size: 0.2°, step time: 5s

FTIR-ATR spectra of all calcined samples show a strong decrease of related (hydrogeno) carbonated impurities (**Figure 4-11**) which nonetheless cannot be totally removed from Ce-doped samples. As expected, the OH bending and stretching modes of water decrease in intensity and this decrease is most pronounced when Tc increases.

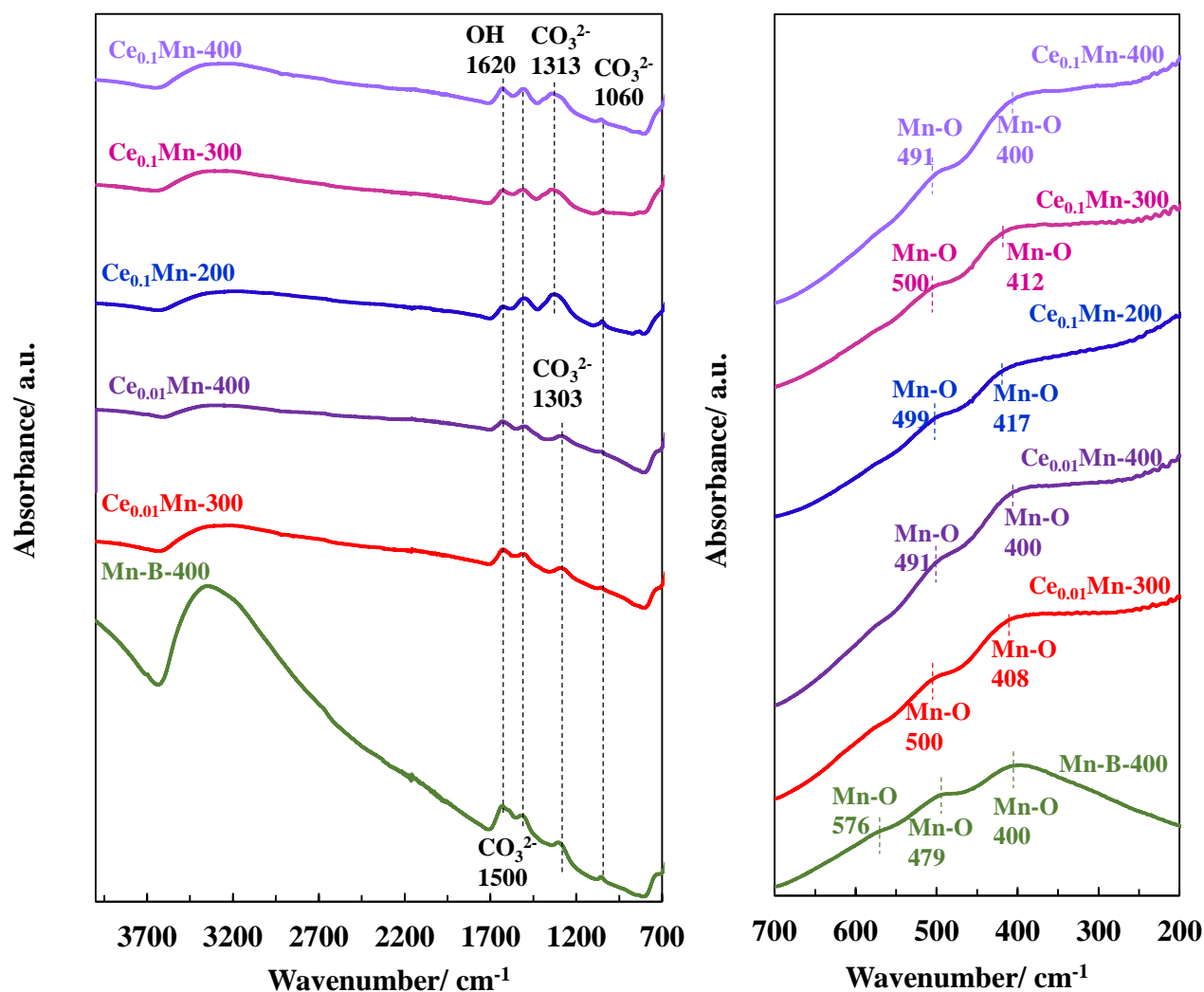


Figure 4 - 11: FTIR-ATR spectra of the calcined samples

The calcined samples have also been characterized by TG/DTG/DSC (**Figure 4-12 (a) (b) and (c)**). For $\text{Ce}_{0.01}\text{Mn}$, the total weight loss, the interlayered water as well as the dehydroxylation and oxygen release decrease linearly as the T_c increases (**Figure 4-12(d)**). However, for $\text{Ce}_{0.1}\text{Mn}$, the total weight loss decreases as a function of T_c , while the interlayered water decreases until $T_c = 300^\circ\text{C}$, and then increases with $T_c = 400^\circ\text{C}$, whereas an increase in the weight loss is observed in the dehydroxylation and oxygen release step when comparing the as-synthesized samples to $\text{Ce}_{0.1}\text{Mn-200}$ and then this loss decreases as the T_c increases. However, when increasing the Ce content, the interlayered water released decreases while the hydroxyl group and O from MnO_6 octaedra released increases. These observation hold our hypothesis that when increasing the Ce content, Ce is rather present on particle edges and that the hydrolysis and polymerization of Ce (Hydr)oxide are promoted.

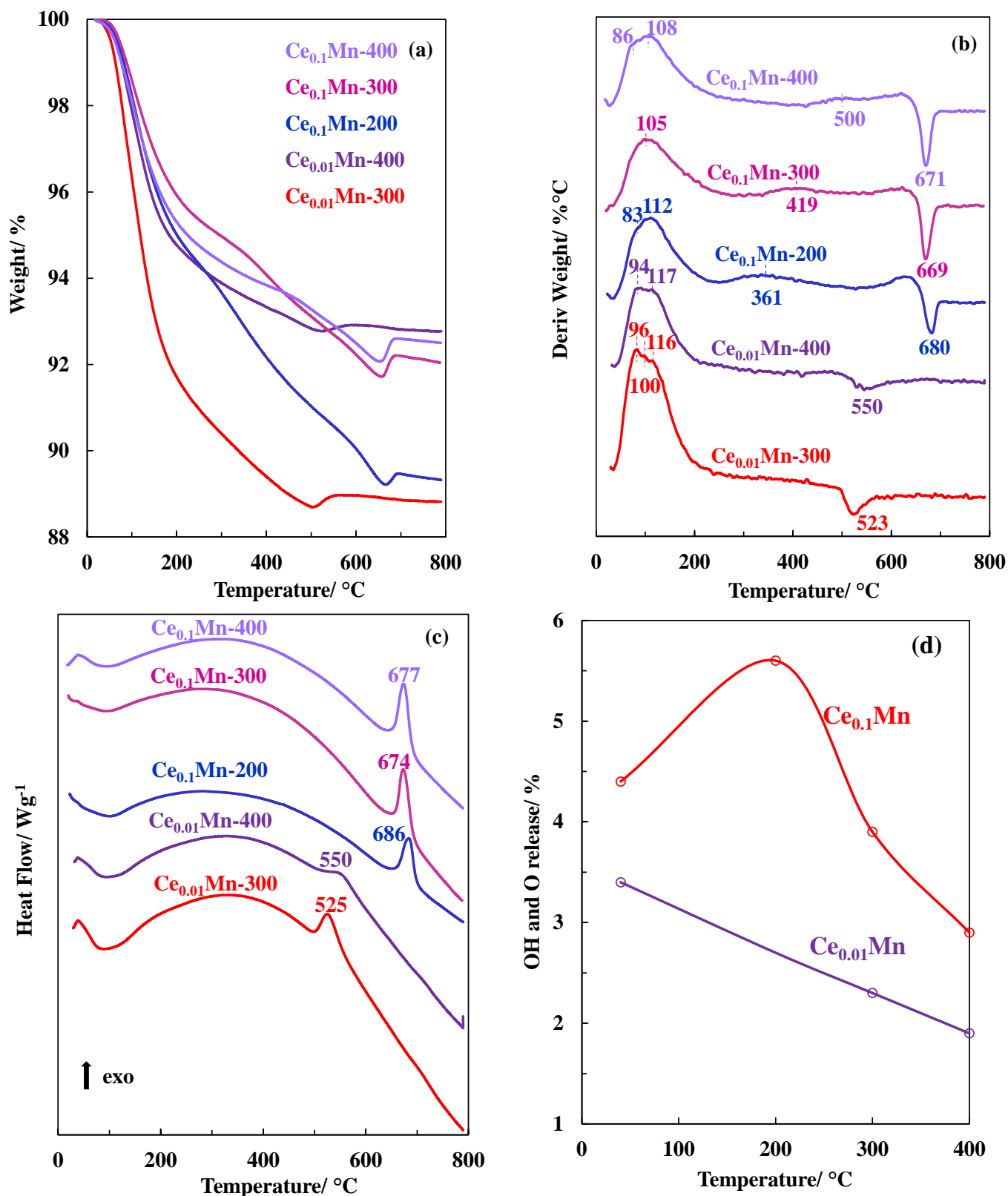


Figure 4 - 12: (a) TGA, (b) DTA and (c) DSC profiles for the calcined $\text{Ce}_{0.01}\text{Mn}$ and $\text{Ce}_{0.1}\text{Mn}$ (d) dehydroxylation and O release for $\text{Ce}_{0.01}\text{Mn}$ and $\text{Ce}_{0.1}\text{Mn}$

Table 4 - 8: Weight loss as a function of temperature for the calcined samples

Catalyst	Total loss (%)	25-220°C (100-220°C) (%)	220°C-T _i * (%)	Weight gain (%)
Ce _{0.01} Mn-300	11.0	9.0 (5.3)	2.3 (525)	0.30
Ce _{0.01} Mn-400	7.2	5.4 (4.0)	1.9 (554)	0.12
Ce _{0.1} Mn-200	10.6	5.2 (3.9)	5.6 (676)	0.23
Ce _{0.1} Mn-300	7.8	4.3 (2.8)	3.9 (670)	0.49
Ce _{0.1} Mn-400	7.4	5 (3.1)	2.9 (674)	0.52

T_i*: Temperature of phase transformation

The calcined Mn-B and Ce_{0.01}Mn samples exhibit a type IV isotherm profile with a H3 hysteresis loop as previously observed for the the as-synthesized samples (**Figure 4-13**). The BET surface area increases by a factor 3.4 for Mn-B after calcination. The BET surface area of 127 m²/g for Ce_{0.01}Mn increases to 165 m²/g and then decreases to 132 m²/g when increasing T_c from 300 °C to 400 °C, respectively. The V_p of 0.32 cm³/g decreases to 0.22 cm³/g after calcination (**Table 4-9; Figures 4-13 (b)**). The calcined Ce_{0.1}Mn samples exhibit a similar type IV isotherm profile with a H2 hysteresis loop as previously observed for the as-synthesized sample. The lower closure point is at P/P₀ ≈ 0.42 and the upper closure point increases from 0.73 to 0.87 when increasing T_c from 200 °C to 300 °C. The BET surface area of 243 m²/g for Ce_{0.1}Mn decreases to 213 m²/g to futher increases to 256 m²/g and finally decreases to 196 m²/g when increasing T_c. V_p shows a similar evolution going from 0.20 cm³/g to 0.25 cm³/g through a maximum of 30 cm³/g while D_p monotonically increases from 4 to 6 nm..

Table 4 - 9: Textural properties of the calcined samples

Catalyst	S _{BET} (m ² /g)	D _p max (nm)	V _p tot (cm ³ /g)
Mn-B-400	148	4; 6.7; 30	0.29
Ce _{0.01} Mn-300	165	4; 5	0.22
Ce _{0.01} Mn-400	132	4; 5	0.22
Ce _{0.1} Mn-200	213	4	0.20
Ce _{0.1} Mn-300	256	5	0.30
Ce _{0.1} Mn-400	196	6	0.25

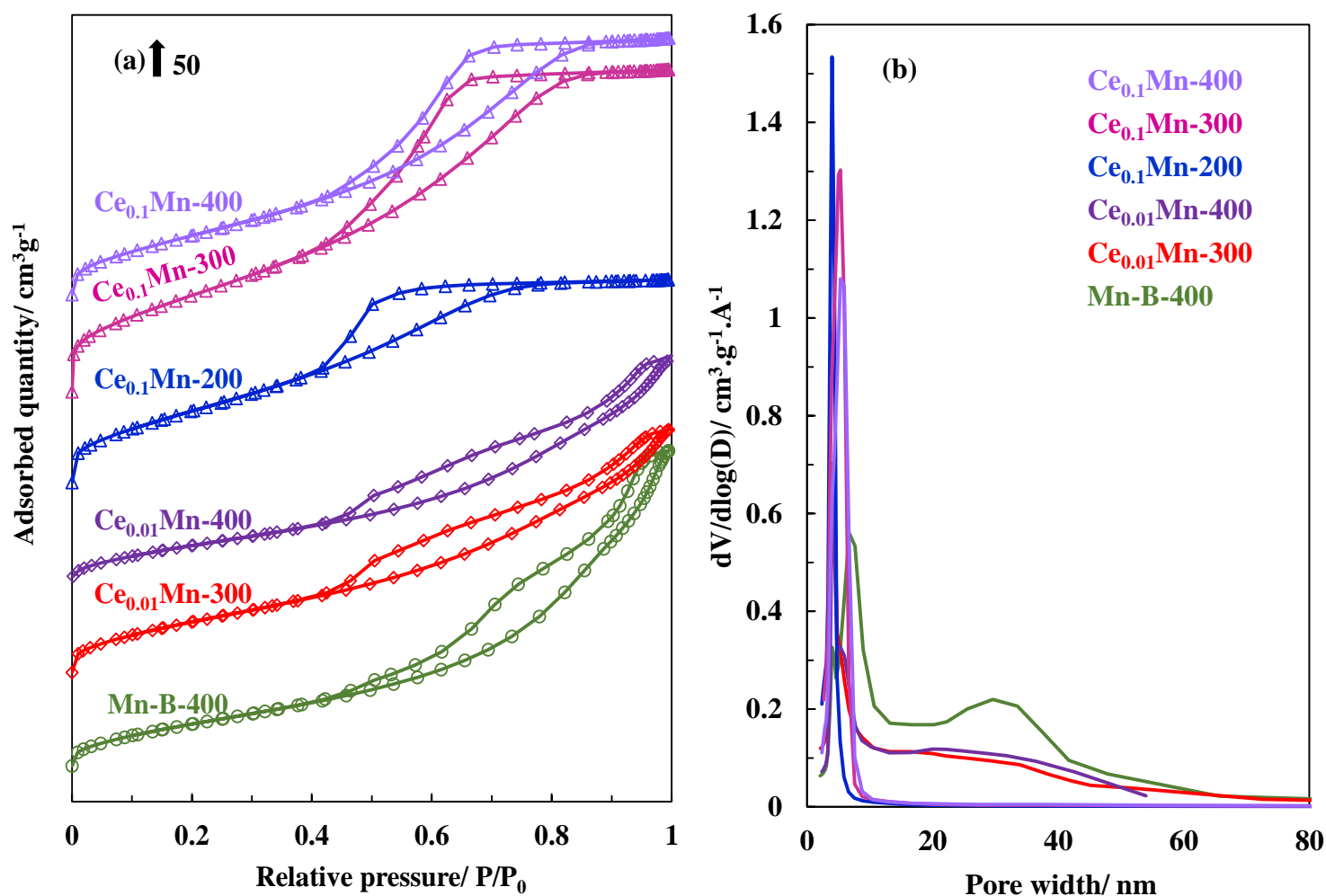


Figure 4 - 13: (a) N_2 isotherms and (b) PDS of the calcined samples

ICP-OES analysis of the calcined samples are summarized in **Table 4-10**. The results indicate that the amount of Mn and Ce increases while the amount of K and Na decreases. The K/Mn, Na/Mn and Ce/Mn ratios remain unchanged as a function of T_c in accordance with water removal because these counterions are present in the birnessite structure but in a specific hydration state [51].

Table 4 - 10: ICP analysis of the calcined samples

Catalyst	Weight %			Mn	Atomic %		
	K	Na	Ce		K/Mn	Na/Mn	Ce/Mn
Mn-B-400	8.10	2.08	-	50.2	0.39	0.058	-
$\text{Ce}_{0.01}\text{Mn-400}$	7.10	1.99	1.18	49.2	0.34	0.057	0.0091
$\text{Ce}_{0.1}\text{Mn-200}$	5.43	1.93	10.5	38.8	0.33	0.069	0.105
$\text{Ce}_{0.1}\text{Mn-300}$	5.63	1.88	10.5	41.9	0.32	0.063	0.098
$\text{Ce}_{0.1}\text{Mn-400}$	5.47	1.70	10.8	40.6	0.32	0.058	0.104

The H_2 -TPR traces of the calcined samples shown in **Figure 4-14** are significantly modified as compared to those of the as-synthesized samples. The global H_2 consumption envelope is shift to lower temperature for Mn-B-400. The H_2 -TPR traces for the calcined

Ce_xMn shift also to lower temperature with increasing T_c and the amount of the relative LT H₂ consumption is now increased. The α peak corresponding to the consumption of H₂ at low temperature became larger as the calcination temperature increase. Additionally, the consumed hydrogen amounts of the calcined samples are much higher than those of the as-synthesized catalysts, and show a maximum for Ce_{0.01}Mn-400 (9.28 mmol/g) (**Table 4-11**). In any case, the calcination step induces a decrease of the reduction onset temperature, an increase of the LT H₂ consumption and a downward shift in temperature of the peaks. Hence, the calcination step allows to improve the reducibility of the material which imply higher mobility of oxygen leading to the formation of more oxygen vacancies.

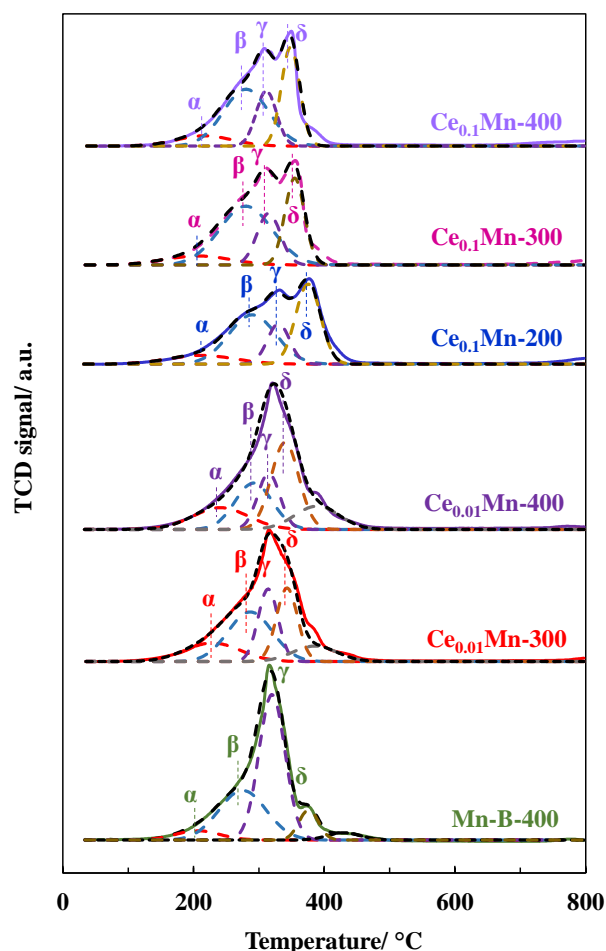


Figure 4 - 14: H₂-TPR traces of the calcined samples

Table 4 - 11: H₂-TPR of the calcined samples

Catalyst	T _{onset} [*] (°C)	Temperature peak (°C)					n (H ₂) (mmol/g _{cat})
		α peak	β peak	γ peak	δ peak	λ peak	
Mn-B-400	120	202	280	323	378		9.13
Ce _{0.01} Mn-300	110	228	286	314	343	385	9.22
Ce _{0.01} Mn-400	100	240	292	315	340	389	9.28
Ce _{0.1} Mn-200	115	212	290	330	375		7.57
Ce _{0.1} Mn-300	105	206	280	315	354		8.20
Ce _{0.1} Mn-400	105	216	280	311	348		7.65

*: Onset temperature of reduction

Raman spectra of $\text{Ce}_{0.1}\text{Mn}$ in situ and ex-situ are shown in **figure 4-15**. Two primary Raman features emerged at $573\text{-}575\text{ cm}^{-1}$ (in-plane symmetric stretching of Mn–O) and $642\text{-}645\text{ cm}^{-1}$ (out-of-plane symmetric stretching of Mn–O of MnO_6 groups) accompanied with two other contributions at 510 cm^{-1} and 732 cm^{-1} [52] for the ex situ analysis which not shift as a function of temperature. A red shift of 10 cm^{-1} and of 13 cm^{-1} is observed regarding the in-plane and out-of-plane symmetric stretching frequency respectively, when the analysis is performed in-situ and the catalyst was heated at 400°C . These shifts indicate the formation of defects in the structure due to the calcination (dehydration) [40]. However, when coming back to the room temperature, the in plane and out-of –plane stretching come back to their initial positions which can be explained by the rehydration process. This behavior is also observed by Johnson *et al.* [53]. They study the effect of temperature on the dehydration process of the birnessite by in-situ FTIR, and they found that by increasing the temperature, the water is lost and when water is totally lost they have collapse of the birnessite structure. Thus, they attest that after being fully (or almost fully) dehydrated during heating, a rehydration is observed when coming back to room temperature. The rehydration capacity depend on the type of the interlayer cations, related to its charge and size.

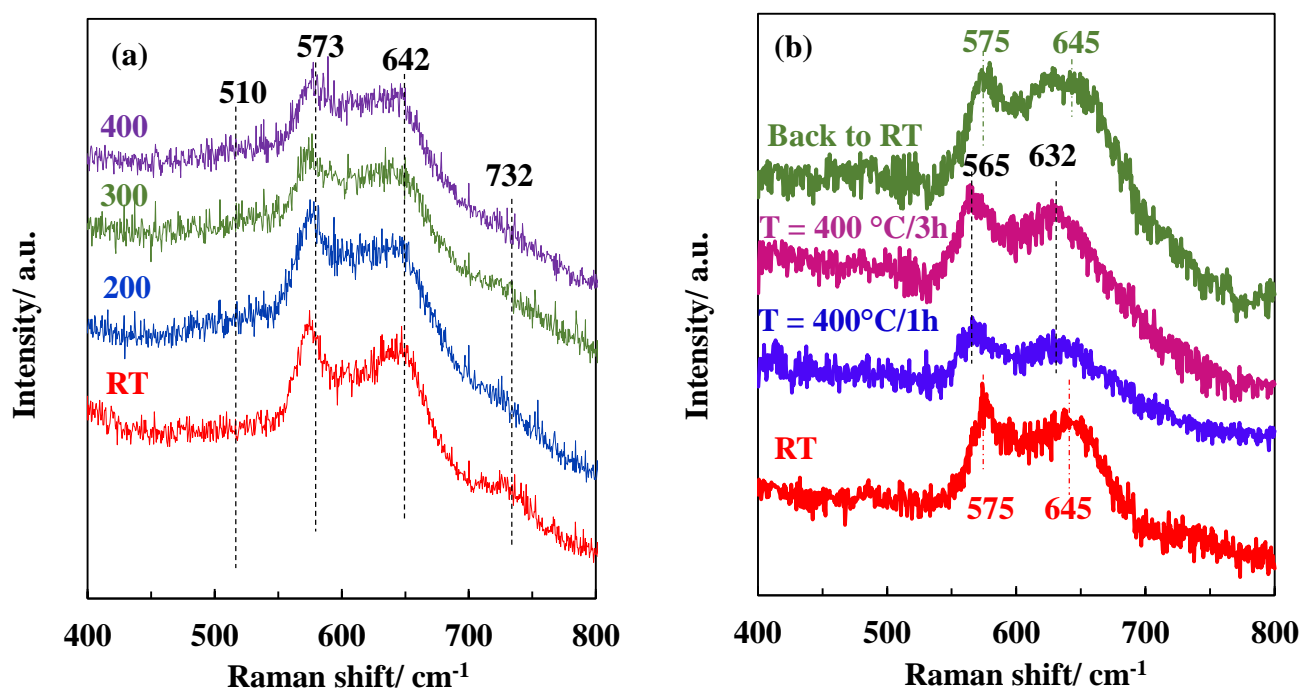


Figure 4 - 15: Raman spectra of $\text{Ce}_{0.1}\text{Mn}$ (a) ex situ as-synthesized and calcined at 200, 300 and 400°C and (b) in-situ calcined at 400°C for 1h and for 3h

O_2 -TPD was conducted to characterize the evolution of oxygen with temperature (**Figure 4-16**) for the samples calcined at 400°C . The desorption peak below 500°C , can be

ascribed to the release of chemisorbed oxygen which was formed through the conversion of surface lattice oxygen around vacancy [54]. The onset temperature (T_{onset}) of O_2 desorption for the calcined samples are present in **Table 4-12**. T_{onset} moved to lower temperature after Ce doping. The O_2 desorbed between 500 and 700 °C can be ascribed to the subsurface lattice oxygen [54]. The O_2 -desorption behavior in this temperature range for $\text{Ce}_{0.1}\text{Mn}$ calcined at 400 °C is different than Mn-B, and a new weak peak around 700 °C is observed, this phenomena is also observed with Liu *et al.* [55], which indicate the replacement of the lattice Mn by Ce ions would weaken the metal oxygen bonds, making the lattice oxygen easier to release [55,56]. However, the intense peak at 820 °C observed for Mn-B is attributed to the release of oxygen lattice [54], which shifts to low temperature (677 °C) as the Ce content increase. The desorbed O_2 content (**Table 4-12**) of Ce_xMn is higher than parent birnessite, representing better oxygen desorption ability this behavior is also observed with Guan *et al.* [56]. Combined with the above results of hydrogen consumption, it can be concluded that the highly mobile lattice oxygen species were related to the active oxygen vacancies (which increase after Ce doping) and would enhance the mobility of lattice oxygen [55–57].

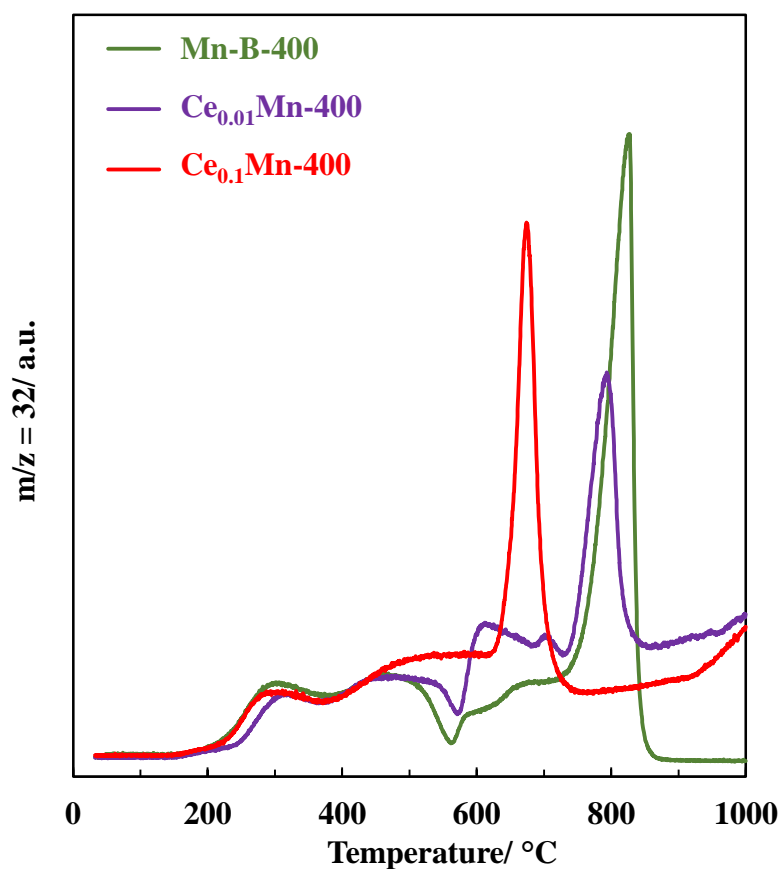


Figure 4 - 16: O_2 -TPD traces of the calcined samples at 400 °C

Table 4 - 12: O_2 -TPD quantitative analysis of the calcined samples at 400°C

Catalyst	T_{onset}^* ($^\circ\text{C}$)	$n(\text{O}_2)$ (mmol/g _{cat})	$n(\text{O}/\text{Ce}+\text{Mn})$
Mn-B-400	174	1.70	0.32
$\text{Ce}_{0.01}\text{Mn}$ -400	154	2.20	0.49
$\text{Ce}_{0.1}\text{Mn}$ -400	158	2.11	0.52

The XPS results for the calcined samples are present in **Tables 4-13 and 4-14**. As a result, if the relative proportion of Mn^{2+} is assumed to be negligible, the calculated $\text{Mn}^{3+}/\text{Mn}^{4+}$ ratio increases after calcination for Mn-B as well as for Ce_xMn (**Table 4-13, Figure 4-17-b**) which is also in line with the Mn AOS calculated from the Mn3s splitting except for $\text{Ce}_{0.1}\text{Mn}$ -400 (**Table 4-14**). As discussed in the literature, the higher $\text{Mn}^{3+}/\text{Mn}^{4+}$ ratio implies a higher content of oxygen vacancies, because once Mn^{3+} appears in the manganese dioxides, oxygen vacancies will be generated to maintain the electrostatic balance. The $\text{O}_{\text{II}}/\text{O}_{\text{I}}$ atomic ratio also decreases after calcination (**Table 4-13 and Figure 4-17-a**) except for the catalyst Mn-B-400. The enhancement of $\text{O}_{\text{II}}/\text{O}_{\text{I}}$ atomic ratio of Mn-B after calcination is consistent with a marked increase in BET surface area.

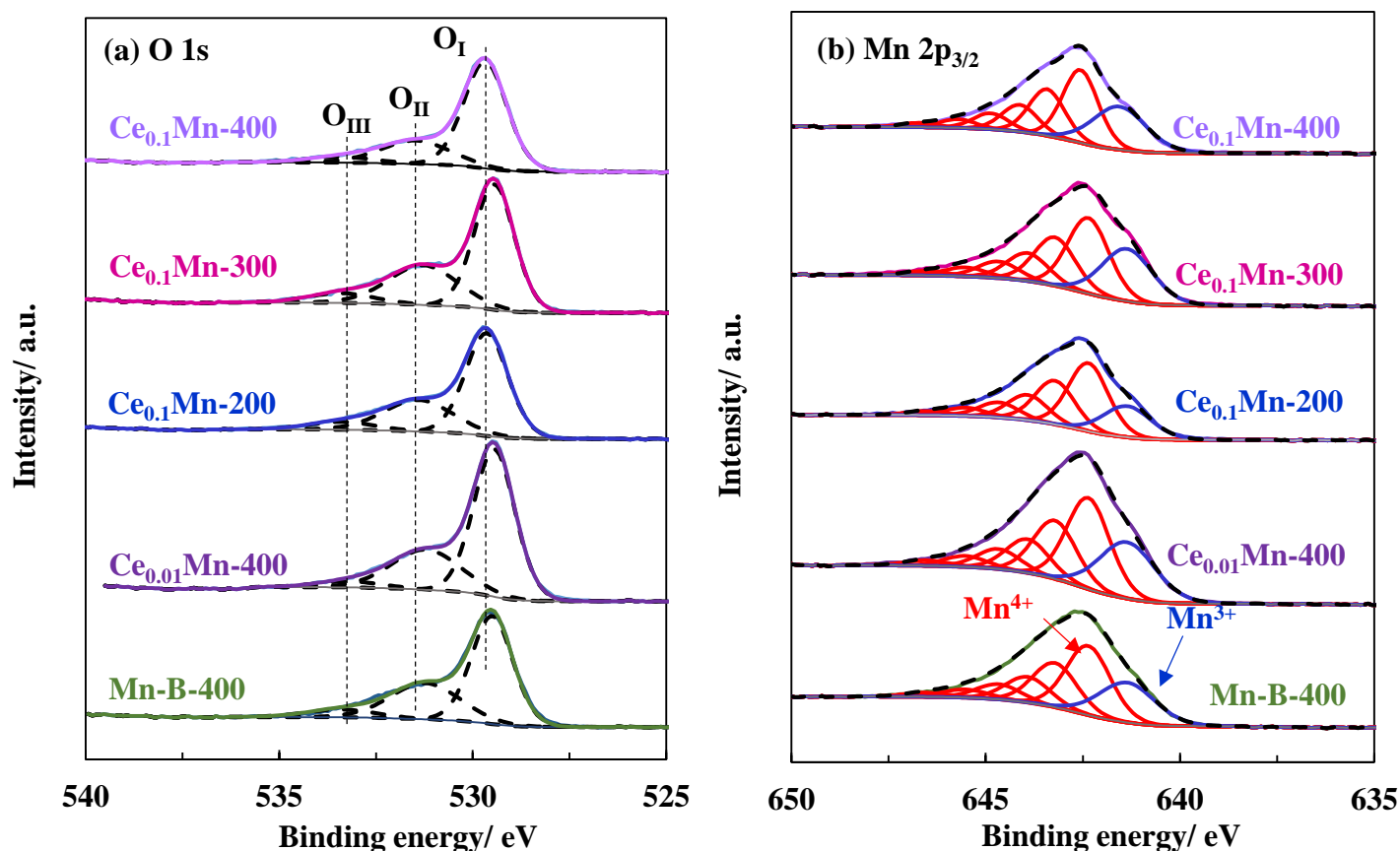


Figure 4 - 17: XPS (a) O1s and (b) Mn $2p_{3/2}$ core levels of the calcined samples

Table 4 - 13: Quantified results by XPS analysis for the calcined samples

Catalyst	O/Mn	K/Mn	Na/Mn	Ce/Mn	Mn ³⁺ /Mn ⁴⁺	O _{II} /O _I
Mn-B-400	2.13	0.24	0.089	-	0.30	0.47
Ce _{0.01} Mn-400	2.07	0.18	0.049	0.015	0.33	0.44
Ce _{0.1} Mn-200	1.65	0.16	0.071	0.11	0.23	0.56
Ce _{0.1} Mn-300	1.57	0.17	0.069	0.083	0.35	0.55
Ce _{0.1} Mn-400	2.13	0.19	0.080	0.11	0.37	0.32

Table 4 - 14: Binding energy (eV) determined by XPS analysis for the calcined samples

Catalyst	O _I	O _{II}	O _{III}	K 2p _{3/2} (FWHM)	K 2p _{1/2} (FWHM)	Na 1s	ΔE Mn3s (AOS)
Mn-B-400	529.5	531.1	533.4	292.5 (1.57)	295.3 (1.57)	1070.4	4.90 (3.44)
Ce _{0.01} Mn-400	529.6	531.2	533.2	292.5 (1.46)	295.2 (1.46)	1070.4	4.90 (3.44)
Ce _{0.1} Mn-200	529.6	531.4	533.4	292.6 (1.48)	295.4 (1.48)	1070.7	4.90 (3.44)
Ce _{0.1} Mn-300	529.4	531.3	533.4	292.4 (1.45)	295.2 (1.45)	1070.7	4.97 (3.35)
Ce _{0.1} Mn-400	529.7	531.4	533.4	292.5 (1.56)	295.3 (1.56)	1070.7	4.82 (3.52)

Static ToF-SIMS has been performed on as-synthesized Ce_xMn (x = 0.1 ; 0.01) and calcined Ce_xMn-X00 (X=4 for x = 0.01; X=2,3,4 for x=0.1) samples to get surface chemistry information (\approx 3 nm depth) [58]. For example, secondary ions related to Ce and Mn, detected in (+) and (-) polarities from all ToF-SIMS spectra, have been reported in **Table 4-16**. Irrespective of the Ce/Mn doping ratio, it is observed an increase of the secondary ion intensity Ce⁺/Mn⁺ ratio after calcination which indicates a cerium enrichment (**Table 4-15**). **Figure 4-18 a and b** shows positive ion ToF-SIMS spectra in the m/z 200-220 range for Ce_xMn-400. The secondary ions at m/z = 211 and 212 are assigned to CeMnO⁺ and CeMnOH⁺, respectively. Additionally, several secondary ions Ce_xMn_yO_zH_w^{+/-} have also been detected (**Table 4-16**) attesting of the presence of Ce-O-Mn interactions. By comparing the secondary ion intensity CeOMn^{+/} (Ce⁺+Mn⁺) ratios it is shown that the amount of Ce-O-Mn interactions increases after calcination while the variations with Tc are less sensitive. **Figure 4-18 c and d** shows positive ion ToF-SIMS spectra in the range m/z 135-160 for Ce_xMn-400. The Ce⁺ and CeO⁺ secondary ions are observed at m/z = 140 and 156 respectively. Interestingly, the secondary ion intensity CeO⁺/Ce⁺ ratio decreases strongly after calcination at 200 °C and keeps rather stable when increasing further Tc. For Ce_{0.01}Mn, the CeO⁺/Ce⁺ ratio is approximately 16 times lower after calcination at 400 °C (**Table 4-15**). These results indicate a significant lowering of the Ce³⁺/Ce⁴⁺ atomic ratio after calcination at 400 °C for low Ce doping. The secondary ions CeO₄⁺, Ce₂O₂⁺, Ce₂O₃⁺ are also detected for the Ce_{0.1}Mn derived samples as expected for CeO₂ containing samples. The absence of Ce₂O_x⁺ ions for Ce_{0.01}Mn-400 may indicate the high dispersion of Ce in the birnessite, which is in accordance with the TEM results. In addition, the identification of KNa⁺ as well as K₂NaMnO⁺ and K₂NaMnOH⁺ as secondary ions provide direct

evidence of a close interaction between potassium and sodium as interspacing cations in a mixed (Na, K)-birnessite.

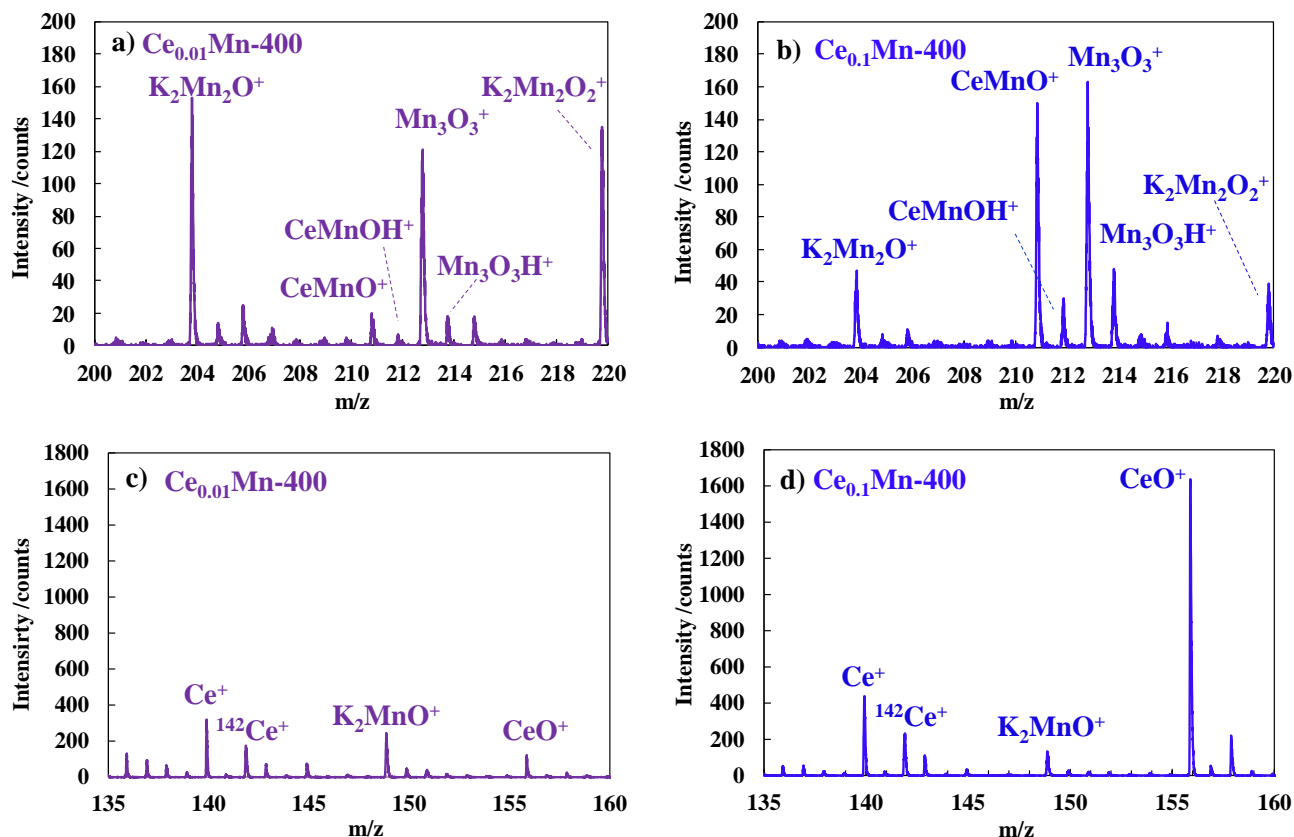


Figure 4 - 18: ToF-SIMS positive ion spectra (a) and (b) in the 200-220 m/z range and (c) and (d) in the range 135-160 m/z of $\text{Ce}_{0.01}\text{Mn-400}$ and $\text{Ce}_{0.1}\text{Mn-400}$.

Table 4 - 15: ToF-SIMS results

Catalyst	Ce^+/Mn^+	CeO^+/Ce^+	$\text{CeOMn}^+ / (\text{Ce}^+ + \text{Mn}^+) \times 10^3$
$\text{Ce}_{0.01}\text{Mn}$	0.002	5.995	0.867
$\text{Ce}_{0.01}\text{Mn-400}$	0.023	0.367	1.432
$\text{Ce}_{0.1}\text{Mn}$	0.015	13.191	7.087
$\text{Ce}_{0.1}\text{Mn-200}$	0.057	3.069	10.321
$\text{Ce}_{0.1}\text{Mn-300}$	0.029	4.750	9.262
$\text{Ce}_{0.1}\text{Mn-400}$	0.042	3.359	10.889

Table 4 - 16: Secondary ions of the positive and negative ToF-SIMS of $\text{Ce}_{0.1}\text{Mn}$ -400

	$\text{Mn}_y\text{O}_z\text{H}_w$	$\text{Ce}_x\text{O}_z\text{H}_w$	$\text{Ce}_x\text{Mn}_y\text{O}_z\text{H}_w$	$\text{K}_x\text{O}_z\text{Mn}_y\text{H}_w$	$\text{K}_x\text{Na}_p\text{O}_z\text{Mn}_y\text{H}_w$
Positive polarity	MnO	CeO	CeMnO	K_2MnO	K_2NaMnO
	MnOH	^{142}CeO	CeMnOH	KMn_2O_2	K_2NaMnOH
	Mn_2O	CeOH	CeMnO_2	$\text{K}_2\text{Mn}_2\text{O}_2$	
	Mn_3O_3	Ce_2O_2	CeMnO_3		
	$\text{Mn}_3\text{O}_3\text{H}$	Ce_2O_3	CeMnO_3H		
	Mn_4O_4	$\text{H}_2\text{Ce}_3\text{O}_3$	CeMn_2O_3		
	Mn_5O_5	Ce_3O_4	CeMn_2O_4		
	Mn_6O_6	Ce_3O_5	CeMn_3O_4		
			Ce_2MnO_4		
			CeMn_4O_5		
Negative polarity	MnO_2	CeO_2	CeMnO_4	KMn_2O_5	
	MnO_2H	CeO_2H	CeMnO_4H	$\text{K}_4\text{Mn}_4\text{OH}_2$	
	MnO_3	CeO_3	CeMn_2O_5		
	MnO_4	CeO_3H	$\text{CeMn}_2\text{O}_5\text{H}$		
	MnO_2O_2	$\text{Ce}_2\text{O}_5\text{H}$	CeMn_3O_6		
	$\text{Mn}_2\text{O}_2\text{H}$				
	Mn_2O_3				
	Mn_2O_4				
	$\text{Mn}_2\text{O}_4\text{H}$				
	Mn_2O_5				
	$\text{Mn}_2\text{O}_5\text{H}$				
	Mn_3O_5				
	$\text{Mn}_3\text{O}_5\text{H}$				
	Mn_3O_6				
	$\text{Mn}_3\text{O}_6\text{H}$				
	Mn_4O_5				
	Mn_4O_6				
	Mn_4O_7				
	Mn_5O_6				
	Mn_5O_7				

4-3-3- Catalytic activity

Figure 4-19a shows the HCHO conversion into CO_2 as a function of temperature over the catalysts calcined at 400 °C and commercial Hopcalite at a HCHO concentration of 100 ppmv and a GHSV of 60 L/(g_{cat}.h). T_{10} , T_{50} and T_{90} (corresponding to 10 %, 50 % and 90 % HCHO conversion) summarized in **Table 4-17** have been used to compare the catalyst activity. As expected, the catalytic activity for HCHO oxidation using Ce-doped samples is better than that of the parent birnessite and even better than that of the commercial Hopcalite. $\text{Ce}_{0.01}\text{Mn}$ -400 exhibits the best catalytic activity with T_{50} and T_{90} of 50 °C and 73 °C, respectively (**Figure 4-19 a**). The T_{50} of 50 °C is close to values reported in literature for the most active MnO_2 based catalysts as shown in **Table 4-18** [3,11,56,59–63]. The effect of T_c on activity has

also been investigated on the Ce-doped catalysts (**Figure 4-19 b and c**). Irrespective of the Ce/Mn ratio, the catalytic activity increases with increasing Tc until 400°C. Further increases of Tc lead to reduce the catalytic activity. In addition, to get a more accurate comparison, the apparent activation energy (E_a) has also been calculated according to the Arrhenius plot of the catalysts for HCHO oxidation (**Figure 4-19 d**). $\text{Ce}_{0.01}\text{Mn-400}$ exhibits an E_a value of 22 kJ.mol^{-1} which is less than the value of 27 kJ.mol^{-1} reported for the very active K-birnessite-type MnO_2 with moderate K^+ content [61].

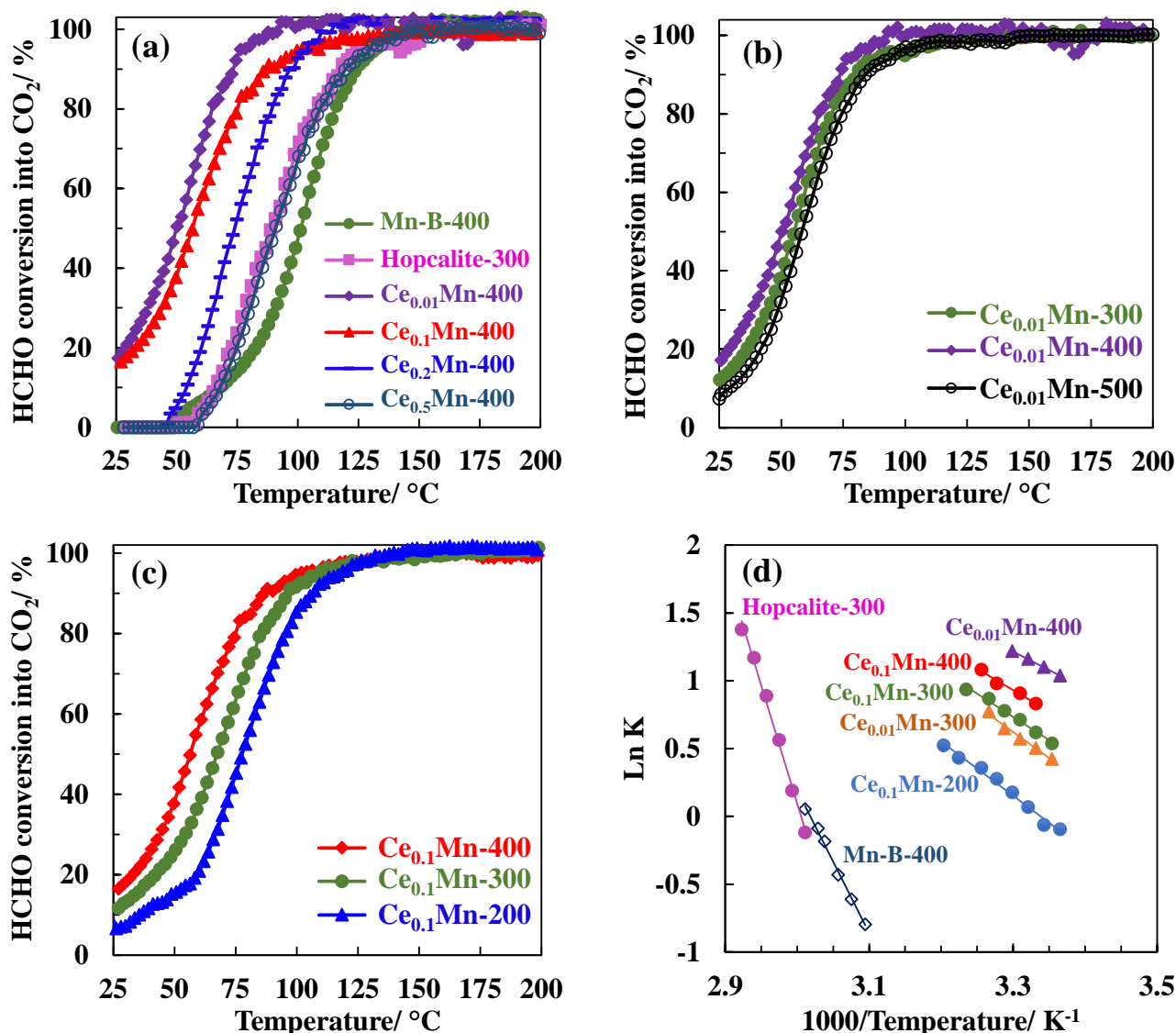


Figure 4 - 19: Light-off curves over (a) Mn-B-400, $\text{Ce}_x\text{Mn-400}$ and Hop-300; (b) $\text{Ce}_{0.01}\text{Mn-X00}$ and (c) $\text{Ce}_{0.1}\text{Mn-X00}$ catalysts. HCHO = 100 ppm, O_2 = 20%, N_2 balance, GHSV = 60 L/(gcat.h); (d) Arrhenius plot of the tested samples.

Table 4 - 17: Catalytic results

Catalyst	T ₁₀ (°C)	T ₅₀ (°C)	T ₉₀ (°C)	E _a (kJ/mol)
Mn-B-400	69	101	124	61
Ce _{0.01} Mn-300	-	56	80	32
Ce _{0.01} Mn-400	-	50	73	22
Ce _{0.1} Mn-200	37	78	107	33
Ce _{0.1} Mn-300	25	68	96	28
Ce _{0.1} Mn-400	-	56	90	26
Hopcalite-300	66	89	118	130

Table 4 - 18: Overview study for HCHO catalytic oxidation

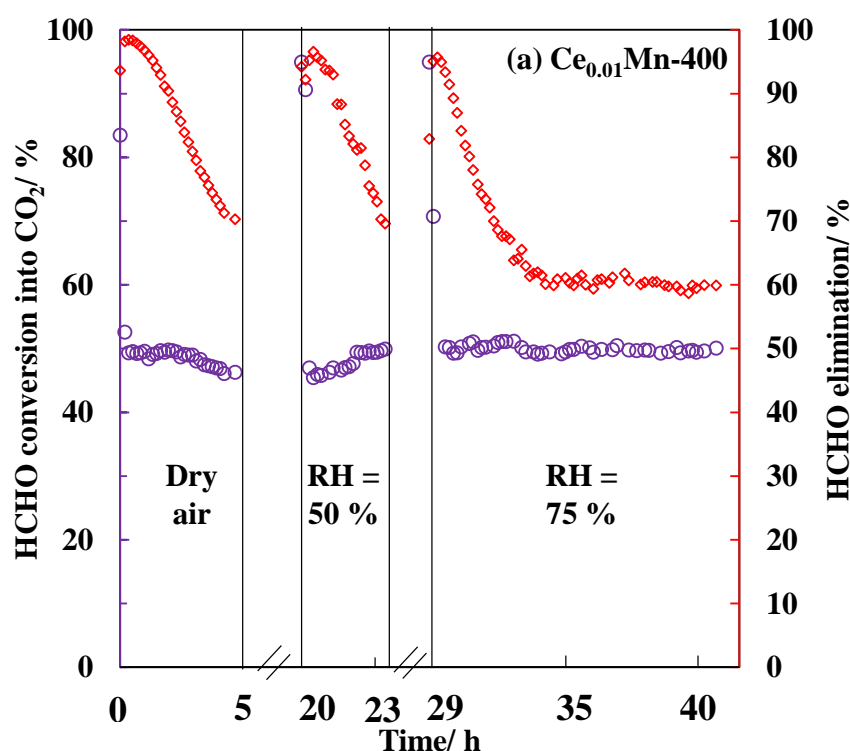
Catalyst	Test conditions	T ₅₀	T ₉₀	Ref.
Mn-B-400	100 ppm HCHO, 20 % O ₂ , N ₂ balance, GHSV ~ 60 L/ (g _{cat} .h)	101	124	Our work
Ce _{0.01} Mn-400		50	73	
Ce _{0.1} Mn-400		56	90	
Hopcalite-300		89	117	
MnO ₂	200 ppm HCHO, 21 % O ₂ , N ₂ balance, 45 % relative humidity, GHSV ~ 120 L/ (g _{cat} .h)	85	110	[57]
MnO ₂ -P1		74	97	
MnO ₂ -P2		62	86	
Birnessite (V _{Mn} -1)	40 ppm HCHO, 21 % O ₂ , N ₂ balance, 45 % relative humidity, GHSV ~ 120 L/ (g _{cat} .h)	84	107	[8]
Birnessite (V _{Mn} -2)		77	102	
Birnessite (V _{Mn} -3)		53	96	
MnO ₂	100 ppm HCHO, 21 % O ₂ , N ₂ balance, 70 % relative humidity, GHSV ~ 90 L/ (g _{cat} .h)	68	93	[58]
1K/MnO ₂		56	82	
2.5K/MnO ₂		61	87	
5K/MnO ₂		78	100	
8K/MnO ₂		86	105	
MnO ₂ (1.5)-CeO ₂	20 ppm HCHO, 20 % O ₂ , N ₂ balance, GHSV ~ 120 L/ (g _{cat} .h)	30	60	[53]
MnO _x -CeO ₂	580 ppm HCHO, 18 % O ₂ , He balance, GHSV ~ 21 L/ (g _{cat} .h)	82	90	[59]
Ce-MnO ₂ (1:10)	190 ppm HCHO, 20 % O ₂ , N ₂ balance, GHSV ~ 90 L/ (g _{cat} .h)	70	93	[37]
MnO _x -CeO ₂ (0.25)	400 ppm HCHO, 20 % O ₂ , N ₂ balance, GHSV ~ 30 L/ (g _{cat} .h)	120	140	[56]
MnO _x -CeO ₂ (CeMn80)	580 ppm HCHO, 20 % O ₂ , N ₂ balance, GHSV ~ 30 L/ (g _{cat} .h)	70	100	[60]

T₅₀: The reaction temperature corresponding to HCHO conversions of 50%

T₉₀: The reaction temperature corresponding to HCHO conversions of 90%

Besides the activity of the catalysts, stability issues should be taken into account. **Figure 4-20 a** shows the HCHO conversion and HCHO elimination as a function of time on stream at 50 °C (corresponding to 50 % HCHO conversion based on the light-off curve result) over Ce_{0.01}Mn-400 performed in three successive steps with increasing water content (%RH: 0; 50 and 75) in flowing air. The catalyst shows good stability and an excellent water-tolerance behavior, even after 13 h at high RH, maintaining its initial HCHO conversion into CO₂. Conversely, the HCHO elimination close to 100 % at the beginning of each step decreases quite

linearly for 5 h to get final values of 75 % (%RH: 0; 50) and a stabilized value of about 60 % at RH = 75 %. The higher HCHO elimination as compared to HCHO conversion into CO_2 indicates that approximately 25 %-10 % of HCHO is trapped on the surface. For $\text{Ce}_{0.1}\text{Mn-400}$ (**Figure 4-20 b**), the HCHO conversion into CO_2 drops to 25 % in 5 hours in dry air. However, when adding water, the activity is partly restored reaching 30 % HCHO conversion after 5 h at RH=50 %. The activity keeps constant when increasing RH to 75 %. As well as $\text{Ce}_{0.01}\text{Mn-400}$ the HCHO elimination also decreases gradually in dry air to remain stable over time in moist air exceeding the HCHO conversion of 15-20 %. The HCHO conversion and elimination as a function of time on stream performed at 75 °C (corresponding to T_{50}) over Hopcalite is shown in **Figure 4-21**. HCHO conversion as well as HCHO elimination gradually decrease in dry air while the catalyst is quite stable at RH=50 % achieving 37 % HCHO conversion after 60 h in moist air.



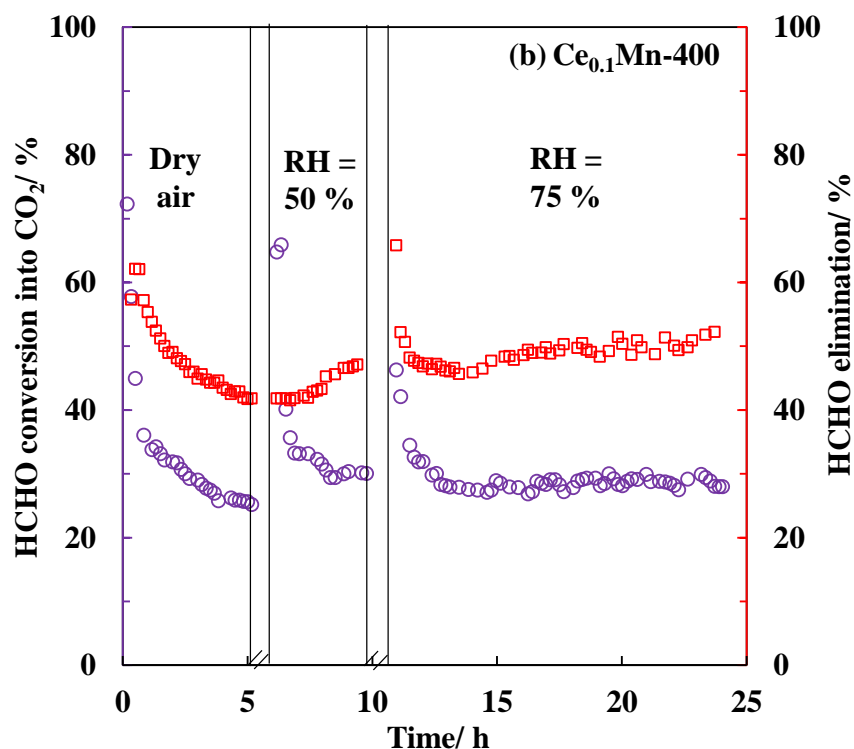


Figure 4 - 20: Effect of RH on HCHO elimination and HCHO conversion over (a) $\text{Ce}_{0.01}\text{Mn-400}$ and (b) $\text{Ce}_{0.1}\text{Mn-400}$. $T = 50^\circ\text{C}$, $\text{HCHO} = 100\text{ ppm}$, $\text{O}_2 = 20\%$, N_2 balance, $\text{GHSV} = 60\text{ L}/(\text{g}_{\text{cat}}\cdot\text{h})$.

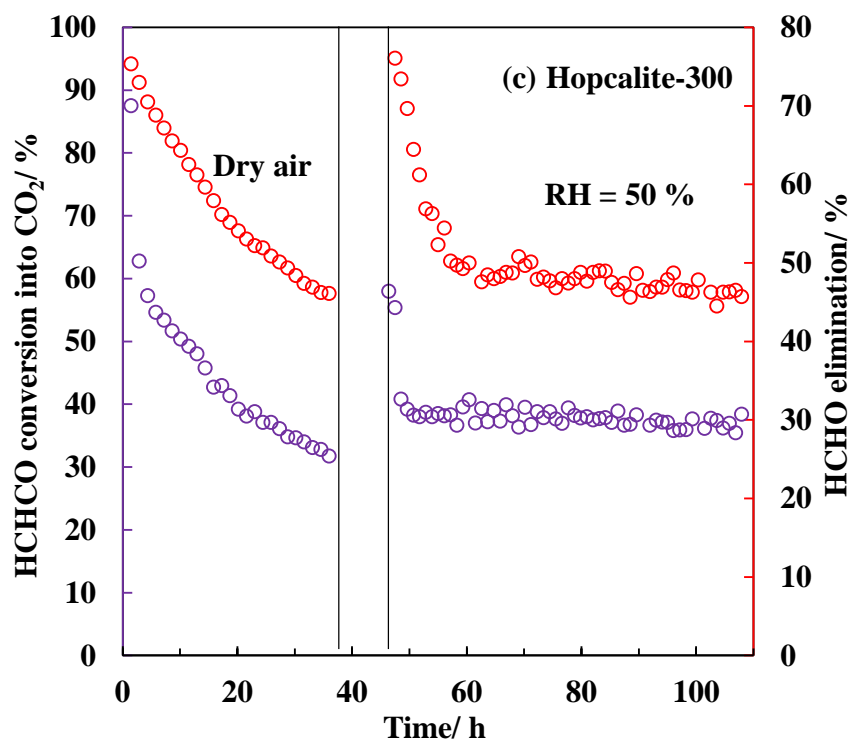


Figure 4 - 21: Effect of RH on HCHO elimination and HCHO conversion over Hopcalite. $T = 75^\circ\text{C}$, $\text{HCHO} = 100\text{ ppm}$, $\text{O}_2 = 20\%$, N_2 balance, $\text{GHSV} = 60\text{ L}/(\text{g}_{\text{cat}}\cdot\text{h})$.

In addition, in order to assess the possible participation of the catalyst oxygen in HCHO oxidation, reaction without oxygen in the feed were performed over $\text{Ce}_{0.01}\text{Mn-300}$, $\text{Ce}_{0.01}\text{Mn-}$

400 and $\text{Ce}_{0.1}\text{Mn-400}$. Experiments were conducted by saturating first the catalyst at 25°C as shown in **Figure 4-22 (a)**, then the evolution of HCHO and CO_2 were recorded as a function of temperature **Figure 4-22 (b)**. The amount of HCHO retained, desorbed and CO_2 formed are summarized in **Table 4-19**. The HCHO retained over $\text{Ce}_{0.1}\text{Mn-400}$ is the highest, while comparing $\text{Ce}_{0.01}\text{Mn}$ calcined at 300 and 400 is the same. Irrespective of the calcination temperature and Ce content, HCHO desorption occurs between 30°C and 100°C with a maximum value around 35°C . This value is lower than 50°C obtained by Selvakumar *et al.* [64] over birnessite during HCHO-TPD. However, in the temperature range $25\text{--}180^\circ\text{C}$, CO_2 concentration firstly rapidly increased, to a maximum at almost 100°C , then decreased rapidly until temperature reach 180°C , then CO_2 concentration descended gradually to a low level. Zhang *et al.* [65], explained the CO_2 behavior as follow: First the surface lattice oxygen of the catalyst participate in the oxidation of HCHO. After the surface oxygen is partly consumed, then the subsurface oxygen even the lattice oxygen gradually shift to the surface to participate in the oxidation. As the mobility of oxygen to shift from lattice to surface became lower, the rate of supplementary oxygen decreases which lead to a drop in the CO_2 formation. This study indicates that the CO_2 formed in HCHO-TPD experiments was mainly produced by the oxidation of some adsorbed HCHO or intermediates. The CO_2 concentration in the temperature range is the highest with $\text{Ce}_{0.1}\text{Mn-400}$ follow by $\text{Ce}_{0.01}\text{Mn-400}$ and then $\text{Ce}_{0.01}\text{Mn-300}$. However, it is well known that the quantity of HCHO retained, desorbed and CO_2 released are proportional to the specific surface area of the material. As a results $\text{Ce}_{0.1}\text{Mn-400}$ ($S_{\text{BET}} = 196 \text{ m}^2/\text{g}$) show better catalytic activity compared to $\text{Ce}_{0.01}\text{Mn-400}$ ($S_{\text{BET}} = 132 \text{ m}^2/\text{g}$). Whereas by increasing the calcination temperature from 300 to 400°C over the catalyst $\text{Ce}_{0.01}\text{Mn}$, the mobility of oxygen at low temperature increases. In addition to get more accurate comparison about the mobility of catalyst oxygen in the oxidation of HCHO the evolution of $n(\text{O})/n(\text{Mn}+\text{Ce})$ was calculated as a function of temperature (**figure 4-22 c and d, table 4-19**). As a result, the catalyst calcined at 400 show a higher mobility of oxygen which is in good agreement with the improvement of catalytic activity observed above as a function of T_c .

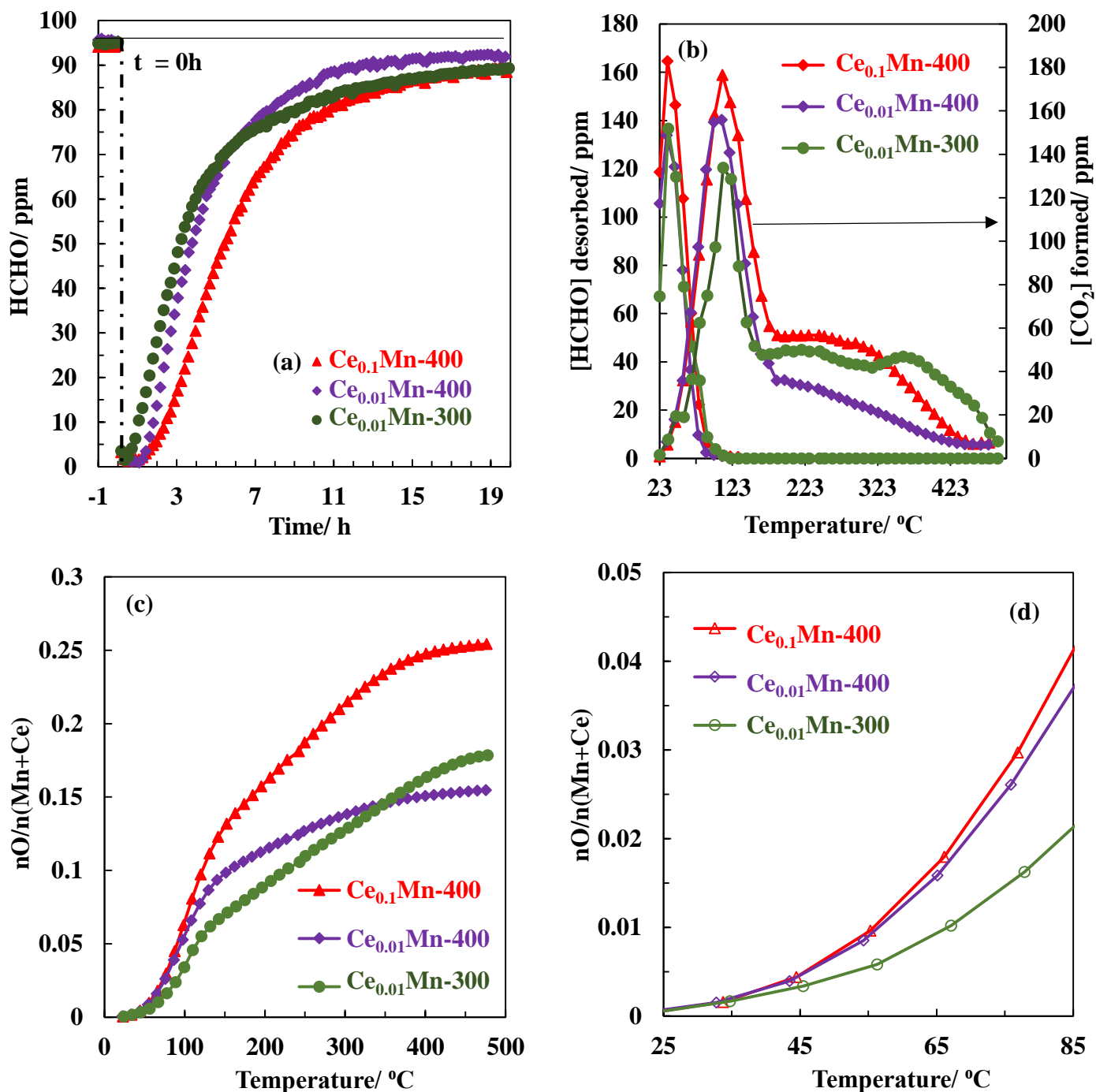


Figure 4 - 22: HCHO-TPD (a) HCHO adsorption as a function of time, (b) evolution of gaseous species (HCHO and CO_2) and (c) evolution of the atomic ratio $\text{O}/(\text{Mn}+\text{Ce})$ as a function of temperature in HCHO oxidation under helium of $\text{Ce}_{0.1}\text{Mn-400}$, $\text{Ce}_{0.01}\text{Mn-400}$ and $\text{Ce}_{0.01}\text{Mn-300}$.

Table 4 - 19: Adsorption and thermo-desorption of formaldehyde results

Catalyst	n (HCHO) _{retained} ($\mu\text{mol/g}$)	n (HCHO) desorbed ($\mu\text{mol/g}$)	n (CO ₂) _{formed} ($\mu\text{mol/g}$)	nO/n(Mn+Ce)
Ce _{0.01} Mn-300	97.34	18.5	83.1	0.18
Ce _{0.01} Mn-400	97.7	17.9	71.3	0.15
Ce _{0.1} Mn-400	131.7	23	98	0.25

To sum up Ce doped birnessite as well as the calcination step enhance the catalytic oxidation of HCHO. Low doping of Ce lead to an improvement in the textural properties in line with decreasing the material crystallinity. However, the stacked curled layers observed by TEM for Ce_xMn ensured high defective structures, and the presence of ceria nanocrystals, allows a close contact between CeO₂ and MnO₂. Thus doping with cerium increase the number of oxygen vacancies. However, As the calcination increases the Mn³⁺/Mn⁴⁺ ratio increases as evidenced by XPS analysis, and the H₂-TPR analysis show that the reducibility of the material increases which mean that the mobility of oxygen increases. In addition, the formation of Mn^{x+}-O-Ce^{y+} bonds increases and concomitantly decrease the Ce³⁺/Ce⁴⁺ atomic ratio. The local charge imbalance between the two cations is well known to promote the reactivity of oxygen in these asymmetric active sites [66–69]. However, by increasing the temperature, the phase transformation of birnessite into cryptomelane will occur. This transformation is well known that it's consistent with the high content of Mn³⁺ (almost 1/3 per layer octahedron) and then the migration of these Mn³⁺ from layer into interlayer to release the strains related to Jahn-teller distortion[47,70–73]. In our work the calcination step was performed in a condition that no phase transformation it will ensue, which mean they have migration of Mn³⁺ from layer into the interlayer but not reaching the maximum value. The migration of Mn³⁺ led to a vacant site in the layer structure. However, it is prove that the energy of the formation of oxygen vacancy will decrease if it is near to manganese vacancy. This energy will decreases also if K interlayer cation will shift near to the Mn vacancy to compensate the charge. Thus, the effect of calcination is herein to increases number of manganese and oxygen vacancies which led to a higher mobility of oxygen species may explain the higher activity of the catalyst towards HCHO oxidation. In the case of Ce_{0.01}Mn-400, the presence of numerous Mn⁴⁺-O- Ce³⁺ interactions leading to asymmetric oxygen/vacancy sites are believed to improve in that way the catalytic performance in HCHO oxidation.

To better apprehend the scheme of HCHO oxidation, infrared spectroscopic measurements have been performed after stability tests. ATR-FTIR spectra recorded after the HCHO catalytic oxidation tests are shown in **Figure 4-23**. For used Hopcalite, two intense

bands at 1570 cm^{-1} and 1320 cm^{-1} with a shoulder at 1370 cm^{-1} are found. The bands at 1570 cm^{-1} and 1370 cm^{-1} belong to formate species $\nu_s(\text{COO})$ and $\nu_{as}(\text{COO})$ [74] and the energy difference of 200 cm^{-1} is herein indicative of a bidentate formate [1]. The band at 1320 cm^{-1} is ascribed to carbonate species $\nu_s(\text{COO})$ [60]. For the used Ce_xMn catalysts overlapping bands are observed in the $1650\text{--}1250\text{ cm}^{-1}$ region which are less intense than those relative to Hopcalite. In addition, the bands at 1500 cm^{-1} and 1480 cm^{-1} already ascribed to carbonate and hydrogenocarbonate species at the surface of the fresh catalysts are again detected but with a lower intensity. These results indicate that the oxidation of HCHO generates formate species in small amounts. Less intermediates generated over Ce_xMn due to the high content of vacancies may explain their higher activity.

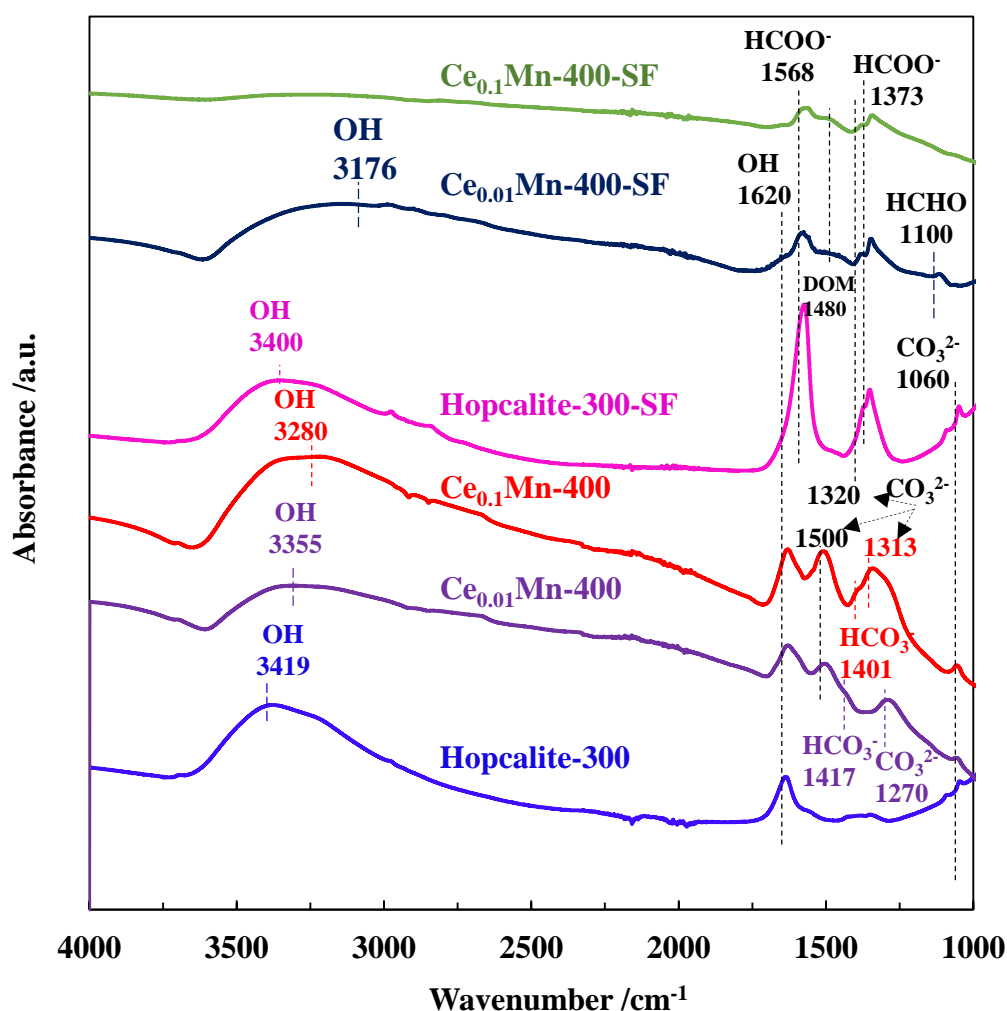


Figure 4 - 23: FTIR-ATR spectra of the fresh and used catalysts after stability tests

According to the above results, the possible reaction pathway of HCHO over Ce doped birnessite is illustrated in **Figure 4-24**. Adsorbed HCHO would be oxidized into dioxymethylene (DOM), formate, carbonate and CO_2 sequentially, via the participation of

surface oxygen and surface hydroxyl ($-\text{OH}$). No DOM peaks are observed in the FTIR spectra after test which indicates that DOM species are more quickly converted into formate. The conversion of formate is the rate determining step since formate species are the dominant intermediates. An adsorbed oxygen will be consumed for HCHO oxidation and an oxygen vacancy (V_o) will occur. Then dioxygen molecule in air would be adsorbed on V_o and dissociated: $\text{O}_2 + V_o \rightarrow \text{O}_2^- + \text{O}^-$. Due to the existence of manganese vacancy, potassium ion compensates its charge facilitating the formation of surface active oxygen, which in turn acts as the active site for HCHO oxidation. In the presence of water the catalytic activity is more stable than in dry air and that could be explained by the fact the surface hydroxyl group is replenished via the reaction with water ($\text{O}_2 + \text{H}_2\text{O} \rightarrow 2\text{OH}$)

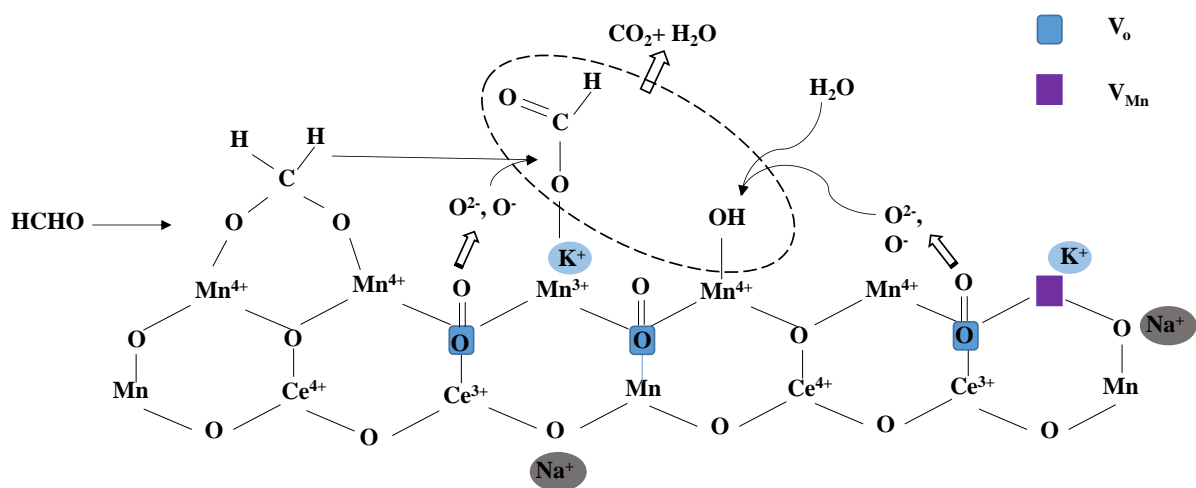


Figure 4 - 24: Scheme of the possible reaction pathway of HCHO oxidation over Ce doped birnessite

4-4- Conclusion

Cerium-doped (K, Na) birnessite type MnO_2 with low doping ratios were prepared from a simple, fast and inexpensive redox reaction using permanganate potassium and sodium lactate at ambient with addition of cerium nitrate. At these doping ratios the particle growth was inhibited and the textural properties were improved. Imbricated assemblies consisting of a few stacked curled layers ensured high defective structures and the presence of nano-ceria particles allowed an improved $\text{CeO}_2/\text{MnO}_2$ interface. Enhancement of the catalytic performances with increasing calcination temperature are due to improved local environment of the active sites linked to numerous Ce-O-Mn interactions, high atomic ratio $\text{Mn}^{3+}/\text{Mn}^{4+}$, lower $\text{Ce}^{3+}/\text{Ce}^{4+}$ balance, and high mobility of oxygen at low temperature. $\text{Ce}_{0.01}\text{Mn}$ calcined at 400 °C, which exhibited the best activity, showed a T_{50} of 50 °C for the abatement of 100 ppmv of HCHO

with a GHSV of $60 \text{ L g}_{\text{cat}}^{-1} \text{ h}^{-1}$ and outperformed commercial Hopcalite (T_{50} : 89°C). High oxygen mobility of the catalyst to participate in the oxidation of HCHO in an oxygen-free atmosphere. In addition, excellent stability of $\text{Ce}_{0.01}\text{Mn}$ -400 in the presence of water, even at high RH (75 %), confirms the potential of this catalyst for indoor depollution processes.

4-5- References

- [1] J. Wang, P. Zhang, J. Li, C. Jiang, R. Yunus, J. Kim, *Environmental Science & Technology* 49 (2015) 12372–12379.
- [2] S. Rong, P. Zhang, F. Liu, Y. Yang, *ACS Catal.* 8 (2018) 3435–3446.
- [3] L. Zhu, J. Wang, S. Rong, H. Wang, P. Zhang, *Applied Catalysis B: Environmental* 211 (2017) 212–221.
- [4] C. Zhang, F. Liu, Y. Zhai, H. Ariga, N. Yi, Y. Liu, K. Asakura, M. Flytzani-Stephanopoulos, H. He, *Angew. Chem.* 124 (2012) 9766–9770.
- [5] C. Zhang, Y. Li, Y. Wang, H. He, *Environ. Sci. Technol.* 48 (2014) 5816–5822.
- [6] G. Rochard, J.-M. Giraudon, L.F. Liotta, V. La Parola, J.-F. Lamonier, *Catal. Sci. Technol.* 9 (2019) 3203–3213.
- [7] J. Quiroz Torres, S. Royer, J.-P. Bellat, J.-M. Giraudon, J.-F. Lamonier, *ChemSusChem* 6 (2013) 578–592.
- [8] B. Bai, Q. Qiao, J. Li, J. Hao, *Chinese Journal of Catalysis* 37 (2016) 102–122.
- [9] S. Zhu, J. Wang, L. Nie, *ChemistrySelect* 4 (2019) 12085–12098.
- [10] Y. Sekine, *Atmospheric Environment* 36 (2002) 5543–5547.
- [11] J. Wang, J. Li, C. Jiang, P. Zhou, P. Zhang, J. Yu, *Applied Catalysis B: Environmental* 204 (2017) 147–155.
- [12] W. Yang, Y. Zhu, F. You, L. Yan, Y. Ma, C. Lu, P. Gao, Q. Hao, W. Li, *Applied Catalysis B: Environmental* 233 (2018) 184–193.
- [13] Q. Wang, P. Yang, M. Zhu, *Geochimica et Cosmochimica Acta* 250 (2019) 292–310.
- [14] N. Ma, S. Kosasang, P. Chomkhuntod, S. Duangdangchote, N. Phattharasupakun, W. Klysubun, M. Sawangphruk, *Journal of Power Sources* 455 (2020) 227969.
- [15] Y. Lou, X.-M. Cao, J. Lan, L. Wang, Q. Dai, Y. Guo, J. Ma, Z. Zhao, Y. Guo, P. Hu, G. Lu, *Chem. Commun.* 50 (2014) 6835–6838.
- [16] V.A. Drits, E. Silvester, A.I. Gorshkov, A. Manceau, *American Mineralogist* 82 (1997) 946–961.
- [17] M. Händel, T. Rennert, K.U. Totsche, *Geoderma* 193–194 (2013) 117–121.
- [18] K.L. Holland, *Clays and Clay Minerals* 44 (1996) 744–748.
- [19] S. Grangeon, A. Fernandez-Martinez, F. Claret, N. Marty, C. Tournassat, F. Warmont, A. Gloter, *Chemical Geology* 459 (2017) 24–31.
- [20] S. Lee, H. Xu, W. Xu, X. Sun, *Acta Crystallogr B Struct Sci Cryst Eng Mater* 75 (2019) 591–598.
- [21] C.M. Julien, M. Massot, C. Poinsignon, *Spectrochimica Acta Part A: Molecular and Biomolecular Spectroscopy* 60 (2004) 689–700.
- [22] E.A. Johnson, J.E. Post, *American Mineralogist* 91 (2006) 609–618.
- [23] S. Royer, D. Duprez, S. Kaliaguine, *Journal of Catalysis* 234 (2005) 364–375.

- [24] R. Vidruk, M.V. Landau, M. Herskowitz, M. Talianker, N. Frage, V. Ezersky, N. Froumin, *Journal of Catalysis* 263 (2009) 196–204.
- [25] H. Hojo, T. Mizoguchi, H. Ohta, S.D. Findlay, N. Shibata, T. Yamamoto, Y. Ikuhara, *Nano Lett.* 10 (2010) 4668–4672.
- [26] Q. Fu, W.-X. Li, Y. Yao, H. Liu, H.-Y. Su, D. Ma, X.-K. Gu, L. Chen, Z. Wang, H. Zhang, B. Wang, X. Bao, *Science* 328 (2010) 1141–1144.
- [27] M. Sakai, Y. Nagai, Y. Aoki, N. Takahashi, *Applied Catalysis A: General* 510 (2016) 57–63.
- [28] W. Gac, G. Słowik, W. Zawadzki, *Applied Surface Science* 370 (2016) 536–544.
- [29] N. Birkner, A. Navrotsky, *Proc Natl Acad Sci USA* 114 (2017) E1046–E1053.
- [30] C.L. Lopano, P.J. Heaney, J.E. Post, J. Hanson, S. Komarneni, *American Mineralogist* 92 (2007) 380–387.
- [31] A. Putnis, *Mineral. Mag.* 66 (2002) 689–708.
- [32] D.R. Mullins, S.H. Overbury, D.R. Huntley, *Surface Science* 409 (1998) 307–319.
- [33] T. Mathew, K. Suzuki, Y. Ikuta, N. Takahashi, H. Shinjoh, *Chem. Commun.* 48 (2012) 10987.
- [34] H. Over, *Science* 297 (2002) 2003–2005.
- [35] L. Nie, J. Yu, X. Li, B. Cheng, G. Liu, M. Jaroniec, *Environ. Sci. Technol.* 47 (2013) 2777–2783.
- [36] B. Bai, J. Li, *ACS Catal.* 4 (2014) 2753–2762.
- [37] B.-B. Chen, X.-B. Zhu, Y.-D. Wang, L.-M. Yu, J.-Q. Lu, C. Shi, *Catalysis Today* 281 (2017) 512–519.
- [38] Y. Yang, J. Huang, S. Zhang, S. Wang, S. Deng, B. Wang, G. Yu, *Applied Catalysis B: Environmental* 150–151 (2014) 167–178.
- [39] P. Hu, Z. Amghouz, Z. Huang, F. Xu, Y. Chen, X. Tang, *Environ. Sci. Technol.* 49 (2015) 2384–2390.
- [40] X. Wang, W. Huo, Y. Xu, Y. Guo, Y. Jia, *New J. Chem.* 42 (2018) 13803–13812.
- [41] Y. Wang, H. Liu, P. Hu, Z. Huang, J. Gao, F. Xu, Z. Ma, X. Tang, *Catal Lett* 145 (2015) 1880–1884.
- [42] Y. Chen, Z. Huang, P. Hu, J. Chen, X. Tang, *Catalysis Communications* 75 (2016) 74–77.
- [43] A.-C. Gaillot, B. Lanson, V.A. Drits, *Chem. Mater.* 17 (2005) 2959–2975.
- [44] R. Chen, P. Zavalij, M.S. Whittingham, (n.d.) 6.
- [45] M.A. Cheney, P.K. Bhowmik, S. Qian, S.W. Joo, W. Hou, J.M. Okoh, *Journal of Nanomaterials* 2008 (2008) 1–8.
- [46] M.A. Cheney, P.K. Bhowmik, S. Moriuchi, M. Villalobos, S. Qian, S.W. Joo, *Journal of Nanomaterials* 2008 (2008) 1–9.
- [47] A.L. Atkins, *Geochimica et Cosmochimica Acta* (2016) 26.
- [48] Z. Wu, *Geochimica et Cosmochimica Acta* (2020) 20.
- [49] S.H. Kim, S.J. Kim, S.M. Oh, *Chem. Mater.* 11 (1999) 557–563.

- [50] A.-C. Gaillot, D. Flot, V.A. Drits, A. Manceau, M. Burghammer, B. Lanson, *Chem. Mater.* 15 (2003) 4666–4678.
- [51] W. Cheng, J. Lindholm, M. Holmboe, N.T. Luong, A. Shchukarev, E.S. Iltton, K. Hanna, J.-F. Boily, *Langmuir* 37 (2021) 666–674.
- [52] C. Julien, *Solid State Ionics* 159 (2003) 345–356.
- [53] E.A. Johnson, J.E. Post, *American Mineralogist* 91 (2006) 609–618.
- [54] J. Ji, X. Lu, C. Chen, M. He, H. Huang, *Applied Catalysis B: Environmental* 260 (2020) 118210.
- [55] Y. Liu, H. Zhou, R. Cao, T. Sun, W. Zong, J. Zhan, L. Liu, *Materials Chemistry and Physics* 221 (2019) 457–466.
- [56] S. Guan, Q. Huang, J. Ma, W. Li, A.T. Ogunbiyi, Z. Zhou, K. Chen, Q. Zhang, *Ind. Eng. Chem. Res.* 59 (2020) 596–608.
- [57] J. Ma, X. Li, C. Zhang, Q. Ma, H. He, *Applied Catalysis B: Environmental* 264 (2020) 118498.
- [58] L.-T. Weng, *Applied Catalysis A: General* 474 (2014) 203–210.
- [59] J. Quiroz, J.-M. Giraudon, A. Gervasini, C. Dujardin, C. Lancelot, M. Trentesaux, J.-F. Lamonier, *ACS Catal.* 5 (2015) 2260–2269.
- [60] J. Wang, G. Zhang, P. Zhang, *J. Mater. Chem. A* 5 (2017) 5719–5725.
- [61] S. Rong, K. Li, P. Zhang, F. Liu, J. Zhang, *Catal. Sci. Technol.* 8 (2018) 1799–1812.
- [62] X. Tang, Y. Li, X. Huang, Y. Xu, H. Zhu, J. Wang, W. Shen, *Applied Catalysis B: Environmental* 62 (2006) 265–273.
- [63] X. Liu, J. Lu, K. Qian, W. Huang, M. Luo, *Journal of Rare Earths* 27 (2009) 418–424.
- [64] S. Selvakumar, N. Nuns, M. Trentesaux, V.S. Batra, J.-M. Giraudon, J.-F. Lamonier, *Applied Catalysis B: Environmental* 223 (2018) 192–200.
- [65] J. Zhang, Y. Li, L. Wang, C. Zhang, H. He, *Catalysis Science & Technology* 5 (2015) 2305–2313.
- [66] K. Yu, L. Lou, S. Liu, W. Zhou, *Adv. Sci.* 7 (2020) 1901970.
- [67] G.E. Murgida, V. Ferrari, M.V. Ganduglia-Pirovano, A.M. Llois, *Phys. Rev. B* 90 (2014) 115120.
- [68] P. Zhang, H. Lu, Y. Zhou, L. Zhang, Z. Wu, S. Yang, H. Shi, Q. Zhu, Y. Chen, S. Dai, *Nat Commun* 6 (2015) 8446.
- [69] S. Ramana, B.G. Rao, P. Venkataswamy, A. Rangaswamy, B.M. Reddy, *Journal of Molecular Catalysis A: Chemical* 415 (2016) 113–121.
- [70] A.L. Atkins, S. Shaw, C.L. Peacock, *Geochimica et Cosmochimica Acta* 144 (2014) 109–125.
- [71] S. Grangeon, B. Lanson, M. Lanson, *Acta Crystallogr B Struct Sci Cryst Eng Mater* 70 (2014) 828–838.
- [72] S. Grangeon, B. Lanson, M. Lanson, *Structural sciences engineering ND materials* 16 (2015) 828–838.

- [73] M.R. Jo, Y. Kim, J. Yang, M. Jeong, K. Song, Y.-I. Kim, J.-M. Lim, M. Cho, J.-H. Shim, Y.-M. Kim, W.-S. Yoon, Y.-M. Kang, *Nat Commun* 10 (2019) 3385.
- [74] Y. Zhang, M. Chen, Z. Zhang, Z. Jiang, W. Shangguan, H. Einaga, *Catalysis Today* 327 (2019) 323–333.

Chapter 5:
**OZONE AND NITROGEN OXIDE FORMATION THROUGH
10 PIN-TO-PLATE NEGATIVE DC CORONA DISCHARGE**

5-1- Introduction

Non-Thermal Plasma (NTP) technology has been investigated since several decades for the abatement of diluted (< 1000 ppmv) Volatile Organic Compounds (VOCs) present in waste gas and indoor air [1]. The use of atmospheric pressure NTP working at $20\text{ }^{\circ}\text{C}$ has several advantages for air pollution control resulting from its operating conditions, quick start-up and low cost technology. NTP is an attractive technology in such a way that the energy delivered to the plasma allows to get very energetic electrons while the temperature of the gas keeps at ambient. These highly accelerated electrons trigger multiple chemical processes such as excitation, ionization and dissociation of background molecules (N_2/O_2) enabling an efficient decomposition of the VOC. However, this high reactivity towards VOC removal is tempered by a low selectivity into $\text{CO}_2/\text{H}_2\text{O}$ and the production of toxic by-products such as nitrogen oxides, O_3 and other gaseous harmful VOCs cannot be discarded [2,3]. Since these two last decades NTP technology has partly regained interest through Post-Plasma catalysis (PPC) which results from the combination of NTP technology and heterogeneous catalysis. Two reactors are connected in series. In that configuration the catalytic reactor is located downstream of the plasma reactor. This resulting hybrid technology can overpass NTP and total oxidation catalysis in terms of selectivity, efficiency and energy cost [4,5]. In this configuration catalytic reactions can take advantages of the NTP emitted O_3 as a potential source of active oxygen species enabling further oxidation at ambient or very low temperatures of the NPT non processed parent VOC and potential NTP gaseous hazardous by-products [4–6].

Consequently, in this chapter, the functioning of plasma as ozoner is investigated. The ozone and concomitant nitrogen oxide formations by negative DC (Direct Current) corona discharge at atmospheric pressure using a 10-pin-to-plate reactor in dry/humid air stream have been discussed. The effects of operating parameters such as energy density (ED), flow rate (F) and relative humidity (RH) on the ozone and nitrogen oxide production have been investigated. A reaction scheme is proposed to account for the N_2O_5 and HNO_3 formations based on the NO_x oxidation by ozone.

5-2- Experimental conditions

The detail information can be seen in [chapter 3](#). Briefly, dry ($\text{RH} = 0.7\%$) or humid air ($\text{RH} = 15\%$) are flushed into the plasma reactor at a fix flow rate ($Q = 0.5; 1; 1.5\text{ L/min}$). The energy density was allowed to increase between 50 and 250 J/L.

5-3- Experimental results

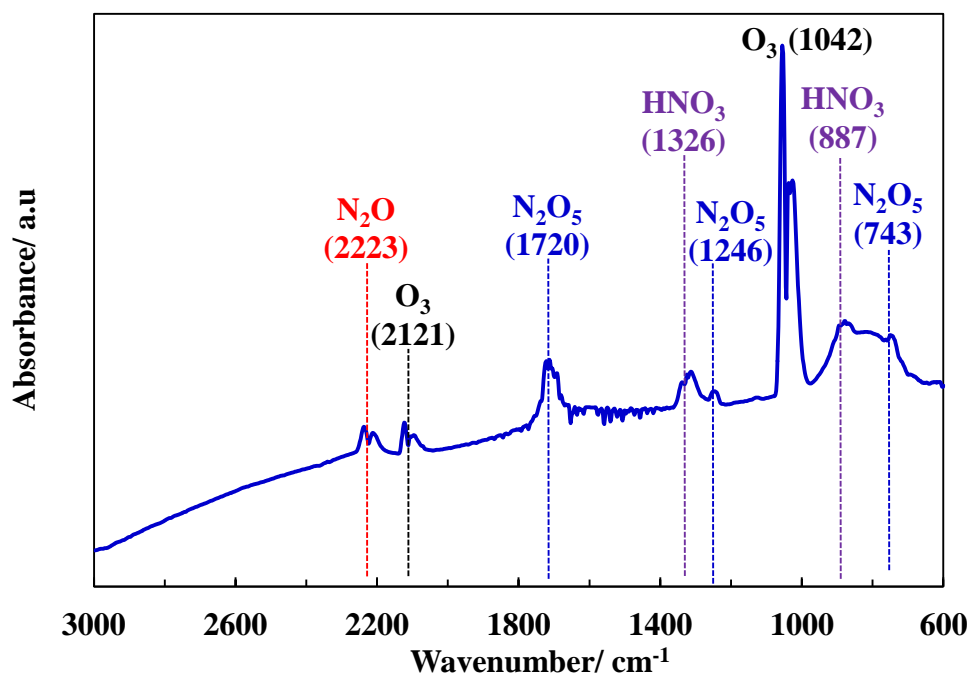


Figure 5 - 1: FT-IR spectrum of the plasma generated gaseous species. Dry air; F = 1L/min; ED = 150J/L

Figure 5-1, shows a typical *in situ* IR spectrum of the plasma generated gaseous species in dry air. The presence of the IR bands located at 1042 and 2121 cm⁻¹ evidences the presence of ozone. Furthermore, the generation of N₂O, N₂O₅ as well as HNO₃ is also observed consistent with the absorbance band positions. The characteristics band for HNO₃, N₂O₅ and N₂O was observed at 743, 1246, 1720 and 887, 1326 and 2223 cm⁻¹ respectively.

Using a DC negative corona discharge, it is found that O₂ is partly converted into ozone and N₂ into N₂O, N₂O₅ and HNO₃. The ozone formation can be initiated by the electron impact dissociation of molecular O₂ and N₂ owing to the reactions (1) and (2). The produced atomic oxygen reacts with O₂ and a third collision partner (M = O₂, N₂) through reaction (3) producing ozone as already reported [7]:



The formation of N₂O₅ can be explained through the postulated generation of small amounts of NO in line with the reactions (4) and (5) given below and NO can then be oxidized by O₃ into NO₂.



At that stage NO_2 can be further oxidized into NO_3 by O_3 and the retrodismutation between NO_2 and NO_3 can afford N_2O_5 . The residual H_2O present in the gas carrier contributes to the formation of HNO_3 . The reaction scheme depicting the formation of N_2O_5 and HNO_3 is given in **Figure 5-2** in accordance with the work of C. Sun *et al.* [8].

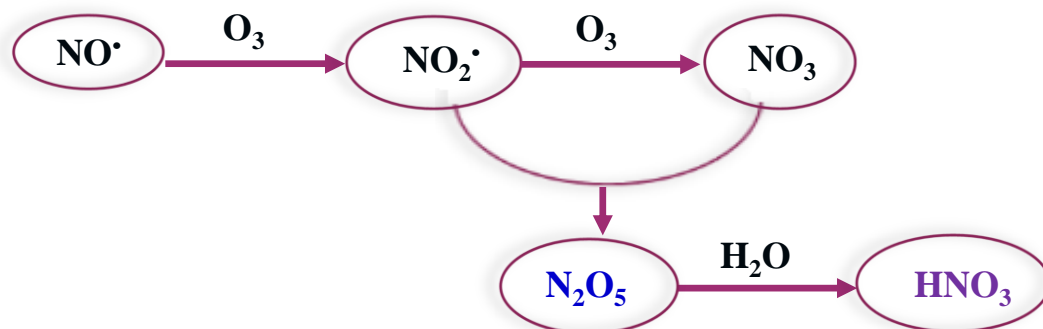


Figure 5 - 2: Scheme of N_2O_5 and HNO_3 production *via* NO_x oxidation by O_3

Considering the production of N_2O , it has been previously reported [9] that the most important reaction can be the following:



5-3-1- Effect of energy density (ED)

Figure 5 - 3, shows the typical effect of the energy density of plasma on the production of ozone. A linear increase of the production is observed at low ED (100 J/L) while a downward departure from linearity is observed afterwards. A maximum of about 840 ppmv can be achieved for an ED equal to 250 J/L in dry air and $F = 1\text{L/min}$.

The ED is specific to the current which is itself proportional to the production of ozone. Increasing current lead to an increase in the number and density of electrons and so more ozone can be formed. In this regards, the linear increase of ozone concentration with ED in dry air may be due to the increase of electron density with appropriate energy [10].

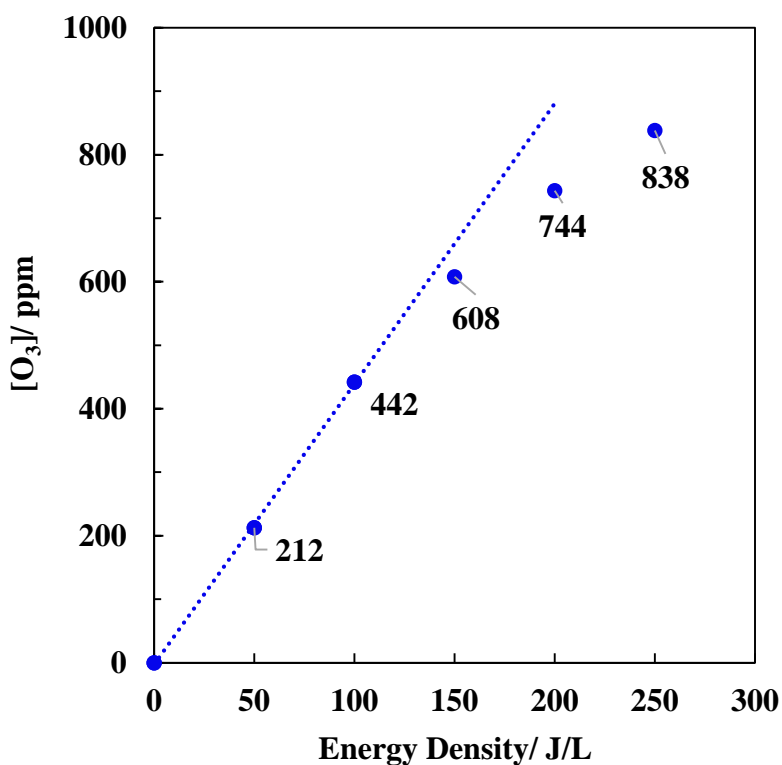


Figure 5 - 3: Ozone concentration as a function of ED. Dry air; Q = 1 L/min

Figure 5-4, shows the evolution of the I_X/I_{250} intensity ratio (where I_X and I_{250} are the intensities of selected bands for ED of a given X value and ED for 250 J/L) for each nitrogen containing species as a function of ED. A linear N_2O production increase with ED is observed whereas the intensity ratio traces relative to N_2O_5 and HNO_3 productions show a maximum at 200 J/L.

The ozone concentration increases linearly at low ED. The downward departure from linearity at high ED may be due to competing reactions (nitrogen oxides production) affording an ozone concentration less than that expected.

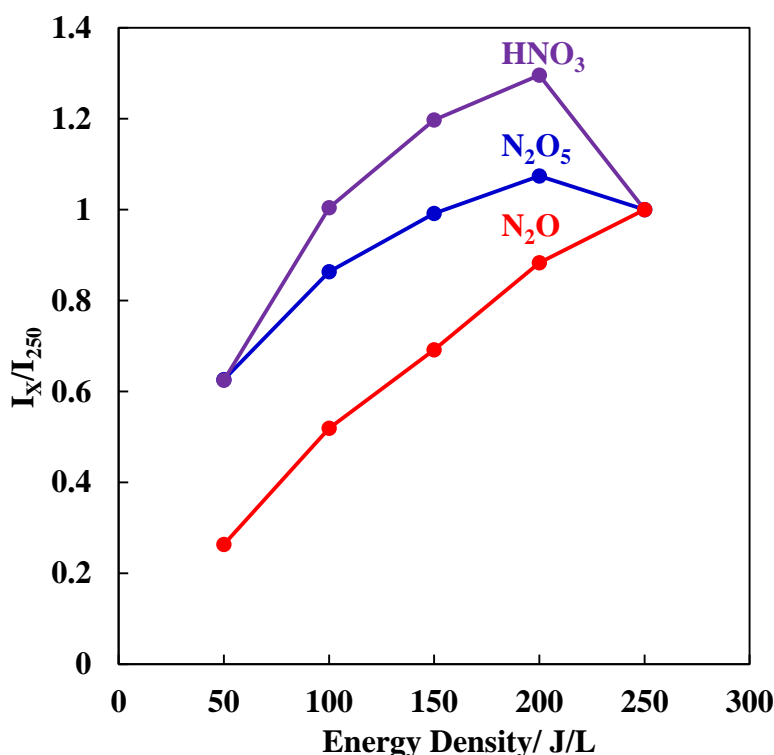


Figure 5 - 4: I_x/I_{250} as a function of ED; Dry air; $Q = 1\text{ L/min}$

5-3-2- Influence of Flow rate (Q)

The air flow rate inside the reactor was allowed to vary from 0.5 L/min to 1.5 L/min, with a corresponding residence time varying from 10.8 s to 3.6 s. **Figure 5 - 5**, shows the ozone concentration as a function of ED at different flow rates. For $ED \leq 200\text{ J/L}$, while increasing the flow rate from 0.5 L/min up to 1.0 L/min increases the ozone concentration a further increase of Q keeps the ozone concentration unchanged. In contrast, for $ED = 250\text{ J/L}$ no changes in the ozone concentration are observed with the two flow rate 0.5 and 1 L/min. For $Q = 1.5\text{ L/min}$, ED maximal achieved is 200J/L for ED greater than that, the plasma regime changes from glow discharge into spark discharge.

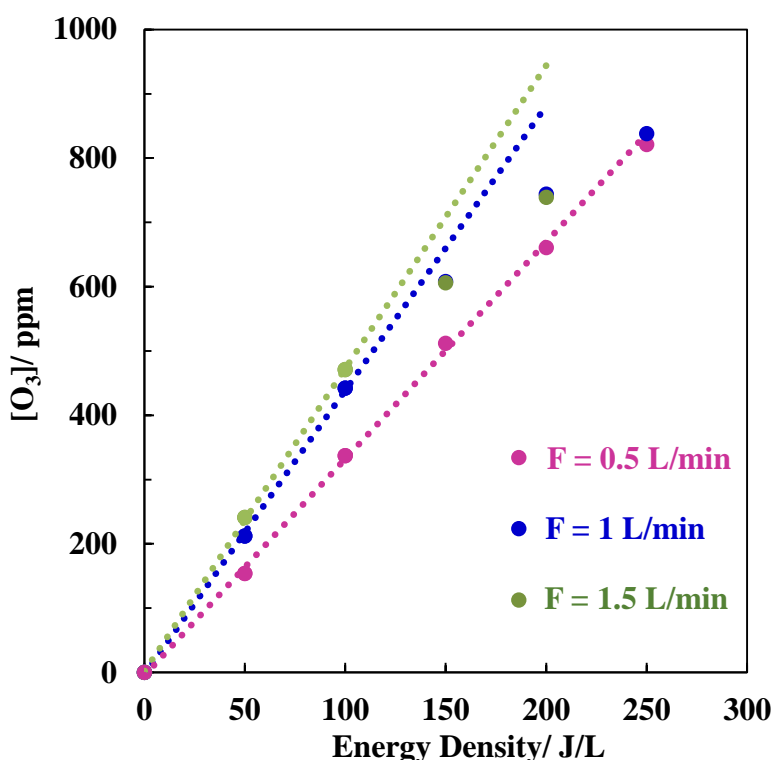


Figure 5 - 5: Evolution of $[O_3]$ as a function of ED. Dry air; $Q = 0.5, 1$ and 1.5 L/min

Figure 5 - 6, shows the rate of ozone production r_{O_3} as a function of the flow rate. It is found an increase of r_{O_3} by a factor of 1.5 with a threefold increase of Q . Hence a decrease of the residence time has a beneficial effect on O_3 production which is all the more important that ED is important.

The effect of the flow rate on the nitrogen oxide and HNO_3 productions was performed through the evolution of the integrated area as a function of Q as shown in **Figure 5- 7**. While the areas relative to HNO_3 and N_2O were unchanged a maximum was observed for the integrated area of N_2O_5 for a flow rate of 1 L/min.

The effect of the flow rate on ozone concentration is complex. Anyway, the ozone production increases with lowering the residence time in the reactor.

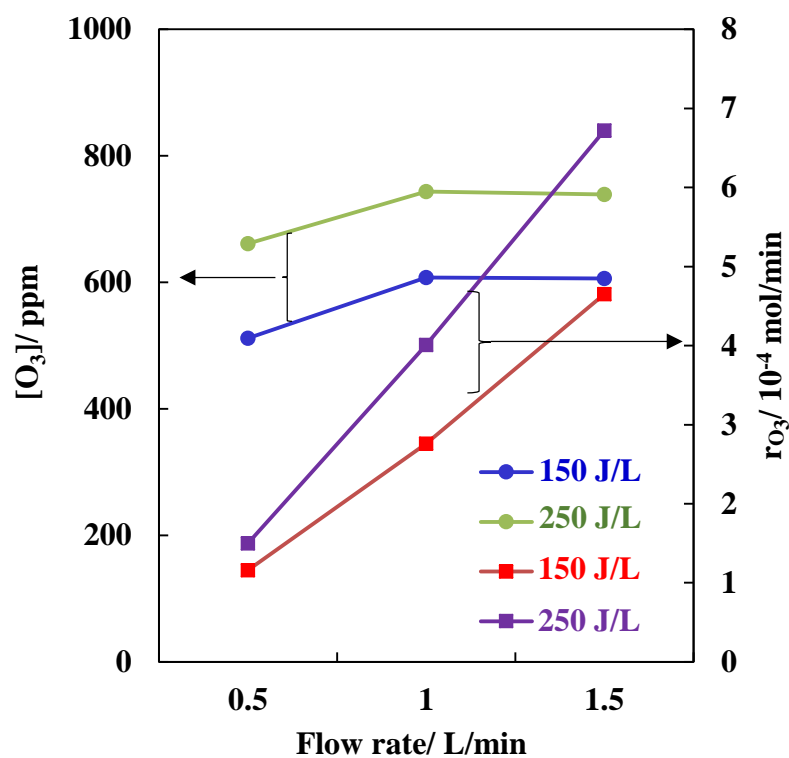


Figure 5 - 6: Effect of Q on $[O_3]$ and r_{O_3}

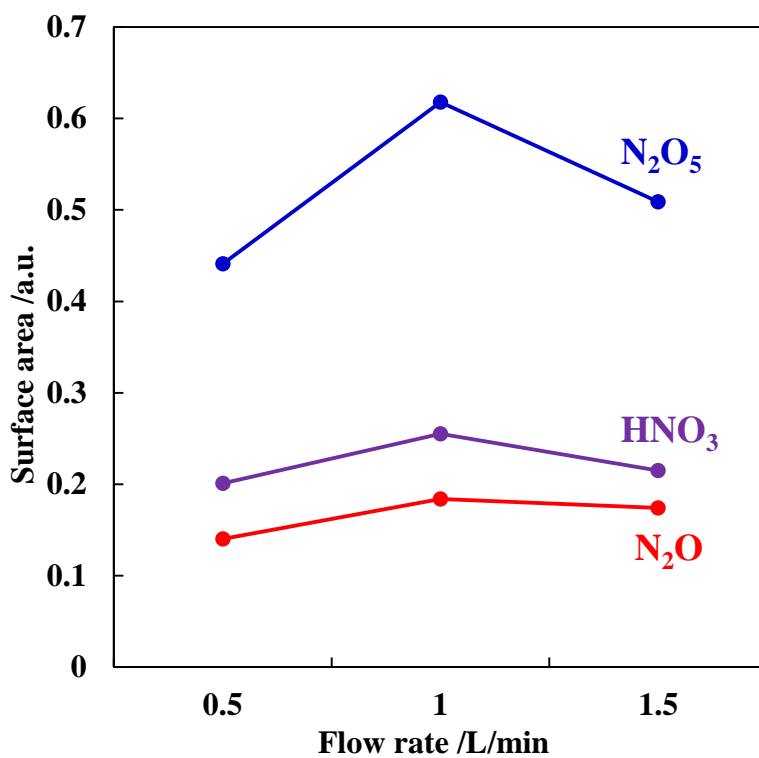


Figure 5 - 7: Evolution of the integrated area as a function of Q. Dry air; ED = 150 J/L

5-3-3- Influence of Relative Humidity (RH):

Figure 5-8, shows the evolution of the ozone concentration as a function of ED in dry and humid air (RH = 15%). In the presence of humidity, the ozone concentration drops significantly as compared to that obtained in dry air. This relative decrease in ozone concentration is enhanced with ED. In that respect, the ozone concentration is about four times lower than that obtained in dry air for ED equal to 250 J/L.

In the presence of 15% of relative humidity, N_2O , N_2O_5 and HNO_3 were detected by FT-IR but their relative contributions appear very low as compared to those obtained in dry air as shown in **Figure 5-9**.

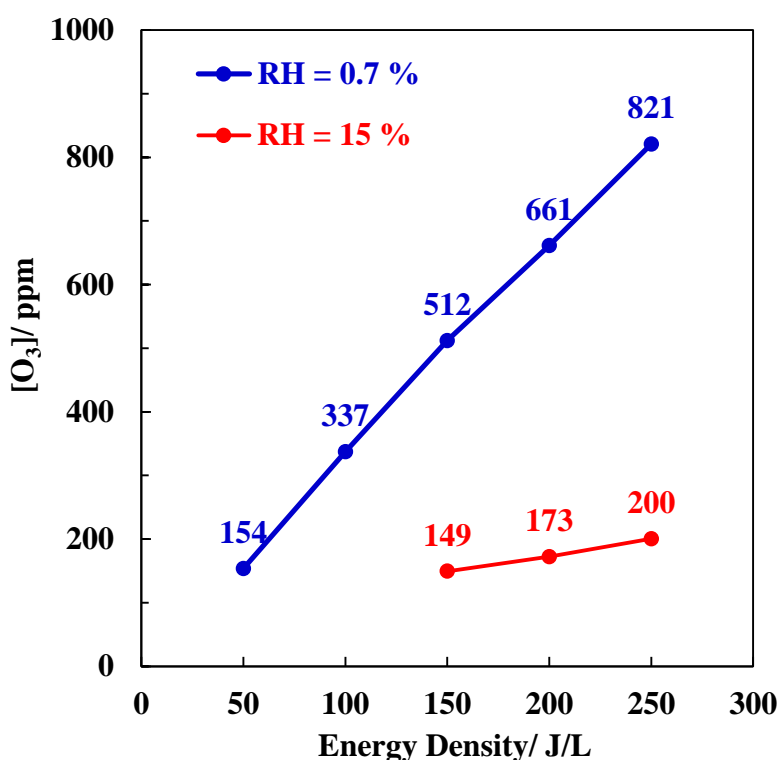


Figure 5 - 8: Evolution of $[O_3]$ as a function of ED in dry air and humid air; $Q = 0.5$ L/min

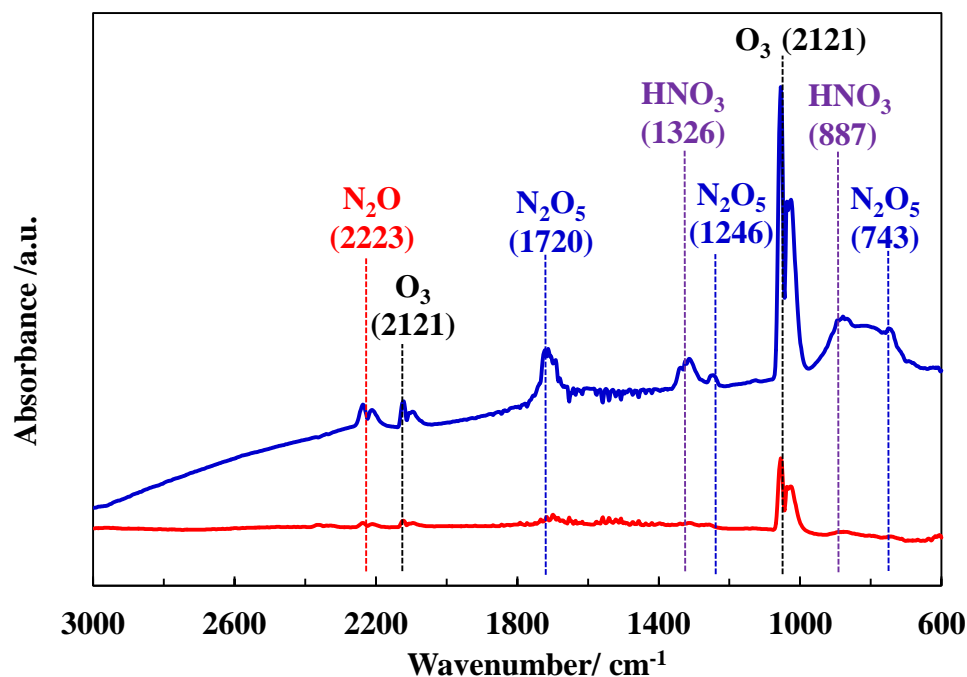
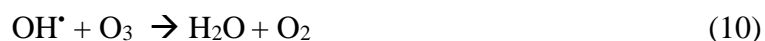


Figure 5 - 9: FT-IR for the plasma generated gaseous species in dry air and in 15 % as relative humidity. Q = 0.5L/min; ED = 250 J/L

The decrease of ozone concentration in the presence of humidity can be ascribed to the changes induced in the plasma content due to the initial presence water through OH and H radicals. Hence, H₂O may be decomposed into OH and H radicals as reported elsewhere [8,11] following the formal reactions (7) - (9):



Such OH radicals may react with ozone to give water and dioxygen following reaction (10):



5-4- Conclusion

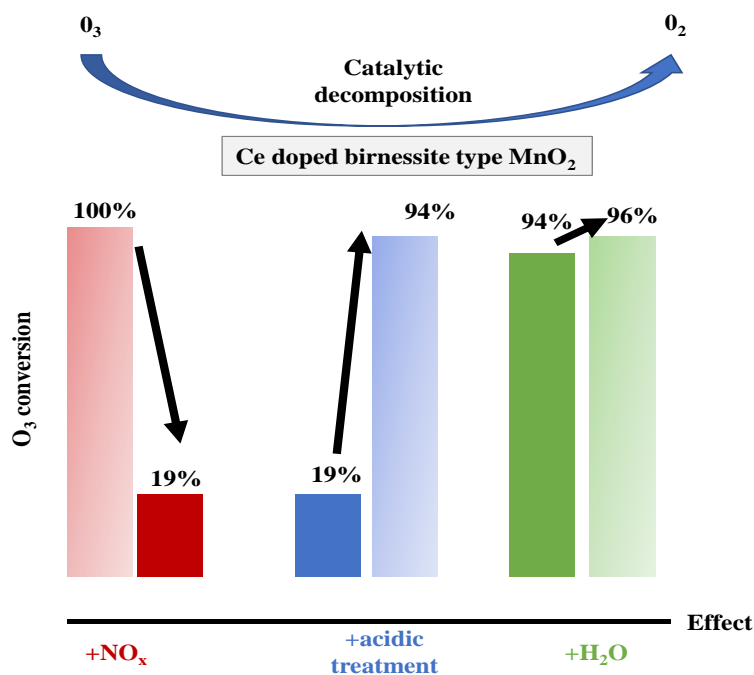
In this chapter ozone production using negative DC corona discharge in the presence of concomitant nitrogen oxides was investigated as a function of the plasma key parameters. Ozone production increases with increasing the energy density (ED) and flow rate (Q). A partial destruction of ozone due to nitrogen oxides production was observed. N_2O_5 and HNO_3 show an apparent maximum at 200 J/L as increasing the ED while N_2O increases linearly. However, N_2O and HNO_3 productions linearly increases as a function of flow rate while N_2O_5 shows a maximum with 1L/min as Flow rate. Furthermore a negative effect of humidity on ozone production as well as on N_2O_5 and HNO_3 productions.

References

- [1] A.M. Vandenbroucke, R. Aerts, W. Van Gaens, N. De Geyter, C. Leys, R. Morent, A. Bogaerts, *Plasma Chem. Plasma Process.* 35 (2015) 217–230.
- [2] A.M. Vandenbroucke, R. Morent, N. De Geyter, C. Leys, *J. Adv. Oxid. Technol.* 14 (2011) 165–173.
- [3] H. Conrads, M. Schmidt, *Plasma Sources Sci. Technol.* 9 (2000) 441.
- [4] M. Magureanu, N.B. Mandache, P. Eloy, E.M. Gaigneaux, V.I. Parvulescu, *Appl. Catal. B Environ.* 61 (2005) 12–20.
- [5] X. Tang, F. Feng, L. Ye, X. Zhang, Y. Huang, Z. Liu, K. Yan, *Catal. Today* 211 (2013) 39–43.
- [6] Z. Ye, PhD Ghent and Lille Universities (2018) 230.
- [7] A.J. Al-abdul, PhD Newcastle University (2015) 224.
- [8] C. Sun, N. Zhao, Z. Zhuang, H. Wang, Y. Liu, X. Weng, Z. Wu, *J. Hazard. Mater.* 274 (2014) 376–383.
- [9] L. Sivachandiran, A. Khacef, *RSC Adv* 6 (2016) 29983–29995.
- [10] R. Morent, C. Leys, *Ozone Sci. Eng.* 27 (2005) 239–245.
- [11] R. Peyrous, *Ozone Sci. Eng.* 12 (1990) 41–64.

Chapter 6:

ACID TREATED Ce MODIFIED BIRNESSITE-TYPE MnO_2 FOR OZONE DECOMPOSITION AT LOW TEMPERATURE: EFFECT OF NITROGEN CONTAINING CO-POLLUTANTS AND WATER



Part of this chapter has been published as an article in the following International journal:

Grâce Abdallah, Rim Bitar, Savita Kaliya Perumal Veerapandian, Jean-Marc Giraudon, Nathalie De Geyter, Rino Morent, Jean-François Lamonier, “ Acid treated Ce modified birnessite-type MnO_2 for ozone decomposition at low temperature: effect of nitrogen containing co-pollutants and water”, Applied Surface Science, 2021, 151240.

6-1- Introduction

As seen in [chapter 2](#), the second validation approach is to investigate the efficiency of the catalyst in terms of ozone degradation in the presence of other pollutants such as nitrogen oxides species in dry and humid air using NTP as an ozoner.

Briefly as discussed in [chapter 1](#), transition metal oxides, especially manganese-based oxides, have been widely studied for catalytic ozone decomposition because of their low cost and high efficiency due to the presence of large amounts of surface oxygen vacancies [1,2]. However, their efficiency is reduced in the course of the reaction and a deactivation over time is observed. This deactivation is generally explained by an adsorption competition between ozone and water molecules (also present in the gas stream) which leads to a blockage of the active sites [3]. Nitric acid-treated birnessite-type MnO_2 has been demonstrated to be an efficient and hydrophobic catalyst for humid ozone decomposition [4]. The addition of cerium element to manganese oxides could be also an efficient way in preventing the deactivation of the catalysts under high humidity conditions [5]. Furthermore, the addition of cerium in MnO_x may contribute to a significant improvement of the catalytic performance in the ozone decomposition reaction owing to (i) an increase in surface area, (ii) a decrease in crystallinity, and (iii) a larger amount of surface oxygen vacancies [6]. It is believed that the oxygen transfer between Ce^{4+} and Ce^{3+} species on the surface of the catalysts allows abundant oxygen species storage and leads to superior redox properties compared to those obtained with simple manganese oxides [7,8]. The introduction of Ce also leads to an electron transfer between manganese and cerium which improves the redox capacity of the material and consequently its catalytic performance [7].

Moreover, the development of novel catalysts for the ozone decomposition reaction that are highly active and stable at low temperatures in the presence of water but also in the presence of other molecules is required. It is particularly important to estimate the sensitivity of these new catalysts to nitrogen oxides [9]. An inhibiting effect of NO_x on ozone decomposition is observed in the presence several catalyst compositions such as Ni-Mn spinel [10] and activated carbon [11]. Very recently, ozone decomposition has been investigated in the presence of NO_x at low temperature over a commercial $\text{Pd}/\text{Al}_2\text{O}_3$. NO_x species have been shown to significantly poison the catalyst, resulting in a significant decrease of ozone conversion over time on stream [12].

In this chapter nitric acid treated Ce_xMn have been tested in comparison with the non-acid treated catalysts in non-thermal plasma generated ozone decomposition at low temperature in nearly dry and moist air. The presence of nitrogen containing contaminants has been assessed by the generation of ozone from air using a negative DC discharge plasma. The structure-performance relationship has been established and the role of the acid treatment and of the promote role of cerium on ozone decomposition has been discussed considering the nitrogen gaseous species.

6-2- Experimental conditions

Table 6-1, summarizes the basic experimental conditions used in this chapter. The detailed experimental conditions can be seen in [chapter 3](#).

Table 6 - 1: Experimental conditions

Air source	Air liquide, alphagaz 1
Flow rate	1 L/min
Relative humidity (RH)	0.7 % / 15%
Energy density	50 J/L
Initial ozone concentration	300 ppmv
Catalysts	Ce_xMn and $\text{Ce}_x\text{Mn-AT}$ 0.1 g of Ce_xMn mixed with 1g of SiC 0.05 g of $\text{Ce}_x\text{Mn-AT}$ mixed with 1g of SiC
Activation conditions	200 mL/ min, 150°C for 8 hour for Ce_xMn
Catalyst temperature	Room temperature

6-3- Results and discussion

6-3-1- Characterization studies of the acid-treated catalysts

The X-ray diffraction pattern of Mn-B-AT which exhibits three broad peaks of low intensity centered at 12.2° , 37.0° and 66.2° (**Figure 6-1**) can be consistent with the formation of a related disordered birnessite [13]. These results suggest the formation of a layer structure with coexisting amorphous state domains. Besides, the diffraction peaks become even less resolved as cerium is added. At the highest doping ratio of 0.5 only a very broad peak of low intensity at about 30° is observed due to cubic CeO_2 phase (JCPDS No.00-034-0394) which implies an extensive destruction of the crystallized layer structure.

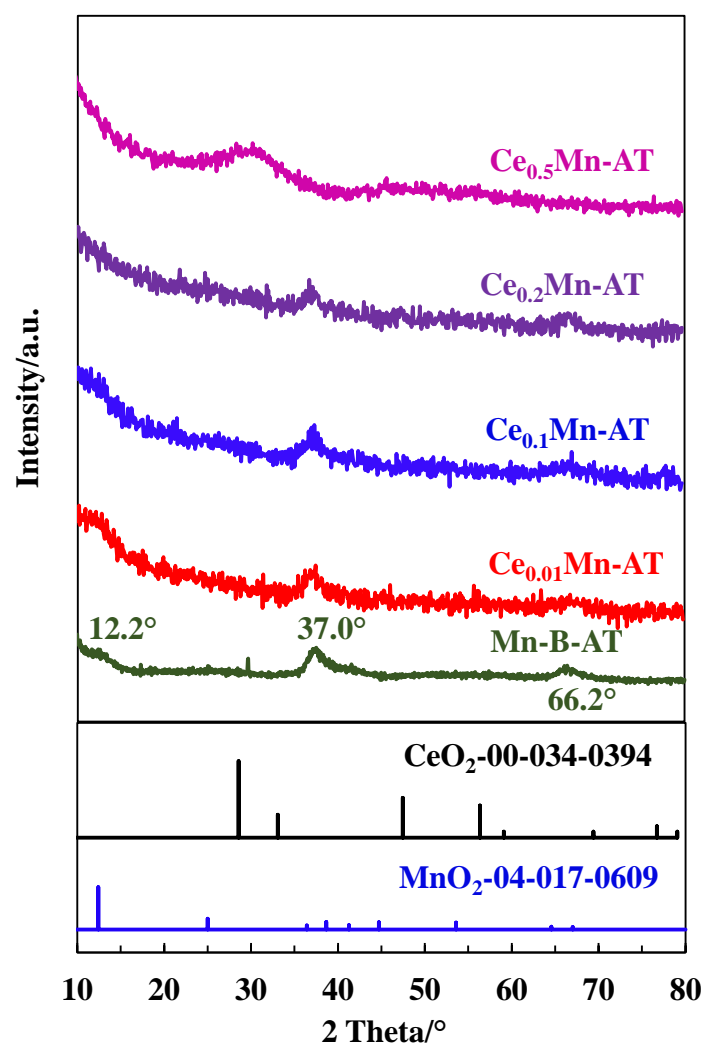


Figure 6 - 1: XRD patterns of the fresh acid- treated samples

The results of elemental analysis performed by ICP-EOS are given in **Table 6-2**. For Mn-B-AT it is observed a K/Mn atomic ratio of 0.065 consistent with the value of 0.05 obtained by Liu *et al.* [4] for an acid-treated birnessite MnO_2 which is substantially lower than for a conventional birnessite (~ 0.26). The loss of K^+ is consistent with K^+/H^+ exchange at the interlayer position as already pointed out [2]. While this K/Mn ratio is poorly affected by a low loading of cerium, it markedly decreases with increasing cerium nominal content. This can be explained by an increase amount of leached K^+ resulting from partial substitution of K^+ by H^+ and/or Ce^{4+} . Besides, the Ce/Mn ratio is consistent with the nominal one for the lowest doping ratio while a two-fold decrease is observed for higher doping ratio (Ce/Mn: 0.1, 0.2). Such higher release of cerium could be correlated with different speciations of Ce in the material.

Table 6 - 2: Chemical composition, textural and redox properties of the fresh acid-treated samples

Catalyst	ICP-EOS		Textural properties		Redox properties (H_2 -TPR)		
	K/Mn	Ce/Mn	S_{BET} (Fresh) (m^2/g)	V_p (cm^3/g)	Tonset ($^\circ\text{C}$)	n (H_2) ($\text{mmol}/\text{g}_{\text{cat}}$)	n (H_2) / n (Mn+Ce)
Mn-B-AT	0.065	-	334 (44)	0.55	140	9.20	0.90
$\text{Ce}_{0.01}\text{Mn-AT}$	0.059	0.0079	385 (127)	0.48	75	9.17	0.96
$\text{Ce}_{0.1}\text{Mn-AT}$	0.024	0.054	337 (243)	0.37	110	8.69	0.81
$\text{Ce}_{0.2}\text{Mn-AT}$	0.014	0.097	280 (269)	0.65	115	7.53	0.78
$\text{Ce}_{0.5}\text{Mn-AT}$	0.0025	0.65	355 (249)	0.26	150	2.03	0.19

The HRTEM images of the $\text{Ce}_{0.1}\text{Mn-AT}$ sample are given in **Figure 6-2**. In agreement with XRD results, large amorphous areas coexist with crystallized regions. Blurred stacked layers of less than 5 nm are observed attesting of the layered structure of the material. The lattice spacing of 0.71 nm has been assigned to the (001) plane of the birnessite. In the crystallized regions, it is observed the (111) lattice planes of CeO_2 with lattice spacing of 0.31 nm. The formation of such an interface structure has been recognized as to promote Ce- \square -Mn interactions allowing the generation of plenty of oxygen vacancies, which might improve the mobility of the adsorbed and lattice oxygen species [14–19].

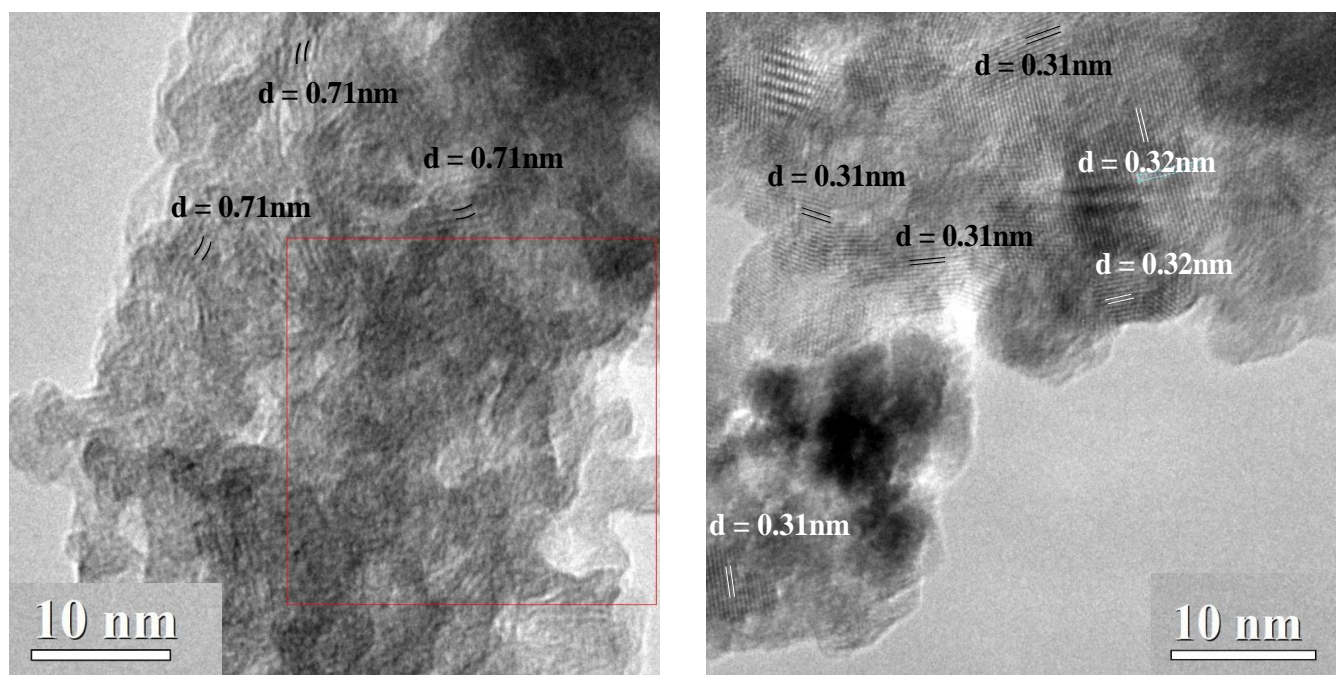


Figure 6 - 2: TEM images of $\text{Ce}_{0.1}\text{Mn-AT}$

N_2 physisorption isotherms are shown in **Figure 6-3 (a)**. Specific surface area (S_{BET}) as well as pore volume V_p values are compared in **Table 6-2**. All catalysts exhibit a type IV isotherm profile with a hysteresis loop in line with a mesoporous structure. High S_{BET} (280 - 385 m^2/g), important V_p (0.25 - 0.65 cm^3/g) and a small mean pore size D_p in the range: 3.8 - 6.0 nm (**Figure 6-3 b**) are obtained which are known to be beneficial for O_3 decomposition [6].

It is worthy to note that a significant enhancement of the specific surface area occurs in most cases after acid-treatment (**Table 6-2**) due to the formation of enhanced amorphous zone and low crystallinity of the layered structure observed by TEM analysis.

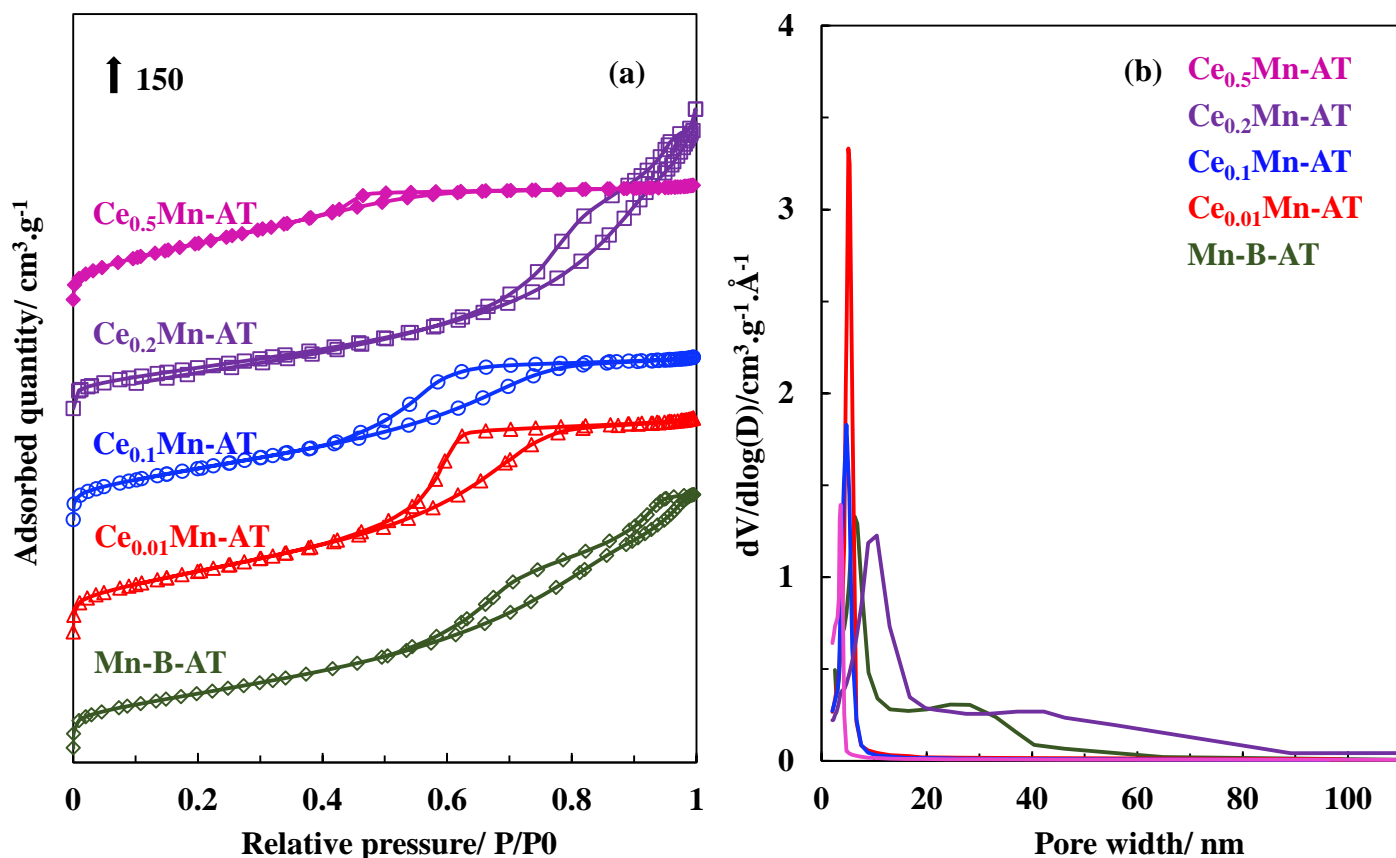


Figure 6 - 3: (a) N_2 adsorption-desorption isotherms and (b) pore size distribution of the fresh acid-treated samples

The reducibility of the samples has been evaluated by H_2 -TPR (**Figure 6-4**). The H_2 -TPR traces of the acid-treated Ce_xMn oxides ($x = 0-0.2$) samples can be divided into 4 components α , β , γ and δ . While the α consumption is linked to the removal of surface oxygen species, the other components are related to the near surface and bulk oxygen removal. As compared to the undoped sample, the addition of Ce decreases the onset reduction temperature, increases the relative β consumption while the γ and δ peaks move to higher temperature. These results indicate that the reducibility of the samples is enhanced with a low cerium doping which might be related from the formation of more surface oxygen vacancies [1,4,7,20–22].

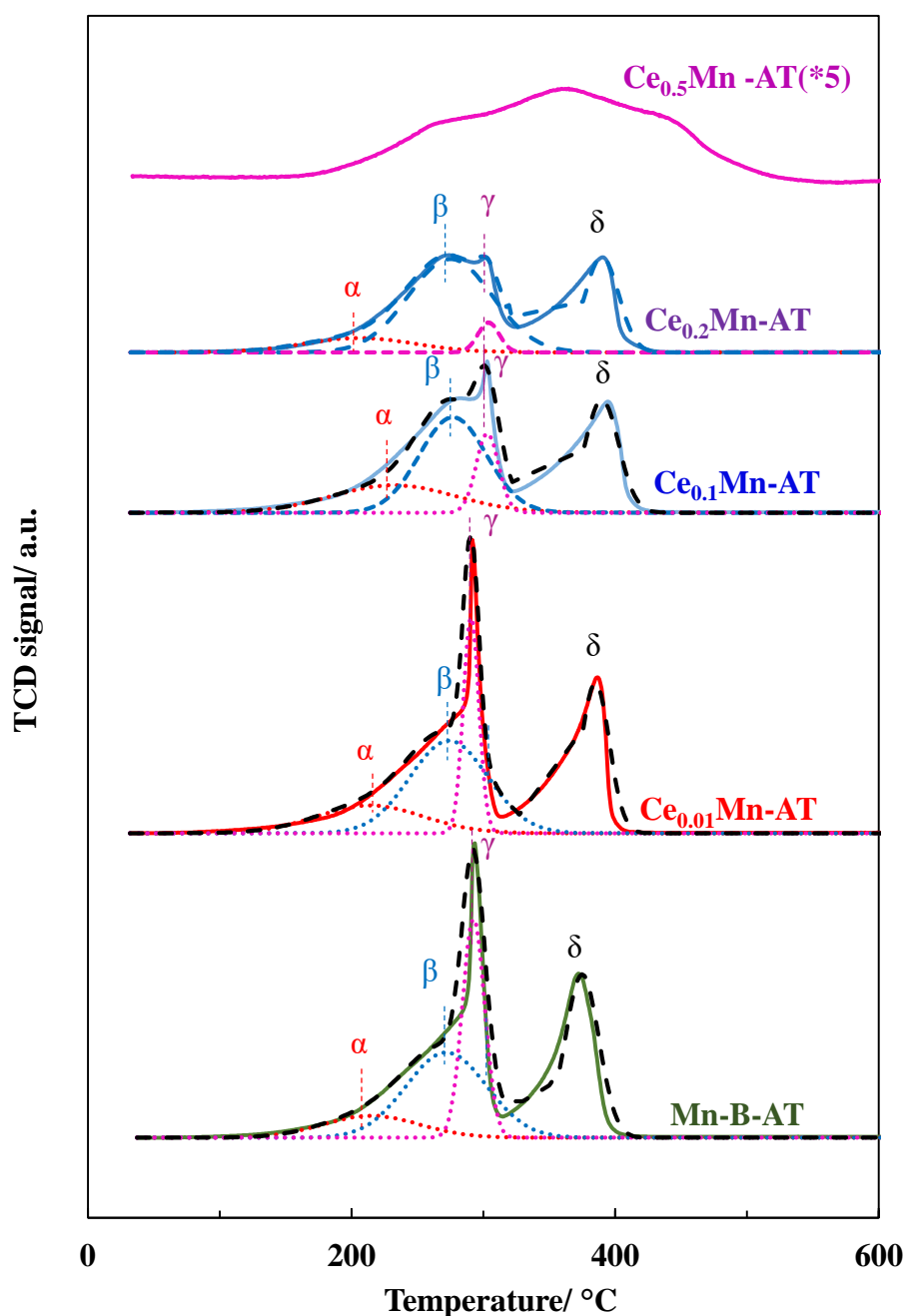


Figure 6 - 4: H_2 -TPR traces of the fresh acid-treated samples

With the addition and increasing content of cerium, the hydrogen consumption decreases per gram of catalyst from 9.20 to 7.53 mmol/g_{cat} while it reaches a maximum value of 0.96 for $\text{Ce}_{0.01}\text{Mn}$ when expressed as total metal amount (**Table 6-2**).

Besides oxygen vacancies, surface acidity is also an important factor that should be taken into consideration for ozone decomposition. The changes of surface acidity induced by the acid treatment have been assessed by adsorption of pyridine on selected samples monitored by FTIR spectroscopy. FTIR analysis of pyridine adsorption allows to determine the balance between Brønsted acid sites (B sites) and Lewis acid sites (L sites). The pyridine FTIR spectra

recorded at 105 °C are shown in **Figure 6-5** for the doped samples $\text{Ce}_{0.1}\text{Mn}$ (a) and $\text{Ce}_{0.2}\text{Mn}$ (b) before and after acid treatment. In accordance with the literature [23–27], the band assignments have been realized as follows: bands at 1635 and 1540 cm^{-1} have been attributed to pyridine adsorbed on Brønsted acid sites and the bands at 1610 and 1445 cm^{-1} have been attributed to pyridinium derived from chemisorbed pyridine on L-sites. The band at 1490 cm^{-1} is assigned to pyridine adsorbed on both L-sites and B-sites. The two remaining bands at 1573 cm^{-1} and 1471 cm^{-1} have been ascribed to pyridine physisorption (P) [21,27]. B acid sites can originate from acidic hydroxyl groups attached to metal atoms (Mn, Ce) while L acid sites are regarded as empty orbitals of metal ions in the oxides ($\text{Mn}^{4+/3+}$; $\text{Ce}^{4+/3+}$). From **Figure 6-5**, it can be shown that no acidity can be detected on the pristine samples. In contrast, L and B sites can be observed on the acid treated samples. The L sites dominated over the B sites when cerium content increases in the sample. As discussed previously, a low doping amount of Ce enhances the surface area throughout an increase of the number of defects and especially of the number of oxygen vacancies. However, some oxygen vacancies may be occupied by water or its dissociative species like hydroxyl groups, which act as Brønsted acid sites.

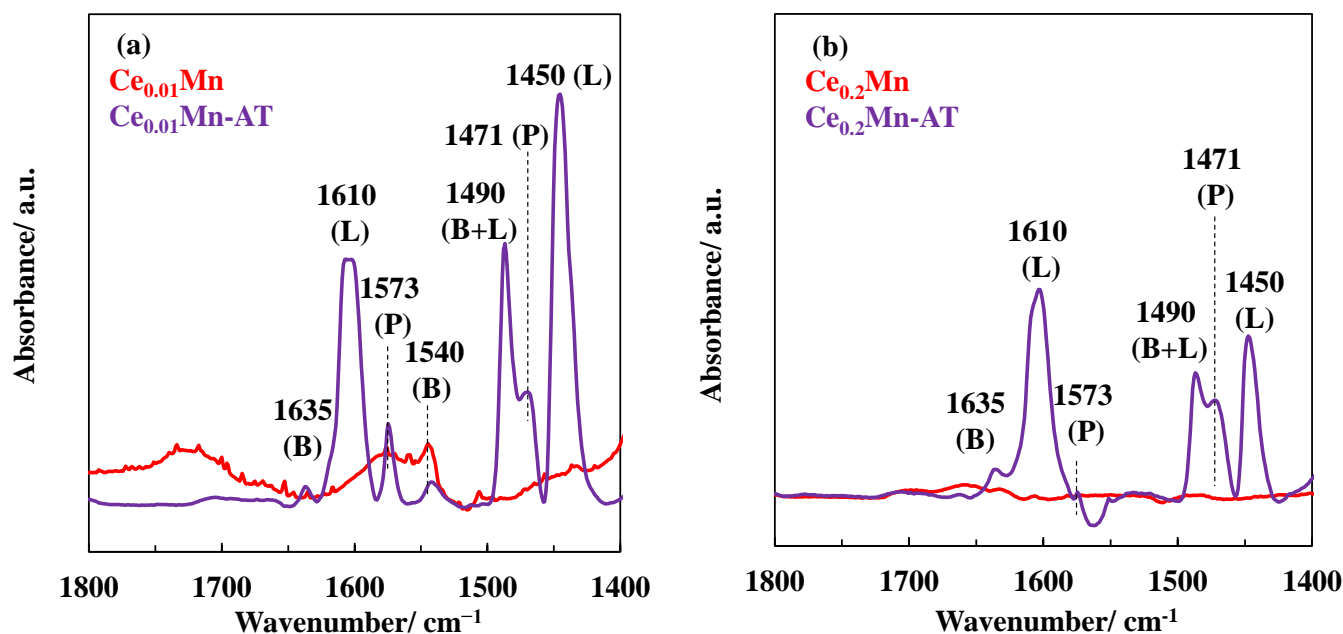


Figure 6 - 5: Pyridine-FTIR spectra before and after acid treatment for (a) $\text{Ce}_{0.01}\text{Mn}$ and (b) $\text{Ce}_{0.2}\text{Mn}$

In order to investigate the effect of acid treatment on the hydrophobicity of the acid-treated samples the amount of adsorbed water per BET specific surface area has been determined from TGA measurements (**Table 6-3**) and has been compared to those obtained on the fresh non-treated catalysts as seen in **Figure 6-6**.

Table 6- 3: Water loss between 25 °C and 100 °C determined from TGA measurements expressed in mg/gcat

	Mn-B	Ce _{0.01} Mn	Ce _{0.1} Mn	Ce _{0.2} Mn	Ce _{0.5} Mn
Fresh	39.40	34.61	28.55	24.74	23.83
AT	21.32	48.18	40.93	53.03	35.28

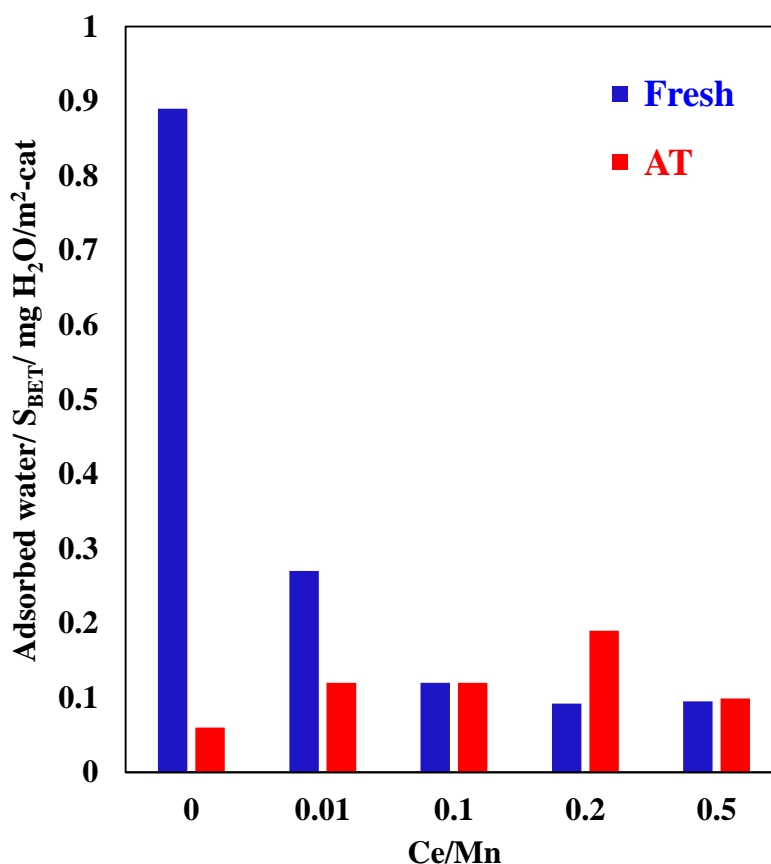


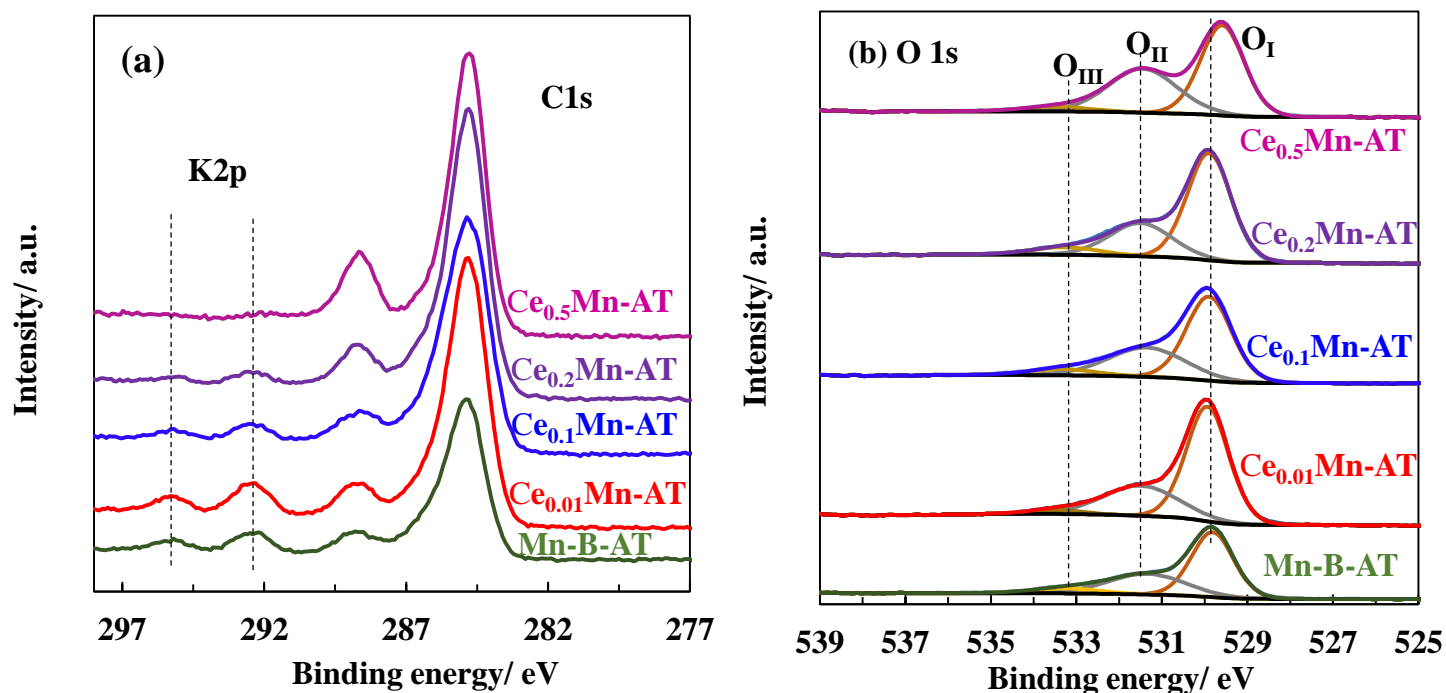
Figure 6 - 6: Amount of adsorbed water normalized to the specific surface area

Based on the results, it is shown that the acid-treated catalysts are more resistant to water than the non-treated counterparts in agreement with previous results [15].

Figure 6-7 shows the XPS core level spectra of K 2p (a), O 1s (b), Mn 2p_{3/2} (c) and Mn 3s (d) of the acid-treated samples and the salient XPS results are given in **Table 6-4**. The intensity of the K 2p signals is very weak, all the more so as cerium content is high, in accordance with the ICP-OES results (**Table 6-2**). The O 1s XPS spectra can be decomposed into three components located at ~ 529.7 eV, ~ 531.3 eV and ~ 533.4 eV which can be attributed to surface lattice oxygen (O_I), oxygen adspecies (O_{II}) and adsorbed H₂O (O_{III}), respectively [28]. Taken into account the decomposition results of Mn 2p_{3/2} and O 1s spectra, the Mn³⁺/Mn⁴⁺ ratio and the surface adsorbed oxygen concentration (O_{II}/(O_I + O_{II})) have been calculated and listed in **Table 6-4**. It has to be noted that the possible presence of carbonates on the surface

precludes a direct correlation between these two ratios. However the high simultaneous $\text{Mn}^{3+}/\text{Mn}^{4+}$ ratios, whose values increase with Ce content and high adsorbed oxygen concentration, correspond to high content of oxygen vacancies [23,29,30].

Considering both the values of $\text{Mn}^{3+}/\text{Mn}^{4+}$ ratios and those of the Ce/Mn ICP ratio the highest density of oxygen vacancies can be expected on the $\text{Ce}_{0.01}\text{Mn-AT}$ and $\text{Ce}_{0.1}\text{Mn-AT}$ samples based on charge balance process. It has also to be mentioned that the direct comparison of the $\text{Mn}^{3+}/\text{Mn}^{4+}$ ratio determined from the $\text{Mn } 2p_{3/2}$ core level to the Mn AOS determined from the Mn 3s splitting (**figure 6-7 (d)**) indicates that the extent of reduction is more pronounced in the first layers of the samples. Except $\text{Ce}_{0.5}\text{Mn-AT}$ which exhibits a high enrichment in cerium, the Ce/Mn ratios ranging from 0.008 to 0.097 are consistent with those determined from ICP-OES results.



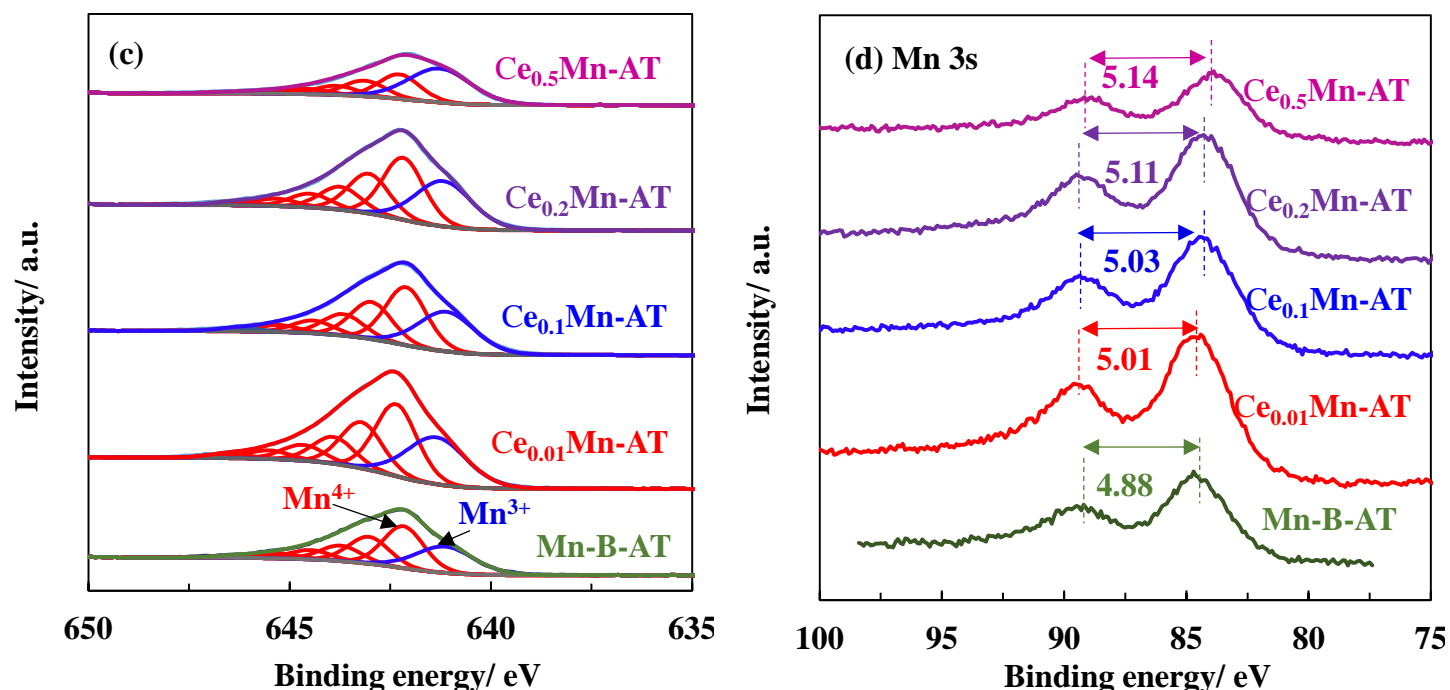


Figure 6 - 7: XPS spectra of the fresh acid treated samples

Table 6 - 4: XPS results of the fresh acid-treated samples

Catalyst	K/Mn	Ce/Mn	N/Mn	$\text{Mn}^{3+}/\text{Mn}^{4+}$	$\text{O}_I/(\text{O}_I + \text{O}_{II})$	$\Delta E \text{ Mn } 3s$ (Mn AOS)
Mn-B-AT	0.04	-	0.03	0.36	0.41	4.92 (3.41)
$\text{Ce}_{0.01}\text{Mn-AT}$	0.06	0.018	0.05	0.38	0.31	5.01 (3.32)
$\text{Ce}_{0.1}\text{Mn-AT}$	0.04	0.078	0.06	0.39	0.37	5.08 (3.23)
$\text{Ce}_{0.2}\text{Mn-AT}$	0.02	0.12	0.05	0.41	0.30	5.15 (3.16)
$\text{Ce}_{0.5}\text{Mn-AT}$	-	0.78	0.07	0.87	0.37	5.14 (3.16)

Static ToF-SIMS has also been performed in order to extract surface molecular changes induced by the acid treatment and the results are reported in Table 6-5. In any case, the mixed oxide formation can be easily evidenced by ToF-SIMS through the detection of mixed oxide fragments $\text{Ce}_x\text{Mn}_y\text{O}_z\text{H}_w^{+/-}$. The enhancement of the $\text{CeMnOH}^+/\text{CeOMn}^+$ secondary ion ratio after acid treatment suggests an increase of the Brønsted acidity in line with the results of acidic surface site probing by pyridine. Furthermore, comparison of the $\text{MnOH}^+/\text{MnO}^+$ secondary ion ratio and $\text{CeOH}^+/\text{CeO}^+$ ratio suggests that Mn is more affected than Ce in surface OH related species.

Table 6 - 5: ToF-SIMS results of the Fresh acid-treated samples

Catalyst	MnOH ⁺ /MnO ⁺	CeOH ⁺ /CeO ⁺	CeMnOH ⁺ /CeOMn ⁺	CeMnOH ⁺ /(CeO ⁺ +MnO ⁺)
Ce _{0.01} Mn	1.05	0.035	0.17	0.0027
Ce _{0.01} Mn-AT	3.04	0.036	1.15	0.0055
Ce _{0.1} Mn	1.62	0.020	0.16	0.0049
Ce _{0.1} Mn-AT	2.36	0.034	0.74	0.0047

6-3-2- Catalytic tests for ozone decomposition

The decomposition of 300 ppmv of O₃ generated from air at 20 °C as a function of time over the pristine and acid-treated catalysts is shown in **Figure 6-8**. The non-treated catalysts exhibit a strong deactivation behaviour over time (**Figure 6-8(a)**). By opposition, the acid-treated catalysts are much more active and deactivate in a lesser extent than before to reach a quasi-stationary state after 5 h on stream (**Figure 6-8(b)**). While the undoped acid treated catalyst Mn-B-AT deactivates strongly within the first four hours to reach a stable conversion of O₃ amounting to 64 % after 5 h, the Ce_{0.01}Mn-AT catalyst exhibits a constant conversion of O₃ of 94 % after 2 h on stream. For higher cerium content, the O₃ conversion declines nearly linearly with time for Ce_{0.1}Mn-AT and Ce_{0.2}Mn-AT to reach final values of 83 % and 76 %, respectively. A further increase in Ce content to 0.5 leads to O₃ conversion even lower than the undoped material of 33 %. This is mainly attributed to the decrease of Mn oxide content which constitutes the effective constituent of the catalytic reaction.

Besides, if ozone is generated from O₂ diluted in Ar, 100 % O₃ conversion is observed over time on Ce_{0.01}Mn (**Figure 6-9**).

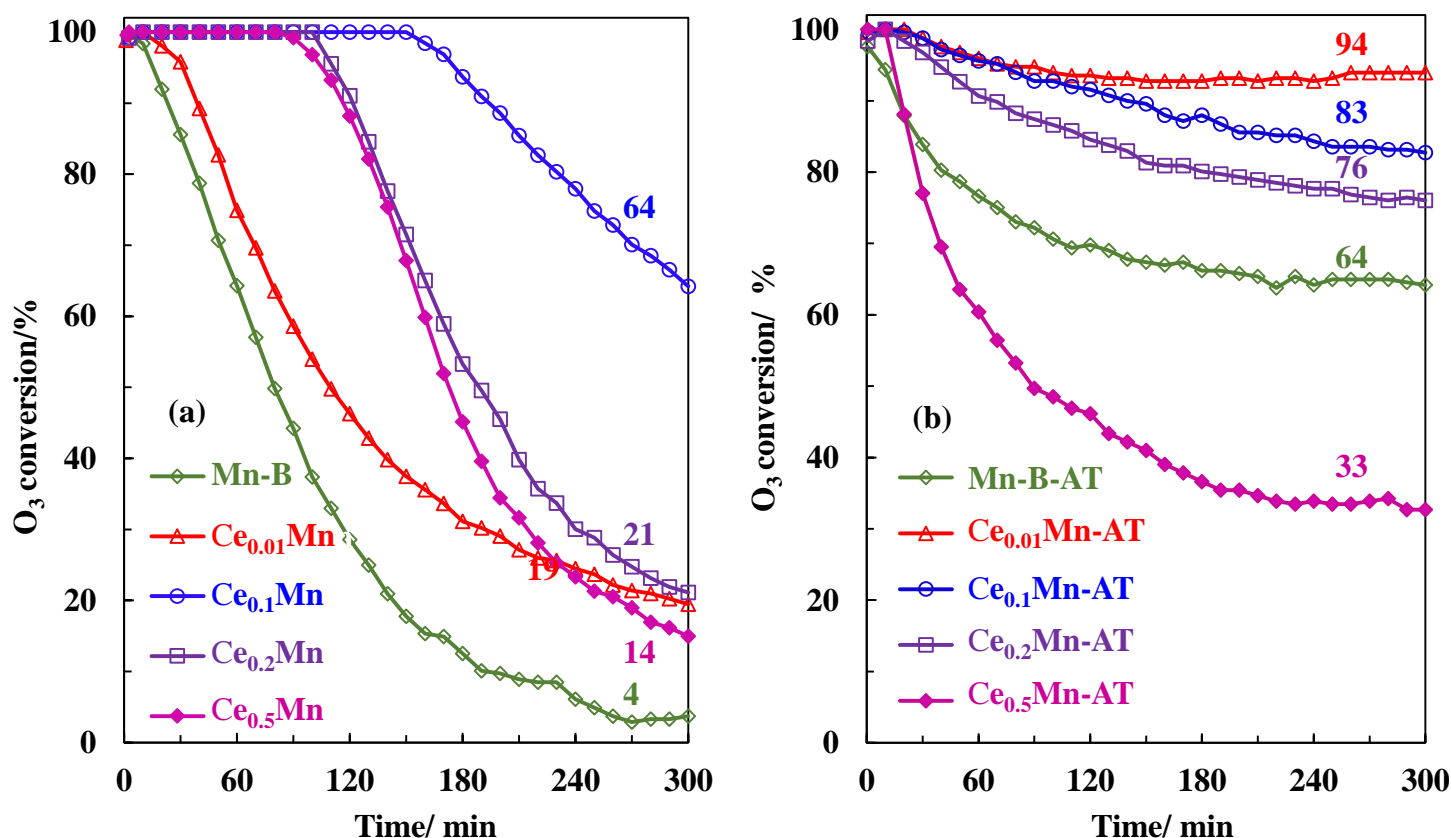


Figure 6 - 8: O_3 conversion (O_3 inlet concentration: 300 ppm) vs time in nearly dry air, 20 °C (a) on the pristine catalysts, GHSV = 600 L/(g h); (b) on the acid-treated catalysts, GHSV = 1200 L/(g h)

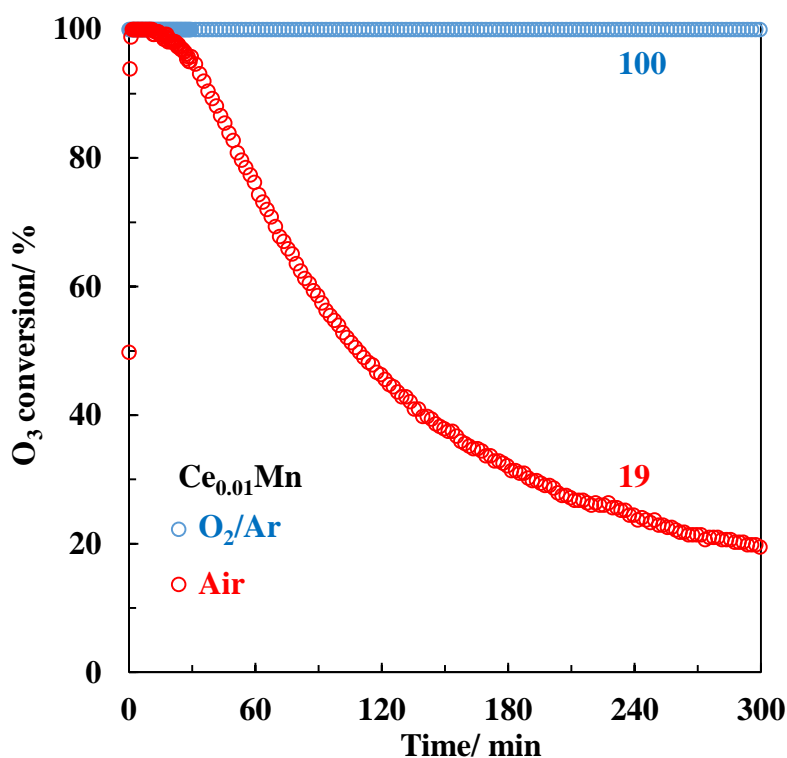


Figure 6 - 9: O_3 conversion (O_3 inlet concentration: 300 ppm) vs time over $\text{Ce}_{0.01}\text{Mn}$ in O_2/Ar and air, GHSV = 600 L/(g h)

These results suggest that the decrease in ozone conversion can be related to the formation of nitrogen containing pollutants in the plasma discharge in the presence of nitrogen in air as previously reported in the literature [31]. The catalytic decomposition of ozone generated from air has also been investigated on the two best catalysts, namely $\text{Ce}_{0.01}\text{Mn-AT}$ and $\text{Ce}_{0.1}\text{Mn-AT}$, at 40 °C in moist air (RH = 30 %) to examine their moisture tolerance. As shown in **Figure 6-10(a)** the O_3 conversion increases strongly in the first 15 minutes in any case to reach after that period about 100 % and 96 % before to stabilize after 5 h at 96 % and 98 % for $\text{Ce}_{0.01}\text{Mn-AT}$ and $\text{Ce}_{0.1}\text{Mn-AT}$, respectively. Even at 30 °C, the $\text{Ce}_{0.1}\text{Mn-AT}$ catalyst exhibits again a high O_3 conversion of 91 % (**Figure 6-10(b)**).

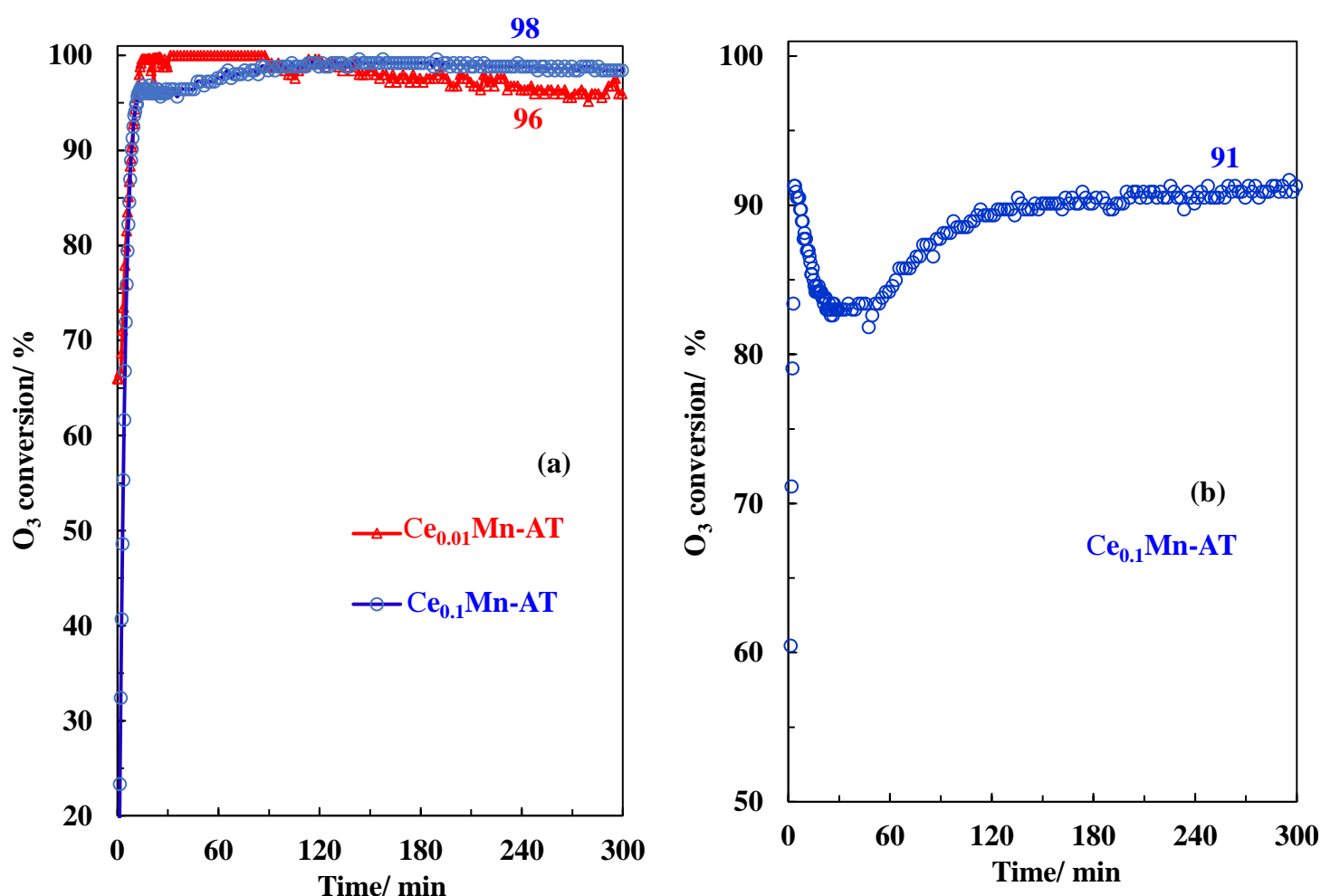


Figure 6 - 10: O_3 conversion vs time on the acid treated catalysts (O_3 inlet concentration: 300 ppm, GHSV = 1200 L/(g h)) (a) in moist air RH = 30 %; 40 °C; (b) in moist air RH = 30 %; 30 °C.

Overall, minimization of the catalyst deactivation for ozone decomposition in air in the presence of traces of nitrogen containing species (as seen below) and water can be achieved by performing an acid treatment on the cerium modified MnO_2 catalysts. Additionally, the acid-

treated $\text{Ce}_{0.01}\text{Mn}$ and $\text{Ce}_{0.1}\text{Mn}$ catalysts show remarkable catalytic performances for O_3 decomposition at RH of 30 % in the presence of nitrogen pollutants.

6-3-3- Gas phase characterization by FTIR

To assess the involvement of related nitrogen containing species in the activity decrease for O_3 decomposition the formation of gaseous species in the plasma discharge (PD) in the presence of air with low humidity ($\text{RH} = 0.7 \%$) was evaluated by FTIR and their temporal evolutions have been monitored at the outlet of the catalyst reactor in the course of the reaction for $\text{Ce}_{0.01}\text{Mn}$ and $\text{Ce}_{0.01}\text{Mn-AT}$ as shown in **Figure 6-11**, respectively. A typical FTIR spectrum at the inlet of the catalyst reactor (Inlet CR) shows bands at 2223 cm^{-1} , 1720 cm^{-1} and 1325 cm^{-1} assigned to N_2O , N_2O_5 and HNO_3 , respectively, along with those at 2111 cm^{-1} and 1056 cm^{-1} attributed to O_3 . To sum up, the NTP processed air allows the formation of N_2O , N_2O_5 and HNO_3 as nitrogen gaseous pollutants along with the formation of O_3 in the PD. The temporal evolutions of N_2O_5 and HNO_3 differ by the near non-observance of the characteristic bands relative to these species in the first 3 h for $\text{Ce}_{0.01}\text{Mn}$ (**Figure 6-11(a)**) unlike $\text{Ce}_{0.01}\text{Mn-AT}$ (**Figure 6-11(b)**) for which slight variations in band intensity decrease occur. In contrast, the relative content of N_2O is unaffected by post-plasma catalysis. Therefore, the uptake of N_2O_5 and HNO_3 in the first hours of reaction is clearly observed in the plasma-catalysis experiment when using $\text{Ce}_{0.01}\text{Mn}$ as catalyst while this gaseous uptake seems to be lower for $\text{Ce}_{0.01}\text{Mn-AT}$.

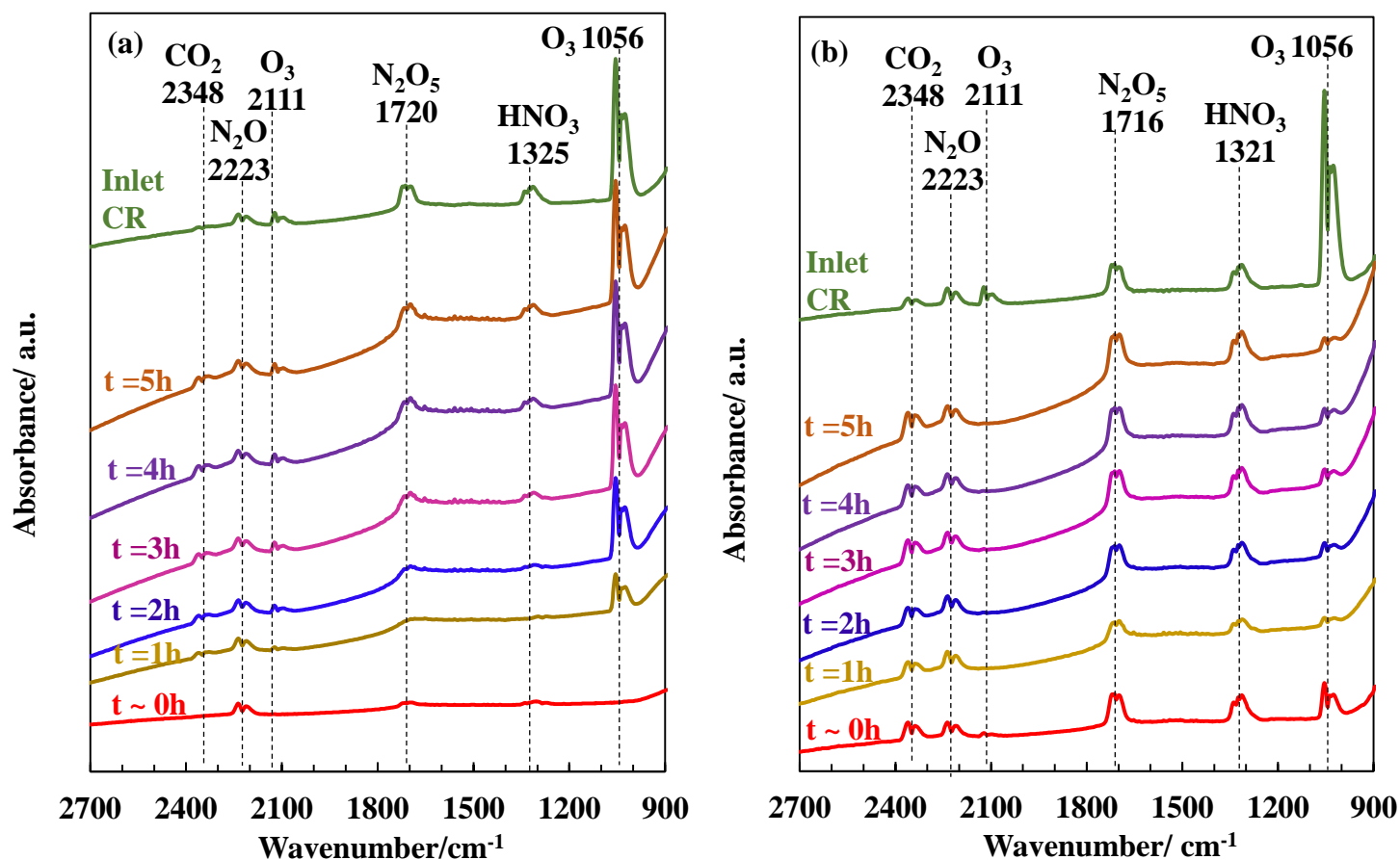


Figure 6 - 11: Temporal evolution of the gas phase species for O_3 decomposition in air (RH~0.7 %) over (a) $\text{Ce}_{0.01}\text{Mn}$, (b) $\text{Ce}_{0.01}\text{Mn-AT}$

In the presence of humidity, the FTIR spectrum of the inlet gaseous stream is significantly affected (**Figure 6-12**). N_2O_5 is no longer observed while the band intensity ascribed to HNO_3 is enhanced. Additionally, some broad bands at 1409 cm^{-1} and 1477 cm^{-1} are now observed whose assignments are currently unclear. Besides, the strong band at 1627 cm^{-1} has been assigned to water. N_2O_5 reacts with H_2O to give HNO_3 . Interestingly, the release of CO_2 in the early stages of the reactions can be linked to the destruction of surface carbonate species at the catalyst surface of $\text{Ce}_{0.01}\text{Mn-AT}$. Consequently, the activation period of the catalyst can be partly explained by a progressive recovery of active sites poisoned by carbonate like species. It is worthwhile to note that the distribution of the nitrogen containing species keeps rather unchanged in the course of the reaction.

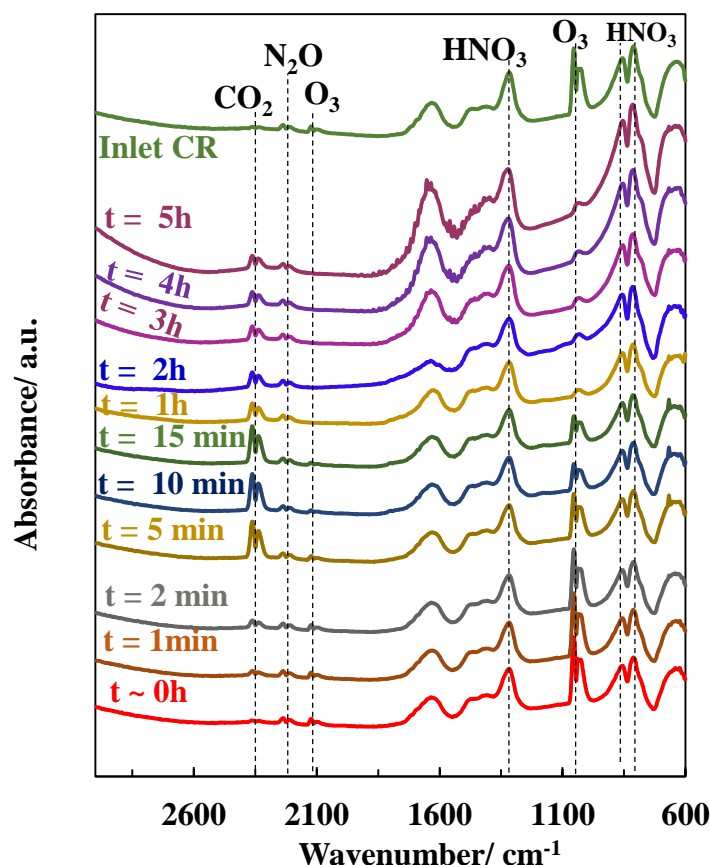
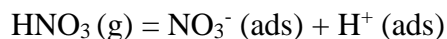


Figure 6 - 12: Temporal evolution of the gas phase species for O_3 decomposition in moist air (RH~30 %) over $\text{Ce}_{0.01}\text{Mn-AT}$

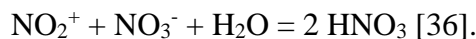
6-3-4- Characterizations studies after O_3 testing

X-ray photoelectron spectroscopy has been used to evidence adsorbed nitrogen related products on the non-treated Ce_xMn catalyst surfaces as a consequence of the uptake of N_2O_5 and HNO_3 in the gas phase at the early stages of O_3 decomposition. The high-resolution spectra of the N 1s region shown in **Figure 6-13** highlight the presence of adsorbed nitrogen containing species that differ in the oxidation state of nitrogen atom and the pertinent data have been given in **Table 6-6**. Considering the non-treated catalyst (**Figure 6-13(a)**) a predominant peak at BE of ~ 406.8 eV and small contributions at ~ 403.2 eV and about 400.0 eV have been assigned to adsorbed nitrate (NO_3^-) [32], nitrite (NO_2^-) [32] and to reduced N such as NO^- [33]. It has to be noted that the N/Mn atomic ratio of 0.08 on Mn-B- O_3 increases slightly for low Ce/Mn ratios but increases significantly for higher ratios to reach a value of 0.24 for $\text{Ce}_{0.5}\text{M-O}_3$ (see **Table 6-6**).

Formation of predominantly adsorbed nitrate is observed upon uptake of gaseous HNO_3 and N_2O_5 . The formation of NO_3^- (ads) species can occur owing to:



Nitrates can react with Mn/Ce cationic sites and the protons on oxygen sites [34,35]. Formation of adsorbed nitrate ions has been previously observed after exposure of hematite (α -Fe₂O₃) surface to gaseous HNO₃ [32]. Regarding N₂O₅, it can autoionize to NO₂⁺ and NO₃⁻ and react with water owing to:



The presence of NO₂⁻ and NO⁻ are believed to occur from the partial reduction of nitrate into nitrite on the catalysts.

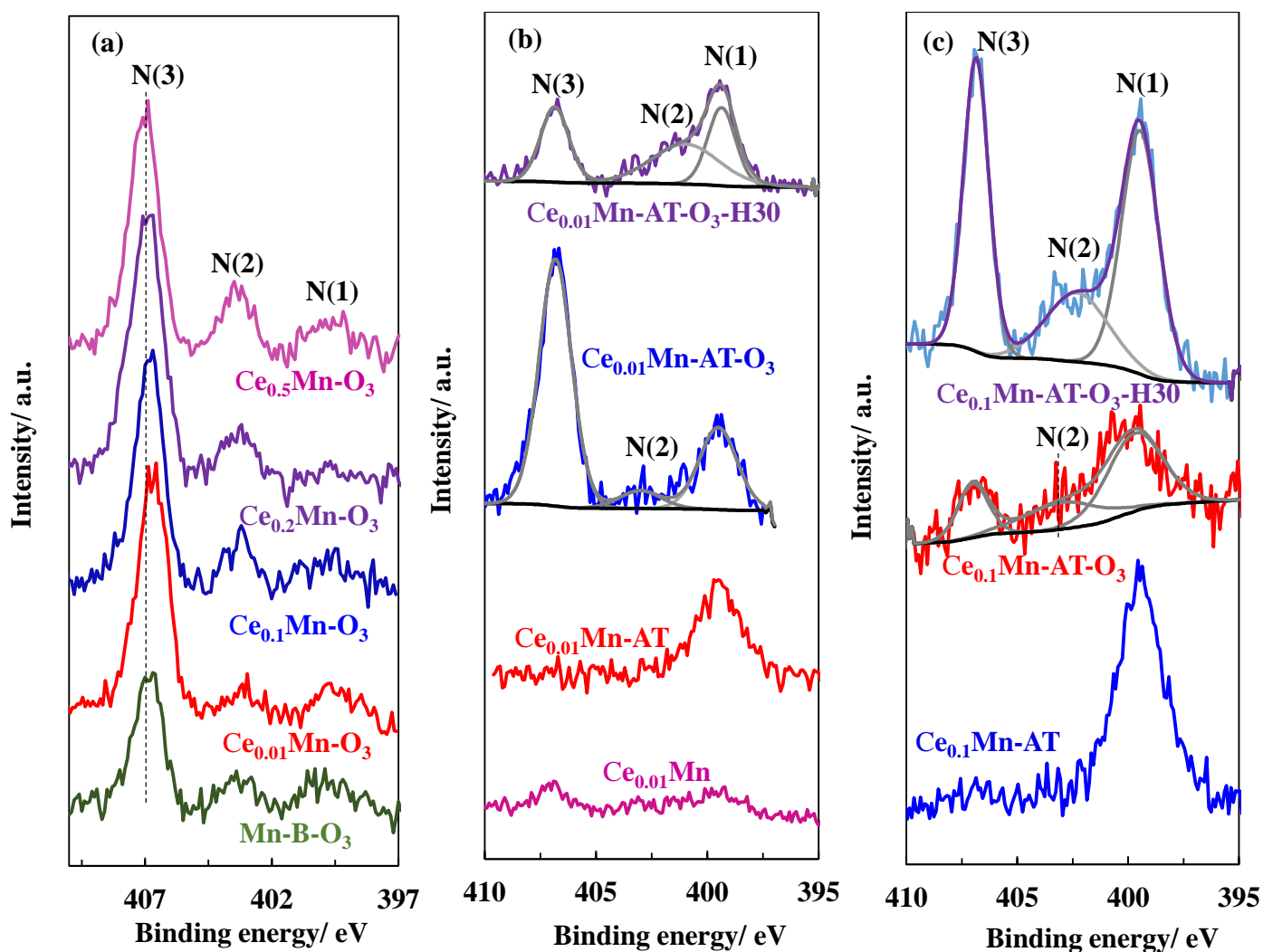


Figure 6 - 13: X-ray photoelectron spectra of the N 1s core level of the tested catalysts (a) untreated; (b-c) acid treated

Considering now the acid treated catalysts, it has to be mentioned that a small but significant contribution of N 1s at about 400.0 eV is always detected for the fresh acid treated catalysts indicating the presence of reduced nitrogen species induced by the acid treatment. Taking this N 1s contribution into account, a corrected N/Mn atomic ratio (N/Mn)_c which is the

difference between the N/Mn atomic ratios of the tested and fresh catalysts has been calculated. It has a value of 0.09 for Mn-B-AT and for the cerium-based catalysts it increases from 0.04 to 0.25 with increasing Ce content. Besides, it is remarkable to note that this ratio correlates with O₃ conversion in agreement with a poisoning of the catalytic sites (**Figure 6 - 14**). Besides, in the presence of significant amount of water (RH = 30 %) (N/Mn)_c drops strongly to reach 0.01 and 0.02 for Ce_{0.01}Mn-O₃-H and Ce_{0.01}Mn-O₃-H, respectively. Additionally, the N 1s contribution located at 403.0 eV disappears and a new N 1s component emerges at 401.0 eV and 402.3 eV for Ce/Mn of 0.01 and 0.1, respectively as seen in **Figure 6-13 (b) and (c)**. Consequently, water enhances both the presence of reduced surface-bound nitrogen related products and decreases substantially the amount of nitrogen adsorbed species.

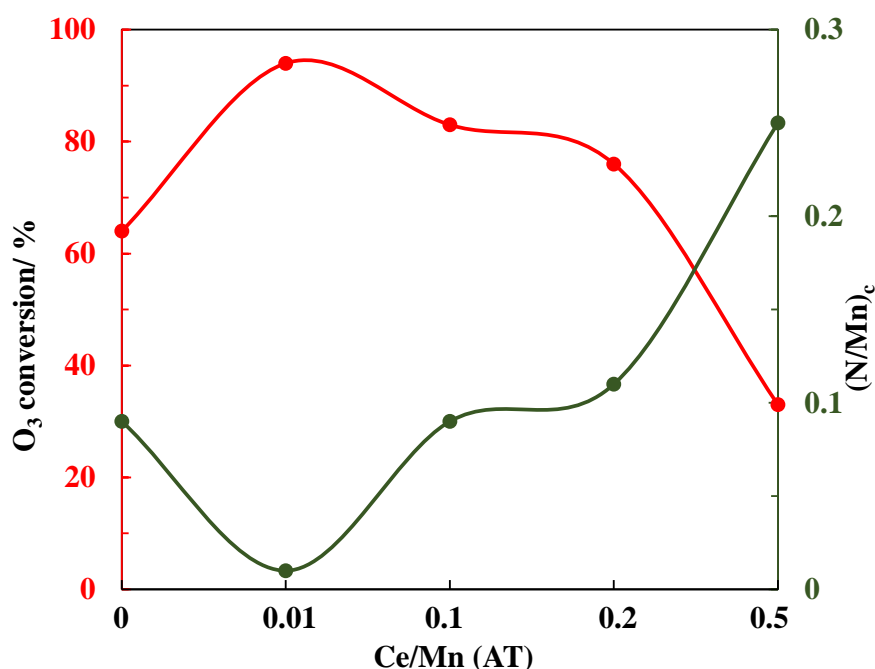


Figure 6 - 14: Correlation between O₃ conversion and poisoning of active sites by N adspecies for the catalysts treated with acid

Table 6 - 6: N1s components and N/Mn XPS ratios for the treated catalysts

Catalyst	Position (eV)			% atom			N/Mn	(N/Mn) _c
	N (1)	N (2)	N (3)	N (1)	N (2)	N (3)		
Mn-B-O ₃	399.8	403.3	406.9	21.3	15.5	63.1	0.08	-
Ce _{0.01} Mn-O ₃	399.5	403.2	406.7	16.7	12.7	70.6	0.11	-
Ce _{0.1} Mn-O ₃	399.8	403.3	406.8	12.9	14.1	73.0	0.10	-
Ce _{0.2} Mn-O ₃	399.7	403.3	406.9	2.2	14.3	83.4	0.16	-
Ce _{0.5} Mn-O ₃	399.7	403.4	407.0	12.5	18.1	69.4	0.24	-
Mn-B-AT-O ₃	399.5	401.5	406.8	18.7	18.1	63.2	0.12	0.09
Ce _{0.01} Mn-AT-O ₃	399.5	403.0	406.8	26.3	6.3	67.4	0.09	0.04
Ce _{0.01} Mn-AT-O ₃ -H	399.3	401.0	406.8	31.1	38.7	30.2	0.06	0.01
Ce _{0.1} Mn-AT-O ₃	399.7	403.0	407.0	54.2	25.3	20.5	0.15	0.09
Ce _{0.1} Mn-AT-O ₃ -H	399.5	402.3	406.8	43.6	20.5	35.8	0.08	0.02
Ce _{0.2} Mn-AT-O ₃	399.7	403.0	407.0	22.5	11.0	66.5	0.16	0.11
Ce _{0.5} Mn-AT-O ₃	399.6	403.4	407.0	17.9	14.3	67.7	0.32	0.25

FTIR-ATR has been used for detecting surface nitrogen containing species. Tentative band assignments of FTIR-ATR spectra have been performed based on XPS results showing that most nitrogen containing species on Ce_xMn catalysts are nitrates. In addition to free nitrate ion, NO_3^- can be coordinated in different ways (monodentate, bidentate chelating and/or bridging) [34]. The FTIR-ATR spectra of the different series of catalysts recorded between 700 cm^{-1} and 1820 cm^{-1} are displayed in **Figure 6-15**.

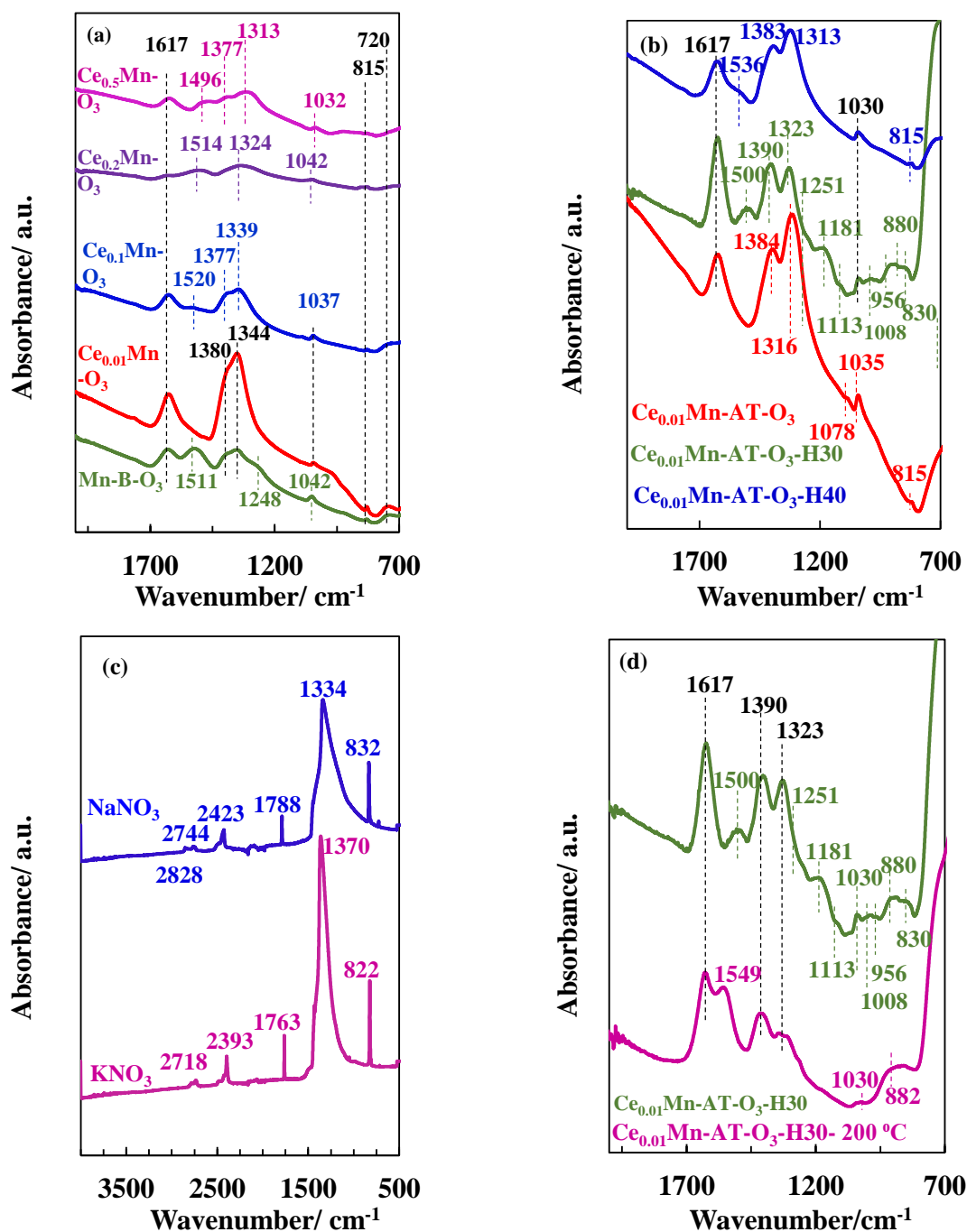


Figure 6 - 15: FTIR-ATR spectra of the tested catalysts (a): at RH = 0.7 % ; (b) at RH = 30 % and (c) reference FTIR-ATR spectra of metal alkali nitrates ; (d) FTIR-ATR spectra of $\text{Ce}_{0.01}\text{Mn-AT-O}_3\text{-H30}$ and after heating at $200\text{ }^\circ\text{C}$ for 4 h.

Considering the non-treated catalysts after testing (**Figure 6-15 (a)**) with Ce/Mn ratios lower than 0.2 the band which appears at highest frequency positioned at 1617 cm^{-1} has been principally assigned to the bending mode of water [27]. There are at least three different bands in the medium frequency range ($1400\text{--}1200\text{ cm}^{-1}$) around 1380 , 1340 and 1250 cm^{-1} . By comparison with reference spectra of alkali metal nitrates (**Figure 6-15 (c)**) the two intense bands located at about 1380 cm^{-1} and 1340 cm^{-1} have been assigned to adsorbed ionic nitrate in interaction with K^+ and Na^+ , respectively, in line with the presence of a band at about 815 cm^{-1} attributed to the out-of-plane rocking mode. Considering the FTIR spectra of Mn-B-O_3 the remaining distinct three bands at 1511 cm^{-1} , 1248 cm^{-1} and 1042 cm^{-1} can be ascribed to bidentate nitrato ligands [34] linked to manganese cations in accordance with the works of D. Pozdnyakov *et al.* [37]. In the presence of low cerium content, it is observed that the relative intensity of these bands is decreasing indicating that this mode of interaction decreases with Ce content. For higher Ce/Mn ratio, although the bands are larger and overlap, the above general conclusions hold on. In (**Figure 6-15 (b)**) are represented the FTIR-ATR spectra of the acid treated $\text{Ce}_{0.01}\text{Mn}$ catalyst after testing in nearly dry and moist air at $30\text{ }^\circ\text{C}$ and $40\text{ }^\circ\text{C}$. It turns out that the spectrum of $\text{Ce}_{0.01}\text{Mn-AT-O}_3$ is rather similar than that of $\text{Ce}_{0.01}\text{Mn-O}_3$ except that the most intense band is now shifted from 1344 cm^{-1} to 1310 cm^{-1} . In moist air ($\text{RH} = 30\%$) the number of bands increases and all the more that temperature decreases. At $30\text{ }^\circ\text{C}$ the band characteristic of water at 1617 cm^{-1} is the most intense. A new band appears at about 1500 cm^{-1} attributed again to bidentate NO_3^- . However, the presence of such nitrato species does not seem to affect greatly the activity of the catalyst. The effect of temperature on the adsorbed nitrogen containing species has also been investigated in the case of $\text{Ce}_{0.2}\text{Mn}$. **Figure 6-15 (d)** compares the FTIR-ATR spectrum of $\text{Ce}_{0.2}\text{Mn-O}_3$ with that obtained after heating the sample at $200\text{ }^\circ\text{C}$ for 4h in an oven. It is observed that the prominent IR bands at 1390 cm^{-1} and 1323 cm^{-1} decrease strongly in intensity as compared to the other ones. This indicates clearly that the ionic nitrates interact in a less manner than the nitrato ligands.

ToF-SIMS in static mode has been applied to get valuable insight on the outermost surface. In the negative ToF-SIMS spectra, the detection of secondary ions NO_3^- ($m/z = 62$), NO_2^- ($m/z = 46$) and NO^- ($m/z = 30$) reveals the presence of adsorbed nitrate/nitrite species at the surface of all samples. Observance of HNO_3^- at $m/z = 63$ indicates that nitric acid adsorbed also molecularly to some extent. Additionally, a series of MNO_x^- ($\text{M} = \text{Mn, Ce}$) secondary ions have been observed (see **Table 6-7**) which provided direct evidence of interactions between nitrogen containing species and cerium and manganese cations on the catalyst surface.

Table 6- 7: Nitrogen containing secondary ions from ToF-SIMS spectra in polarity (-) of the tested catalysts

NO_2H_w^-	$\text{Ce}_x\text{NO}_2\text{H}_w^-$	$\text{Mn}_y\text{NO}_2\text{H}_w^-$
NO	CeN ₂ O ₃	MnNO ₂
NO ₃	CeN ₂ O ₃ H	MnNO ₂ H
HNO ₃	CeNO ₄	MnNO ₃
	CeNO ₄ H	MnNO ₃ H
	CeN ₃ O ₃ H	
	CeNO ₅	
	CeNO ₅ H	
	CeNO ₆	

Besides, the effect of ozone decomposition has been investigated in polarity (+) by ToF-SIMS for the Ce_{0.1}Mn sample as shown in **Table 6-8**. A significant enrichment of K⁺ and Na⁺ is noticed in line with the presence of ionic NO₃⁻ previously postulated from FTIR-ATR results.

Table 6 - 8: ToF-SIMS data in positive polarity for Ce_{0.1}Mn before and after ozone decomposition

Catalyst	CeO ⁺ /MnO ⁺	K ⁺ /MnO ⁺	Na ⁺ /MnO ⁺	CeOMn ⁺ / MnO ⁺
Ce _{0.1} Mn	4.67	1.90	5.90	0.17
Ce _{0.1} Mn-O ₃	3.75	18.74	54.54	0.13

Figure 6 - 16 exhibits the normalized MS profiles during TPD on Mn-B-AT-O₃, Ce_{0.01}Mn-AT-O₃ and Ce_{0.1}Mn-AT-O₃. It is shown that NO **Figure 6 - 16 (a)** (m/z = 30) and O₂ (m/z = 32) **Figure 6 -16 (b)** are the major decomposition products of nitrogen containing adsorbates. A decrease in the NO desorption onset and peak temperature is observed with increasing Ce content which indicates that addition of cerium decreases the interaction of the NO_x⁻ adsorbates with the catalyst. Additionally, the relative amount of desorbed NO increases with S_{BET}. It is suggested that the wide temperature range of NO desorption can be linked to various forms of nitrate/nitrite interaction with M⁴⁺/M³⁺ (M = Mn, Ce) cations of the cerium modified birnessite.

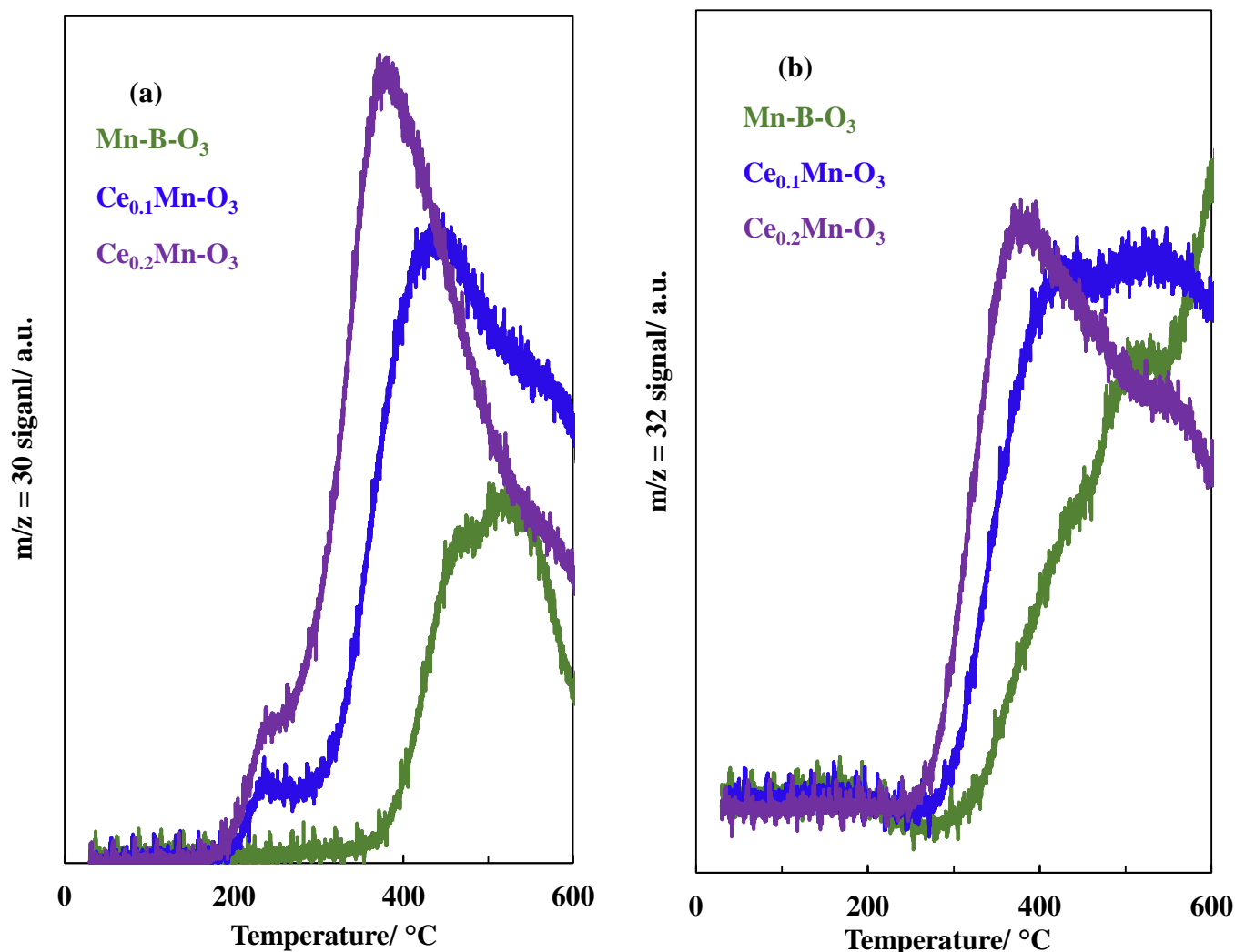


Figure 6 - 16: Temporal evolution during TPD (a) of the signal $m/z = 30$ and (b) of the signal $m/z = 32$ for Mn-B-AT-O₃, Ce_{0.01}Mn-AT-O₃ and Ce_{0.1}Mn-AT-O₃

6-3-5- Effect of nitrogen containing co-pollutants for gaseous ozone decomposition

On the basis of the different results, the deactivation of the non-treated Ce modified birnessite-type MnO_2 catalysts in nearly dry air with nitrogen containing co-pollutants results from adsorbed nitrogen based species which poison to a high extent the catalytic surface. It has been noted that the contribution of adsorbed nitrate is the most important. Ionic nitrates in interaction with alkali metal cations (K^+ , Na^+) and nitrato ligands in interaction with the $\text{M}^{4+}/\text{M}^{3+}$ ($\text{M} = \text{Mn}$, Ce) have been clearly identified. Such various adspecies having different modes of interactions with the surface can account for the wide window of temperature observed for NO and O_2 evolutions during TPD-MS experiments of some used catalysts. For the acid-treated catalysts the extent of deactivation is lower and cannot be explain solely on the basis of an increase of the specific surface area as no clear correlation appears between the specific surface area and extent of deactivation. In contrast the final activity of the catalysts

correlates well with the onset temperature of reduction of the catalysts (**Figure 6 – 17**) which may signify that the oxygen vacancies play an important role. In addition, the acidity resulting from the acid treatment must also be taken into account because $\text{Ce}_{0.1}\text{Mn-AT}$, which is more active than $\text{Ce}_{0.2}\text{Mn-AT}$, has more active sites.

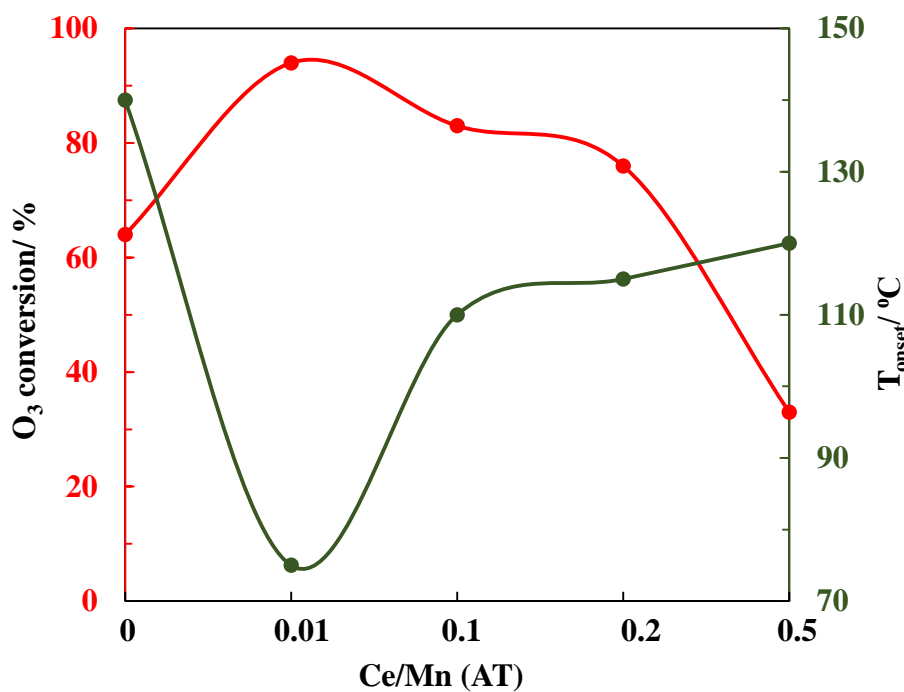


Figure 6 - 17: Correlation between O_3 conversion and T_{onset} for the acid treated catalysts

Additionally, the high activity of $\text{Ce}_x\text{Mn-AT}$ ($x = 0.01; 0.1$) in moist air ($\text{RH} = 30\%$) in the presence of nitrogen containing co-pollutants can be envisioned considering the mechanism for O_3 decomposition in humid air involving acid sites and oxygen vacancies proposed by Liu. *et al.* [15]. More water acid sites in interaction with oxygen vacancy results in a better hydrophobic catalyst that can facilitate adsorption and subsequent decomposition of gaseous ozone. Furthermore, in the presence of water, the contribution of N-adspecies is significantly reduced and the distribution of reduced N-based adspecies is much larger, suggesting a catalytic reduction of NO^{3-} -adsorbed species.

6-4- Conclusion

A pioneer series of experiments were performed to study the decomposition of ozone in the presence of nitrogen pollutants and humidity on acid-treated Ce modified birnessites. The main findings could be summarized as follows: The performances of ozone decomposition were closely related to the presence of nitrogen pollutants. At very low humidity, the acid treated catalysts showed a minimization of deactivation while the non-treated catalysts deactivate rapidly over time on stream due to nitrate poisoning. At higher RH, after an induction period, the acid treated catalysts were effective for the elimination of ozone and stable during 5 h of reaction. Higher amounts of oxygen vacancies and acid sites were invoked to improve water resistance properties and to decrease nitrate interaction. The generation of such efficient catalysts open new perspectives for ozone decomposition from polluted air.

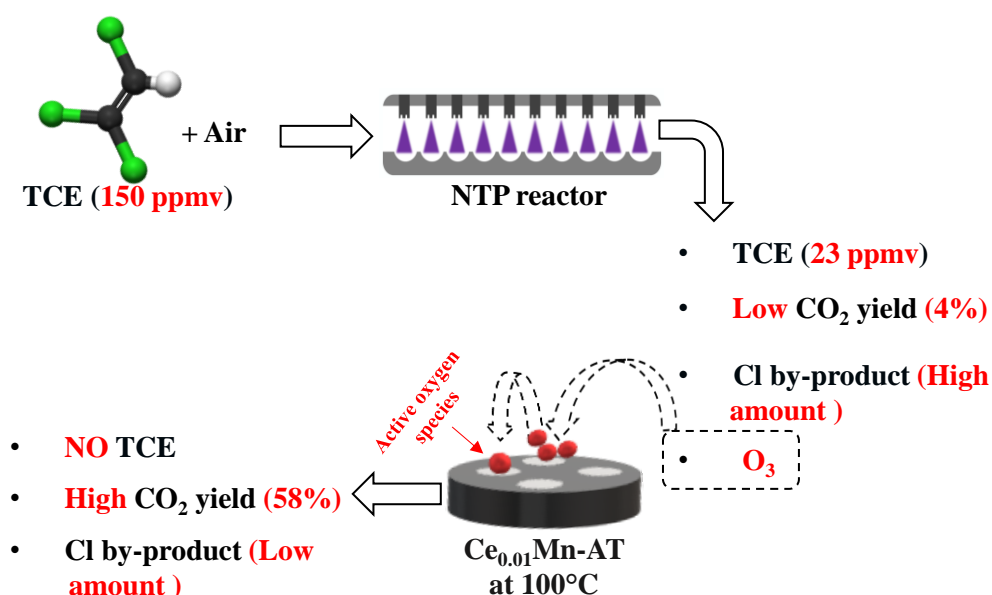
6-5- References

- [1] T. Gopi, G. Swetha, S. Chandra Shekar, C. Ramakrishna, B. Saini, R. Krishna, P.V.L. Rao, *Catal. Commun.* 92 (2017) 51–55.
- [2] J. Jia, P. Zhang, L. Chen, *Appl. Catal. B Environ.* 198 (2016) 210–218.
- [3] G. Zhu, J. Zhu, W. Jiang, Z. Zhang, J. Wang, Y. Zhu, Q. Zhang, *Appl. Catal. B Environ.* 209 (2017) 729–737.
- [4] Y. Liu, W. Yang, P. Zhang, J. Zhang, *Appl. Surf. Sci.* 442 (2018) 640–649.
- [5] Y. Wang, F. Wang, Q. Song, Q. Xin, S. Xu, J. Xu, *J. Am. Chem. Soc.* 135 (2013) 1506–1515.
- [6] Z. Lian, J. Ma, H. He, *Catal. Commun.* 59 (2015) 156–160.
- [7] L. Zhu, J. Wang, S. Rong, H. Wang, P. Zhang, *Appl. Catal. B Environ.* 211 (2017) 212–221.
- [8] Y. Liu, P. Zhang, *Appl. Catal. Gen.* 530 (2017) 102–110.
- [9] R. Sindhu, G. Amba Prasad Rao, K. Madhu Murthy, *Alex. Eng. J.* 57 (2018) 1379–1392.
- [10] D. Mehandjiev, A. Naydenov, G. Ivanov, *Appl. Catal. Gen.* 206 (2001) 13–18.
- [11] C. Subrahmanyam, D.A. Bulushev, L. Kiwi-Minsker, *Appl. Catal. B Environ.* 61 (2005) 98–106.
- [12] H. Touati, A. Guerin, Y. Swesi, C.B. Dupeyrat, R. Philippe, V. Meille, J.-M. Clacens, *Catal. Commun.* 148 (2021) 106163.
- [13] V.A. Drits, E. Silvester, A.I. Gorshkov, A. Manceau, *Am. Mineral.* 82 (1997) 946–961.
- [14] S. Royer, D. Duprez, S. Kaliaguine, *J. Catal.* 234 (2005) 364–375.
- [15] R. Vidruk, M.V. Landau, M. Herskowitz, M. Talianker, N. Frage, V. Ezersky, N. Froumin, *J. Catal.* 263 (2009) 196–204.
- [16] H. Hojo, T. Mizoguchi, H. Ohta, S.D. Findlay, N. Shibata, T. Yamamoto, Y. Ikuhara, *Nano Lett.* 10 (2010) 4668–4672.
- [17] Q. Fu, W.-X. Li, Y. Yao, H. Liu, H.-Y. Su, D. Ma, X.-K. Gu, L. Chen, Z. Wang, H. Zhang, B. Wang, X. Bao, *Science* 328 (2010) 1141–1144.
- [18] M. Sakai, Y. Nagai, Y. Aoki, N. Takahashi, *Appl. Catal. Gen.* 510 (2016) 57–63.
- [19] W. Gac, G. Słowik, W. Zawadzki, *Appl. Surf. Sci.* 370 (2016) 536–544.
- [20] B.-B. Chen, X.-B. Zhu, Y.-D. Wang, L.-M. Yu, J.-Q. Lu, C. Shi, *Catal. Today* 281 (2017) 512–519.
- [21] J. Chen, X. Chen, D. Yan, M. Jiang, W. Xu, H. Yu, H. Jia, *Appl. Catal. B Environ.* 250 (2019) 396–407.

- [22] P. Zhang, H. Lu, Y. Zhou, L. Zhang, Z. Wu, S. Yang, H. Shi, Q. Zhu, Y. Chen, S. Dai, *Nat. Commun.* 6 (2015) 8446.
- [23] Y. Liu, W. Yang, P. Zhang, J. Zhang, *Appl. Surf. Sci.* 442 (2018) 640–649.
- [24] R. Cao, P. Zhang, Y. Liu, X. Zheng, *Appl. Surf. Sci.* 495 (2019) 143607.
- [25] Y. Liu, H. Zhou, R. Cao, X. Liu, P. Zhang, J. Zhan, L. Liu, *Appl. Catal. B Environ.* 245 (2019) 569–582.
- [26] B. de Rivas, R. López-Fonseca, J.R. González-Velasco, J.I. Gutiérrez-Ortiz, *J. Mol. Catal. Chem.* 278 (2007) 181–188.
- [27] E. Eren, H. Gumus, B. Eren, A. Sarihan, (n.d.) 8.
- [28] T. Mathew, K. Suzuki, Y. Ikuta, N. Takahashi, H. Shinjoh, *Chem. Commun.* 48 (2012) 10987.
- [29] D.R. Mullins, S.H. Overbury, D.R. Huntley, *Surf. Sci.* 409 (1998) 307–319.
- [30] H. Wang, J. Zhang, X. Hang, X. Zhang, J. Xie, B. Pan, Y. Xie, *Angew. Chem. Int. Ed.* 54 (2015) 1195–1199.
- [31] C. Sun, N. Zhao, Z. Zhuang, H. Wang, Y. Liu, X. Weng, Z. Wu, *J. Hazard. Mater.* 274 (2014) 376–383.
- [32] C.E. Nanayakkara, P.M. Jayaweera, G. Rubasinghege, J. Baltrusaitis, V.H. Grassian, *J. Phys. Chem. A* 118 (2014) 158–166.
- [33] J. Baltrusaitis, P.M. Jayaweera, V.H. Grassian, *Phys. Chem. Chem. Phys.* 11 (2009) 8295.
- [34] K.I. Hadjiivanov, *Catal. Rev.* 42 (2000) 71–144.
- [35] M. Machida, M. Uto, D. Kurogi, T. Kijima, *Chem. Mater.* 12 (2000) 3158–3164.
- [36] L. Brouwer, M.J. Rossi, D.M. Golden, (n.d.) 5.
- [37] D.V. Pozdnyakov, V.N. Filimonov, *Adv. Mol. Relax. Process.* 5 (1973) 55–63.

Chapter 7:

POST PLASMA CATALYSIS FOR TRICHLOROETHYLENE ABATEMENT WITH Ce DOPED BIRNESSITE DOWNSTREAM DC CORONA DISCHARGE REACTOR



This chapter has been published as an article in the following International journal:

Grâce Abdallah, Jean-Marc Giraudon, Rim Bitar, Nathalie De Geyter, Rino Morent, Jean-François Lamonier, “ Post Plasma Catalysis for Trichloroethylene Abatement with Ce-Doped Birnessite Downstream DC Corona Discharge Reactor”, *Catalysts*, 2021, 11, 946.

7-1- Introduction

The third validation approach as seen in [chapter 2](#), was to investigate the abatement of TCE in dry and humid gas stream in PPC process, by following all the above required conditions: (i) the flow rate and the energy density have been chosen according to [chapter 5](#) in order to optimize the initial molar ratio $[O_3]/[TCE] = 4$. (ii) the most active catalyst for HCHO oxidation ([Chapter 4](#)) and for O_3 decomposition ([Chapter 6](#)) has been chosen for TCE abatement.

Trichloroethylene (TCE), is a chlorinated VOC commonly used in industry as a solvent and acts as a degreaser in the semiconductor and metal industry [1–3]. Due to its adverse impacts on environmental and human health (carcinogenic Group 1), TCE removal from waste gas streams is an issue of major concern. Conventional techniques, such as adsorption, thermal incineration, or catalytic oxidation can be used for chlorinated VOC removal. However, such techniques are not energy efficient for the removal of diluted VOCs (<1000 ppmv) from the waste gas [4–8]. In these last decades, post plasma catalysis (PPC) resulting from the coupling of a Non-Thermal Plasma (NTP) reactor with a catalytic reactor positioned downstream was recognized as an advanced oxidation process for diluted VOCs removal in waste air [9,10]. Although NTP displays a high reactivity towards VOC removal at 20°C, the selectivity of the process into CO_x (CO and CO₂) is poor and gaseous byproducts hazardous are formed. In PPC configuration catalytic reactions can take advantages of the NTP emitted O_3 as a potential source of active oxygen species enabling further oxidation at ambient or very low temperatures of the NTP non-degraded parent VOC and NTP gaseous hazardous by-products. Therefore, this resulting hybrid technology can overpass NTP and total oxidation catalysis in terms of selectivity, efficiency and energy cost.

The catalyst positioned after the plasma reactor must have specific characteristics such as high efficiency in plasma generated ozone decomposition, high oxygen mobility, high CO₂ selectivity, coupled with an elevated resistance to chlorine. MnO₂ based catalysts have been particularly studied in PPC configuration for TCE removal because of their high ability to decompose ozone to provide surface active oxygen species for the decomposition of plasma-generated polychlorinated by-products [11,12]. However, the plasma-generated by-products are not fully decomposed into CO₂ and the catalysts deactivate over time due to chlorine induced deactivation. In order to promote the efficiency of PPC process towards chlorinated VOC abatement, the catalyst efficiency should be improved.

In this paper the TCE abatement is investigated in PPC configuration in dry and moist air (15 %) with NTP using a 10 pin-to plate negative DC corona discharge and with PPC using $\text{Ce}_{0.01}\text{Mn}$ as catalyst calcined at 400 °C ($\text{Ce}_{0.01}\text{Mn}$ -400) or treated with nitric acid ($\text{Ce}_{0.01}\text{Mn}$ -AT). In order to increase the efficiency of the NTP assisted catalyst for TCE total oxidation, particular attention has been paid to regulate the ratio of NTP generated ozone concentration to that of inlet TCE. The effect of humidity towards TCE abatement in plasma alone and in PPC process has been also investigated. Finally, the performance of the plasma-assisted catalysts for TCE abatement have been correlated with the physico-chemical properties of the tested catalysts.

7-2- Experimental conditions

Table 7-1, summarizes the basic experimental conditions used in this chapter. The detailed preparation process, characterization process of catalysts and experiment process can be seen in chapter 3.

Table 7 - 1: Experimental conditions

Air source	Air liquide, alphagaz 1
Flow rate	1 L/min
Relative humidity (RH)	0.7 % / 15 %
Energy density	150 J/L
Initial TCE concentration	150 ppmv
Catalyst	$\text{Ce}_{0.01}\text{Mn}$ -400 and $\text{Ce}_{0.01}\text{Mn}$ -AT 0.1 g of catalyst mixed with 1g of SiC
Activation conditions	200 mL/ min, 100°C for 1 hour
Catalyst temperature	100 °C

7-3- Results and discussion

7-3-1- Main physicochemical characterizations of the fresh materials

The powder XRD patterns of samples are shown in **Figure 7-1**. $\text{Ce}_{0.01}\text{Mn}$ -400 sample is poorly crystallized and exhibits four broad peaks centered at 12.2 ° (001), 24.5° (002), 37.0° (110) and 66.2° (110) which are characteristics for turbostratic birnessite structure [13]. The XRD pattern of $\text{Ce}_{0.01}\text{Mn}$ -AT sample is ill-defined and presents a diffraction peaks centered at 37.0 ° and 66.2 °. However, the two diffraction peaks (001) and (002) are no more visible in the powder XRD pattern of $\text{Ce}_{0.01}\text{Mn}$ -AT sample. This could be related to the diminution of the number of layers stacked in the crystal after the acidic treatment. Indeed, when the coherent

scattering domain size decreases, the intensity of the peaks decreases and their full width at half maximum increase [14,15].

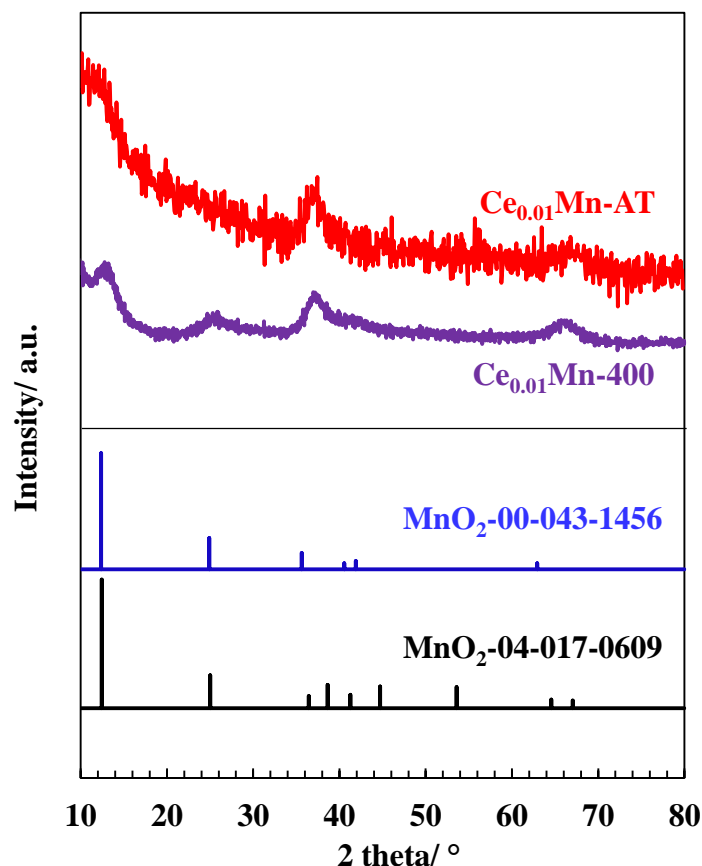


Figure 7 - 1: XRD patterns of $\text{Ce}_{0.01}\text{Mn-400}$ and $\text{Ce}_{0.01}\text{Mn-AT}$ samples

The elemental compositions of the material after calcination and acid treatment are given in **Table 7-2**. The Ce/Mn atomic ratio for $\text{Ce}_{0.01}\text{Mn-400}$ is close to the expected value (0.01) and the value is slightly modified after acid treatment. After acid treatment the Na and K contents decreased drastically: the Na/Mn as well the K/Mn ratio significantly dropped. This result can be partly explained by $\text{Na}^+\text{-H}^+$ and $\text{K}^+\text{-H}^+$ ion exchange reactions [16,17].

Table 7 - 2: Weight composition and atomic ratio for $\text{Ce}_{0.01}\text{Mn-400}$ and $\text{Ce}_{0.01}\text{Mn-AT}$ samples

Sample	Weight / %				Atomic ratio		
	K	Na	Ce	Mn	K/Mn	Na/Mn	Ce/Mn
$\text{Ce}_{0.01}\text{Mn-400}$	7.10	1.99	1.18	49.20	0.340	0.057	0.009
$\text{Ce}_{0.01}\text{Mn-AT}$	1.30	0.01	1.06	52.01	0.059	0.004	0.008

The N_2 adsorption/desorption isotherms and pore size distribution of $\text{Ce}_{0.01}\text{Mn-400}$ and $\text{Ce}_{0.01}\text{Mn-AT}$ samples are shown in **Figure 7-2** and the data coming from these isotherms, BET surface area (S_{BET}), pore diameter (D_p) and total pore volume (V_p), are gathered in **Table 7-3**. The two samples exhibit a type IV isotherm, given by mesoporous materials. However, the two

physisorption hysteresis loops appear in different shapes. $\text{Ce}_{0.01}\text{Mn-400}$ sample presents a H3 loop while $\text{Ce}_{0.01}\text{Mn-AT}$ presents a H2 loop. This change in hysteresis loop from H3 to H2 can be ascribed to the change in pore shape [18] caused by the acid treatment. Both surface area and total pore volume are significantly increased after acid treatment. Such textural properties modification can be explained by the H^+ exchange during the acid treatment which can destabilize the layered structure.

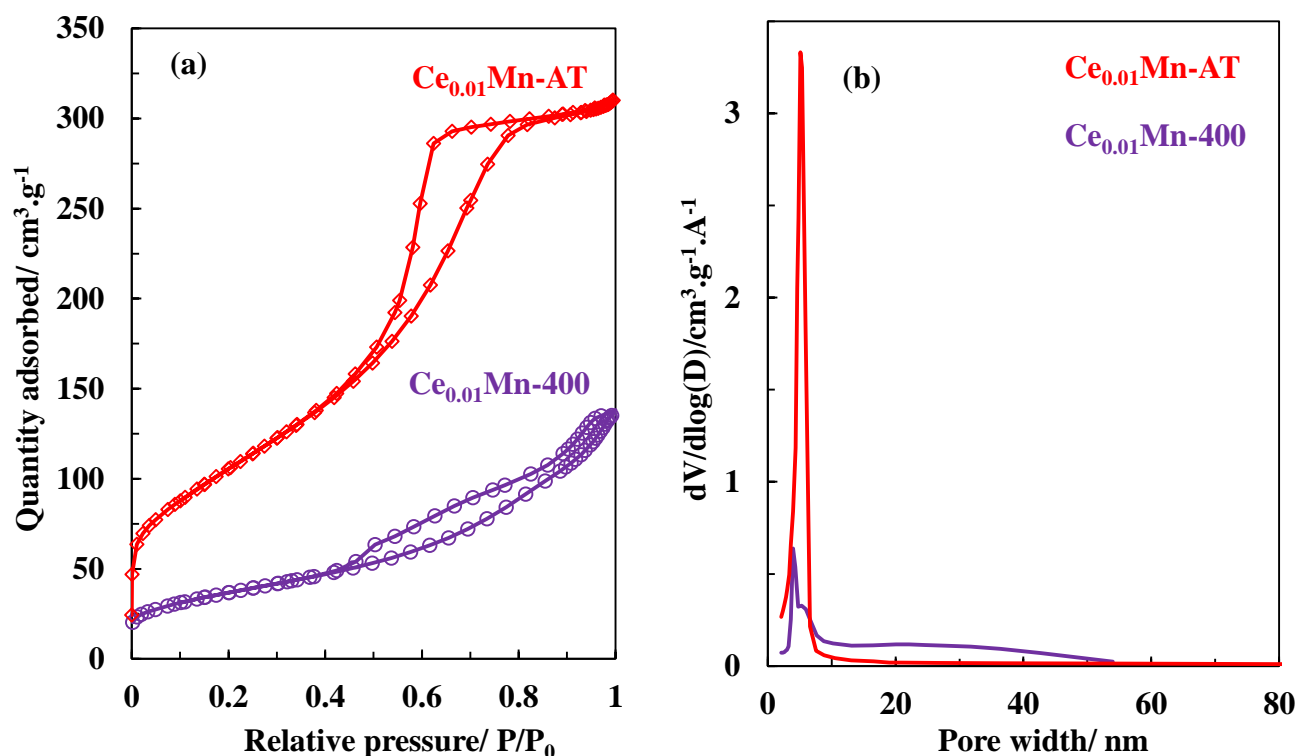


Figure 7 - 2: (a) N_2 adsorption-desorption (b) pore size distribution of $\text{Ce}_{0.01}\text{Mn-400}$ and $\text{Ce}_{0.01}\text{Mn-AT}$ samples

Table 7 - 3: Textural properties of the $\text{Ce}_{0.01}\text{Mn-400}$ and $\text{Ce}_{0.01}\text{Mn-AT}$ samples

Sample	$S_{\text{BET}} / \text{m}^2/\text{g}$	$D_{p_{\text{max}}} / \text{nm}$	$V_{p_{\text{tot}}} / \text{cm}^3/\text{g}$
$\text{Ce}_{0.01}\text{Mn-400}$	132	4.0	0.22
$\text{Ce}_{0.01}\text{Mn-AT}$	385	5.3	0.37

The change in surface acidity has been evaluated using pyridine as infrared probe molecule over dried $\text{Ce}_{0.01}\text{Mn}$ - and $\text{Ce}_{0.01}\text{Mn-AT}$ samples. FTIR spectra of the pyridine region obtained after pyridine adsorption at 150°C for dried $\text{Ce}_{0.01}\text{Mn}$ and $\text{Ce}_{0.01}\text{Mn-AT}$ samples are shown in **Figure 7-3**. The interaction of pyridine with dried $\text{Ce}_{0.01}\text{Mn}$ leads to spectrum with large bands. A narrower band can be observed at 1540 cm^{-1} which can be assigned to the formation of pyridinium ions coming from pyridine protonation on Brønsted acid sites. The interaction of pyridine with $\text{Ce}_{0.01}\text{Mn-AT}$ gives rise to a set of several bands: (i) two bands at

1540 and 1635 cm^{-1} owing to pyridinium ions coming from pyridine protonation on Brønsted acid sites, (ii) two bands at 1450 and 1610 cm^{-1} attributed to pyridine coordinated to Lewis acid sites and (iii) overlapping bands of pyridine on Lewis and Brønsted acid sites at 1487 cm^{-1} [16,19–22]. Moreover the band at 1573 cm^{-1} is attributed to the pyridine physisorption (P) [23] while the band at 1471 cm^{-1} could result from the interaction between the adsorbed pyridine and manganese oxides [24]. Mn^{3+} and Mn^{4+} species, as coordinatively unsaturated metal atom which can accept an electron pair, can be considered as Lewis acid sites while Brønsted acid sites can be identified as hydroxyl groups attached to the metal oxides (Mn-OH) [25].

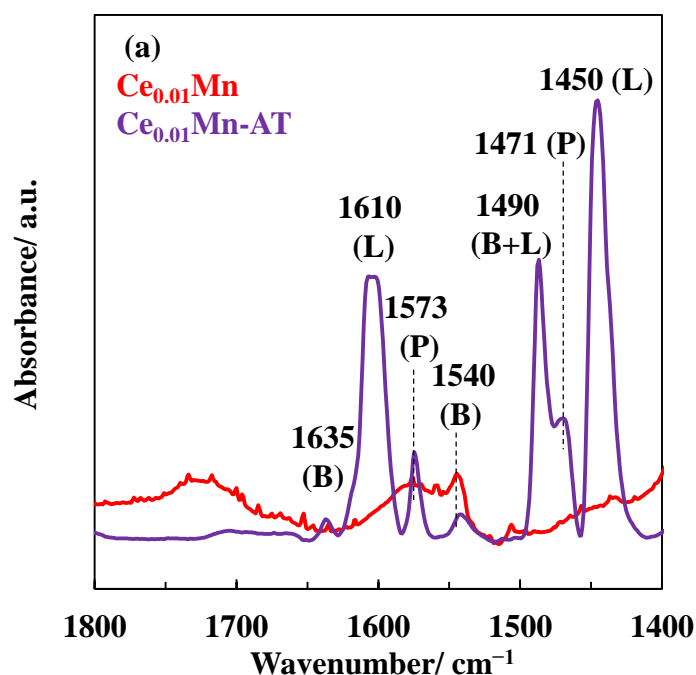


Figure 7 - 3: FTIR spectra of the Py region obtained after Py adsorption at 105°C for dried $\text{Ce}_{0.01}\text{Mn}$ and $\text{Ce}_{0.01}\text{Mn-AT}$ samples

The surface speciation of manganese species in both samples was assessed by analyzing the 2p photopeak of Mn. Mn 2p_{3/2} signal has been decomposed considering a mixture of Mn (III) and Mn (IV) as shown in **Figure 7-4** [26]. The obtained $\text{Mn}^{3+}/\text{Mn}^{4+}$ ratio is higher for the acid-treated sample (0.38) compared to the calcined one (0.33). In addition to curve-fitting of the Mn 2p_{3/2} signal, the Mn 3s photopeak can also provide useful insight into the Mn average oxidation state (Mn AOS) [27,28]. Indeed, the Mn 3s photopeak is split into two signals and the value of the splitting is an indication of the average oxidation state of Mn. Mn AOS values calculated from the Mn 3s splitting are 3.44 and 3.32 for $\text{Ce}_{0.01}\text{Mn-400}$ and $\text{Ce}_{0.01}\text{Mn-AT}$ samples, respectively. These results agree with the aforementioned $\text{Mn}^{3+}/\text{Mn}^{4+}$ ratio. As expected the acid treatment generated additional oxygen vacancies to maintain electronic balance, and more Mn^{3+} species are present at the surface of the $\text{Ce}_{0.01}\text{Mn-AT}$ sample [17,29].

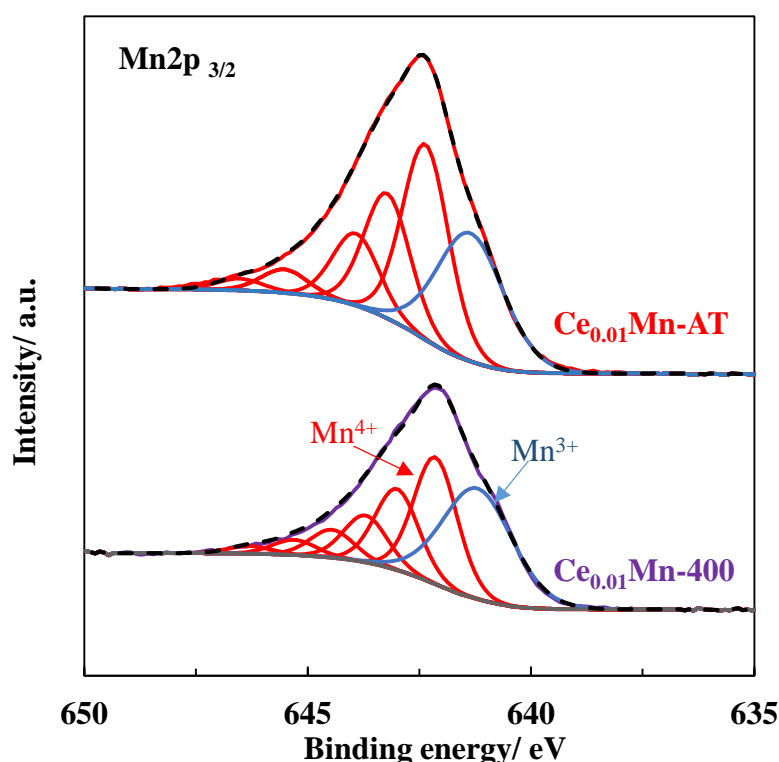


Figure 7 - 4: XPS Mn $2p_{3/2}$ core level decomposition for Ce $_{0.01}$ Mn-400 and Ce $_{0.01}$ Mn-AT samples

It should be noted, however, that it was not possible to assess the proportion of Ce $^{3+}$ /Ce $^{4+}$ in the samples due to Ce 3d and Auger Mn LMN peaks overlap.

7-3-2- O $_3$ decomposition over Ce $_{0.01}$ Mn-400 and Ce $_{0.01}$ Mn-AT samples using non-thermal plasma (NTP) as ozoner

Figure 7-5 presents the ozone decomposition at room temperature as a function of time with Ce $_{0.01}$ Mn-400 and Ce $_{0.01}$ Mn-AT catalysts. Ce $_{0.01}$ Mn-400 maintains high ozone conversion (> 97%) for 140 minutes but then shows a gradual decrease in ozone conversion to 73 % after 5 hours. Ce $_{0.01}$ Mn-AT exhibits different behavior with a low decrease in ozone conversion after 30 minutes of testing from 100 % to 94 % after 120 minutes. Thereafter Ce $_{0.01}$ Mn-AT is able to maintain this high conversion over time. It has been reported earlier that oxygen vacancies play a key role in ozone decomposition on manganese oxides. Therefore, the better catalytic performance of Ce $_{0.01}$ Mn-AT compared to that of Ce $_{0.01}$ Mn-400 is consistent with its more abundant oxygen vacancies in agreement with a higher amount of surface Mn $^{3+}$ species (XPS). This result confirms the important role of oxygen vacancies in the catalytic ozone decomposition as reported in the literature [30–33]. In addition, the larger specific surface area of Ce $_{0.01}$ Mn-AT may contribute to a wider surface exposure of oxygen vacancies. This could

explain the maintain of high ozone conversion in the presence $\text{Ce}_{0.01}\text{Mn-AT}$, while avoiding the saturation of the oxygen vacancies sites, probably at the origin of the observed deactivation in the presence of $\text{Ce}_{0.01}\text{Mn-400}$ [34,35].

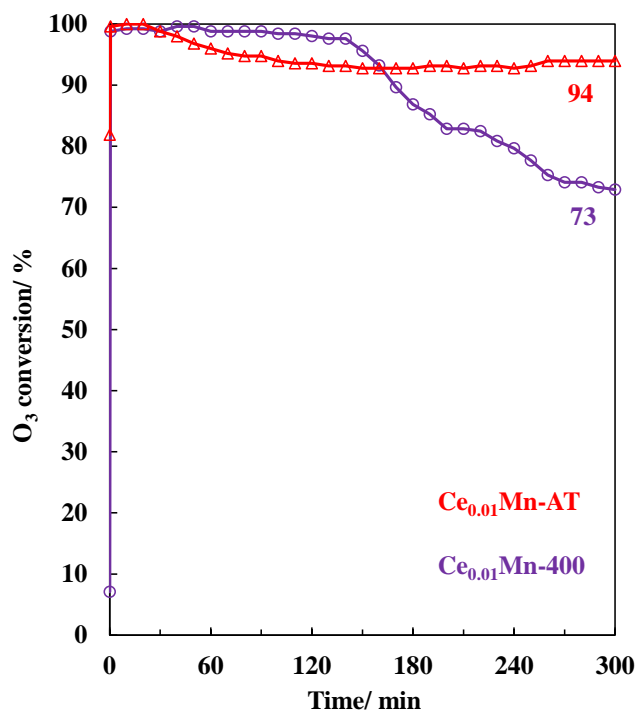


Figure 7 - 5: Ozone conversion over $\text{Ce}_{0.01}\text{Mn-400}$ and $\text{Ce}_{0.01}\text{Mn-AT}$ ($[\text{O}_3] = 300$ ppmv, GHSV = 1200 L/(g_{cata} h); RH = 0.7 %)

7-3-3- TCE abatement by non-thermal plasma (NTP)

The initial TCE concentration ($[\text{TCE}]_0$) was set at 150 ppmv based on the O_3 production through the plasma reactor. Indeed, without TCE and H_2O in the feed, the ozone concentration at the exit of the plasma reactor was 600 ppmv. Thus the $[\text{O}_3]/[\text{TCE}]_0$ ratio equal to the stoichiometric one of 4 considering the total transformation of initial amount of C into CO_2 as follow:



Regardless of the water content in the feed, RH = 0.7% or RH = 15%, TCE molecules are not fully degraded, since TCE conversion reaches 85 % and 59 %, respectively. Moreover, O_3 molecules are still present at the outlet of the plasma reactor, 315 and 190 ppmv. The lowest O_3 concentration at the outlet of the plasma reactor for the NTP-RH15% test despite the lowest obtained TCE conversion can be ascribed to the reaction of OH radicals, coming from the H_2O decomposition in plasma reactor [36,37], which can react with O_3 in the plasma [38–41]. Additionally, the CO_x yields are 46 % and 34 % for the NTP TCE abatement with RH of 0.7

% and 15 %, respectively (Figure 7-6). Interestingly, in comparison with results obtained with the same plasma discharge and plasma reactor (CO_x yield of 15% in humid air ($\text{RH} = 15\%$) for ED of 120 J.L^{-1}), the mineralization of TCE is then much higher, probably as a result of $[\text{O}_3]/[\text{TCE}]_0$ optimized ratio of 4 instead of less than 1 in previous studies [11,12,42,43].

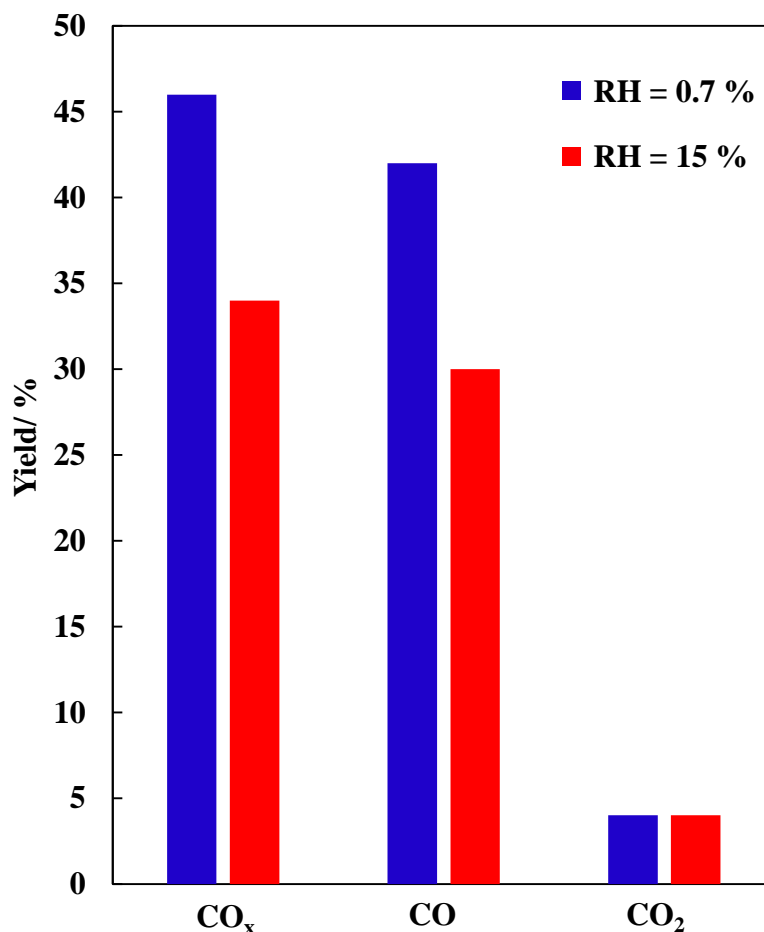


Figure 7 - 6: CO_x , CO and CO_2 yields obtained in NTP TCE abatement with RH of 0.7 % and 15 % (ED = 150 J/L; Q= 1 L/min; $[\text{TCE}]_0 = 150 \text{ ppmv}$)

The FTIR spectra of the inlet TCE and outlet stream after NTP TCE abatement, with 0.7% and 15 % as relative humidity are presented in **Figure 7-7**. The FTIR spectra for inlet TCE show the characteristic bands of TCE. The characteristics bands for TCE at 945 cm^{-1} and 865 cm^{-1} are still present but their relative intensities are higher in humid air according to the lowest TCE conversion aforementioned discussed. Furthermore, (oxi) chlorinated by-products such as dichloroacetylchloride (DCAC) (IR bands at 740, 989, 1076, 1055 (overlap with O_3) and 1773 cm^{-1}), phosgene (PG) (IR bands at 852 (overlap with TCE) and 1827 cm^{-1}) and trichloroacetaldehyde (TCAD) (IR band at 1760 cm^{-1}) are also detected in line with the incomplete gaseous oxidation of TCE. The detection and possible reaction schemes of

formation such (oxi) chlorinated oxidation by products have already been observed and discussed elsewhere [36–38]. With almost no water in the feed ($RH = 0.7\%$), TCE molecules react with ClO radicals to produce DCAC, then DCAC molecules further decompose by attack of Cl radicals to produce CCl_4 , $CHCl_3$ and $COCl_2$ molecules [36,44]. However, with RH of 15%, ClO radicals are certainly quenched by OH radicals (coming from H_2O) leading to less amount of DCAC (Figure 7).

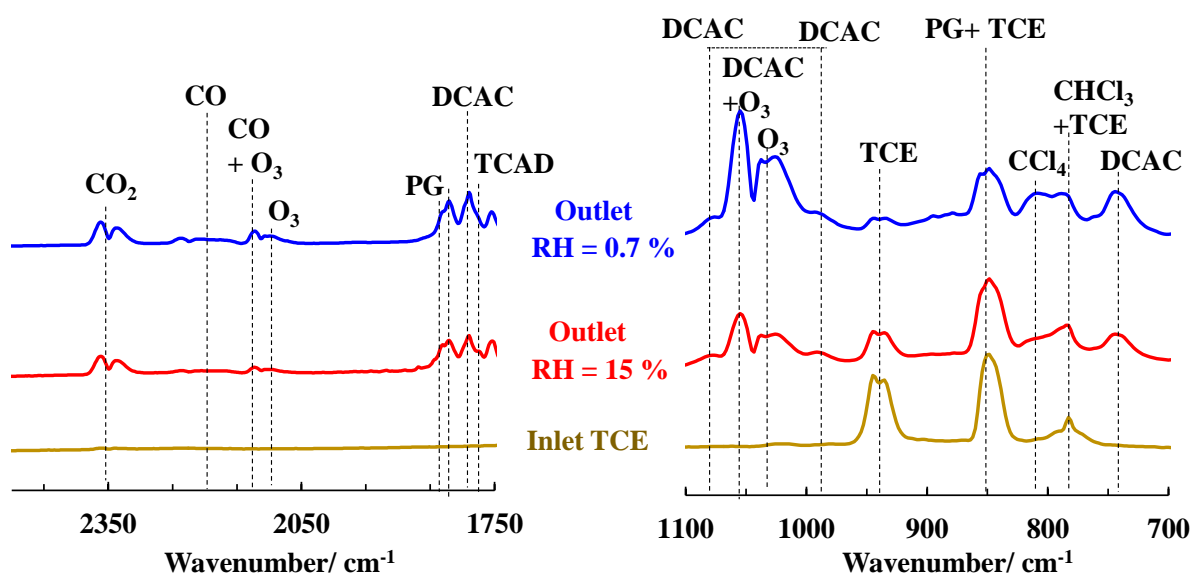


Figure 7 - 7: FT-IR spectra in the range $2500\text{--}1700\text{cm}^{-1}$ and $1110\text{--}700\text{cm}^{-1}$ of outlet stream after NTP in 0.7 % and 15 % as relative humidity ($ED = 150\text{ J/L}$, $Q = 1\text{ L/min}$) (PG : phosgene; DCAC : dichloroacetylchloride and TCAD : trichloroacetaldehyde)

7-3-4-TCE abatement by Post plasma catalysis (PPC)

In PPC configuration with $RH = 0.7\%$, TCE is fully converted regardless of the catalysts ($Ce_{0.01}Mn\text{-AT}$ and $Ce_{0.01}Mn\text{-400}$) used. Figure 8 shows the CO_x and CO_2 yields as a function of time with the two catalysts. As compared with NTP, CO_x yield increased and especially CO_2 yield is significantly improved from 4 % to 58 % at $t = 0$. Among the two PPC configurations, that with $Ce_{0.01}Mn\text{-AT}$ downstream of the NTP outperforms the one with $Ce_{0.01}Mn\text{-400}$ for the 5-hour test. For both configurations, CO_x and CO_2 yields decreased with time of reaction. However, for $Ce_{0.01}Mn\text{-400}$ the decay is more pronounced during the first 30 minutes. After 120 minutes the catalysts seem to reach a steady state as CO_x and CO_2 yields values are rather constant (**Figure 7-8**).

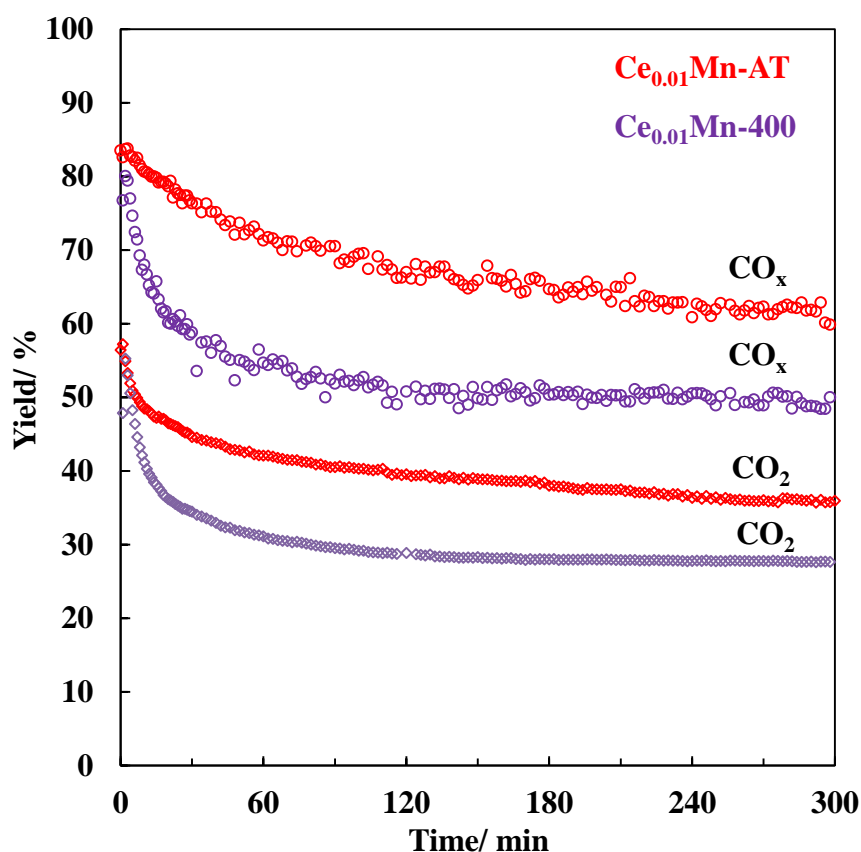


Figure 7 - 8: CO_x and CO₂ yields obtained for TCE abatement (RH = 0.7%) in PPC configuration with Ce_{0.01}Mn-400 and Ce_{0.01}Mn-AT as catalysts

Figure 7-9 and **Figure 7-10** present the FTIR spectra recorded between 700 and 1110 cm⁻¹ and 1700-1800 cm⁻¹, of the inlet TCE and the outlet gaseous stream after post plasma treatment using Ce_{0.01}Mn-400 and Ce_{0.01}Mn-AT with RH= 0.7%. In PPC configurations, as compared with NTP, band at 945 cm⁻¹ corresponding to TCE is not observed while the intensity of the bands corresponding to CO₂ vibration increases whatever the catalyst under concern. Similarly, the ozone band disappears. Interestingly, the characteristic bands of DCAC and TCAC decreased in intensity when Ce_{0.01}Mn-400 is used as catalyst and even disappeared with Ce_{0.01}Mn-AT catalyst. Such result could be related to the efficient O₃ activation over catalysts allowing the DCAC and TCAC by-products decomposition. Based on the relative intensity of the PG band it seems that after one hour the PG amount is almost the same irrespective of the catalyst. It is noticeable the emergence of new bands corresponding to C-Cl bond vibration relative to CHCl₃ and CCl₄ located at wavenumber of 774 cm⁻¹ and 794 cm⁻¹ respectively. These C1 chlorinated formations can be explained by the reaction of CHCl₂ and CCl₃ radicals resulting mainly from the easy cleavage of the carbon-carbon bond of DCAC with adsorbed chlorine.

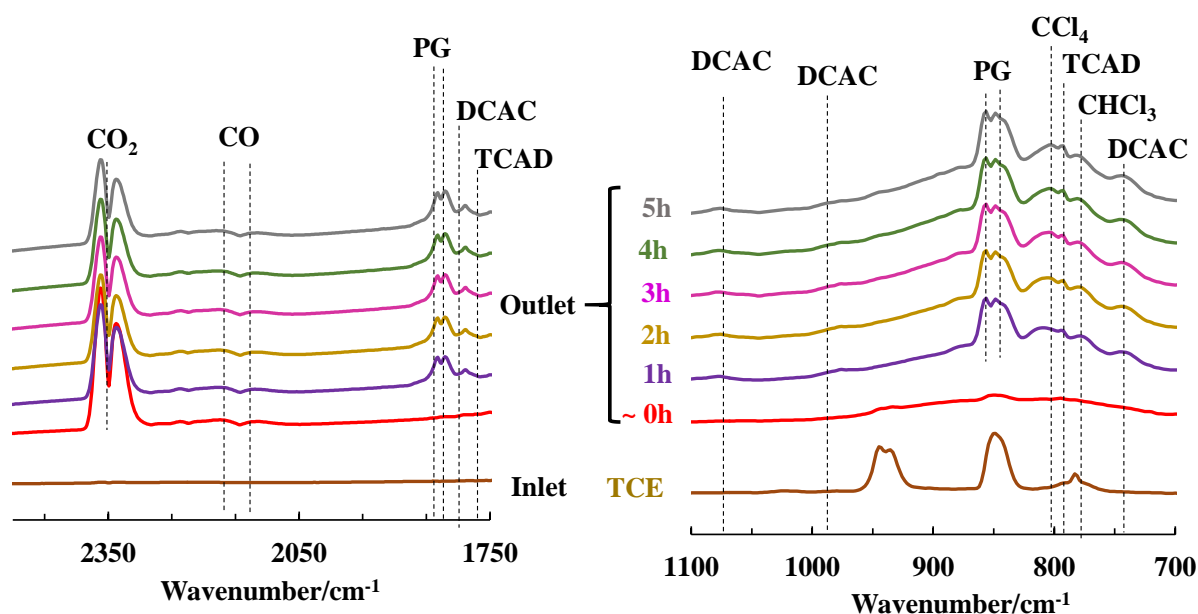


Figure 7 - 9: FT-IR spectra of the inlet TCE and outlet gaseous stream after PPC process (RH = 0.7 %) as a function of time with $\text{Ce}_{0.01}\text{Mn-400}$ as catalyst (PG : phosgene; DCAC : dichloroacetylchloride ;TCAD : trichloroacetaldehyde)

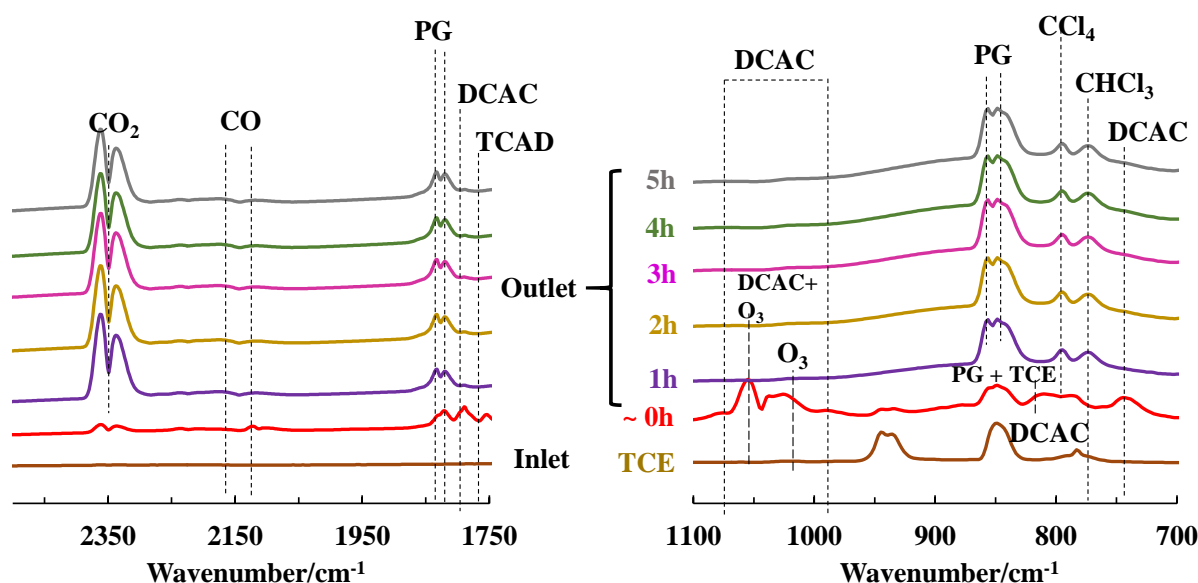


Figure 7 - 10: FT-IR spectra of the inlet TCE and outlet gaseous stream after PPC process (RH = 0.7 %) as a function of time with $\text{Ce}_{0.01}\text{Mn-AT}$ as catalyst (PG: phosgene; DCAC: dichloroacetylchloride; TCAD: trichloroacetaldehyde)

7-3-5- TCE abatement in post plasma catalysis (PPC) configuration RH = 15%

The effect of relative humidity on PPC process for TCE decomposition has been studied in the presence of $\text{Ce}_{0.01}\text{Mn-AT}$ as the best catalyst. **Figure 7-11** shows the CO_x and CO_2 yields obtained as a function of time in humid air (RH = 15 %). In comparison with RH = 0.7% condition, the yields are lower but rather stable during the 5 hours of experiment.

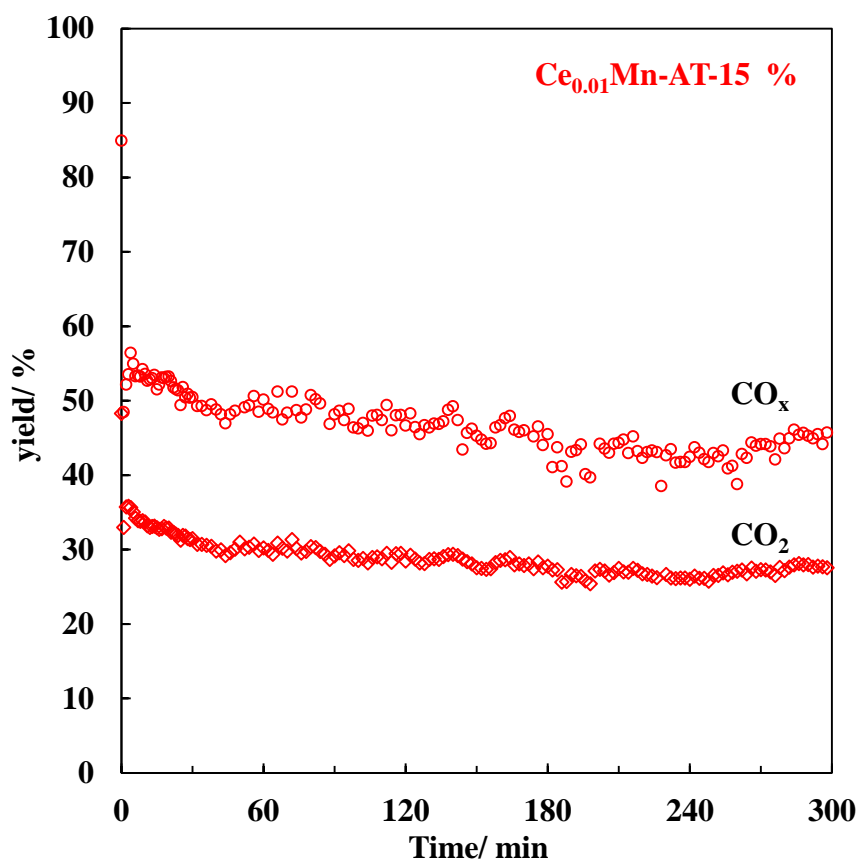


Figure 7 - 11: CO_x and CO₂ yields obtained for TCE abatement (RH = 15%) in PPC configuration with Ce_{0.01}Mn-AT as catalyst

Figure 7-12 presents the FT-IR spectra of the inlet TCE and outlet gaseous stream after PPC process (RH = 15 %) as a function of time with Ce_{0.01}Mn-AT as catalyst. As previously observed with RH = 0.7 %, neither bands for TCE nor ozone are observed after PPC process. DCAC and TCAD bands are observed in contrast to what we observed in PPC process with RH = 0.7 %. However, it is usually reported that (i) the DCAC formation comes from the reaction of TCE with ClO radicals and (ii) in the presence of water, DCAC formation is suppressed because of the quenching of ClO radicals by OH radicals according to the following reaction: $\text{ClO} + \text{OH} \rightarrow \text{HCl} + \text{O}_2$. This discrepancy could be explained by the presence of ozone in higher quantity in our experimental conditions in comparison with that found in the literature. In our experimental conditions, OH radicals could react with O₃ in sufficient quantity instead of ClO radicals. This result could also explain the lowest CO_x yield value owing to O₃ consumption by OH radicals.

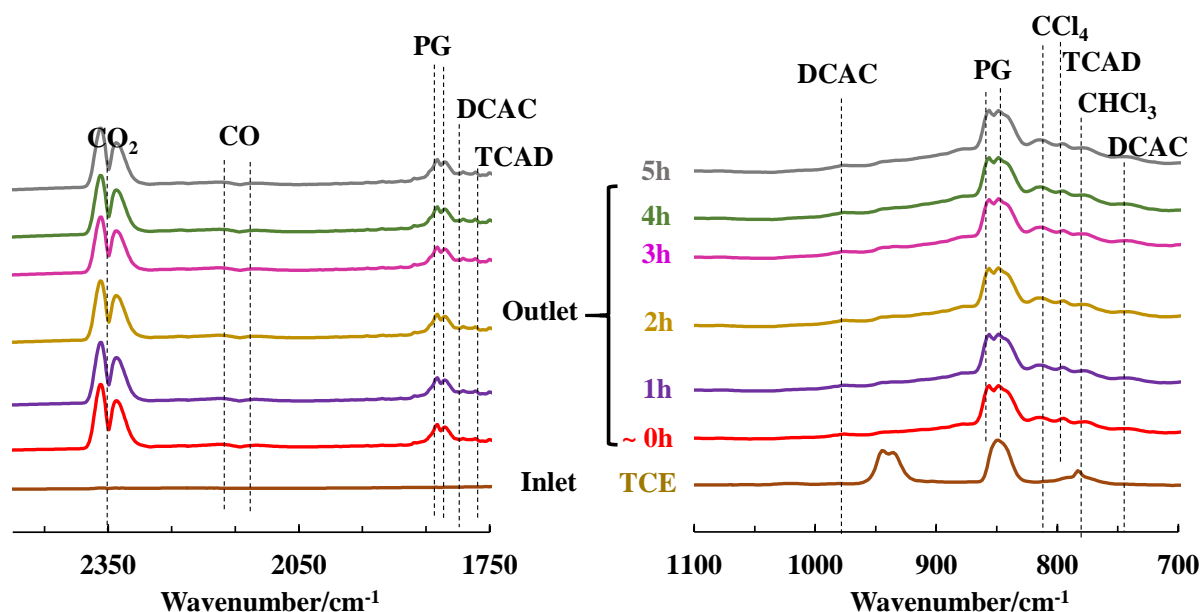


Figure 7 - 12: FT-IR spectra of the inlet TCE and outlet gaseous stream after PPC process (RH = 15 %) as a function of time with $\text{Ce}_{0.01}\text{Mn-AT}$ as catalyst (PG: phosgene; DCAC: dichloroacetylchloride; TCAD: trichloroacetaldehyde)

7-4- XPS characteriations of the used catalysts after PPC process

After PPC process a slight oxidation of manganese species is observed at the surface regardless of the catalysts. Indeed, the $\text{Mn}^{3+}/\text{Mn}^{4+}$ decreases (**Figure 7-13(a)**) in agreement with the increase of Mn AOS calculated from Mn 3s splitting (**Table 7-4**). All catalysts present also a surface Ce enrichment over Mn after PPC process. After reaction, chlorine element has been detected at the surface of both catalysts (**Table 7-4**). This chlorine detection can be explained by the incomplete degradation of TCE during the PPC process. The Cl 2p core level envelope can be simulated by considering two types of chlorine (**Figure 7-13(b)**). The Cl 2p_{3/2} photopeak at 198.5 ± 0.2 eV can be attributed to metal (M) chloride, with M = Ce and/or Mn [39,42] while the Cl 2p_{3/2} photopeak at 200.6 ± 0.2 eV is ascribed to (oxi)chlorinated organic species such as $\text{CH}_x\text{Cl}_y(\text{O}_z)$ [39,42]. The organic chlorine over mineral chlorine ratio ($\text{Cl}_{\text{org}}/\text{Cl}_{\text{min}}$) has been calculated for the tested catalysts. The best catalyst in TCE degradation ($\text{Ce}_{0.01}\text{Mn-AT}$) presents a lower $\text{Cl}_{\text{org}}/\text{Cl}_{\text{min}}$ ratio (0.14) in comparison with the ratio obtained for $\text{Ce}_{0.01}\text{Mn-400}$ (0.42), suggesting that the formation of (oxi)-chlorinated organic species at the surface is detrimental to the catalytic performance. This assumption is reinforced by comparing the ratios obtained for the catalyst tested in different RH conditions. Indeed, with RH = 15% the activity of $\text{Ce}_{0.01}\text{Mn-AT}$ was lower and the $\text{Cl}_{\text{org}}/\text{Cl}_{\text{min}}$ ratio is higher (0.35).

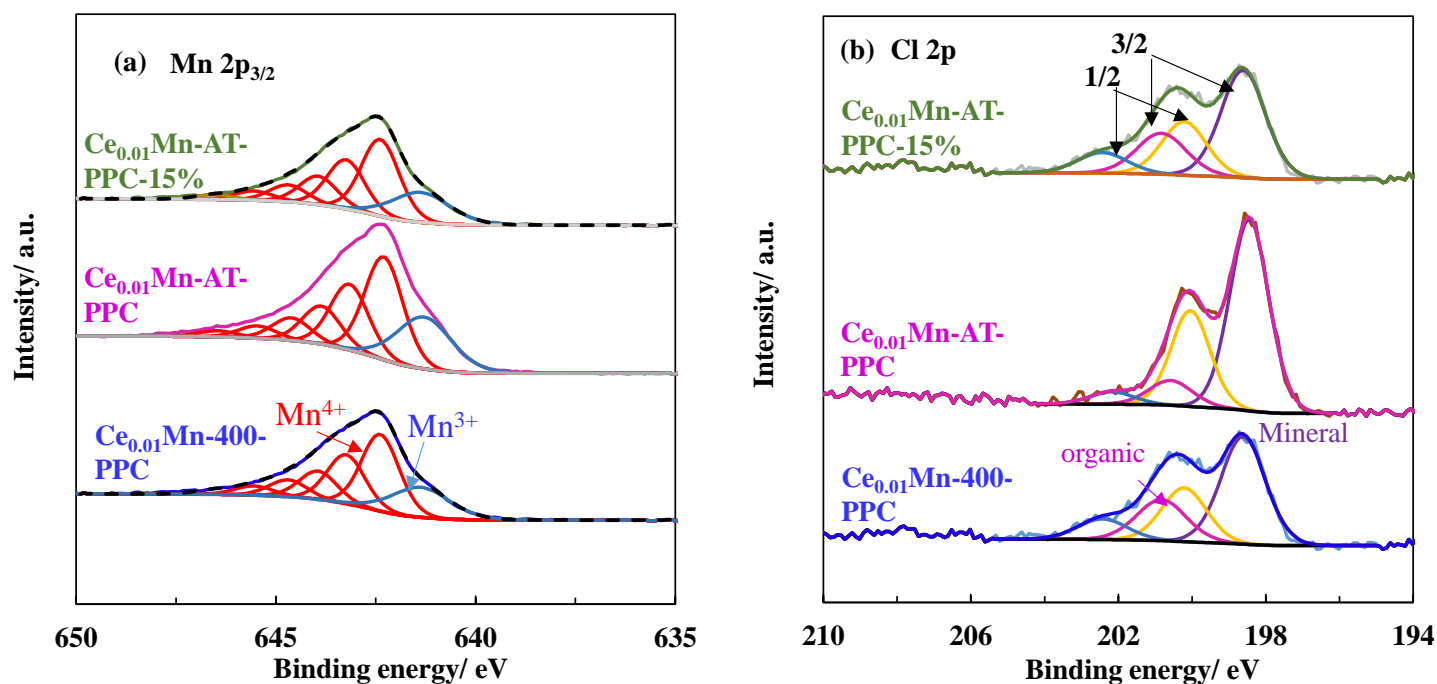


Figure 7 - 13: XPS (a) Mn2p_{3/2} and (b) Cl2p core levels decomposition after PPC process

Table 7 - 4: Semi quantitative XPS analysis for used (PPC) catalysts

Catalyst	O/Mn	K/Mn	Na/Mn	Ce/Mn	Cl/Mn	Mn ³⁺ /Mn ⁴⁺	Mn AOS from Mn 3s splitting
Ce _{0.01} Mn-400	2.07	0.18	0.05	0.015		0.34	3.44
Ce _{0.01} Mn-400-PPC	2.34	0.26	0.05	0.024	0.18	0.21	3.56
Ce _{0.01} Mn-AT	1.97	0.06	-	0.018		0.38	3.32
Ce _{0.01} Mn-AT-PPC	1.91	0.04	-	0.028	0.16	0.29	3.42
Ce _{0.01} Mn-AT-PPC-15%	1.81	0.04	-	0.025	0.22	0.28	3.41

7-5- Conclusion

In this work TCE abatement was investigated at 100 °C in nearly dry (RH = 0.7 %) and moist air (RH = 15 %) in PPC configuration using a 10 pin-to plate negative DC corona discharge NTP reactor and cerium modified birnessites calcined at 400 °C or treated with nitric acid as catalysts. The plasma conditions were chosen in order to treat a low concentration of TCE (150 ppmv) to be as close as industrial issue in terms of VOC concentration abatement. A stoichiometric ratio $[O_3]/[TCE]_0$ of 4 was adopted in order to take advantage of the efficient properties of the catalysts for O_3 decomposition.

In these conditions, the TCE removal efficiency was 85 % but the CO_x yield was only 46 % for the NTP process alone. Adding a catalyst downstream of the NTP reactor enhanced the performances of the process in dry and humid air in terms of TCE removal efficiency and CO_2 selectivity due to the ability of the catalyst to totally decompose ozone to generate surface active oxygen species able to oxidize the unreacted TCE and part of the polychlorinated by-products. Plasma assisted $Ce_{0.01}Mn$ -AT catalyst presents the best CO_2 yield in dry air (58 %) at the beginning of the experiment to reach after 5 hours 40 % with no production of DCAC and TCAD in hard experimental conditions such as high GHSV of 600 L/g.h, with only 0.1g of catalyst. In this configuration the formation of gaseous chlorinated by-products was minimized but not totally suppressed. Both catalysts exhibited a good stability for TCE abatement which mean they were chlorine tolerant. $Ce_{0.01}Mn$ -AT was tested in moist air and was also stable over time which means also its water tolerance.

7-6- References

- [1] B. Huang, C. Lei, C. Wei, G. Zeng, *Environ. Int.* 71 (2014) 118–138.
- [2] C. Wu, J. Schaum, *Environ. Health Perspect.* 108 (2000) 359–363.
- [3] R.E. Doherty, *Environ. Forensics* 1 (2000) 69–81.
- [4] F. Holzer, F.D. Kopinke, U. Roland, *Plasma Chem. Plasma Process.* 25 (2005) 595–611.
- [5] M. Schiavon, V. Torretta, A. Casazza, M. Ragazzi, *Water. Air. Soil Pollut.* 228 (2017) 388.
- [6] F. Thevenet, L. Sivachandiran, O. Guaitella, C. Barakat, A. Rousseau, *J. Phys. Appl. Phys.* 47 (2014) 224011.
- [7] H.L. Chen, H.M. Lee, S.H. Chen, M.B. Chang, S.J. Yu, S.N. Li, *Environ. Sci. Technol.* 43 (2009) 2216–2227.
- [8] Ch. Subrahmanyam, A. Renken, L. Kiwi-Minsker, *Chem. Eng. J.* 160 (2010) 677–682.
- [9] J. Wu, Q. Xia, H. Wang, Z. Li, *Appl. Catal. B Environ.* 156–157 (2014) 265–272.
- [10] X. Tu, H.J. Gallon, J.C. Whitehead, *J. Phys. Appl. Phys.* 44 (2011) 482003.
- [11] S. Sultana, Z. Ye, S.K.P. Veerapandian, A. Löfberg, N. De Geyter, R. Morent, J.M. Giraudon, J.F. Lamonier, *Catal. Today* 307 (2018) 20–28.
- [12] S.K.P. Veerapandian, Z. Ye, J.-M. Giraudon, N. De Geyter, R. Morent, J.-F. Lamonier, *J. Hazard. Mater.* 379 (2019) 120781.
- [13] V.A. Drits, E. Silvester, A.I. Gorshkov, A. Manceau, *Am. Mineral.* 82 (1997) 946–961.
- [14] A.-C. Gaillot, *Dr. Univ. Joseph Fourier – Grenoble I* (2002) 1–392.
- [15] M. Villalobos, B. Lanson, A. Manceau, B. Toner, G. Sposito, *Am. Mineral.* 91 (2006) 489–502.
- [16] Y. Liu, W. Yang, P. Zhang, J. Zhang, *Appl. Surf. Sci.* 442 (2018) 640–649.
- [17] T. Gopi, G. Swetha, S. Chandra Shekar, C. Ramakrishna, B. Saini, R. Krishna, P.V.L. Rao, *Catal. Commun.* 92 (2017) 51–55.
- [18] L. Li, P. Zhang, R. Cao, *Catal. Sci. Technol.* 10 (2020) 2254–2267.
- [19] R. Cao, P. Zhang, Y. Liu, X. Zheng, *Appl. Surf. Sci.* 495 (2019) 143607.
- [20] Y. Liu, H. Zhou, R. Cao, X. Liu, P. Zhang, J. Zhan, L. Liu, *Appl. Catal. B Environ.* 245 (2019) 569–582.
- [21] B. de Rivas, R. López-Fonseca, J.R. González-Velasco, J.I. Gutiérrez-Ortiz, *J. Mol. Catal. Chem.* 278 (2007) 181–188.
- [22] E. Eren, H. Gumus, B. Eren, A. Sarihan, (n.d.) 8.

- [23] J. Chen, X. Chen, D. Yan, M. Jiang, W. Xu, H. Yu, H. Jia, *Appl. Catal. B Environ.* 250 (2019) 396–407.
- [24] X. Tang, J. Li, L. Sun, J. Hao, *Appl. Catal. B Environ.* 99 (2010) 156–162.
- [25] M. Sun, B. Zhang, H. Liu, B. He, F. Ye, L. Yu, C. Sun, H. Wen, *RSC Adv.* 7 (2017) 3958–3965.
- [26] M.C. Biesinger, B.P. Payne, A.P. Grosvenor, L.W.M. Lau, A.R. Gerson, R.St.C. Smart, *Appl. Surf. Sci.* 257 (2011) 2717–2730.
- [27] V.R. Galakhov, M. Demeter, S. Bartkowski, M. Neumann, N.A. Ovechkina, E.Z. Kurmaev, N.I. Lobachevskaya, Ya.M. Mukovskii, J. Mitchell, D.L. Ederer, *Phys. Rev. B* 65 (2002) 113102.
- [28] V.P. Santos, M.F.R. Pereira, J.J.M. Órfão, J.L. Figueiredo, *Appl. Catal. B Environ.* 88 (2009) 550–556.
- [29] Y. Liu, W. Yang, P. Zhang, J. Zhang, *Appl. Surf. Sci.* 442 (2018) 640–649.
- [30] B. Dhandapani, S.T. Oyama, *Appl. Catal. B Environ.* 11 (1997) 129–166.
- [31] W. Li, S.T. Oyama, *J. Am. Chem. Soc.* 120 (1998) 9047–9052.
- [32] W. Li, G.V. Gibbs, S.T. Oyama, R.V. April, *J Am Chem Soc* 120 (1998) 9041–9046.
- [33] G. Zhu, J. Zhu, W. Jiang, Z. Zhang, J. Wang, Y. Zhu, Q. Zhang, *Appl. Catal. B Environ.* 209 (2017) 729–737.
- [34] T. Gopi, G. Swetha, S. Chandra Shekar, C. Ramakrishna, B. Saini, R. Krishna, P.V.L. Rao, *Catal. Commun.* 92 (2017) 51–55.
- [35] X. Li, J. Ma, H. He, *J. Environ. Sci.* 94 (2020) 14–31.
- [36] A.M. Vandenbroucke, M.T.N. Dinh, J.M. Giraudon, R. Morent, N. De Geyter, J.F. Lamonier, C. Leys, *Plasma Chem. Plasma Process.* 31 (2011) 707–718.
- [37] A.M. Vandenbroucke, R. Morent, N. De Geyter, C. Leys, *J. Adv. Oxid. Technol.* 14 (2011) 165–175.
- [38] A.M. Vandenbroucke, R. Aerts, W. Van Gaens, N. De Geyter, C. Leys, R. Morent, A. Bogaerts, *Plasma Chem. Plasma Process.* 35 (2015) 217–230.
- [39] A.M. Vandenbroucke, M.T. Nguyen Dinh, N. Nuns, J.-M. Giraudon, N. De Geyter, C. Leys, J.-F. Lamonier, R. Morent, *Chem. Eng. J.* 283 (2016) 668–675.
- [40] R. Peyrous, *Ozone Sci. Eng.* 12 (1990) 41–64.
- [41] J. Chen, P. Wang, *IEEE Trans. Plasma. Sci* 33 (2005) 808–812.
- [42] M.T.N. Dinh, J.-M. Giraudon, A.M. Vandenbroucke, R. Morent, N. De Geyter, J.-F. Lamonier, *Appl. Catal. B Environ.* 172–173 (2015) 65–72.

- [43] M.T.N. Dinh, J.M. Giraudon, J.F. Lamonier, A. Vandenbroucke, N. De Geyter, C. Leys, R. Morent, *Appl. Catal. B Environ.* 147 (2014) 904-911.
- [44] A. Vandenbroucke, PhD University of Ghent (2015) 371.

General conclusion and outlook

Conclusion

In this thesis, the use of PPC for the abatement of trichloroethylene is investigated with the objective to optimize the PPC process that means, total VOC decomposition with a low energy consumption. Thus, Focus was on operating the PPC system at low energy density in combination with a catalyst at low temperature to improve the efficiency of the abatement of low TCE concentration (150 ppmv) to be as close as industrial issues. Special attention was paid to adapt the molar ratio of NTP produced O_3 to the initial concentration of TCE, namely $[O_3] / [TCE]_0$ to supply enough reactive oxygen species to quantitatively oxidize TCE into CO_2 . The choice of a suitable catalyst for PPC process is based on some basic requirements such as, ozone decomposition ability, oxygen mobility, and high CO_2 selectivity coupled with a chlorine and water tolerance. Ce doped birnessite type- MnO_2 are chosen as a base catalysts as they are known to be highly efficient for ozone decomposition due to improved textural properties, a modification of Mn average oxidation state and an increase of structural defects e.g oxygen vacancies resulting from the formation of crystal boundaries between MnO_2 and CeO_2 . These materials were synthesized *via* a redox method using $KMnO_4$ as oxidant and $NaC_3H_5O_3$ as reductant with a ratio $KMnO_4 / NaC_3H_5O_3 = 1.2$. In order to improve the water and chlorine tolerance a nitric acid treatment is also performed.

In a first step (chapter IV), the decomposition of HCHO using cerium doped birnessite as a catalysts has been systematically studied. Indeed, this reaction is well known to correlate the density of oxygen vacancies in the material, which are the active center for ozone decomposition and TCE oxidation. The effect of calcination temperature ($T_c = 200, 300$ and $400\text{ }^\circ\text{C}$), Ce content (Ce_xMn ; $x = 0, 0.01, 0.1, 0.2$ and 0.5) for the materials calcined at $400\text{ }^\circ\text{C}$, and relative humidity ($RH = 0, 50$ and 75%) on formaldehyde oxidation has been evaluated. Four important conclusions were made from this work: (1) Regardless of Ce content, calcined Ce_xMn exhibited higher catalytic performance than calcined parent birnessite. (2) Low Ce doping ratio are beneficial for formaldehyde oxidation. (3) The catalytic activity increases as increasing the calcination temperature. These superior performance of Ce_xMn calcined at $400\text{ }^\circ\text{C}$ was attributed to improved textural properties such as high surface areas, low crystallinity and structural disorder (presence of oxygen vacancies) and to its high reducibility. Additionally, the overall characterization (H_2 -TPR, TEM, ToF-SIMS), can ensure the interaction between Ce and Mn even at low doping ratio which improves the content of oxygen vacancies and enhance

the oxygen mobility of Ce_xMn surface, which contributes to the enhancement of catalytic activity as well as reaction rate for HCHO removal since less intermediates were formed over Ce_xMn . The high extent of Ce reduced state for $\text{Ce}_{0.01}\text{Mn}$ calcined at 400 °C accounted for its improved performances for HCHO oxidation in dry and moist air (RH: 75 %). (4) Catalytic experiments performed in a free oxygen atmosphere showed the high mobility of catalyst oxygen to participate in HCHO oxidation which increases as increasing the calcination temperature (T_c).

In a second step (chapter V), the ozone and concomitant nitrogen oxide formations by negative DC (Direct Current) corona discharge at atmospheric pressure using a 10-pin-to-plate reactor in dry/humid air stream have been discussed. The effects of operating parameters such as energy density (ED), flow rate (F) and relative humidity (RH) on the ozone and nitrogen oxide formation production have been investigated. A reaction scheme is proposed to account for the N_2O_5 and HNO_3 formations based on the NO_x oxidation by ozone. With a $Q = 1$ L/min and $ED = 150$ J/L, ozone concentration is almost 600 ppmv with a stable plasma in a glow discharge regime.

In a Third step (chapter VI), ozone decomposition over Ce doped birnessite treated or not with nitric acid has been investigated at low temperature (20 - 40 °C). The effect of Ce content ($\text{Ce}/\text{Mn} = 0, 0.01, 0.1, 0.2$ and 0.5), nitric acid treatment (0.2M HNO_3 , at 50°C for 6 hours) in the presence or absence of nitrogen containing co-pollutants and water. Three important conclusions were made from this work: (1) Ce_xMn catalysts processed better activity for ozone decomposition than that of the parent birnessite but these non-acid treated catalysts deactivate rapidly over time due to presence of $\text{N}_2\text{O}_5/\text{HNO}_3$. Detailed surface characterizations show that nitrogen adspecies, especially NO_3^- , poison the non-treated catalysts (2) acid treated catalysts exhibited better catalytic performance in ozone decomposition than as synthesized samples in dry and moist air (30%). (3) Catalysts treated with acid with low Ce doping ratio are more active for ozone decomposition. The better tolerance of the best acid-treated catalysts ($\text{Ce}_{0.01}\text{Mn-AT}$ and $\text{Ce}_{0.1}\text{Mn-AT}$) to co-pollutants and water can be explained by the high density of acid sites and oxygen vacancies which facilitate the adsorption and decomposition of ozone and allow to minimize the amount of nitrogen containing adspecies which can affect the catalytic performances for O_3 decomposition.

In the final experimental chapter, trichloroethylene (TCE) abatement was investigated in dry and moist air (15%) with NTP using a 10-pin-to-plate negative DC corona discharge and

with PPC using $\text{Ce}_{0.01}\text{Mn}$ as catalysts calcined at 400°C ($\text{Ce}_{0.01}\text{Mn-400}$) or treated with nitric acid ($\text{Ce}_{0.01}\text{Mn-AT}$). In comparison with NTP process, PPC was found to be more efficient. Total conversion of TCE was obtained in PPC process irrespective of the catalyst used with catalyst temperature at 100°C in dry and moist air. A remarkable increase of CO_2 yield has been observed in PPC configuration and explained by the facile oxidation of polychlorinated by-products (adsorbed at the surface) by active oxygen species coming from the catalytic decomposition of ozone. Plasma assisted $\text{Ce}_{0.01}\text{Mn-AT}$ catalyst (100°C) presents the best CO_2 yield in dry air with minimization of the formation of gaseous chlorinated by-products in hard experimental conditions such as high GHSV of 600 L/g.h , with only 0.1 g of catalyst. This result is attributed to high content of oxygen vacancies with a higher amount of Mn^{3+} , to improved specific surface area and to strong surface acidity. These features allow also a promoting ozone decomposition efficiency. Both catalysts exhibited a good stability towards chlorine. $\text{Ce}_{0.01}\text{Mn-AT}$ tested in moist air ($\text{RH} = 15 \%$) showed a good stability as a function of time indicating also a good water tolerance.

Conclusion Table 1: Summary of the important results obtained in this work

HCHO catalytic oxidation	<p>$\text{Ce}_{0.01}\text{Mn-400}$ exhibited the best activity, showed a T_{50} of 50°C for the abatement of 100 ppmv of HCHO with a GHSV of $60 \text{ Lg}_{\text{cat}}^{-1}\text{h}^{-1}$ in dry air with 0.2 g of catalyst.</p> <p>Excellent stability vs time of $\text{Ce}_{0.01}\text{Mn-400}$ in the presence of water ($\text{RH} = 75\%$). 50% HCHO conversion into CO_2 at 50°C for 13 h</p>
O_3 catalytic decomposition	<p>$\text{Ce}_{0.01}\text{Mn-AT}$ exhibited the best activity, showed 94% and 96% conversion of 300 ppmv of O_3 with a GHSV of $1200 \text{ Lg}_{\text{cat}}^{-1}\text{h}^{-1}$ in dry air at RT and moist air ($\text{RH} = 30 \%$) at 40°C respectively with 0.05 g of catalyst in the presence of nitrogen containing co-pollutants.</p>
TCE abatement in PPC process	<p>These two best previous catalyst ($\text{Ce}_{0.01}\text{Mn-400}$ and $\text{Ce}_{0.01}\text{Mn-AT}$) are used for TCE abatement.</p> <p>$\text{Ce}_{0.01}\text{Mn-AT}$ catalyst (100°C) presents the best CO_2 yield in dry air with of minimization of the formation of gaseous chlorinated by-products in hard experimental conditions such as high GHSV of 600 L/g.h, with only 0.1 g of catalyst</p>

Outlook

Last but not least, this work regarding plasma-catalytic configuration for VOCs abatement shows that there are still scientific challenges to overcome. In terms of catalytic formulation further improvement of the energy efficiency could be realized by operating catalyst at room temperature which would exclude catalyst heating and very selective towards CO_2 . The good results obtained with Ce modified birnessite treated with nitric acid open up new frontiers for further research. It would be very interesting to investigate for example the effect of palladium on the performances on these material in terms of TCE abatement. Recently, it is published that $\text{Pd}/\text{Al}_2\text{O}_3$ is a very good catalyst for ozone decomposition in presence of nitrogen oxides and water [1]. However, in real world exhaust gas, the presence of moisture is unavoidable, while in this process water has negative effect on ozone production resulting in a negative effect on TCE abatement. To further take advantage from ozone produced by NTP it could be interesting to study the effect of water by using plasma as ozoner that means to introduce TCE and water after plasma reactor. Indeed, it could also be interesting to use plasma for TCE degradation and for ozone production and study the effect of introduce only the water after the plasma reactor. In general, the typical industrial exhaust emission is rarely composed of well-defined single compounds. On one hand it is reported in the literature a positive effect such as enhanced removal efficiency, formation of reactive intermediates and reduction of the undesired by products, despite having issues of complex interacting chemistry [2–4]. On the other hand other researchers are reported negative effect resulting on the catalyst deactivation and that is related to VOC properties and concentration [5,6]. Thus it is also essential to investigate the performance if plasma-catalytic oxidation of binary and ternary mixtures VOC with different compositions. Furthermore it is very interesting to understand the mechanism of TCE oxidation on post plasma catalysis. Different assumptions of adsorption and desorption of intermediates species, oxidation of chlorinated by products by active oxygen species formed after decomposition of ozone on catalyst surfaces, determination of active sites and which chemical species play the important role in the oxidation process... all these assumptions is based on the observations and characterization observed separately through gas phase characterizations and catalyst surface analysis before and after test. From this point of view, development of well-designed instruments specialized *in-situ* measurements is highly recommended.

References

- [1] H. Touati, A. Guerin, Y. Swesi, C.B. Dupeyrat, R. Philippe, V. Meille, J.-M. Clacens, *Catal. Commun.* 148 (2021) 106163.
- [2] A.M. Harling, J.C. Whitehead, K. Zhang, *J. Phys. Chem. A* 109 (2005) 11255–11260.
- [3] O. Debono, V. Hequet, L. Le Coq, N. Locoge, F. Thevenet, *Appl. Catal. B Environ.* 218 (2017) 359–369.
- [4] W.J. Liang, J. Li, Y.Q. Jin, *J. Environ. Sci. Health Part A* 45 (2010) 1384–1390.
- [5] W. Chen, J.S. Zhang, *Build. Environ.* 43 (2008) 246–252.
- [6] C.H. Ao, S.C. Lee, J.Z. Yu, J.H. Xu, *Appl. Catal. B Environ.* 54 (2004) 41–50.

Appendix A

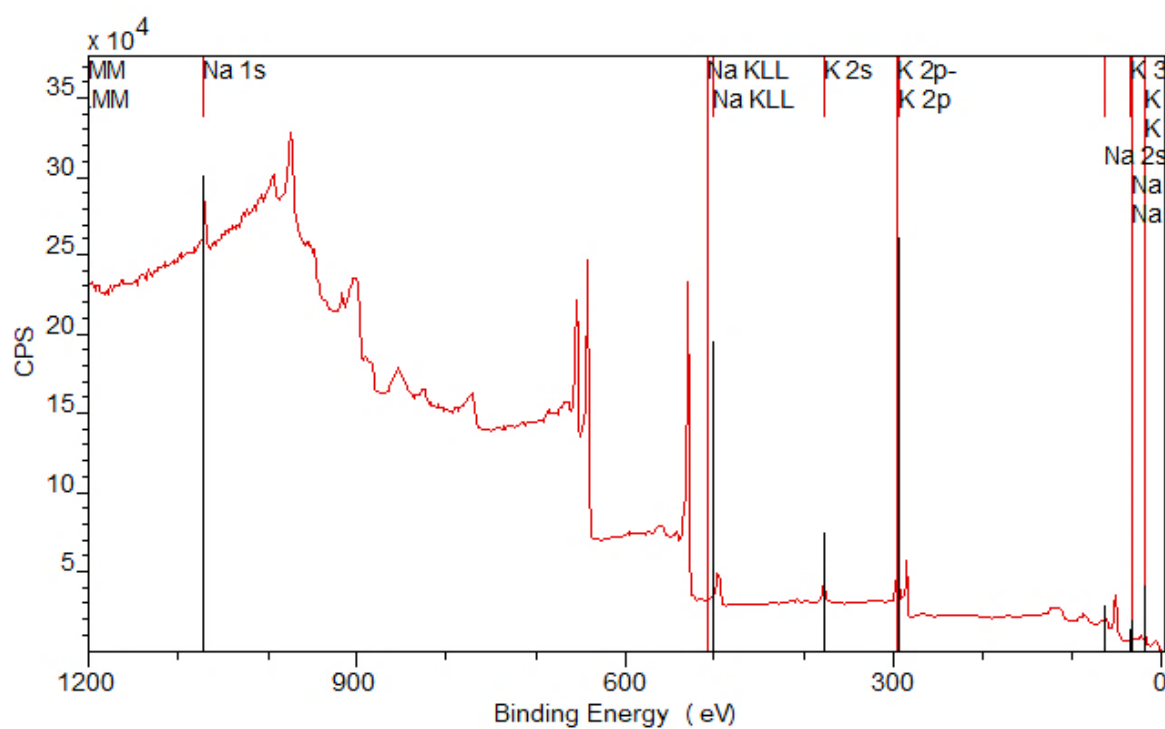


Figure A - 1: Survey XPS spectra of Mn-B